Extrusion-based melt processing of (AB)$_n$ segmented poly(urea-siloxane)s and their modification towards amphiphilic hydrogels

DISSERTATION

zur Erlangung des akademischen Grades

einer Doktorin der Naturwissenschaften (Dr. rer. nat.)

in der Bayreuther Graduiertenschule für Mathematik und Naturwissenschaften

(BayNAT)

der Universität Bayreuth

vorgelegt von

Eva Maria Fürsattel

geboren in Nürnberg

Bayreuth, 2021

Die vorliegende Arbeit wurde in der Zeit von Februar 2016 bis Dezember 2019 in Bayreuth am Lehrstuhl für Makromolekulare Chemie I der Universität Bayreuth unter der Betreuung von Herrn Professor Dr. Hans-Werner Schmidt angefertigt.

Vollständiger Abdruck der von der Bayreuther Graduiertenschule für Mathematik und Naturwissenschaften (BayNAT) der Universität Bayreuth genehmigten Dissertation zur Erlangung des akademischen Grades einer Doktorin der Naturwissenschaften (Dr. rer. nat.).

Dissertation eingereicht am: 16.11.2020

Zulassung durch das Leitungsgremium: 18.11.2020

Wissenschaftliches Kolloquium: 03.03.2021

Amtierender Direktor: Prof. Dr. Markus Lippitz

Prüfungsausschuss:

Prof. Dr. Hans-Werner Schmidt   (Gutachter)

Prof. Dr. Volker Altstädt   (Gutachter)

Prof. Dr. Seema Agarwal   (Vorsitz)

Prof. Dr. Leonid Ionov

Für meine Familie

Die vorliegende Arbeit ist als Monographie verfasst.

Teile der Arbeit sind bereits in den folgenden Publikationen erschienen:

Melt Electrowriting of Thermoplastic Elastomers

Gernot Hochleitner[1], Eva Fürsattel[1], Reiner Giesa, Jürgen Groll, Hans-Werner Schmidt and Paul D. Dalton

Macromolecular Rapid Communications, ***2018****, 1800055.*

[1] *Contributed equally to this work.*

Diese Publikation ist in der vorliegenden Arbeit mit der Literaturstelle [85] zitiert.

Soft-hard polymer gradient materials based on thermoreversible urea-siloxane networks

Eva Fuersattel, Reiner Giesa, Hans-Werner Schmidt

Abstracts of Papers, 255th ACS National Meeting & Exposition, New Orleans, LA, United States, March 18-22, 2018, POLY-785 **2018**.

Dieser Konferenzbeitrag ist in der vorliegenden Arbeit mit der Literaturstelle [163] zitiert.

Table of Contents

List of abbreviations

^{1}H-NMR	Proton nuclear magnetic resonance spectroscopy
2,4-TDI	Toluene-2,4-diisocyanate
3D	3-dimensional
a.u.	Arbitrary unit
ABS	Acrylonitrile-butadiene-styrene
AM	Additive manufacturing
ASA	Acrylonitrile-styrene-acrylate-copolymers
ATR	Attenuated total reflection
Bz-NH$_2$	Benzylamine
CA	Contact angle
CAD	Computer-aided design
cf.	Lat. *confer*
CTS	Critical translation speed
DI	Deionized water
DMTA	Dynamic mechanical thermal analysis
DSC	Differential scanning calorimetry
EEE	2-Ethoxyethyl ether
E-Modulus	Young's modulus
FDM	Fused deposition modeling
FT-IR	Fourier-transform infrared
HMDI	1,6-Hexamethylene diisocyanate
HS	Hard segment
i.e.	Lat. *id est*
IPDI	Isophorone diisocyanate
mbCHDI	4,4'-Methylene bis(cyclohexyl isocyanate)
MEW	Melt electrowriting
n.a.	Not available
n.d.	Not determined
n.o.	Not observed
p.a.	Pro analysis
PCL	Poly(ε-caprolactone)

PDMS	Poly(dimethylsiloxane)
PEG	Poly(ethylene glycol)
PEI	Poly(ether imide)
PLA	Poly(lactic acid)
PPO	Poly(propylene oxide)
PTFE	Poly(tetrafluoroethylene)
PU	Poly(urethane)
RI	Refractive index
SAXS	Small angle X-ray scattering
SEC	Size exclusion chromatography
SEM	Scanning electron microscopy
SS	Soft segment
TE	Tissue engineering
TEM	Transmission electron microscopy
TGA	Thermogravimetric analysis
THF	Tetrahydrofuran
TPE	Thermoplastic elastomer
UPy	Ureidopyrimidinone
UV	Ultraviolet
vs.	*Versus*
wt.	Weight

List of symbols

ξ	Number of functional groups
δ	Solubility parameter
ε	Strain
σ	Stress
η^*	Complex viscosity (oscillating)
ΔG	Free energy change
ΔH_m	Melt enthalpy
η_{melt}	Melt viscosity (rotational)
σ_r	Radial stress
$\dot{\gamma}$	Shear rate
$°C$	Degree Celsius
A	Area
c	Concentration
$Đ$	Dispersity
d	Interdomain spacing length
dV/dt	Flow rate
E	Field strength
E'	Elastic storage modulus
E''	Elastic loss modulus
F	Force
$f_\varnothing$	Fiber diameter
g	Gram
G'	Shear storage modulus
G''	Shear loss modulus
h	Hour
Hz	Hertz
J	Joule
K	Kelvin
m	Meter
$M_{critical}$	Critical molecular weight, when polymer chains start to entangle
min	Minute

mL	Milliliter
$\overline{M_n}$	Number average molecular weight
$\overline{M_w}$	Weight average molecular weight
$N_{A/B}$	Number of A/B functional groups
p	Conversion
p	Pressure
Pa	Pascal
Q	Degree of swelling
q_{max}	Scattering vector maximum
R	Cell radius
r	Stoichiometric ratio
$r*$	Critical radius
rpm	Rounds per minute
R_v	Volume expansion ratio
s_c	Collector speed
sec	Second
s_j	Jet speed
T	Temperature
t	Time
T_c	Crystallization temperature
T_{cross}	Crossover temperature
T_g	Glass transition temperature
T_m	Melting temperature
U	Voltage
V	Volt
W	Water content
$\overline{X_n}$	Degree of polymerization
ω	Angular frequency
ρ_{foam}	Foam density

Summary

(AB)$_n$ segmented copolymers combine in a unique way melt processing which is important for extrusion-based additive manufacturing (AM), and thermally reversible network formation based on physical crosslinks. The objective of this thesis is to tailor this type of copolymers regarding their thermal, mechanical, and rheological properties and to establish structure-property relationships in view of different extrusion-based AM techniques, preparation of gradient materials, and foaming. These copolymers are modified towards amphiphilic (ABAC)$_n$ segmented copolymers by the incorporation of an additional hydrophilic segment. This modification allows to tune the swelling behavior in water and the preparation of mechanical stable hydrogels and hydrogel gradients. In view of biofabrication both (AB)$_n$ and (ABAC)$_n$ segmented copolymer systems are of interest as hydrophobic supporting materials and hydrogels.

(AB)$_n$ segmented poly(urea-siloxane) copolymers

This part of the thesis focuses on the *synthesis* and *optimization* of (AB)$_n$ segmented poly(urea-siloxane)s regarding their thermal, mechanical, and rheological properties with respect to extrusion-based AM techniques. The copolymers are obtained by polyaddition of poly(dimethylsiloxane) diamines (PDMS), acting as soft segments, and diisocyanates, forming the urea hard segments. The urea segments disassemble at elevated temperatures forming a processable melt. Upon cooling, self-assembly of the urea units occurs inducing solidification. Copolymers with different properties were obtained by varying the PDMS segment length and the chemical structure of the diisocyanate. Among all tested urea segments, units based on *1,6-hexamethylene diisocyanate* were found optimal for melt processing. The molecular weight and thus the *melt viscosity* was in addition tailored by adding a monofunctional reagent to match the requirements regarding melt viscosity and temperature for the applied extrusion-based processing techniques.

The copolymer composed of the shortest PDMS diamine (M_n = 1513 g mol^{-1}) and *1,6-hexamethylene diisocyanate* was utilized for *extrusion-based AM*. Using *melt electrowriting* (MEW) uniform fiber diameters below 20 μm were achieved. Accurate deposition and high stacking up to a building height of 50 layers were accomplished. This copolymer is a perfect candidate for MEW, even surpassing in some points the benchmark material poly(ε-caprolactone). Processing soft, elastic materials via *fused deposition modeling* (FDM) is still challenging because soft filaments are not transported accurately into the die. To nevertheless print a soft, elastic copolymer with a Young's modulus of 36 MPa, the existing FDM setup was modified by improving the feeding system. At 125 °C, a 5 cm high, defect-free square tube was fabricated, demonstrating for the first time the potential of the copolymers for FDM.

Summary

Using two (AB)$_n$ segmented copolymers with a high difference in their Young's modulus, a *longitudinal mechanical gradient material* was prepared from the *melt*. As a result, a mechanical gradient with a total length of 70 mm and a width of 10 mm was obtained. This variation of the Young's modulus from 5 to 40 MPa was measured with non-destructive tensile tests.

Several chemically different (AB)$_n$ segmented copolymers were investigated regarding their foam forming ability. Utilizing a *pressure-induced batch foaming process* the copolymers form soft foams. The foam properties depend strongly on the soft segment length and the chemical structure of the hard segment. Foams with the hard segment based on *1,6-hexamethylene diisocyanate* are stable. By varying temperature and pressure, optimal processing parameters were determined: A pressure of 150 bar and 40 °C are optimal parameters for this copolymer. The density was reduced by more than 70% and cell sizes around 1 µm were obtained. The compression moduli can be adjusted between 10 kPa and 220 kPa.

Amphiphilic (ABAC)$_n$ segmented poly(urea-siloxane) copolymers combining hydrophobic and hydrophilic segments

The objective of the second part of this thesis was to design a versatile class of stable hydrogels based on melt processable (ABAC)$_n$ segmented copolymers. The incorporation of hydrophobic and hydrophilic segments in the same copolymer enables tuning of hydrogel properties while maintaining melt processability. Thermally reversible physical crosslinks are provided again by urea segments.

Thus poly(urea-siloxane)s with additional hydrophilic segments were synthesized by combining in addition to the hydrophobic PDMS component, diamines based on poly(ethylene glycol) (PEG). These amphiphilic (ABAC)$_n$ segmented PDMS-PEG copolymers were characterized with small angle X-ray scattering, transmission electron microscopy, and other methods. The best results with respect to hydrogel formation were obtained using a commercial PEG with terminal poly(propylene oxide) diamine (Jeffamine) as hydrophilic segments. The hydrogel stability depends on the built-in ratio of the hydrophobic to hydrophilic component. Up to a Jeffamine content of 38 wt.% stable hydrogels with a water content of 54% were obtained.

The PDMS-Jeffamine copolymers with a Jeffamine content of 8 wt.% and 38 wt.% were selected for *extrusion-based 3D printing*. These copolymers possess a suitable melt viscosity at 130 °C. Structures with accurate stacking of homogenous strands were printed. The drying process of these water swollen 3D constructs were investigated by environmental scanning electron microscopy. Further a *hydrogel gradient* with a length of 50 mm was fabricated. The gradient was characterized by measuring the contact angle at several spots along the axis. A change from 98.2° to 90.4° was determined demonstrating a continuously increasing hydrophilicity.

Zusammenfassung

(AB)ₙ segmentierte Copolymere kombinieren auf elegante Weise die Verarbeitung aus der Schmelze, welche für extrusionsbasierte additive Fertigungsverfahren (AM) wichtig ist, und eine thermisch reversible Netzwerkbildung durch physikalische Vernetzung. Ziel dieser Arbeit ist es, diese Copolymere hinsichtlich ihrer thermischen, mechanischen und rheologischen Eigenschaften maßzuschneidern und Struktur-Eigenschafts-Beziehungen aufzustellen. Im Hinblick auf verschiedene extrusionsbasierte AM Techniken, sowie für die Herstellung von Gradientenmaterialien und Schäumen. Diese Copolymere werden durch den Einbau eines zusätzlichen hydrophilen Segments zu amphiphilen (ABAC)ₙ segmentierten Copolymeren modifiziert. Diese Modifikation ermöglicht die Anpassung des Quellverhaltens in Wasser und die Herstellung von mechanisch stabilen Hydrogelen und Hydrogelgradienten. Im Hinblick auf die Biofabrikation sind sowohl (AB)ₙ als auch (ABAC)ₙ segmentierte Copolymersysteme als hydrophobe Trägermaterialien und Hydrogele von großem Interesse.

(AB)ₙ segmentierte Poly(urea-siloxan) Copolymere

Dieser Teil der Arbeit konzentriert sich auf die *Synthese* und *Optimierung* von (AB)ₙ segmentierten Poly(urea-siloxan)en hinsichtlich ihrer thermischen, mechanischen und rheologischen Eigenschaften für die Anwendung in extrusionsbasierten AM Techniken. Die Copolymere werden durch Polyaddition von Poly(dimethylsiloxan)diaminen (PDMS), welche als Weichsegmente fungieren, und Diisocyanate, die die Harnstoffhartsegmente bilden, erhalten. Die Harnstoffsegmente disaggregieren bei erhöhten Temperaturen unter Bildung einer verarbeitbaren Schmelze. Während des Abkühlens kommt es zur Selbstassemblierung der Harnstoffeinheiten, die ein Erstarren der Schmelze bewirkt. Copolymere mit unterschiedlichen Eigenschaften wurden durch Variation der PDMS-Segmentlänge und der chemischen Struktur des Diisocyanats erzielt. Unter allen getesteten Harnstoffsegmenten wurden Systeme basierend auf *1,6-Hexamethylendiisocyanat* als optimal für die Schmelzverarbeitung befunden. Das Molekulargewicht wurde zusätzlich durch Zugabe eines monofunktionellen Reagenzes hinsichtlich Schmelzviskosität und Temperatur für die angewandten extrusionsbasierten Verarbeitungsverfahren angepasst.

Das Copolymer, bestehend aus dem kürzesten PDMS-Diamin (M_n = 1513 g mol^{-1}) und *1,6-Hexa-methylendiisocyanat*, wurde in verschiedenen AM Verfahren eingesetzt. Unter Verwendung von *melt electrowriting* (MEW) wurden einheitliche Faserdurchmesser kleiner 20 µm realisiert. Präzise Ablage und hohe Stapelung bis zu einer Höhe von 50 Schichten wurden erzielt. Dieses Copolymer ist ein ausgezeichneter Kandidat für MEW und übertrifft in einigen Punkten sogar Poly(ε-caprolacton), das als Benchmark in der MEW Technik gilt. Die Verarbeitung weicher, elastischer Materialien mittels FDM (*Fused Deposition Modeling*) ist noch immer eine Herausforderung, da weiche Filamente mit der herkömmlichen Technik nicht präzise durch die Düse gefördert werden können. Um dennoch ein weiches, elastisches Copolymer mit einem Elastizitätsmodul von nur 36 MPa drucken zu können, wurde der bestehende FDM-Aufbau durch Optimierung des Fördersystems modifiziert. Bei 125 °C wurde ein 5 cm hoher, fehlerfreier offener Quader gedruckt, was zum ersten Mal das Potenzial der Copolymere für FDM demonstriert.

Unter Verwendung von zwei (AB)$_n$ segmentierten Copolymeren, die sich in ihren Elastizitätsmoduln stark unterscheiden, wurde aus der *Schmelze* ein Streifen mit einem *longitudinalen mechanischen Gradienten* hergestellt. Erhalten wurde ein Gradient mit einer Gesamtlänge von 70 mm und einer Breite von 10 mm. Diese kontinuierliche Änderung des Elastizitätsmoduls von 5 bis 40 MPa wurde mit zerstörungsfreien Zugversuchen ermittelt.

Mehrere chemisch verschiedene (AB)$_n$ segmentierte Copolymere wurden hinsichtlich ihrer Fähigkeit Schäume zu bilden untersucht. Unter Verwendung eines *druckinduzierten Batch-Schäumprozesses* bilden die Copolymere weiche Schäume. Die Schaumeigenschaften hängen hauptsächlich von der Länge des Weichsegments und der chemischen Struktur des Hartsegments ab. Schäume mit einem Hartsegment basierend auf *1,6-Hexamethylendiisocyanat* sind stabil. Durch Variation von Temperatur und Druck wurden außerdem die Verarbeitungsparameter optimiert. Ein Druck von 150 bar und 40 °C sind die besten Parameter für dieses Copolymer. Die Dichte wurde um mehr als 70% reduziert und es wurden Zellgrößen um 1 µm realisiert. Die Kompressionsmodule können zwischen 10 kPa und 220 kPa eingestellt werden.

Amphiphile (ABAC)$_n$ segmentierte Poly(urea-siloxan) Copolymere mit einer Kombination von hydrophoben und hydrophilen Segmenten

Der zweite Teil dieser Arbeit beschäftigt sich mit der Synthese einer Serie von stabilen Hydrogelen auf der Basis von schmelzverarbeitbaren (ABAC)$_n$ segmentierten Copolymeren. Der Einbau von hydrophoben und hydrophilen Segmenten in ein und dasselbe Copolymer ermöglicht die Einstellung der Hydrogeleigenschaften unter Beibehaltung der Schmelzverarbeitbarkeit. Thermisch reversible physikalische Netzwerke werden erneut durch Harnstoffsegmente realisiert.

Poly(urea-siloxan)e mit hydrophilen Segmenten wurden durch einpolymerisieren von Diaminen auf Basis von Poly(ethylenglykol) (PEG), zusätzlich zu der hydrophoben PDMS-Komponente, erhalten. Diese amphiphilen (ABAC)$_n$ segmentierten PDMS-PEG-Copolymere wurden mit Kleinwinkel-Röntgenstreuung, Transmissionselektronenmikroskopie und weiteren Methoden charakterisiert. Die besten Ergebnisse bezüglich der Hydrogelbildung wurden mit einem kommerziellen PEG mit endständigen Poly(propylenoxid)gruppen (Jeffamin) als hydrophiles Segment erzielt. Die Hydrogel-stabilität hängt vom Einbauverhältnis der hydrophoben zur hydrophilen Komponente ab. Bis zu einem Jeffamingehalt von 38 Gew.-% wurden stabile Hydrogele mit einem Wassergehalt von 54% erhalten.

PDMS-Jeffamin-Copolymere mit einem Jeffamingehalt von 8 Gew.-% und 38 Gew.-% wurden für den *extrusionsbasierten 3D-Druck* ausgewählt, da diese Copolymere eine geeignete Schmelzviskosität bei 130 °C aufweisen. Hierbei wurden Strukturen mit gleichmäßiger Stapelung von homogenen Strängen gedruckt. Der Trocknungsprozess von in Wasser gequollenen 3D-Strukturen wurde mittels *environmental scanning electron microscopy* untersucht. Zudem wurde ein *Hydrogelgradient* mit einer Länge von 50 mm hergestellt und durch Kontaktwinkelmessungen an mehreren Positionen entlang der Achse charakterisiert. Es wurde eine Änderung von 98,2° auf 90,4° ermittelt, die eine kontinuierlich zunehmende Hydrophilie anzeigt.

1.   Introduction

1.1.   Thermoplastic elastomers

Synthetic polymers can be classified into four major groups: thermoplastics, thermosets, elastomers, and thermoplastic elastomers (TPE). *Thermoplastics* are characterized by their reversible thermal processability and solubility in solvents owed to their non-crosslinked nature. Heating above the glass transition temperature T_g of amorphous thermoplastics and beyond the melting temperature T_m in case of semi-crystalline thermoplastics results in the formation of homogenous processable melts.[1] Common examples are polystyrene, polyamides, polyesters, poly(ethylene), or poly(propylene).[1] *Thermosets* and *elastomers* are both covalently crosslinked polymer networks which cannot be melt processed or dissolved. *Thermosets* are highly crosslinked polymers with a high thermomechanical stability and a high heat resistance. Owed to these properties they are used as electrical insulators, in a variety of car parts, coatings, and sealing to name a few. Common examples are phenols, epoxides, and unsaturated polyesters.[1] *Elastomers* are more loosely chemically crosslinked polymer networks with long polymer chains between the crosslinking points and a glass transition temperature T_g below service temperature. Thus they are highly flexible and possess the ability to be stretched and return to their original shape after releasing the stress. Such elastomers cannot be melt processed, however they swell in solvents. Elastomers are also known for their good resistance to abrasion and high impact strength even at low temperatures. Below T_g these materials become brittle, yet above they are flexible and due to that are applicable in for example tires, sealing rings, elastic bands, and medical applications such as tubing and membranes. Typical examples are natural rubber, silicone rubber, or poly(isoprene) and poly(chloroprene) based rubbers.[2,3] *Thermoplastic elastomers* combine the properties of thermoplastic polymers and elastomers. They benefit from both features since they can be melt processed at elevated temperatures or from solution and can be stretched to a moderate elongation while upon stress release they return to their original shape.[4,5] A physically crosslinked network is responsible for the thermoreversible nature while a T_g below service temperature results in rubber like properties.[6] In general, TPEs exhibit a two-phase morphology with thermoplastic segments (often referred to as hard segments) being chemically coupled to soft segments with glass transition temperatures below service temperature. The material properties are based on the combined properties of both phases. TPEs can be categorized into block copolymers and graft copolymers containing a hard, crystalline segment and a soft, amorphous matrix.[6,7] Such copolymers undergo microphase separation since immiscible segments are covalently bonded within the polymer backbone.[3] Common examples of TPEs are styrene block copolymer TPEs such as styrene-butadiene-styrene rubber (SBS), polyolefin TPEs, thermoplastic copolyester elastomers, polyether block amide elastomers, and thermoplastic elastomers based on polyurethanes.[4,6]

In Figure 1.1 a multi-block copolymer based TPE, more precisely an (AB)$_n$ segmented TPE, is shown schematically, illustrating the phase separation of the amorphous soft matrix and the aggregated crystalline hard phase, acting as physical crosslinks. The hard phase of (AB)$_n$ segmented TPEs, such as polyurethanes, exhibit a melting point well above service temperature. In case of SBS-type TPEs the T_g of the hard polystyrene phase determines the upper service temperature. The lower service temperature of TPEs is given by the glass transition temperature of the amorphous soft phase. These characteristic temperatures of a TPE, high T_m or T_g of the hard phase combined with a low T_g of the soft matrix, determine on the one hand the thermal processability at elevated temperatures and on the other hand provide the elastic properties at service temperature.[3,4]


Amorphous matrix
(Soft segment)

Crystalline domains
(Hard segment)

Thermoplastic elastomer
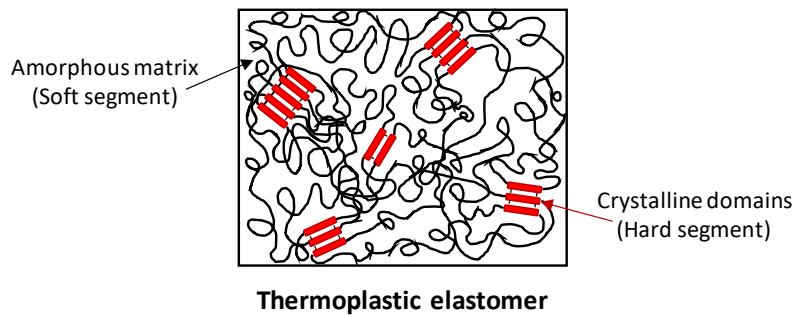
Figure 1.1: Schematic illustration of thermoplastic elastomers based on (AB)$_n$ segmented copolymers compose of discrete crystalline hard segments (red) and amorphous soft segments (black) being covalently connected within the polymer backbone. Due to their immiscibility they undergo phase separation while the crystalline domains act as physical crosslinks.

The physical and chemical properties of TPEs can be tailored by varying the ratio of the soft and hard segments by changing the chain length of the soft segment or chemical structure of the hard segment. The combination of these phases determines the specific material properties. Next to the upper service temperature the hard segments influence as multiple crosslinking points mainly the tensile strength. While the soft segment is mainly responsible for the elastic properties and flexibility of the material as well as the lower service temperature.[6,8] The (AB)$_n$ segmented copolymers with alternating sequences of soft and hard segment units are tailored to microphase separate owed to the incompatibility of the two segments of the soft segment matrix and hard segment domains. In Figure 1.2 the modulus of typical TPEs as a function of the temperature is shown. Below the T_g of the soft segment, being equal to the lower service temperature, the material is brittle and stiff, while above the T_g it shows elastic characteristics. The modulus remains at a plateau until reaching the melting temperature or T_g of the hard segments. At that point the elastic material turns into a viscous melt and the modulus decreases.[8]
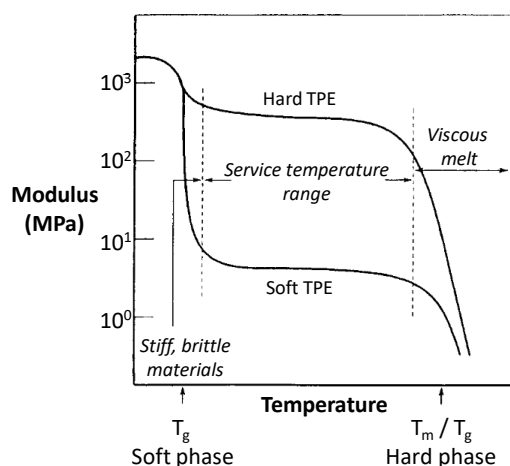
Figure 1.2: Thermomechanical behavior of TPEs is described by the materials stiffness in dependency of the temperature. Below the T_g of the soft segment the materials appear brittle, while above they are elastic up to T_m or T_g of the hard segment. Above that transition a viscous melt is obtained and the moduli decrease. The service temperature of TPEs is defined as the temperature range between T_g of the soft segment and the T_m or T_g of the hard segment. [Adapted and printed with permission from [8]; © 2014 William Andrew Publishing]

The general synthesis of $(AB)_n$ segmented TPEs is carried out in a step-growth polymerization. To obtain a high degree of polymerization stoichiometric ratios of the monomers are necessary, as well as a high conversion since the degree of polymerization increases steadily throughout the whole reaction time. Two main routes to synthesize $(AB)_n$ segmented copolymers are used in literature: one-step and two-step/prepolymer-route. The one-step route is based on a polymerization by adding all components at the beginning of the reaction while the prepolymer-route primarily includes the synthesis of a prepolymer which is coupled by a chain extender in a second step to increase the molecular weight.[9] Thermoplastic elastomers can be processed by common melt processing techniques like extrusion and injection molding. However, there are multiple parameters to be considered before melt processing a material, such as melt viscosity, melt flow, and solidification behavior upon cooling. Specifically, the melt viscosity of a material has a large impact on processing. If it is too high, the melt flow is reduced or even stopped and blocks the setup. The melt viscosity of polymers can be influenced by the applied shear rate $\dot{\gamma}$ and temperature T. Yet the temperature cannot be increased infinitely to reduce the melt viscosity owed to the limited thermal stability of polymers. Neither the applied shear rate since increasing back pressure can arise. The molecular weight of a polymer is the main factor of the melt viscosity. At low molecular weight the zero shear viscosity η_0 increases proportionally with the weight average molecular weight M_w, but at a critical molecular weight $M_{critical}$, when the polymer chains start to entangle the dependency becomes steeper with $\eta_0 \sim M^{3.4}$ (Figure 1.3).[10] Meaning with decreasing the molecular weight of a polymer the melt viscosity decreases.
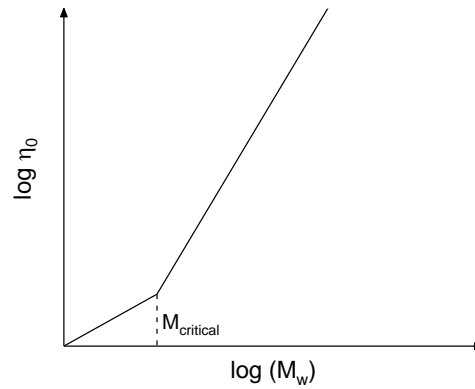
Figure 1.3: Effect of molecular weight on shear viscosity. Zero shear viscosity η_0 is proportional to the molecular weight up to a critical molecular weight $M_{critical}$, when chain entanglements occur. From that point the viscosity increases steeper with $\eta_0 \sim M^{3.4}$. [Adapted and printed with permission from [10]; © 2013 Springer]

The degree of polymerization $\overline{X_n}$ of AA-BB-type copolymers in case of a completely stoichiometric polymerization (r = 1) depends only on the conversion *p* and is given by the modified and simplified Carothers equation as shown in equation **(1.1)**:[11]

$$\overline{X_n} = \frac{1}{1-p} \qquad (1.1)$$

Tailoring the molecular weight of a polymer and consequently the melt viscosity can be achieved in different ways such as by stopping the polymerization at a given conversion or by inducing an imbalance of the educts by adding one reactant in excess. Further, a reduction of the molecular weight can be achieved by adding a certain amount of a monofunctional reagent to the reaction mixture. Changing the stoichiometric ratio of the functional groups of a step-growth polymerization, the relationship between the degree of polymerization $\overline{X_n}$ and the reaction conversion can be quantified by the Carothers equation (equation **(1.2)**):[10,11]

$$\overline{X_n} = \frac{1+r}{1+r-2p} \qquad (1.2)$$

If a monofunctional reagent is used to tailor the molecular weight, the stoichiometric ratio *r* is defined as given in equation **(1.3)**.[11]

$$r = \frac{N_A}{N_B + 2N_{B'}} \qquad (1.3)$$

With N_A being the number of A functional groups, N_B the number of B functional groups and $N_{B'}$ the number of functional groups of the monofunctional reagent. The factor 2 takes into account that each monofunctional reagent is equally as effective as one excess of difunctional B monomer in reducing the molecular weight.[10,11]

Applying this theory for the polyaddition of (AB)$_n$ segmented copolymers the molecular weight can be reduced and the melt viscosity can be tailored in order to adopt to the selected melt processing techniques.
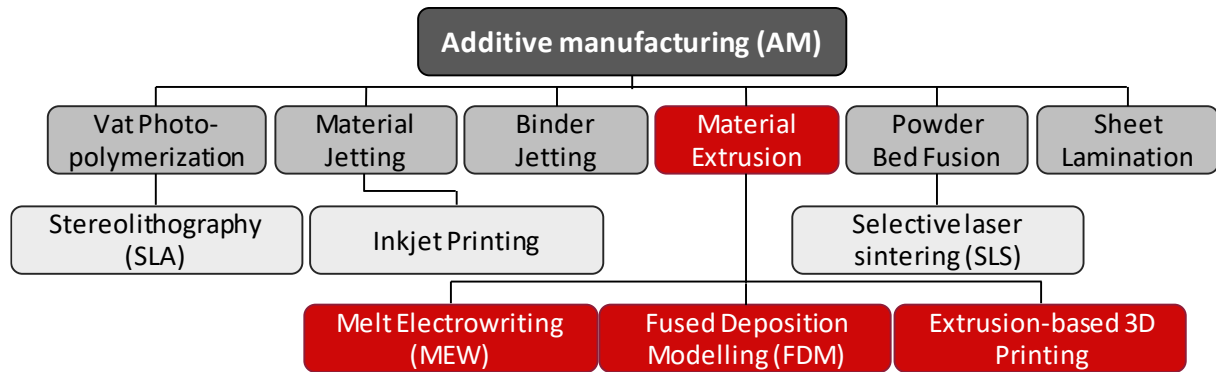
1.2. Additive manufacturing

A wide range of polymers are presented in the literature forming fibers on the micro- and nanometer scale which have multiple outstanding properties including a high surface area to volume ratio and flexibility of surface functionalities. These features make them ideal for many applications such as biomedical materials, tissue engineering, filtration, membranes, catalysis, and optical electronics.[12–15] One widely used method to fabricate such micro-/nanoscale fibers is electrospinning. However, the fiber formation and deposition using electrospinning is typically chaotic and not controlled.

Since there is a tremendous demand on 3D structures using single fiber deposition on different length scales ranging from nano- up to the centimeter scale, the research field around additive manufacturing increased rapidly in the last years. Additive manufacturing (AM) describes techniques which build 3D constructs in a directed layer-by-layer material deposition process using computer-aided design data (CAD) without the need for molds or machining.[16–18] This is achieved by adding, bonding or modifying materials in single layers. It was first introduced in the 1980s and the research field has grown in the last decade due to the possibility to produce complex objects within relatively short time.[19,20] A huge advantage of AM is that it enables a decentralized fabrication of customized products on demand with high reproducibility and low costs. In comparison to conventional subtractive or formative technologies, AM approaches can save raw material and minimize waste during the process by avoiding additional cutting and shaping steps.[18,21] Yet the throughput is comparatively low for AM in contrast to polymer mass production such as injection molding. AM finds several applications in the fields of medicine, in tissue engineering and also in the automotive and aerospace industry only to name few.[17,21] AM includes multiple techniques which are summarized in Figure 1.4. AM can be classified into six major processes differing in their way of material deposition and curing. *Vat polymerization* is based on liquid photosensitive polymers which are selectively cured by light-activated polymerization (ultraviolet light or laser). One example of such a technique is referred to as stereolithography (SLA) which was first investigated by Kodama in 1981.[22] *Material jetting* deposits single droplets of a building material. 3D objects fabricated by inkjet printing belong to this category for instance. Further *binder jetting* is an AM technique depositing a liquid bonding agent to fuse powdered materials. *Powder bed fusion* also referred to as selective laser sintering (SLS) which was introduced and patented by Deckard in 1989.[23] It is based on a powder bed which is selectively fused by thermal energy provided by a laser or an electron beam. Fusing single sheets of a material together to form a 3D object is called *sheet lamination*. Another important AM technique is based on *material extrusion* where a material is selectively extruded through a heated nozzle and deposited. Controlling the movement of the printing head and the collector plate allows a distinct deposition of the extruded molten polymer jet in a predefined pattern. This AM technique comprises melt electrowriting (MEW), fused deposition modeling (FDM) and extrusion-based 3D printing.[16,17,24] Within this thesis the focus

is on material extrusion AM based techniques. A wide range of polymers including thermoplastics, thermosets, elastomers, hydrogels, functional polymers, polymer blends, and biological systems have been used for diverse AM techniques.[17] Each technique has its advantageous and disadvantageous like limitations in resolution, printing, and fabrication speed and viscosity range only to name few.

Figure 1.4: Classification of additive manufacturing methods. Depending on material deposition, fusion, and curing of the material it can be distinguished between six major techniques which are given with respective examples. The red highlighted methods are utilized within this thesis.[17]

Melt electrowriting (MEW) is a relatively new AM technique originating from melt electrospinning. In contrast to electrospinning MEW is based on electrohydrodynamic stabilization of a molten polymer jet to fabricate defined 3D structures. A polymer is molten within a syringe and by applying a gas pressure it is extruded through a needle tip. A high voltage applied between tip and collector stabilizes the molten jet while by adjusting the collector speed the fibers can be deposited in a controlled manner while moving the printing head. Fiber diameters on the micrometer scale can be fabricated since the fiber jet is additionally thinned by the applied electrical field. The final fiber diameter and placement depends on material properties, such as the melt viscosity but can also be influenced by the intensity of the applied voltage, temperature, and applied pressure which is correlated to the flow rate.

Fused deposition modeling (FDM) results in more macroscopic objects on a centimeter scale. Therefor larger amounts of raw material are necessary than for MEW. FDM was first introduced in 1992 by Stratasys.[19] This filament-based method is widely used owed to its cost-efficiency, simplicity, and reproducibility.[20] A filament is transferred to a liquefier and a heated nozzle. Moving the printing head in a distinct manner a predesigned object is generated by depositing the extruded polymer jet on a base plate. Critical parameters during processing such as nozzle temperature, path, and speed as well as worktable temperature need to be adjusted in regard for the printed part performance and quality.[20]

Extrusion-based 3D printing is also based on a molten polymer being extruded through a nozzle tip. Yet no high voltage is applied as used for MEW. Solely by applying a pneumatic pressure on the melt it is extruded though the tip which mainly determines the fiber diameter. Moving the printing head in x-, y-, and z-direction defined 3D objects can be generated. Detailed introduction of the additive manufacturing techniques utilized within this thesis will be given in the respective chapters.

1.3. Hydrogels

Biomaterials applied in the biomedical field cover a broad Young's modulus range. Depending on their toughness and Young's modulus, they are used as dermal fillers (0.02 – 3 kPa),[25] soft contact lenses (0.2 – 1.5 MPa),[26] wound dressing (0.5 – 25 MPa),[27,28] orthopedic implants (5 – 300 GPa),[29] silicone gel-filled breast implant shells (2 – 12 MPa),[30] and catheter (0.4 – 300 MPa)[31,32] only to name few (Figure 1.5).[33,34]
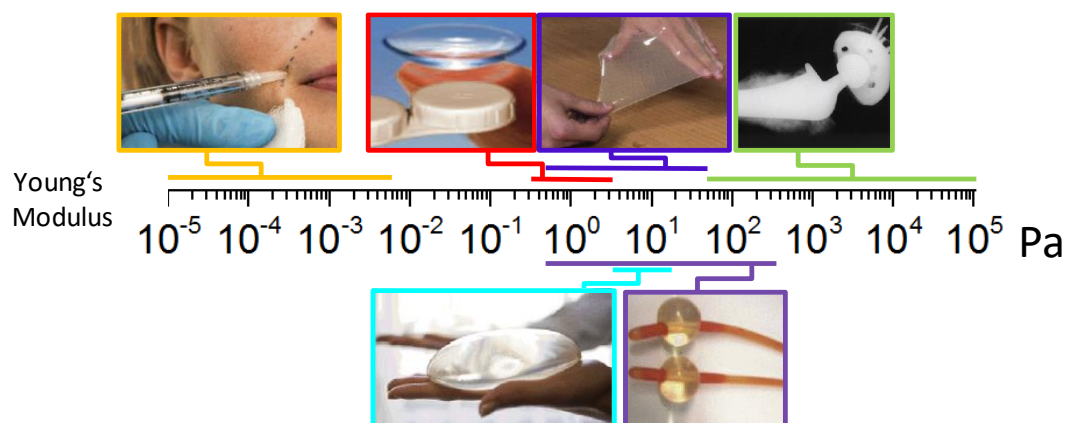
Figure 1.5: Biomaterials with different Young's moduli and their application in the biomedical field, such as contact lenses, breast implants, wound dressing etc. [Adapted and printed with permission from [33]; © 2016 Elsevier]

Hydrogels are water-swollen 3-dimensional crosslinked hydrophilic polymer networks with properties similar to soft biological tissues.[34] They find broad applications in the biomedical field and as biomaterials and are of great interest due to a large number of unique physicochemical properties, such as water-retention ability, drug loading capacity, biocompatibility, biostability but also in some cases biodegradability. Next to these features they also have drawbacks owing to their high water content which may limit their application range. This includes an extremely weak and fragile behavior, making it difficult to handle these materials.[35,36] To overcome these drawbacks in the last years the demand for synthetic biocompatible hydrogels with adjustable mechanical strength increased. Not only an easy synthesis but also processability are preferential requirements of hydrogels. Tailored mechanical properties including a combination of stiffness, strength, fatigue resistance, damping, self-healing, and high toughness are demanded.[37,38] In contrast, biological materials can have robust mechanical properties in the hydrated state, such as rubber-like proteins which can be strained to a certain degree without rupture.[39]

To match the properties of natural tissue, synthetic hydrogels based on either covalent or physical crosslinking are investigated.[34] *Chemically crosslinked hydrogels* are commonly based on photochemistry, click chemistry, or thermal crosslinking these include for example double-network hydrogels, and tetra-poly(ethylene glycol)-based hydrogels. Applying double networks[40,41] and sliding crosslinkers[42] results in complex architectures with interesting properties. Chemically crosslinked

hydrogels are not able to show self-healing after the crosslinked network is damaged, cannot be thermally processed after crosslinking, and may contain toxic residuals of initiators and catalysts. Their advantage is a high mechanical strength. ABA-systems, block copolymers with physical crosslinks, and $(AB)_n$ segmented copolymers belong to the class of *physically crosslinked hydrogels*. These supramolecular hydrogels are based on reversible, non-covalent crosslinks formed by hydrogen bonding, π-π-stacking, metal-ligand interactions, or hydrophobic interactions. These have the capability of self-healing after the network is damaged. Also a shape memory effect can be introduced by an external stimulus such as temperature or pH change. Moreover, due to the physical crosslinks multiple processing techniques from solution and the melt such as solution casting, solution and melt electrospinning, compression molding, injection molding, and extrusion-based 3D printing techniques can be utilized.

Hence the fabrication of physically crosslinked hydrogels with tunable swelling properties and gel stability matching the performance of natural tissue become more and more interesting for applications in the biomedical field and for biofabrication. Therefore, three main requirements must be met including biocompatibility, adjustment of the hydrogel properties, and an easy adaptable processing.[43] The first requirement is addressed by applying poly(ethylene glycol) (PEG) based hydrogels. Next to that polysiloxanes gained importance in the medical field, finding wide applications in surgical implants and medical devices such as cardiac pacemakers, and artificial cardiac valves due to their transparency and high oxygen permeability.[44] Combining hydrophobic PDMS with hydrophilic PEG in $(ABAC)_n$ segmented copolymers is a promising approach for biomaterials and medical applications especially in regard of the biocompatibility of both materials.[45,46] Such materials can be utilized in many blood contacting applications due to their biocompatibility and water permeability.[47,48]

2.   Objective and motivation

Additive manufacturing by directed layer-by-layer filament deposition is gaining more and more interest owed to the ease of fabricating complex 3D objects. 3D printing from the melt and fabricating 3D constructs with hydrophobic, hydrophilic or amphiphilic properties is of great interest in the 3D printing area, in particular in biofabrication as biocompatible, non-degradable supporting structures. Hence, there is a demand for melt processable polymers with adjustable mechanical and thermal properties as well as hydrophobic and hydrophilic character utilizing the advantageous of extrusion-based additive manufacturing. Furthermore, such materials are of interest for the fabrication of gradient materials and polymer foams.

The objective of this thesis is to synthesize and tailor $(AB)_n$ segmented copolymers regarding their mechanical, rheological, and hydrophilic properties and to reveal structure-property relations. Different extrusion-based additive manufacturing techniques will be applied to fabricate 3D constructs from the melt. Therefore, the melt properties of the polymers have to be optimized with respect to the applied processing technique.

This thesis is divided into two main parts, the first one focuses on *(AB)_n segmented copolymers with hydrophobic segments*, whereas the second one deals with *amphiphilic (AB)_n segmented copolymers combining hydrophobic and hydrophilic segments*. The central structural motif of both hydrophobic and amphiphilic copolymers is based on poly(urea-siloxane)s with poly(dimethylsiloxane) (PDMS) soft and urea hard segments. Hydrogen bonded urea hard segments act as physical crosslinks which disassemble upon heating and re-assemble upon cooling, providing thermoreversibility (Figure 2.1). PDMS soft segments in return provide the elastic properties of the material. By optimizing the mechanical and thermal properties, and particularly the melt viscosity, a material platform for extrusion-based melt processing, gradient fabrication and foam formation should be accessible.
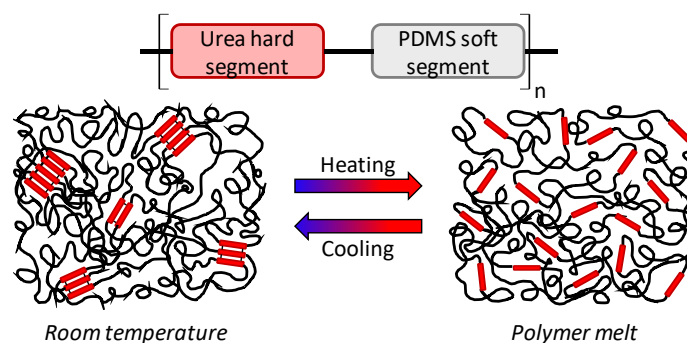
Figure 2.1: Schematic illustration of the thermoreversible nature of $(AB)_n$ segmented poly(urea-siloxane) copolymers. PDMS (black lines) acts as soft segment while at room temperature H-bonded urea units (red bars) form physical crosslinks which disaggregate upon heating. The mechanical, rheological, and thermal properties will be adjusted by varying the PDMS chain length and the chemical structure of the hard segment.

(AB)$_n$ segmented poly(urea-siloxane) copolymers

Synthesis: Series of (AB)$_n$ segmented poly(urea-siloxane) copolymers shall be synthesized and characterized to obtain a copolymer platform with a broad spectrum of properties. Variations can be realized by changing the length of the PDMS soft segment and the chemical structure of the urea hard segment. Diisocyanates containing linear, aliphatic, cycloaliphatic, and aromatic structural units are selected and their influence on the material properties will be explored. Most important is the optimization of the *melt viscosity* in view of the respective applied processing techniques.

Extrusion-based additive manufacturing: From the pool of (AB)$_n$ segmented poly(urea-siloxane)s, suitable candidates shall be selected for the fabrication of 3D constructs with different resolutions and on different length scales. *Melt electrowriting (MEW)* will be explored for the first time with poly(urea-siloxane)s. 3D structures with accurate fiber deposition and homogenous fiber diameters below 20 µm are targeted. Furthermore, *fused deposition modeling* (FDM) shall be tested as processing technique. Stable 3D objects on the cm-scale should be prepared followed by a characterization particularly with respect to layer bonding and warping.

Gradient materials: Gradients are known from nature, such as tendons which mediate between soft tissue and stiff bones by varying the Young's modulus along the material. Most macroscopic gradient materials have been processed from solution containing catalysts or initiators followed by an additional curing step. As outlined above, a series of poly(urea-siloxane)s with different melt viscosities will be available. Using different materials *macroscopic longitudinal gradients* with a continuously varying Young's modulus should be fabricated from the *melt* and mechanically characterized.

Foams: For biomedical applications not only bulk materials are of interest but also lower density materials such as *foams*. Hence, the synthesized (AB)$_n$ segmented poly(urea-siloxane)s shall be investigated also concerning their foam forming ability. Structure-property relations of the foam properties including morphology, cell size and distribution, foam density, and compression modulus should be established varying chemical structure, saturation time, temperature, and pressure of the foaming process.

Amphiphilic (ABAC)$_n$ segmented poly(urea-siloxane) copolymers combining hydrophobic and hydrophilic segments

Depending on their mechanical properties, hydrogels are used in different applications such as contact lenses, implants, and wound dressing. So far physically crosslinked (AB)$_n$ segmented copolymers based on hydrophilic poly(ethylene glycol) soft segments and urea hard segments show weak mechanical hydrogel properties and even tend to slowly dissolve in water. The objective of the second main part of this thesis is to design a novel class of *hydrogels* with fine-tunable hydrogel properties including an improved mechanical hydrogel stability and water uptake, while maintaining melt processability. To

achieve this, the underlying concept of this thesis is to introduce a second, hydrophilic soft segment in the (AB)$_n$ segmented poly(urea-siloxane) system obtaining *(ABAC)$_n$ segmented amphiphilic copolymers*. (Figure 2.2).
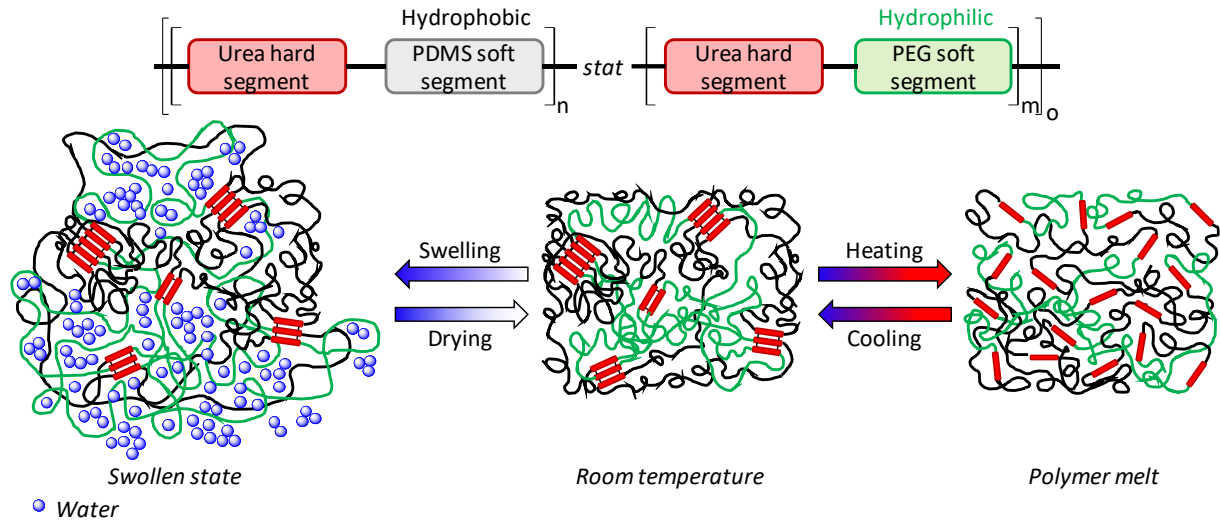
Figure 2.2: Schematic illustration of the concept of (ABAC)$_n$ segmented amphiphilic, physically crosslinked copolymers which are melt processable and are designed to swell in water while maintaining mechanical stability.

Synthesis, characterization and determination of hydrogel properties: Within the amphiphilic copolymer system presented in this thesis, the *hydrophobic* PDMS soft segment should stabilize and improve the mechanical strength of the hydrogel. Additionally, as a new feature, the *hydrophilic* poly(ethylene glycol) (PEG) soft segments will control the water uptake. The thermoreversibility of the copolymers will be maintained by physically crosslinked urea units. The influence of an increasing chain length of the hydrophilic soft segment in combination with the built-in ratio of the hydrophobic and hydrophilic blocks will be studied regarding the melt processability and hydrogel properties.

By adjusting the hydrophilicity of the amphiphilic copolymers and due to their biocompatible nature, such copolymers are also of interest in biofabrication. From the synthesized copolymers suitable candidates should be selected for *melt extrusion-based 3D printing* to fabricate 3D constructs. Processing parameters such as pressure and velocity should be varied in view of printing quality and the strand diameter. Additionally, the drying process of the water swollen 3D construct should be investigated by environmental scanning electron microscopy (ESEM). Similar to the fabrication of hydrophobic gradient materials with continuously changing mechanical properties described in the previous chapter, it is the aim to produce a *hydrogel gradient* on the macroscopic scale with a continuously variation of hydrophilicity along the longitudinal axis. The existence of such a gradient should be proven by contact angle measurements.

11

3. (AB)ₙ segmented poly(urea-siloxane) copolymers

3.1. (AB)ₙ segmented copolymers

Polydimethylsiloxane (PDMS) is one of the most widely used component in silicone elastomers owing to its unique properties such as very low glass transition temperature, high flexibility at low temperatures, high oxidative and thermal stability, UV-resistance, high surface tension, high permeability to many gases, low surface energy, and hydrophobicity as well as biocompatibility.[49–51] The latter makes this class of polymers very interesting for applications in the biomedical area and as biomaterial. Thus they are used as artificial blood vessels, catheters or other implants and fouling-release coatings.[51,52] Linear PDMS behaves as a liquid above its glass transition temperature (T_g = -123 °C).[53] At extremely high molecular weight (> 500 kg mol^{-1}) some solid like characteristics exist and cold flow is observed combined with very weak mechanical strength.[52] In order to obtain an elastomer, PDMS is generally covalently crosslinked and exhibits typically very low tensile strength (0.2 – 0.5 MPa).[52] One approach to improve the mechanical strength uses small silica particles as filler to reinforce the crosslinked silicone rubber. In addition, to improve the mechanical properties of PDMS and make it suitable for other applications there are different approaches.

The strength of silicone elastomers is improved by incorporating rigid segments into the backbone which can be either crystalline or amorphous with high melting or high glass transition temperatures, respectively. Thereby *AB*, *ABA block copolymers* or *(AB)ₙ segmented copolymer* architectures with PDMS as the soft segment were investigated.[52,54–56] The composition and length of the segments have a significant influence on the materials properties. The melt processability is limited when two phase melts occur resulting in extremely high viscosities.[9,57] Yilgör *et al.* introduced for the first time in 1982 the synthesis and characterization of (AB)ₙ segmented poly(urea-siloxane)s which is based on a step-growth polyaddition reaction.[9] The PDMS soft segment provides a high flexibility and elasticity at ambient conditions due to its low glass transition. Urea units are able to form hard segments owed to the formation of the hydrogen bonds within the PDMS soft matrix, acting as physical crosslinks. These prevent the material from flowing and determine the upper service temperature and mechanical strength of this kind of thermoplastic elastomers.[53] The hydrogen bonding capacity has an enormous effect on the morphology and material properties. Quantum mechanical calculations indicated a significantly stronger hydrogen bond energy between urea units (58.5 kJ mol^{-1}) compared to hydrogen bonded urethane groups (46.5 kJ mol^{-1}).[58] This is owed to the formation of stronger bidentate hydrogen bonding of the urea units, which results in a tougher material and improved mechanical strength, while urethane groups can only form hydrogen bonds with monodentate intermolecular strength (Figure 3.1).[59,60]
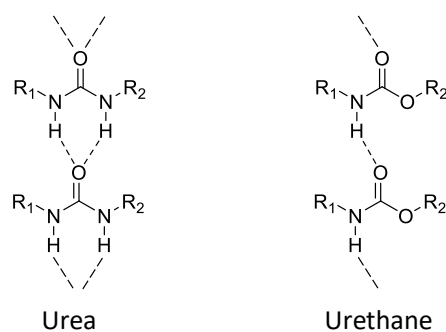
Urea   Urethane

Figure 3.1: Comparison of hydrogen bonding patterns in urea and urethane units. Owed to the formation of bidentate H-bonding between urea units and solely monodentate hydrogen bonding interaction between urethane units the hydrogen bonding strength is higher for the urea system.[60]

Other parameters such as the symmetry of the diisocyanate, the hard segment content and the average length of the hard segments have also a major impact on the material properties.[60] Yilgör *et al.* described a variety of (AB)$_n$ segmented poly(urea-siloxane)s based on *4,4-diphenyl-methane diisocyanate* utilizing a one step and a prepolymer approach.[9] The mechanical behavior was shown to be comparable to filled silicone elastomer systems and segmented siloxane containing polyurethanes. With increasing molecular weight of the PDMS segment a decreasing tensile strength was observed resulting from the reduced amount of hard segment content. The elongation increases with decreasing hard segment content.[57] Small angle X-ray scattering (SAXS) showed that (AB)$_n$ segmented poly(urea-siloxane)s undergo microphase separation owed to the large difference in the solubility parameters δ of the highly nonpolar PDMS (δ = 15.5 (J cm^{-3})$^{0.5}$) and the polar urea hard segment (δ = 45.6 (J cm^{-3})$^{0.5}$).[53,61] The microphase separation is in addition influenced by other factors such as the crystallization of the hard segments, the strength of the physical interaction, hard and soft segment chain lengths and ratios in the copolymer.[60]

Aside from these first studies, Yilgör *et al.* investigated (AB)$_n$ segmented poly(urea-siloxane)s based on aromatic *toluene diisocyanate* and cycloaliphatic *4,4-methylene bis(cyclohexyl isocyanate)*.[52,53] Also the molecular weight of the soft segment was gradually increased showing a decreasing mechanical hysteresis and a dependency of the hard segment concentration on the mechanical properties.[62,63] They further showed that the choice of solvent is very important due to the great differences between the solubility parameters of highly nonpolar PDMS and the highly polar urea hard segments. 2-Ethoxyethyl ether (EEE) and tetrahydrofuran (THF) both resulted in a homogeneous and clear solution throughout the whole reaction and high yields.[52] Further the synthesis of poly(urea-siloxane)s based on *4,4-methylene bis(cyclohexyl isocyanate)* can be conducted in isopropanol, resulting in a higher hard segment content and tensile strength above 20 MPa.[64] It was shown that isopropanol has a very low reactivity towards the diisocyanate at room temperature, excluding side reactions and the formation of chemically crosslinked biuret units. In general, the extend of side reactions is influenced by multiple factors including the diisocyanate chemical structure, reaction temperature, solvent, and

catalyst.[60,64,65] Poly(urea-siloxane) copolymers have a broad service temperature range from the low T_g of the PDMS segments up to the transition temperature when the hard segments disaggregate.

Riess *et al.* investigated the gelation behavior of different (AB)$_n$ segmented poly(urea-siloxane)s in low molecular weight silicon fluids for applications in cosmetics.[66–68] Cyclosilicones are low molecular weight silicon fluids which are widely used as ingredients in cosmetic formulations. In detail, they discussed the influence of the structure of the soft and the hard segment on the gelation behavior. A large number of copolymers with different types of hard segments and different molecular weights of the soft segment were investigated. The synthesis is a one-step synthesis of a PDMS-diamine and a diisocyanate in THF at room temperature. The molecular weight of the PDMS-diamine component ranged from 800 g mol^{-1} to 27000 g mol^{-1} and five diisocyanates with varying chemical structures ranging from linear, aliphatic to sterically hindered and aromatic diisocyanates, were investigated. It was shown that the molecular weight of the (AB)$_n$ segmented poly(urea-siloxane) is essential for the gelation properties and that a certain amount of hard segments is necessary for the thermoreversible crosslinking to obtain stable gels. To form silicon fluids into thermoreversible gels different amounts of poly(urea-siloxane)s were added to the silicon solvent and heated until the polymer was completely dissolved. The gelation was successful when the solution turned hard upon cooling and the system does not flow anymore. Riess *et al.* showed that the gel point depends strongly on the structure of the poly(urea-siloxane) but can be influenced over a wide temperature range. It increases with increasing polymer content. Further the hard segment plays an essential role on the solubility behavior of the polymer in the silicone fluid. Moreover, it was shown that the optical appearance is a major factor for an application as a clear gel. A certain concentration of the poly(urea-siloxane) is required to obtain clear gels. Below that concentration heterogeneous networks are formed consisting of gel particles and free solvent which leads to a turbid material.[66,67]

Long *et al.* introduced an isocyanate-, solvent- and catalyst-free synthetic route towards (AB)$_n$ segmented poly(urea-siloxane)s.[69] In addition, they improved the thermomechanical properties of these (AB)$_n$ segmented poly(urea-siloxane)s by incorporating an additional oxamide unit next to the urea unit.[70] Such (AB)$_n$ segmented copolymers based on PDMS-diamines with molecular weights of 1800 g mol^{-1} and 5000 g mol^{-1} and 4,4-methylene bis(cyclohexyl isocyanate) are shown in Figure 3.2.

ⴧⴧⴧⴧⴧⴧ : Siloxane soft segment
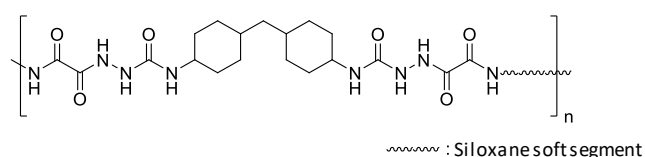
Figure 3.2: Chemical structure of poly(urea oxamide) (AB)$_n$ segmented copolymer introduced by Long *et al.*[70]

The improved thermomechanical properties are due to the pronounced microphase separated morphology proven by SAXS and atomic force microscopy (AFM). AFM phase images revealed a microphase separated morphology showing dark PDMS regions and lighter domains corresponding to the hard segments. This morphology was found to differ from solely PDMS-oxamide based copolymers which show a network of needle-like domains embedded in a matrix.[71] Yet these structures could not be revealed by transmission electron microscopy. Further dynamic mechanical thermal analysis and tensile properties confirmed the increased thermomechanical properties owing to the additional oxamide unit. The (AB)$_n$ segmented copolymers are assumed to show potential for adhesive and biomedical applications.[70]

Next to (AB)$_n$ segmented poly(urea-siloxane)s there are also other research fields concentrating on different types of poly(urea-siloxane)s including ABA type copolymers. Since these are not part of this thesis only a short overview is given for completeness. Bouteiller *et al.* studied ABA-type polymers based on PDMS and bisurea endgroups. They demonstrated the formation of rubbery solids at room temperature owed to the hydrogen bonding of the urea units and their potential for melt processing.[72,73] ABA-type supramolecular copolymers based on PDMS with urea units and ureidopyrimidinone (UPy) functional end groups have been investigated by Botterhuis and coworkers (Figure 3.3).


n = 58, 342
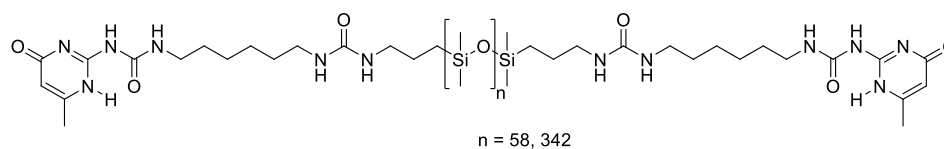
Figure 3.3: Chemical structure of ABA-type supramolecular polymer with urea and ureidopyrimidinone (UPy) functional end groups investigated by Botterhuis *et al*.[74]

They showed that the aggregation of the hydrogen bonding groups is due to the incompatibility of the soft and hard segment and results in a fibrillar morphology proven by AFM. With increasing PDMS chain length they demonstrated a change in morphology from fibrous to spherical by atomic force microscopy.[74] Another research field based on poly(urea-siloxane)s, studied by Li and coworkers, addresses the preparation of microspheres for catalysts, biosensors, and drug carriers. They developed a one-step precipitation polymerization of isophorone diisocyanate and 1,3-bis(3-aminopropyl)-1,1,3,3-tetramethyldisiloxane without the use of surfactants and initiators.[75] Poly(urea-siloxane) microspheres with sizes ranging from 2.14 μm to 7.11 μm were realized depending on the monomer ratios and concentration as well as the solvent mixture ratio.[75]

3.2. Synthesis and characterization of (AB)ₙ segmented poly(urea-siloxane)s

Within this thesis series of (AB)$_n$ segmented poly(urea-siloxane)s will be synthesized and characterized to provide a copolymer platform with a broad spectrum of properties. In Figure 3.4 the schematic illustration of such a (AB)$_n$ segmented poly(urea-siloxane) copolymer is shown in the aggregated, assembled form at room temperature and in the disaggregated, disassembled polymer melt state at elevated temperatures. Owed to hydrogen bonding of the urea units (shown in insert), hard segment domains are present at the service temperature acting as multiple crosslinking points embedded in a PDMS soft matrix. Upon heating, they disaggregate and a homogenous, isotropic melt is observed. This process is thermoreversible, upon cooling the hard segments re-aggregate driven by the formation of hydrogen bonds between the urea segments. These physical crosslinks determine the upper service temperature while the PDMS forms the soft matrix, being responsible for the elastic properties of the material with a T_g well below room temperature.
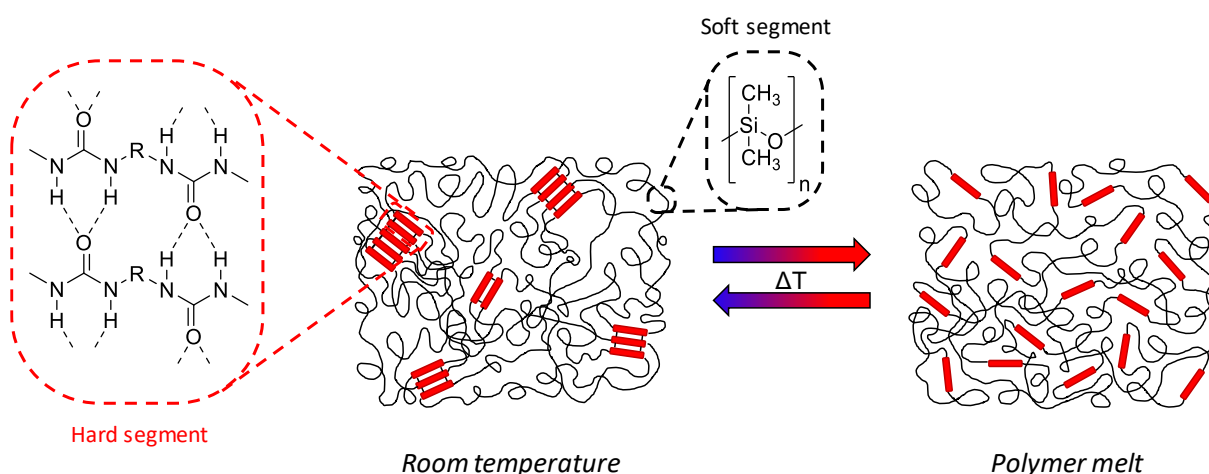
Figure 3.4: Schematic illustration of thermoreversibility of a (AB)$_n$ segmented poly(urea-siloxane) copolymer. The urea units are aggregated into discrete domains at room temperature, the so called hard segments (red bars), which are randomly embedded into the soft PDMS matrix (black lines). Upon heating above a transition temperature the hard segments disaggregate and the polymer forms an isotropic melt. Upon cooling the reverse behavior takes place.

Within this thesis series of (AB)$_n$ segmented poly(urea-siloxane) copolymers are synthesized and characterized concerning thermal, rheological, mechanical, and morphological properties. Moreover, the properties are designed and tailored for melt processing especially in regard of a constant polymer melt flow through narrow capillaries. The material properties are tailored by changing the soft segment chain length and the chemical structure of the hard segment. Three different chain length of PDMS-diamines will be used to study the influence of an increasing soft matrix on the overall material properties. A linear, aliphatic diisocyanate is used as hard segment and compared to a symmetric and an asymmetric cycloaliphatic as well as an aromatic diisocyanate. The aggregation behavior upon cooling and the influence on the mechanical properties will be investigated.

3.2.1. Synthesis

(AB)$_n$ segmented poly(urea-siloxane)s are synthesized via a polyaddition reaction of PDMS-diamines and diisocyanates at an equimolar ratio. Series of (AB)$_n$ segmented poly(urea-siloxane) copolymers differing in their PDMS chain length and the chemical structure of the diisocyanate are synthesized aiming for materials with different mechanical and thermal properties in view of melt processing techniques applied in this thesis, such as melt electrospinning, melt electrowriting, fused deposition modeling and gradient fabrication. Three commercial available PDMS-diamines were used to investigate the influence of increasing soft segment content on the material properties. The molecular weights ranging from 1513 g mol^{-1} (x = 18) to 2871 g mol^{-1} (x = 36) and 4926 g mol^{-1} (x = 64) were determined by potentiometric titration of the amine endgroups. The detailed procedure is described in the experimental part (chapter 5.2). In addition, the diisocyanate component is varied from the linear, aliphatic *1,6-hexamethylene diisocyanate* (HMDI), to the asymmetric, cycloaliphatic *isophorone diisocyanate* (IPDI), the symmetric, cycloaliphatic *4,4'-methylene bis(cyclohexyl isocyanate)* (mbCHDI), and the aromatic diisocyanate, *toluene-2,4-diisocyanate* (2,4-TDI). The general reaction is shown in Scheme 3.1. The synthesis was conducted under dry inert gas atmosphere to avoid oxidation reactions and to exclude traces of water which would disturb the stoichiometry of the polyaddition. The reaction of a diisocyanate with water leads primarily to the formation of the instable intermediate carbamic acid which decomposes to an amine and carbon dioxide. A decreased molecular weight would be the consequence. The (AB)$_n$ segmented copolymers were synthesized in THF at room temperature for 2.5 h. The completion of the reaction was proven by monitoring the absence of the diisocyanate signal at 2270 cm^{-1} using FT-IR spectroscopy. Unreacted isocyanate functionalities could lead to undesired chemical crosslinking and the formation of biuret units. The clear reaction solution was cast into a Teflon$^®$ mold followed by evaporation of THF. Elastic and transparent films with a thickness of about 1 mm were obtained, only the aromatic poly(urea-siloxane)s based on 2,4-TDI showed a slightly yellow color.

Scheme 3.1: Synthesis of (AB)$_n$ segmented poly(urea-siloxane) copolymers based on three different PDMS-diamines with increasing chain length and four diisocyanates namely *1,6-hexamethylene diisocyanate*, *isophorone diisocyanate*, *4,4'-methylene bis(cyclohexyl isocyanate)*, and *toluene-2,4-diisocyanate*.

Varying the PDMS-diamine chain length and as a consequence the concentration of the hard segments embedded in the soft matrix as well as the chemical structure of the hard segments will result in a different aggregation behavior and change the thermal and mechanical properties of the poly(urea-siloxane)s.

3.2.2. Characterization

The reaction progress was controlled by FT-IR spectroscopy. The absence of the NCO vibration (2270 cm^{-1}) indicating the complete conversion of the diisocyanate which is important to exclude any further chemical crosslinking. Figure 3.5 shows the FT-IR spectra of poly(urea-siloxane) **1a** and **3a** as well as the relevant vibrations assigned to the signals. All poly(urea-siloxane)s showed a complete reaction of the diisocyanate. The formation of the urea unit is verified by the N-H stretching vibration of the secondary amine at 3300 cm^{-1} and the C=O stretching vibration at 1625 cm^{-1}. The C-N stretching vibration is found at 1577 cm^{-1} while the C-H stretching vibration can be seen at about 2960 cm^{-1}. The characteristic symmetric CH$_3$ bending and Si-O-Si stretching vibrations are found at 1250 cm^{-1} and 1000 cm^{-1}, respectively. With increasing PDMS chain length from **1a** to **3a** the intensity of the N-H and the C=O vibrations decreases owing to the lower urea content.
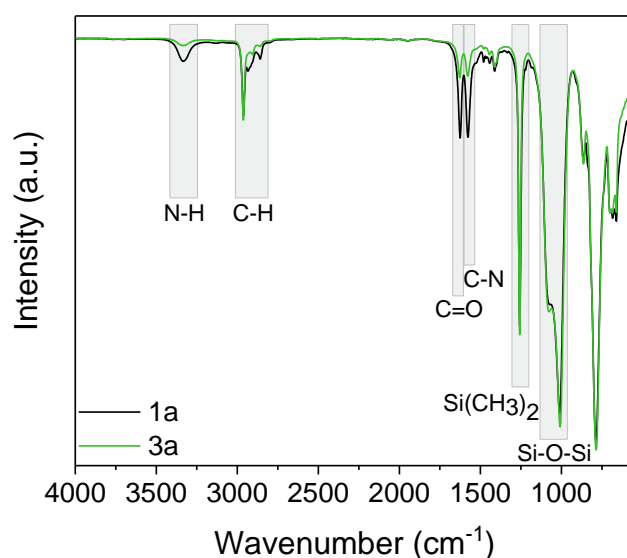
Figure 3.5: FT-IR spectra of poly(urea-siloxane) **1a** and **3a** films with a thickness of about 1 mm were measured utilizing a ATR unit. Signals are assigned to the respective vibrations. Absence of the NCO vibration at 2270 cm^{-1} prove the complete reaction of the diisocyanate. The intensity of the N-H and C=O vibrations decreases with increasing PDMS chain length from **1a** to **3a** due to a dissolution of the urea units within the system.

Moreover, the strength of the hydrogen bonding can be analyzed by FT-IR. From literature it is known that the N-H vibration is found at 3450 cm^{-1} and the C=O vibration at 1690 cm^{-1} for non-hydrogen bonded urea units.[76] Hydrogen bonded systems are found between 3320 – 3340 cm^{-1} (υ_{N-H}) and 1615 – 1650 cm^{-1} ($\upsilon_{C=O}$).[76] In Table 3.1 the wavelength of the N-H and C=O vibrations are given at room temperature for all synthesized poly(urea-siloxane)s. At the first glance it is obvious that they are all hydrogen bonded. The strength of the hydrogen bonding can also be classified by the shift of the

wavenumber. The stronger the hydrogen bonding, the lower the wavelength. The poly(urea-siloxane)s based on *1,6-hexamethylene diisocyanate* (HMDI) show the strongest hydrogen bonding (υ_{N-H} = 3334 cm^{-1} and $\upsilon_{C=O}$ = 1625 cm^{-1}) and slightly increase with decreasing PDMS chain length. The copolymers based on *isophorone diisocyanate* (IPDI) and *toluene-2,4-diisocyanate* (2,4-TDI) show the weakest hydrogen bonding owing to their steric hindrance. The *4,4'-methylene bis(cyclohexyl isocyanate)* (mbCHDI) based poly(urea-siloxane)s show slightly weaker hydrogen bonding than the HMDI copolymers.

Table 3.1: Wavelength of N-H and C=O vibrations determined by FT-IR giving an insight to the hydrogen bonding strength. The $\upsilon_{C=O}$ is between 1615 – 1650 cm^{-1} and υ_{N-H} between 3320 – 3340 cm^{-1} for hydrogen bonded units. The vibrations of free hydrogen bonding units can be assigned to 3450 cm^{-1} for υ_{N-H} and to 1690 cm^{-1} for $\upsilon_{C=O}$.

Poly(urea-siloxane)		υ_{N-H} (cm^{-1})	$\upsilon_{C=O}$ (cm^{-1})
HMDI	1a	3334	1625
	2a	3335	1626
	3a	3334	1627
IPDI	1b	3343	1628
	2b	3339	1627
	3b	3338	1628
mbCHDI	1c	3330	1628
	2c	3334	1627
	3c	3333	1628
2,4-TDI	1d	3329	1637
	2d	3320	1637
	3d	3333	1637

Poly(urea-siloxane) copolymers exhibit hydrogen bonded units acting as physical crosslinks at room temperature and upon heating the ordered, aggregated structure turns into a disordered, non-aggregated form. This behavior was proven by FT-IR spectroscopy exemplarily for **1a** by temperature dependent FT-IR spectroscopy using a heating rate of 5 K min^{-1} and an equilibration time of 3 min prior to each measurement. The sample was heated to 170 °C and cooled to room temperature. The N-H and the carbonyl vibration shift to higher wavenumbers upon heating with decreasing intensity which is due to weakening of the hydrogen bonding (appendix Figure A-6.1). Upon cooling the reverse behavior was observed due to the formation of the urea units (appendix Figure A-6.2). The wavenumber of the N-H and C=O vibrations are shown in dependence of the temperature in Figure 3.6. It can be seen that upon heating the wavenumber of both N-H **(A)** and C=O vibration **(B)** shift to higher values indicating the disaggregation of the hydrogen bonded urea units. Upon cooling the reverse behavior is observed with a retarding shift of the N-H vibration owed to the kinetically controlled process of hydrogen bonding.[60]
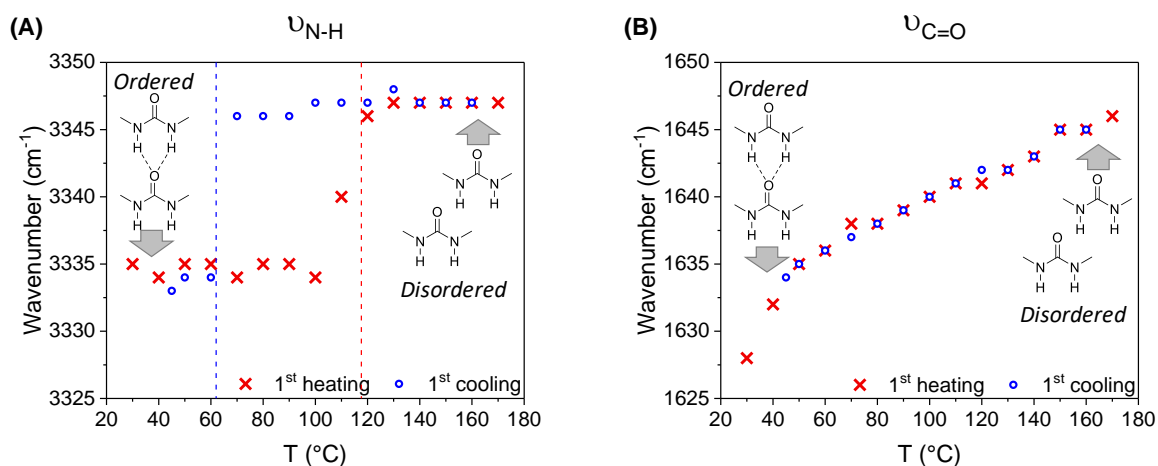
Figure 3.6: Temperature dependent FT-IR spectroscopy of poly(urea-siloxane) **1a** showing the disaggregation of the ordered hydrogen bonded urea units upon heating (crosses) and the reverse behavior upon cooling (circles). In graph **(A)** the N-H and in graph **(B)** C=O vibrations shift towards higher wavenumbers and losing hydrogen bonding strength upon heating. Upon cooling the urea units aggregate again and the wavenumbers shift backwards.

In Figure 3.7 the SEC curves of the poly(urea-siloxane)s **1a**, **2a** and **3a** based on HMDI are shown. The SEC experiments were carried out utilizing THF with 0.25 wt.% tetrabutylammonium bromide as eluent. The other SEC curves can be found in the appendix (Figure A-6.7). A monomodal molecular weight distribution is observed for all copolymers. The dispersity Đ with 1.5 – 1.8 is quite narrow for a polyaddition.
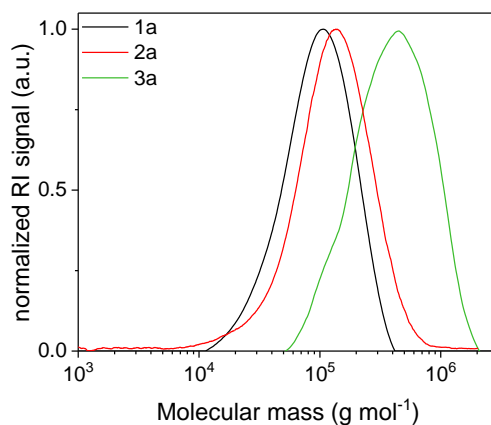
Figure 3.7: SEC chromatograms of poly(urea-siloxane)s **1a**, **2a**, and **3a** based on *1,6-hexamethylene diisocyanate* (HMDI). The SEC experiments were carried out with THF containing 0.25 wt.% tetrabutylammonium bromide as eluent. $\overline{M_n}$ and $\overline{M_w}$ were calculated based on a polystyrene calibration.

The SEC data of all (AB)$_n$ segmented poly(urea-siloxane) copolymers are summarized in Table 3.2. Additionally, the weight fractions of the siloxane soft (SS) and the urea hard segments (HS) within each (AB)$_n$ segmented copolymer are listed.

Table 3.2: SEC data of poly(urea-siloxane)s based on different PDMS chain length and different diisocyanates HMDI, IPDI, mbCHDI, and 2,4-TDI, respectively.

Poly(urea-siloxane)		$\overline{M_n}$ [a] (kg mol^{-1})	$\overline{M_w}$ [a] (kg mol^{-1})	Đ[a]	n[b]	Siloxane SS content[c] (wt.%)	Urea HS content[c] (wt.%)
HMDI	1a	73	115	1.6	43	89	11
	2a	92	156	1.7	30	94	6
	3a	306	491	1.6	60	97	3
IPDI	1b	102	166	1.6	58	86	14
	2b	311	497	1.6	100	92	8
	3b	226	369	1.6	43	94	6
mbCHDI	1c	59	103	1.7	33	85	15
	2c	92	165	1.8	29	90	10
	3c	125	189	1.5	24	95	5
2,4-TDI	1d	38	67	1.7	22	88	12
	2d	64	105	1.6	21	94	6
	3d	63	102	1.6	12	94	6

[a] Determined by SEC, eluent: THF with 0.25 wt.% tetrabutylammonium bromide, $\overline{M_n}$ and $\overline{M_w}$ were calculated based on a polystyrene calibration. Đ = $\overline{M_w}$ / $\overline{M_n}$.
[b] Repeating unit n calculated from $\overline{M_n}$ determined by SEC.
[c] Calculated weight fractions of siloxane soft (SS) and urea hard segments (HS) within the (AB)$_n$ segmented copolymers.

^{1}H-NMR spectra of **1a**, **1b**, **1c** and **1d** are shown in the appendix (Figure A-6.3 - Figure A-6.6). All signals were assigned to the corresponding protons of the poly(urea-siloxane)s.

3.2.3. Thermal properties

Differential scanning calorimetry

Thermal as well as mechanical properties of (AB)$_n$ segmented poly(urea-siloxane)s are mainly influenced by three factors. These are the extend of microphase separation between soft and hard segments, the strength of the hydrogen bonding, and finally the extend of crystallization of the hard segment.[61] Yilgör *et al.* stated that for poly(urea-siloxane)s based on mbCHDI, TDI, and 4,4'-methylene diphenyl diisocyanate (MDI) no distinct transitions attributing to the hard segment aggregation were observed in the DSC measurements since their content is quite small.[53] As can be seen in Figure 3.8, showing the first heating and first cooling curve of the DSC measurement, poly(urea-siloxane)s based on HMDI show weak and broad transitions upon heating and cooling. These are attributed to the urea hard segment disaggregation since the PDMS segment is completely amorphous with a T_g around -123 °C. The 1st heating and cooling curve is shown since the re-aggregation and the equilibrium morphology are strongly time dependent which result in even less dominant and broader transitions upon 2nd heating and cooling.[60]
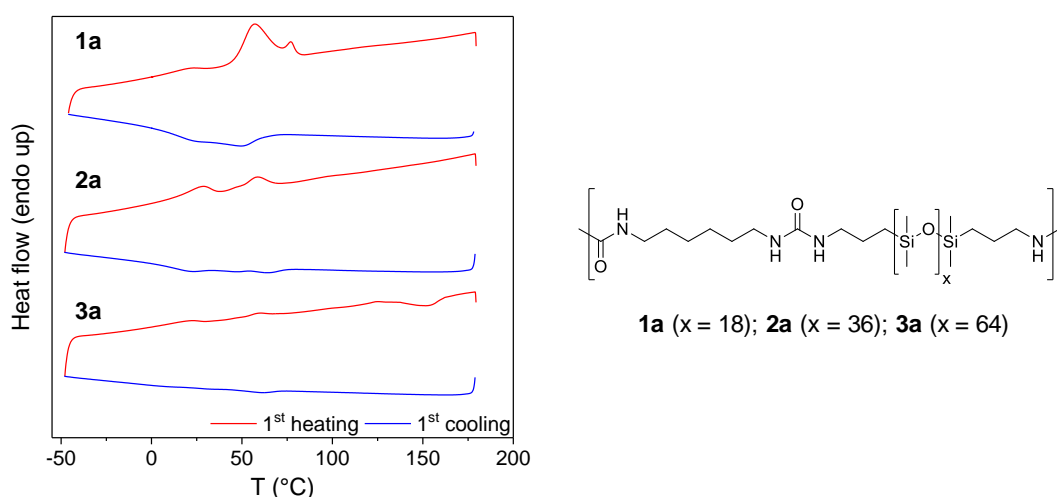
Figure 3.8: DSC curves of poly(urea-siloxane)s **1a**, **2a** and **3a** based on HMDI (heating and cooling rate: 10 K min^{-1}). Thermal transition of the disaggregation of the urea hard segments are observed as multiple broad signals. The melt enthalpy decreases with increasing PDMS chain length due to reduced hard segment weight fraction.

For the poly(urea-siloxane) **1a** which is based on the short chain PDMS (x = 18) and *1,6-hexamethylene diisocyanate* (HMDI) three melting transitions at 20 °C, 57 °C, and 77 °C are observed. The first transition is extremely weak with a melt enthalpy of $\Delta H_m = 0.7$ Jg^{-1} while the other two signals show a total melt enthalpy of $\Delta H_m = 9.9$ Jg^{-1}. Upon cooling the crystallization occurs over a broad temperature range from 70 to 10 °C with an enthalpy of -7.5 Jg^{-1} showing a high degree of re-aggregation. For poly(urea-siloxane) **2a** with a longer PDMS chain length (x = 36) two melting transitions at 28 °C and 58 °C could be detected. Upon cooling the crystallization also occurred over a broad temperature range from about 80 to 15 °C. Yet, with increasing PDMS chain length the enthalpy decreases significantly

23

(Table 3.3). This is explained by the dilution of the urea units within the copolymer and therefore a lower concentration of aggregated hard segment domains. For **3a**, poly(urea-siloxane) with the longest PDMS chain length (x = 64), weak melting transitions at 28 °C, 59 °C and 124 °C could be detected. The crystallization range could be determined between 70 and 40 °C. In each case the melting temperature is more a transition over a broad temperature range rather than a single melting transition. This can be explained by a broad size distribution of the hard segment domains which melt successively according to their domain size.

Table 3.3: DSC data of poly(urea-siloxane)s based on different PDMS chain length and *1,6-hexamethylene diisocyanate* (HMDI).

Poly(urea-siloxane)		T_m (°C)			ΔH_m (Jg^{-1})			$T_{cryst.}$ (°C)		ΔH_c (Jg^{-1})	
HMDI	**1a**	20.2	56.9	77.0	0.7	9.9		49.1	-	-7.5	-
	2a	27.6	58.4	-	1.8	1.9	-	64.4	20.4	-0.7	0.8
	3a	20.1	58.9	124.1	0.6	0.5	3.0	60.4	-	-0.5	-

However, for poly(urea-siloxane)s **1b**, **2b**, and **3b** based on *isophorone diisocyanate* (IPDI) no transitions upon heating or cooling were detected by DSC as can be seen in Figure 3.9. As discussed before the hydrogen bonding of these urea units are weaker which might result in weaker thermal transitions which cannot be detected by DSC. Further it is assumed that the sterically hindrance of the hard segments cannot form hydrogen bonds as efficient.

1b (x = 18); **2b** (x = 36); **3b** (x = 64)
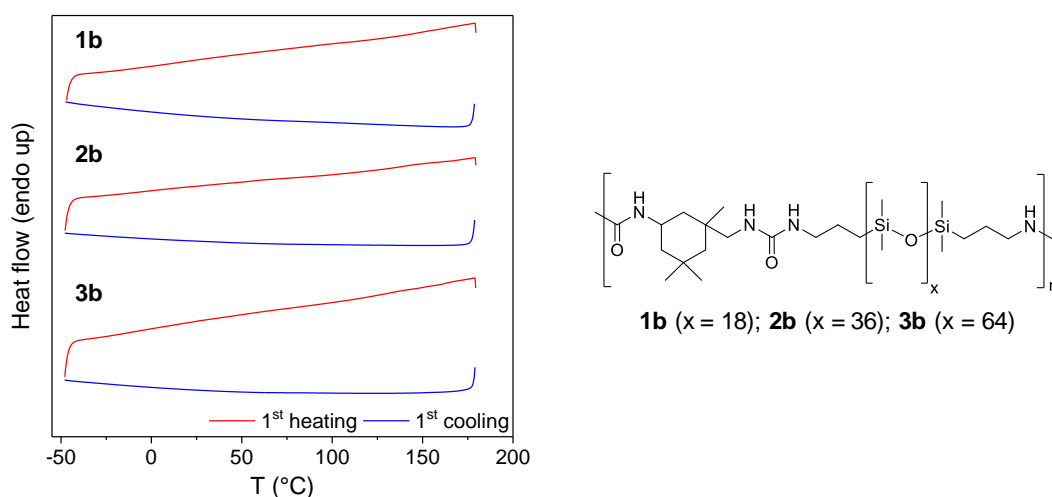
Figure 3.9: DSC curves of poly(urea-siloxane)s **1b**, **2b**, and **3b** based on IPDI (heating and cooling rate: 10 K min^{-1}). Thermal transition of the disaggregation of the urea hard segments cannot be observed due to a broad distribution and low concentration.

The DSC curves of the poly(urea-siloxane)s based on *4,4'-methylene bis(cyclohexyl isocyanate)* (**1c**, **2c**, **3c**) and *toluene-2,4-diisocyanate* (**1d**, **2d**, **3d**) are shown in Figure 3.10. In both cases only for the poly(urea-siloxane)s based on the PDMS-diamines with the two shorter chain length (**1c**, **1d** and **2c**, **2d**) the transitions of the hard segment disaggregation upon heating were detected. Broad and weak

transitions are observed with low melt enthalpies, indicating smaller and more broadly distributed hard segment domains.
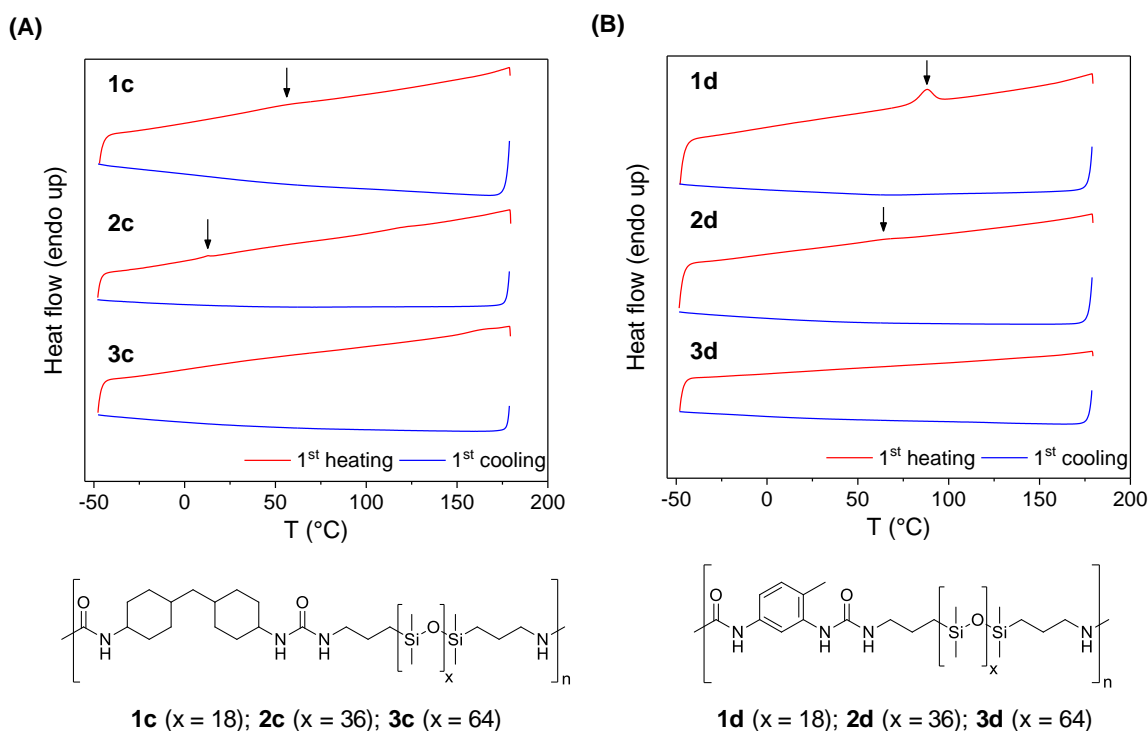
Figure 3.10: DSC curves of poly(urea-siloxane)s **(A) 1c**, **2c** and **3c** based on mbCHDI and **(B) 1d**, **2d** and **3d** based on 2,4-TDI (heating and cooling rate: 10 K min^{-1}). Thermal transition of the disaggregation of the urea hard segments are observed as an extremely weak and broad signal for **1c, 2c** and **1d, 2d**. Yet **3c** and **3d** did not show any thermal transition due to the dissolution of the hard segments.

The results for these two series are summarized in Table 3.4. For the copolymers based on the longest PDMS chain length (**3c**, **3d**) no transitions were observed owing to the low concentration of the hard segments within the material. In comparison to the (AB)$_n$ segmented copolymers copolymers **1a**, **2a**, and **3a** based on HMDI no aggregation upon cooling was detected by DSC. This can be explained by a slower aggregation rate of the hard segments based on mbCHDI and 2,4-TDI upon cooling due to higher steric hindrance compared to the linear, aliphatic HMDI.

Table 3.4: Melting transitions and enthalpies of poly(urea-siloxane)s based on different PDMS chain length and different diisocyanates *4,4'-methylene bis(cyclohexyl isocyanate)* (mbCHDI) (**1c**, **2c**, **3c**) and *toluene-2,4-diisocyanate* (2,4-TDI) (**1d**, **2d**, **3d**), respectively.

Poly(urea-siloxane)		T_m (°C)	ΔH_m (Jg^{-1})
mbCHDI	**1c**	56.2	0.88
	2c	12.7	0.10
	3c	-	-
2,4-TDI	**1d**	88.0	2.02
	2d	64.1	0.50
	3d	-	-

25

Oscillating shear rheology

Considering that the DSC measurements are not as sensitive to determine the transition of the bisurea segments from an aggregated to a non-aggregated state in this type of copolymers other methods such as rheology and dynamic mechanical thermal analysis are explored. For melt processing (AB)$_n$ segmented copolymers, rheological properties are of great interest since they can give more insight into the material properties upon 1st cooling and 2nd heating as well as the transitions between elastic and viscous behavior. This is essential regarding additive manufacturing (AM) since the polymer is initially heated to form a homogenous melt and upon processing the 1st cooling behavior gives information about the solidification behavior. Further the melt viscosity at elevated temperatures can be determined which is of interest for the applied processing techniques.

Therefore, *oscillating shear rheology measurements* were conducted on each poly(urea-siloxane). Figure 3.11 shows the shear storage *G'* and loss modulus *G"* as a function of temperature for the poly(urea-siloxane)s **1a**, **2a**, and **3a** based on *1,6-hexamethylene diisocyanate* (HMDI). Initially it can be seen that both shear moduli *G'* and *G''* decrease with increasing PDMS chain length at low temperatures. While G' = 10 MPa and G'' = 0.8 MPa for **1a** the moduli decrease to G' = 0.4 MPa and G'' = 0.09 MPa for **3a** at 10 °C. This can be explained by the higher soft segment content and consequently a reduced crosslink density with an overall decreased modulus. The rheology measurements for each of these poly(urea-siloxane)s show a similar trend starting from low storage and loss modulus at high temperature (160 °C) with a moderate increase upon cooling before a steep increase of moduli is observed. This phenomenon is attributed to the aggregation of the bisurea hard segments. Due to their linear aliphatic chemical structure these segments form fast a well ordered hydrogen bonded structure. At lower temperature the moduli reach a plateau. The reverse behavior can be observed for the 2nd heating cycle. Moreover, a pronounced hysteresis upon heating is detected resulting from time dependency of the aggregation and disaggregation of the urea hard segments.
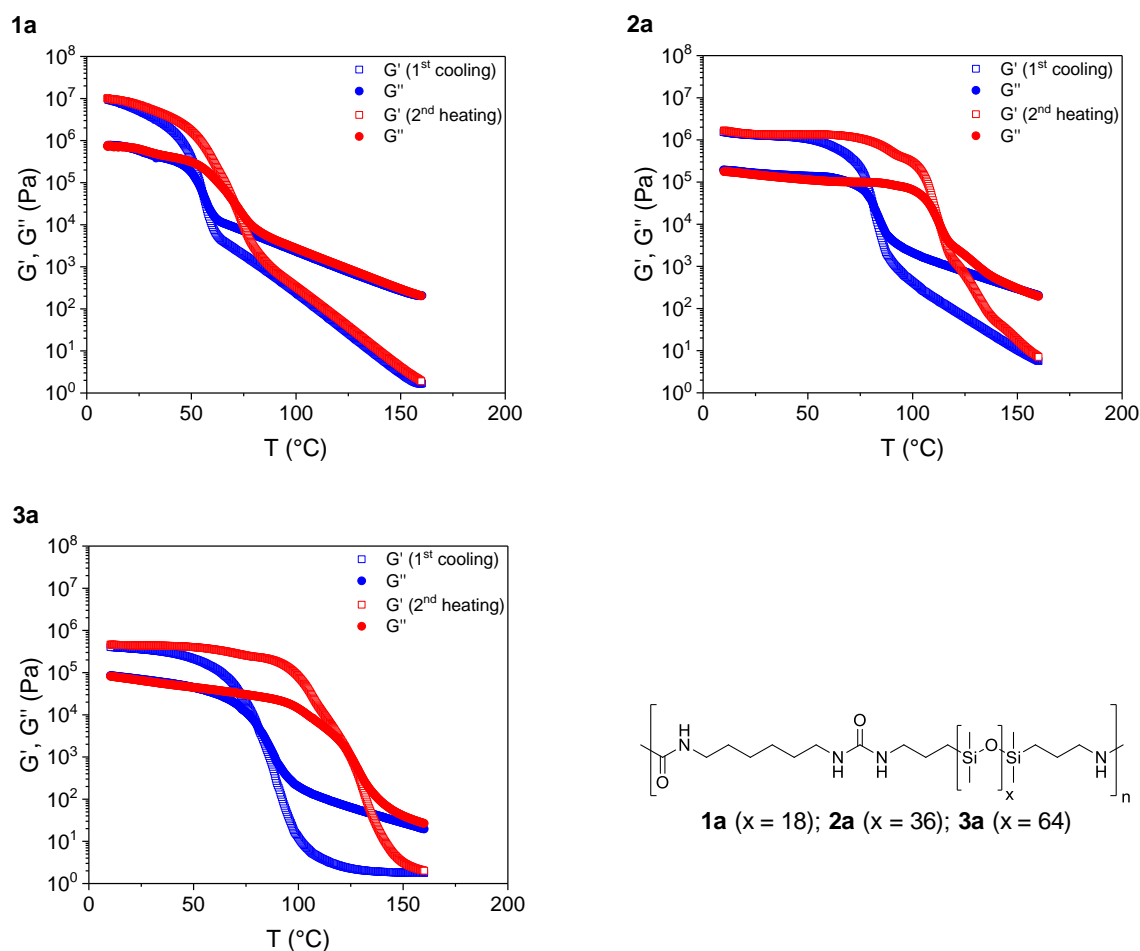
Figure 3.11: Oscillating shear rheology measurements of poly(urea-siloxane)s **1a**, **2a**, and **3a** applying a cooling/heating rate of 2 K min^{-1} and a frequency of 1 Hz. Shear storage *G'* and loss modulus *G''* of 1st cooling and 2nd heating are shown in dependency of the temperature.

The transition from a viscous to an elastic behavior upon cooling is defined as the crossover temperature T_{cross} of the storage and loss modulus (equation **(3.1)**).[77]

$$G' (T_{cross}) = G'' (T_{cross}) \qquad \text{(3.1)}$$

Below the crossover temperature when G' > G'' an elastic behavior is dominant while above T_{cross} with G' < G'' a viscous behavior determines the material properties. The transition from a viscous to an elastic behavior upon cooling is the lowest for **1a** at 55 °C while it increases to about 80 °C for **2a** and **3a**. The crossover temperature upon heating is higher reflecting the kinetics of the hydrogen bonding aggregation of the bisurea segments upon cooling and their disaggregation upon heating. This phenomenon is also observed in other TPEs.

Additionally the complex viscosities $\eta^*_{120\,°C}$ of the poly(urea-siloxane)s which are measured in dependency of the temperature were extracted at 120 °C. The complex viscosities in dependency of the temperature are shown in the appendix in Figure A-6.10 **(A)**. It decreases with increasing PDMS chain length from 150 Pa·s for **1a** to 12 Pa·s for **3a**. This tendency can be explained by a decreasing

27

weight fraction of urea hard segments within the copolymers by increasing the soft segment chain length.

For a time-independent determination of the melt viscosity, isothermal continuous shear rheology measurements were additionally conducted of poly(urea-siloxane) **1a** and **3a**. Cox and Merz postulated in 1958 the following empirical relation (equation **(3.2)**) which allows a comparison of oscillating and rotational viscosity under the assumption that the shear rate is equal to the angular frequency:[78,79]

$$\eta(\dot{\gamma}) = |\eta^*(\omega)| \tag{3.2}$$

With η being the rotational viscosity, $\dot{\gamma}$ (1/s) the shear rate, η^* the oscillating viscosity and ω (rad/s) the angular frequency.

The requirement for the equation to be fulfilled, is a simple polymer structure, meaning only entanglements occur and influencing the rheological properties. Deviations between η and η^* may indicate chemical or physical interactions between the polymer chains.[78,79] The rotational melt viscosity at 120 °C ($\eta_{melt\ 120\ °C}$) was determined to be 350 Pa·s for **1a** and 630 Pa for **3a**. It can be seen that the melt viscosity differs from the complex viscosity which is among others due to inter- and intramolecular interactions. Yet, these results are in good agreement with the molecular weight of the poly(urea-siloxane)s which is also higher for **3a** than **1a**. As well known, the molecular weight has a large impact on the melt properties of a material. However, the complex viscosity determined by oscillating shear rheology is a good indication for the viscosity at elevated temperatures. The results of the rheology measurements are summarized in Table 3.5.

Table 3.5: Crossover temperatures T_{cross} from a viscous to an elastic behavior upon cooling and upon heating are given as well as the complex viscosity $\eta^*_{120\ °C}$ and the melt viscosity determined at 120 °C $\eta_{melt,\ 120\ °C}$ of poly(urea-siloxane)s based on HMDI and different PDMS chain length.

Poly(urea-siloxane)		T_{cross} (°C)[a] *1st cooling*	T_{cross} (°C)[a] *2nd heating*	$\eta^*_{120\ °C}$ (Pa·s)[a]	$\eta_{melt\ 120\ °C}$ (Pa·s)[b]
HMDI	**1a**	55	70	150	350
	2a	81	113	145	n.a.
	3a	80	123	12	630

[a] Determined by oscillating shear rheology measurements with a cooling/heating rate of 2 K min^{-1} and a frequency of 1Hz.
[b] Isothermal continuous shear rheology measurement at 120 °C with a frequency of 0.5 Hz.

In Figure 3.12 the storage and loss moduli of the (AB)$_n$ segmented copolymers **1b**, **2b** and **3b** based on *isophorone diisocyanate* (IPDI) are plotted in dependency of the temperature. As already discussed for the HMDI system, the moduli also decrease with increasing PDMS chain length from **1b** to **3b** at low temperatures due to decreasing weight fractions. **1b** shows a storage modulus of G' = 5 MPa and a loss modulus of G'' = 0.9 MPa at 10 °C while for **3b** G' = 0.3 MPa and G'' = 0.08 MPa at 10 °C was determined. It stands out that no steep increase of moduli upon cooling is observed neither a large hysteresis. Instead the moduli increase steadily over the whole temperature region. This is owed to the steric hindrance of the *isophorone diisocyanate* (IPDI) segments which do not allow such a fast and sufficient aggregation as it was observed for the linear, aliphatic *1,6-hexamethylene diisocyanate* (HMDI) system. This indicates a retarded solidification of the material upon cooling, yet facilitated self-organization characteristics. Additionally, it can be seen that the moduli are slightly lower than for the HMDI based poly(urea-siloxane)s which is attributed to poorer stacking of the asymmetric, cycloaliphatic IPDI hard segments.

1b (x = 18); **2b** (x = 36); **3b** (x = 64)
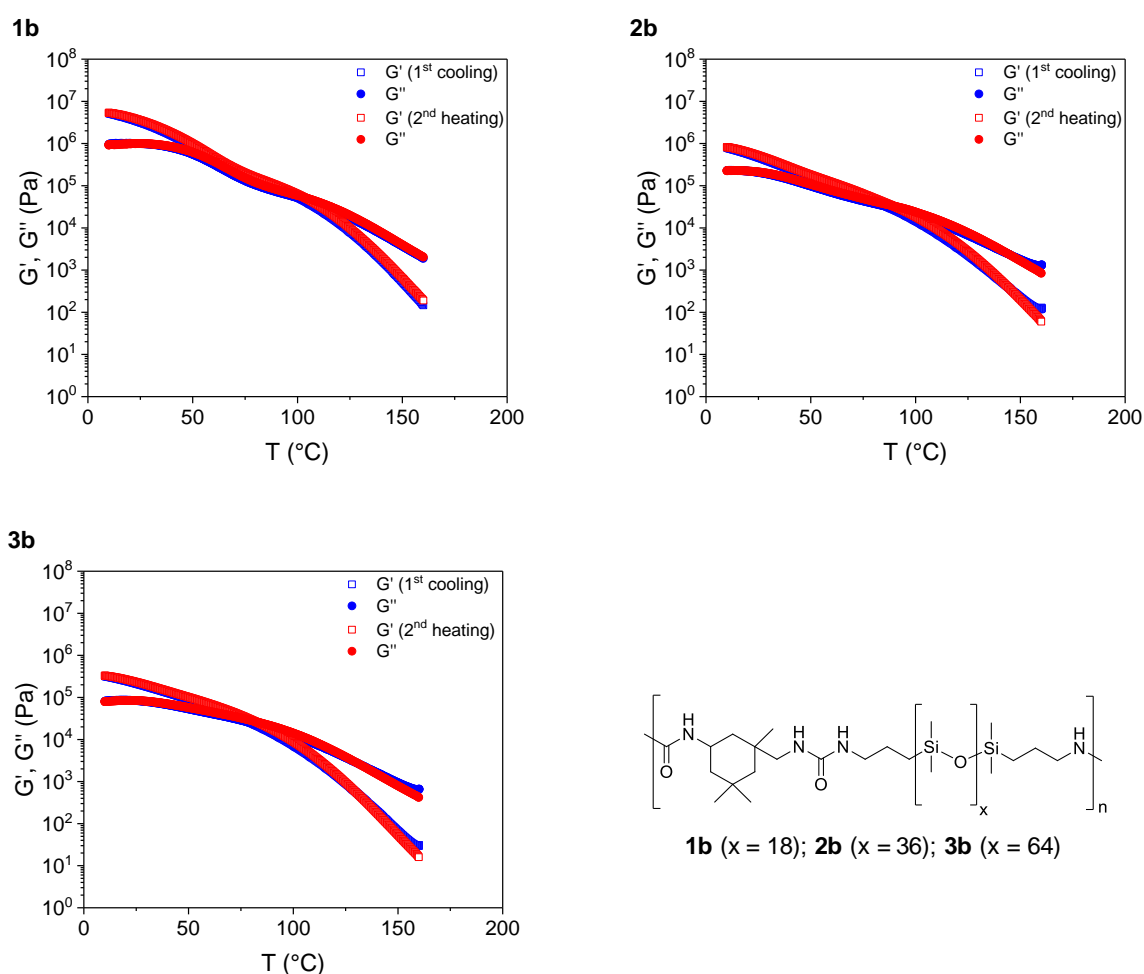
Figure 3.12: Oscillating shear rheology measurements of poly(urea-siloxane)s **1b**, **2b**, and **3b** applying a cooling/heating rate of 2 K min^{-1} and a frequency of 1 Hz. Shear storage *G'* and loss modulus *G''* of 1st cooling and 2nd heating are plotted in dependency of the temperature.

The crossover temperatures upon 1st cooling and 2nd heating are summarized in Table 3.6. Only a hysteresis of 3 °C is observed upon heating for the poly(urea-siloxane)s based on IPDI. **1b** shows the transition from a viscous to an elastic behavior upon cooling at T$_{cross}$ = 101 °C, while they decrease for **2b** T$_{cross}$ = 86 °C and **3b** T$_{cross}$ = 79°C which is due to dilution of the hard segment content and less aggregated urea units. The crossover temperatures upon cooling are higher than for the HMDI systems which is due to a decreased mobility of the polymer chains as a result of the more sterically hindered hard segment structure.

Also, the complex viscosity was determined at 120 °C ($\eta*_{120\,°C}$), the results are shown in Table 3.6. The complex viscosities as a function of the temperature are depicted in the appendix in Figure A-6.10 **(B)**. It is obvious that the viscosities are at least one magnitude larger than for the HMDI systems due to the reduced chain mobility. Yet, the viscosity decreases with increasing PDMS chain length owed to decreasing hard segment weight fraction.

Table 3.6: Crossover temperatures from a viscous to an elastic behavior upon cooling and upon heating are listed as well as the complex viscosity determined at 120 °C of poly(urea-siloxane)s based on IPDI, mbCHDI, and 2,4-TDI with different PDMS chain length.

Poly(urea-siloxane)		T$_{cross}$ (°C)[a] *1st cooling*	T$_{cross}$ (°C)[a] *2nd heating*	$\eta*_{120\,°C}$ (Pa·s)[a]
IDPI	**1b**	101	103	4107
	2b	86	89	1440
	3b	79	82	800
mbCHDI	**1c**	122	127	10300
	2c	137	140	14500
	3c	109	112	3000
2,4-TDI	**1d**	104	108	8500
	2d	123	126	9000
	3d	94	98	2300

[a] Determined by oscillating shear rheology measurements with a cooling/heating rate of 2 K min^{-1} and a frequency of 1Hz.

The poly(urea-siloxane)s based on *4,4'-methylene bis(cyclohexyl isocyanate)* (mbCHDI) and *toluene-2,4-diisocyanate* (2,4-TDI) show a similar behavior as the *isophorone diisocyanate* (IPDI) systems. In Figure 3.13 the rheological measurements of **1c** based on mbCHDI and **1d** based on 2,4-TDI are shown. Other measurements are shown in the appendix in Figure A-6.8 and Figure A-6.9. The storage and loss moduli at 10 °C are in the same magnitude as for the IPDI based system. The moduli increase as seen for the poly(urea-siloxane)s based on IPDI moderately over the whole temperature range upon cooling without a steep increase. This is again attributed to the steric hindrance of both hard segments. This behavior indicates a more moderate solidification upon cooling compared to the HMDI system (cf. Figure 3.11).
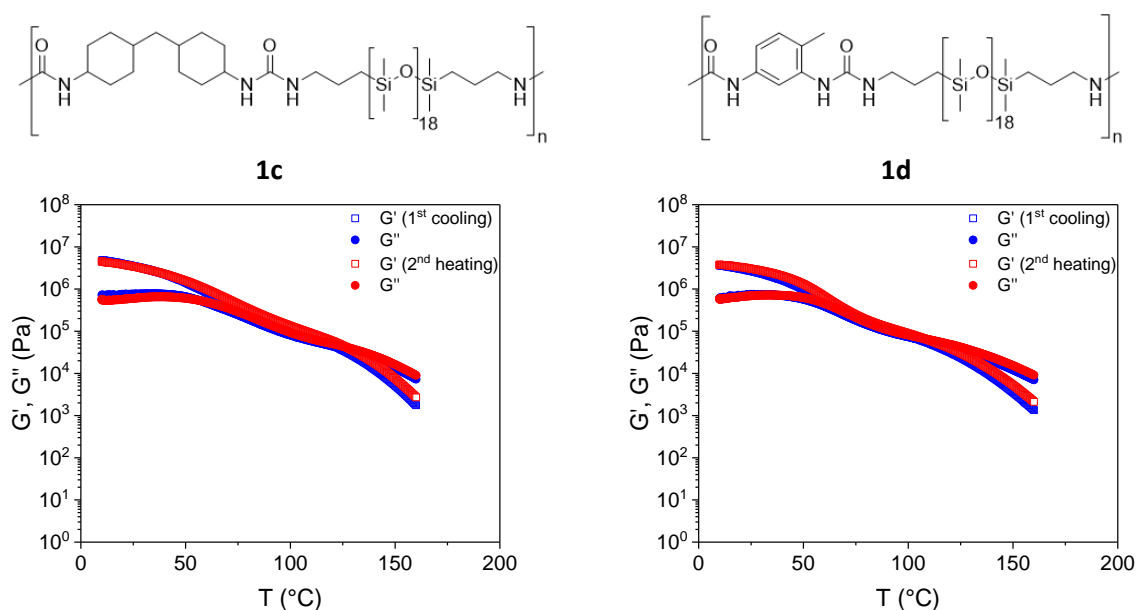
Figure 3.13: Oscillating shear rheology measurements of poly(urea-siloxane)s **1c** and **1d** based on mbCHDI and 2,4-TDI, respectively. A cooling/heating rate of 2 K min^{-1} and a frequency of 1 Hz was applied. Shear storage *G'* and loss modulus *G''* of 1st cooling and 2nd heating are depicted in dependency of the temperature.

The results including the crossover temperatures upon 1st cooling and 2nd heating as well as the complex viscosities of poly(urea-siloxane)s based on mbCHDI and 2,4-TDI are given in Table 3.6. For both poly(urea-siloxane) series the hysteresis upon heating is about 3 °C. The crossover temperatures of the mbCHDI based TPEs are slightly higher than the ones based on 2,4-TDI. Also for the complex viscosity determined at 120 °C it can be seen that they are significantly higher than for the HMDI based copolymers. The highest complex viscosity is observed for the mbCHDI systems **2c** with 14500 Pa·s, followed by the 2,4-TDI based copolymer **2d** with 9000 Pa·s at 120 °C. The complex viscosities as a function of temperature are plotted in the appendix in Figure A-6.10 **(C)** and **(D)**.

Concluding from the oscillating shear rheology measurements of the four poly(urea-siloxane) series, the (AB)$_n$ segmented copolymers based on HMDI are the most promising materials regarding melt processing from a low viscous polymer melt. The other systems based on IPDI, mbCHDI, and 2,4-TDI are expected to become more difficult to process owed to the significantly higher viscosity.

Dynamic mechanical thermal analysis

Rheology measurements provided an insight into the shear properties of 1st cooling and 2nd heating of the (AB)$_n$ segmented poly(urea-siloxane) copolymers. Nevertheless, the 1st heating of a material is also of interest regarding melt processing. Therefore, dynamic mechanical thermal analysis (DMTA) was conducted in tension mode on the bulk material of poly(urea-siloxane)s **1a**, **2a**, and **3a** based on *1,6-hexamethylene diisocyanate* (HMDI). For these measurements specimens were prepared from solution cast films. The DMTA curves representing the elastic storage *E'* and loss modulus *E''* in dependency of the temperature are shown in Figure 3.14. The elastic moduli *E'* and *E''* show the same trend at room temperature as was previously observed by rheology. With increasing PDMS chain length the moduli decrease. Starting with the highest storage modulus of **1a** at 700 MPa and a loss modulus of 220 MPa it decreases to E' of 1.5 MPa and E'' of 0.5 MPa for **3a** at 25 °C. These values differ from the ones determined by rheology. This is due to the different measuring modes, tension *versus* oscillating shear mode. For each copolymer a plateau is obtained up to about 40 °C. Upon further heating both moduli decrease and cross at a certain temperature indicating the transition from an elastic to a viscous behavior.
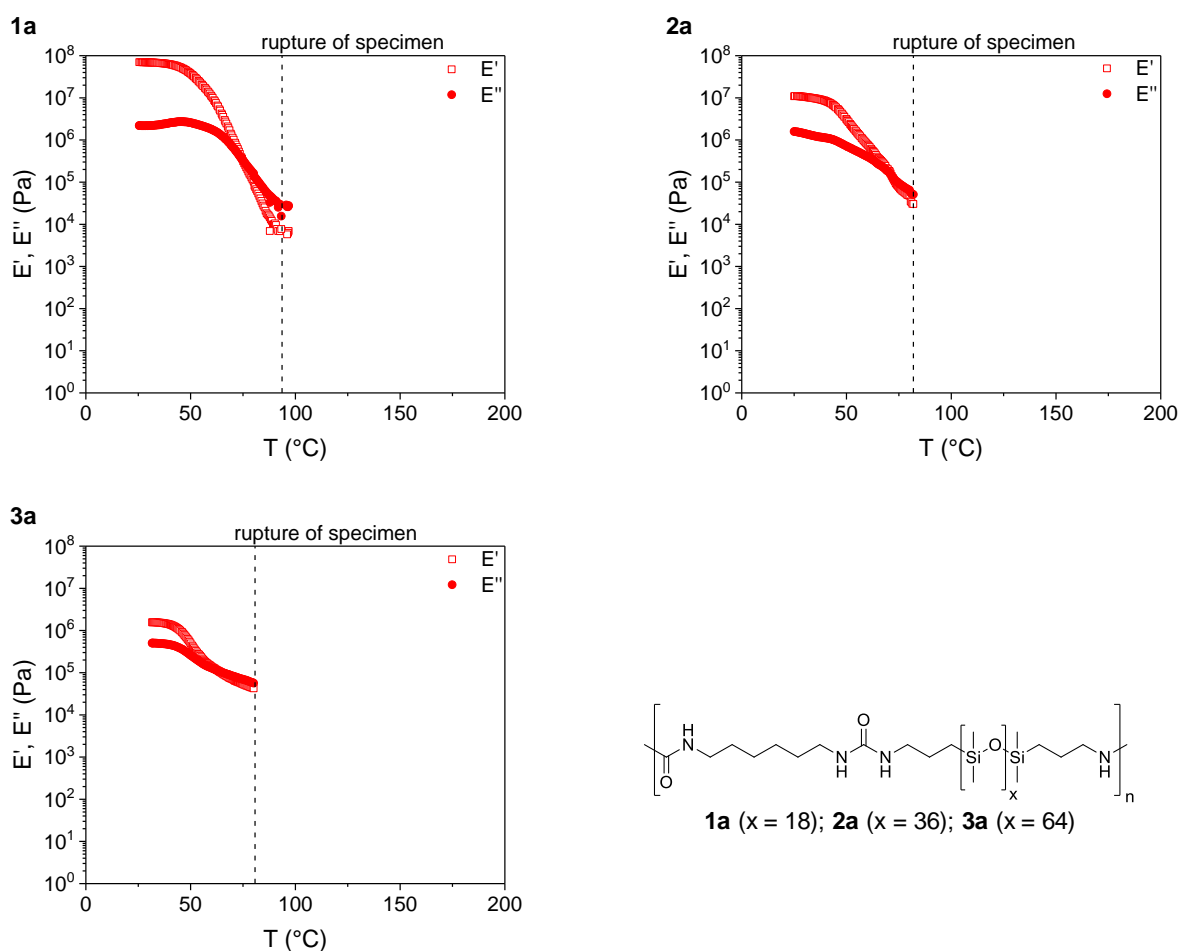
Figure 3.14: DMTA curves of poly(urea-siloxane)s **1a**, **2a**, and **3a** based on HMDI and different PDMS chain length applying a heating rate of 2 K min^{-1} and a frequency of 1 Hz. Elastic storage *E'* and loss moduli *E''* are shown as a function of the temperature measured in tension mode.

The measurement reaches its limits shortly after T_{cross} since the material becomes soft and starts to flow. The crossover temperatures from an elastic to a viscous behavior upon 1st heating range from 63 °C for **3a** to 75 °C for **1a** which differ slightly from the 1st cooling and 2nd heating data determined by rheology yet are in the same order of magnitude. This can be explained by thermo-sensitive kinetics of the aggregation and disaggregation process of the bisurea hard segments and the different measuring mode. The crossover temperatures of the poly(urea-siloxane)s **1a**, **2a**, and **3a** are summarized in Table 3.7. Dynamic mechanical thermal analysis on bulk material in tension mode is restricted by the material properties upon heating. If the material is too soft before the crossover temperature is reached and the measuring parameters cannot be adjusted to such low forces the transition cannot be determined utilizing this method. Nevertheless, dynamic mechanical thermal analysis can be performed within a small metal specimen holder utilizing a single cantilever bending experiment. Additionally, temperatures up to -150 °C can be measured allowing the determination of the glass transition temperature of the PDMS soft segment. Though using the single cantilever bending experiment no true moduli values can be determined owing to the large values of the specimen holder compared to the small difference of the specimen modulus. However, the storage modulus in dependency of the temperature can be evaluated and gives information about the transition temperatures.

In Figure 3.15 the elastic storage modulus E' and $tan\,\delta$ as a function of the temperature determined via a single cantilever bending experiment utilizing a metal specimen holder based on poly(urea-siloxane) **1a**, **2a**, and **3a** are plotted. For all three copolymers two distinct transitions can be observed, indicated by a drop of the elastic storage modulus correlating to the maximum of $tan\,\delta$. $Tan\,\delta$ is defined as the ratio of the loss modulus E'' to the storage modulus E'. The initial drop of E' around -120 °C is assigned to the glass transition temperature of the PDMS soft segment. After which the material shows a rubbery plateau, being in the elastic state. Then another decrease of moduli can be observed resulting from the disaggregation of the bisurea hard segments. These measurements show the thermomechanical behavior in dependency of the temperature upon 1st heating and are typical for common TPEs (cf. Figure 1.2). The service temperature of these (AB)$_n$ segmented poly(urea-siloxane) copolymers is given by the temperature range between T_g of the PDMS soft segment and the T_{cross} of the hard segment ranging from about -121 °C to 54 °C.

The DMTA measurements of the poly(urea-siloxane) copolymers based on *isophorone diisocyanate* (IPDI), *4,4'-methylene bis(cyclohexyl isocyanate)* (mbCHDI), and *toluene-2,4-diisocyanate* (2,4-TDI) were found to behave in a similar way solely with higher T_{cross}. They are shown in the appendix in Figure A-6.11, Figure A-6.12, and Figure A-6.13, respectively.
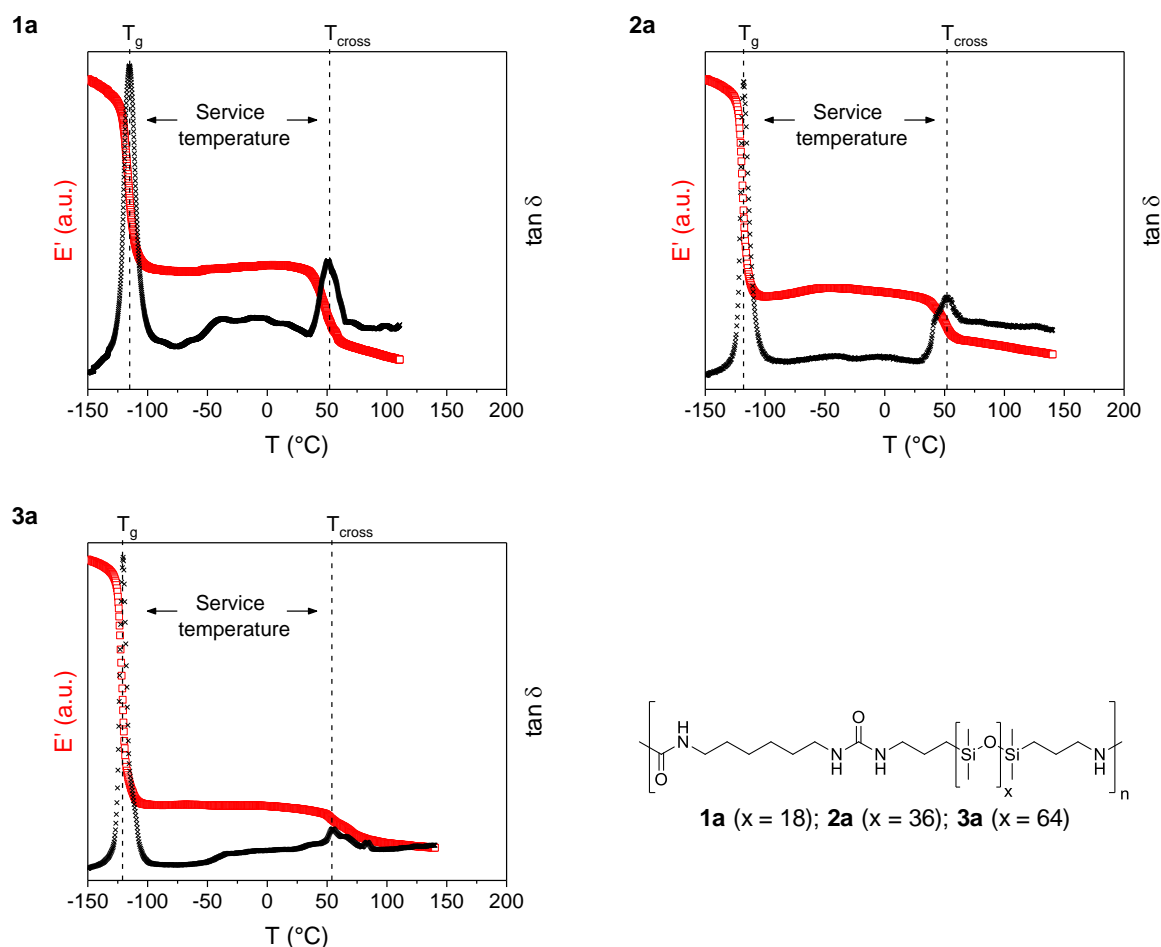
Figure 3.15: Elastic storage modulus *E'* and *tan δ* as a function of the temperature upon 1st heating of poly(urea-siloxane)s **1a**, **2a**, and **3a** based on HMDI and different PDMS soft segment length determined via a single cantilever bending experiment utilizing a metal specimen holder with an applied frequency of 2 Hz and a heating rate of 5 K min⁻¹.

The glass transition temperatures as well as the crossover temperatures upon 1st heating are summarized in Table 3.7 for all poly(urea-siloxane) copolymers. These values correspond to the *tan δ* maxima. Independent of the used hard segment the glass transition temperature T_g decreases with longer PDMS chain length. It is known from the literature that long chain PDMS lower the glass transition temperatures due to the reduced amount of hydrogen bonded hard segments, which limits the soft segment mobility.[53] Compared to neat PDMS (T_g = -123 °C), the T_g of the soft segment within the poly(urea-siloxane)s is slightly higher, since the PDMS chains are phase separated from the hydrogen bonded hard segments. The limited chain mobility results in a higher glass transition.[60] As already seen by the rheology measurements, the lowest crossover temperatures can be observed for the HMDI based poly(urea-siloxane)s ranging from 52 °C to 54 °C. While the other (AB)ₙ segmented poly(urea-siloxane)s show about 20 °C higher crossover temperatures. The T_{cross} determined by DMTA utilizing the single cantilever bending experiment differ slightly from the ones obtained by DMTA in tension mode. This is owed to the different measuring geometry and different measuring parameters. However, they are in reasonable agreement.

Table 3.7: Thermal transitions upon 1st heating of the different poly(urea-siloxane) series determined by dynamic mechanical thermal analysis in tension mode and utilizing a single cantilever bending experiment.

Poly(urea-siloxane)		T_{cross} (°C)[a] 1st heating	T_g (°C)[b]	T_{cross} (°C)[b] 1st heating
HMDI	1a	75	-115	54
	2a	72	-118	52
	3a	63	-121	54
IPDI	1b		-112	72
	2b	n.a.[c]	-117	71
	3b		-120	62
mbCHDI	1c		-112	74
	2c	n.a.[c]	-118	87
	3c		-120	73
2,4-TDI	1d		-112	69
	2d	n.a.[c]	-117	84
	3d		-119	66

[a] Determined by DMTA in tension mode with a heating rate of 2 K min⁻¹ and a frequency of 1 Hz.
[b] Determined by DMTA utilizing a single cantilever bending experiment utilizing a metal specimen holder with a heating rate of 5 K min⁻¹ and a frequency of 2 Hz.
[c] Not available due to measurement limitations.

From these results it can be concluded that all poly(urea-siloxane)s synthesized within this thesis provide thermoplastic elastomeric properties with a broad service temperature window ranging from about -115 °C up to 70 ° and can be melt processed above T_{cross}. Yet for some techniques not all copolymers might be suitable since adequate melt viscosities are necessary to obtain a homogenous melt flow. Poly(urea-siloxane)s based on more sterically demanding cycloaliphatic and aromatic hard segments were found to have higher viscosities compared to the poly(urea-siloxane) copolymers with linear, aliphatic *1,6-hexamethylene diisocyanate* (HMDI) hard segments.

Temperature stability of poly(urea-siloxane)s

Melt processing a material also requires a sufficient thermal stability which will be analyzed in more detail in the following. Thermogravimetric analyses (TGA) show for all poly(urea-siloxane)s a two-step degradation with a 5% weight loss ($T_{-5\,wt.\%}$) starting from 300 to 355 °C. This two-step degradation of poly(urea-siloxane)s is assigned first to instabilities of the hard segment and secondly to the PDMS soft segment resulting in dissociation reactions and random chain scissions.[53,80,81] The weight loss as a function of the temperature of **1a** is shown in Figure 3.16. The temperature at 5% weight loss is at $T_{-5\,wt.\%}$ = 322 °C. The most stable systems are observed for the HMDI based copolymers followed by the IPDI, mbCHDI, and 2,4-TDI copolymers.
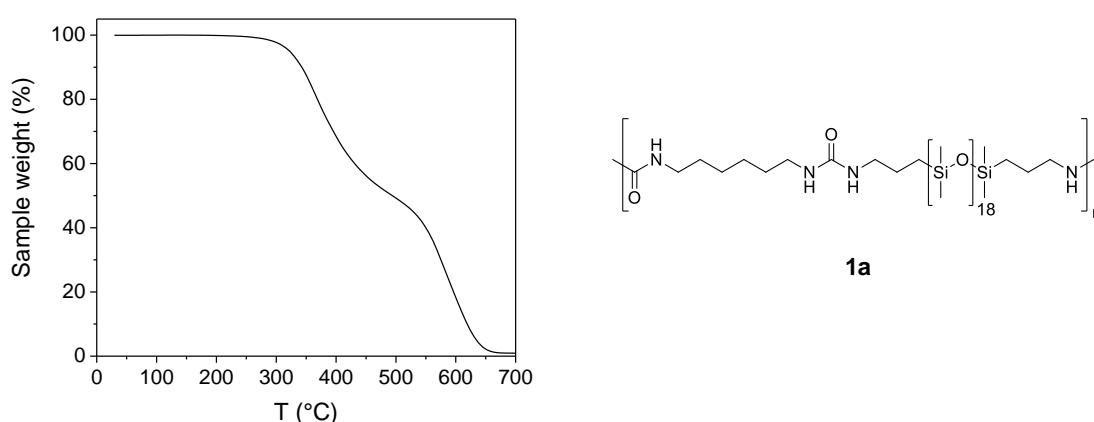
Figure 3.16: TGA curve of poly(urea-siloxane) **1a** showing a 5% weight loss at a temperature of $T_{-5\,wt.\%}$ = 322 °C measured under nitrogen atmosphere and a heating rate of 10 K min^{-1}.

As known from literature the urea bond can undergo back reactions and dissociates at higher temperatures back into isocyanates and primary amines. The formed isocyanate can further react with the urea units to form biuret units which are then chemically and irreversible crosslinked (Scheme 3.2).[82–84]
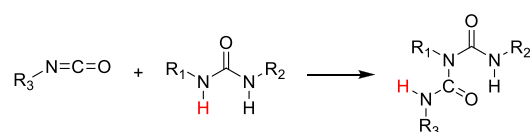
Scheme 3.2: Reaction of isocyanate, which is formed upon thermal decomposition of urea units, with another urea unit forming the covalent crosslinked biuret unit.

This crosslinking leads to a sudden increase in the melt viscosity resulting in a polymer with completely changed material properties.[2] To investigate the thermal stability of the (AB)$_n$ segmented poly(urea-siloxane) copolymers over time, isothermal rotational rheology measurements were conducted on poly(urea-siloxane) **1a** at four different temperatures, 90 °C, 140 °C, 160 °C, and 180 °C. Figure 3.17 depicts the melt viscosity as a function of time. It can be seen that at 90 °C the melt viscosity remains constant around 390 Pa·s over a period of 14 h. A slightly different behavior is observed at 140 °C, initially the viscosity slightly decreases and after about 1 h it steadily increases. This can be explained

36

due to post-addition reactions increasing the molecular weight moderately. A complete different behavior is observed at 160 °C. The melt viscosity shows an abrupt increase after 3 h. At 180 °C a sudden and steep increase of η_{melt} is observed after only 30 min. These steep increases of the melt viscosity are attributed to the back reaction of the polyureas followed by immediate irreversible crosslinking reactions resulting in a dramatic increase in melt viscosity.
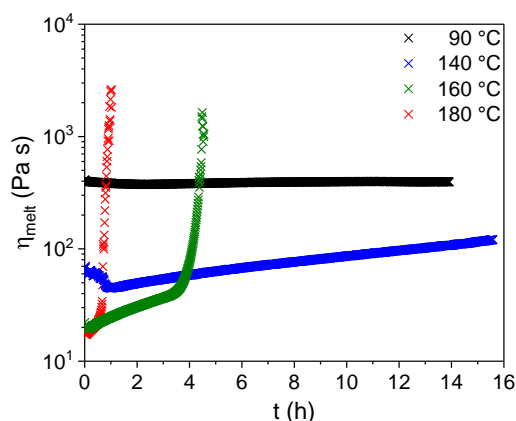
Figure 3.17: Temperature stability of (AB)n segmented poly(urea-siloxane) **1a** characterized by the melt viscosity in dependency of time determined by isothermal rotational rheology measurements. At a temperature of 90 °C the melt viscosity does not change over 14 h. At higher temperatures of 160 °C and 180 °C a sudden increase of the melt viscosity is observed resulting from irreversible crosslinking of the copolymer, changing the material properties completely. [Reprinted with permission from [85]; © 2018 WILEY-VCH]

It is expected that the poly(urea-siloxane)s based on the other hard segments (IPDI, mbCHDI, 2,4-TDI) behave in a similar way since the sudden increase of melt viscosity is attributed to the back reaction of the urea units into isocyanate units and amine units which is known from literature occurs at higher temperatures for urea units.[82,83] From these results it can be concluded that processing temperatures above 140 °C are not advantageous. In regard of melt processing it is crucial to find the ideal balance between a low melt viscosity at a certain temperature and thermal stability.

3.2.4. Mechanical properties

In addition to optimize poly(urea-siloxane)s regarding their thermal properties, the goal was further to explore the mechanical properties by varying the composition of the (AB)$_n$ segmented copolymers. These mechanical properties including Young's modulus, strain at break ε, stress at break σ, and toughness are accessible by tensile testing. The Young's modulus is calculated from the initial slope of the stress-strain curve in the linear elastic region. The toughness which is calculated from the total area under the stress-strain curve is the ability of a material to deform plastically and to absorb energy before rupture. The tensile properties were determined from the average of ten measurements.

In Figure 3.18 representative stress-strain diagrams of all synthesized poly(urea-siloxane)s are shown. Comparing the diagrams, it can be seen that the TPEs with the shortest PDMS chain length (**1**) show the highest stress at break accompanied by the shortest strain at break. The largest elongation can be seen for the copolymers with the longest PDMS chain length (**3**) which is due to an increasing amount of soft matrix.
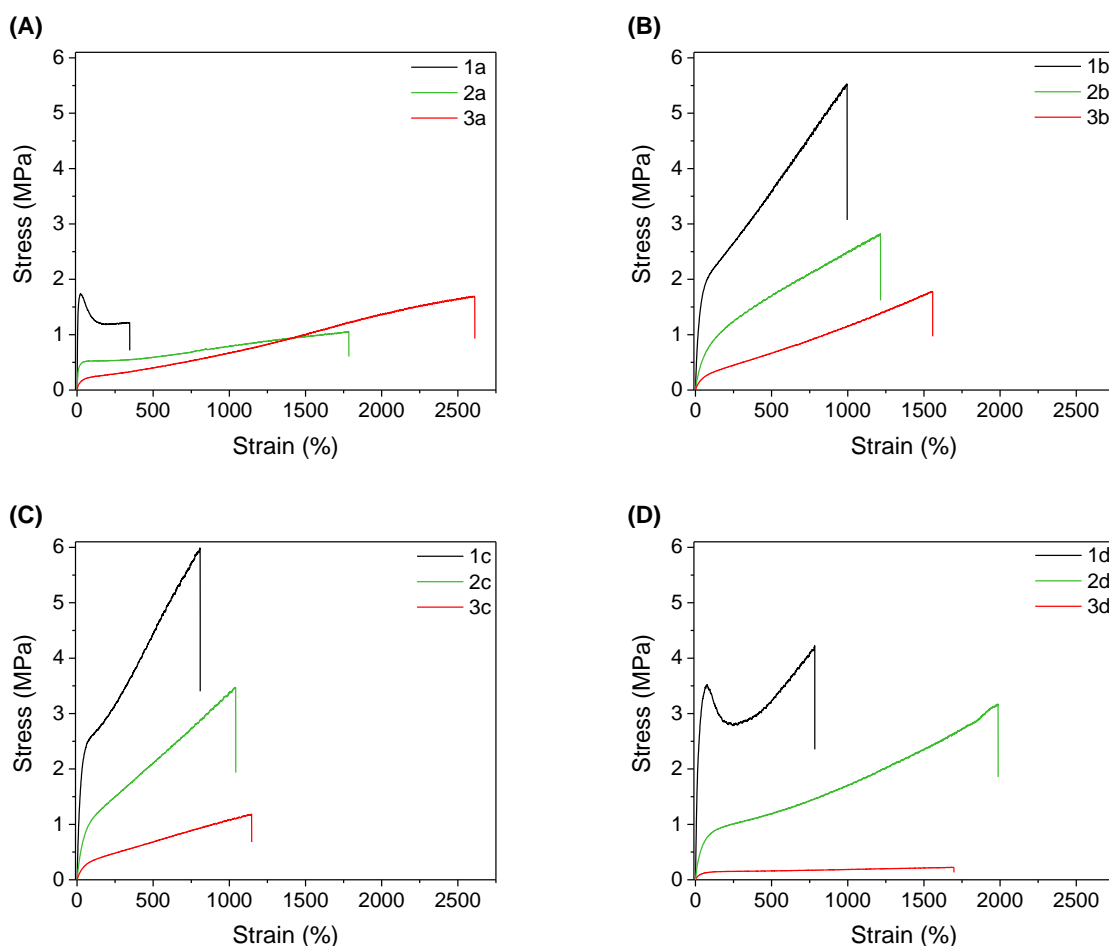
Figure 3.18: Stress-strain diagrams of poly(urea-siloxane)s based on **(A)** HMDI, **(B)** IPDI, **(C)** mbCHDI, and **(D)** 2,4-TDI with different PDMS chain length. The strain at break increases with increasing PDMS chain length while the stress at break decreases. Detailed experimental data can be found in chapter 5.2.

The material with the highest ultimate elongation of ε = 2593% was found to be **3a** which is due to the largest soft matrix. In contrast, **1a** provides the shortest elongation at break ε = 367% owed to strongly aggregated urea hard segments embedded in the short chain PDMS soft matrix. The stress at break decreases with increasing PDMS chain length regardless the hard segment structure, except for **3a**. This behavior can also be explained by the decreasing hard segment weight fraction. It is also noticeable that the copolymers based on *isophorone diisocyanate* (IPDI) (**b**) and *4,4'-methylene bis(cyclohexyl isocyanate)* (mbCHDI) (**c**) show quite similar stress-strain behavior with comparatively high stress at break which is owed to their cycloaliphatic nature of the bisurea hard segments. The two poly(urea-siloxane)s **1a** and **1d** based on short chain PDMS and *1,6-hexamethylene diisocyanate* (HMDI) and *toluene-2,4-diisocyanate* (2,4-TDI), respectively, are the only two copolymers with a yield point. Yilgör *et al.* stated that a yield point is observed for polymers with high hard segment content and is due to continuity of the domains.[53]

Table 3.8 summarizes the tensile properties. It can be seen that the Young's moduli decrease with increasing PDMS chain length independent of the hard segment chemical structure owing to the decreasing urea hard segment content. The poly(urea-siloxane)s based on *1,6-hexamethylene diisocyanate* (HMDI) and the short chain PDMS show the highest Young's modulus with 37 MPa, followed by *toluene-2,4-diisocyanate* (2,4-TDI) (20 MPa), *4,4'-methylene bis(cyclohexyl isocyanate)* (mbCHDI) (10 MPa) and *isophorone diisocyanate* (IPDI) (6 MPa). This is in agreement with the previous discussed hydrogen bonding strength due to their chemical structure. The overall toughness of the poly(urea-siloxane)s was found to range from 340 $Jm^{-3}10^4$ to 3500 $Jm^{-3}10^4$.

Table 3.8: Mechanical properties determined by tensile tests of poly(urea-siloxane)s based on different PDMS chain length and HMDI, IPDI, mbCHDI and 2,4-TDI, respectively. The Young's moduli are calculated from the initial slope of the linear elastic region of the stress-strain curve, while the toughness is a measure for the area under the stress-strain curve. An average of ten measurements is given. Detailed experimental data can be found in chapter 5.2.

| Poly(urea-siloxane)		Young's modulus (MPa)	Strain at break (%)	Stress at break (MPa)	Toughness ($Jm^{-3}10^4$)
HMDI	1a	36.6 ± 1.02	367 ± 15	1.23 ± 0.01	482 ± 19
	2a	5.4 ± 0.13	1773 ± 18	1.02 ± 0.02	1266 ± 30
	3a	1.1 ± 0.04	2593 ± 27	1.70 ± 0.02	2414 ± 56
IPDI	1b	6.4 ± 0.10	987 ± 22	5.46 ± 0.10	3500 ± 125
	2b	1.7 ± 0.02	1213 ± 20	2.89 ± 0.04	2294 ± 61
	3b	0.7 ± 0.01	1548 ± 43	1.76 ± 0.05	1462 ± 76
mbCHDI	1c	10.0 ± 0.19	808 ± 11	5.95 ± 0.05	3184 ± 59
	2c	2.6 ± 0.03	1089 ± 23	3.63 ± 0.06	2431 ± 83
	3c	0.8 ± 0.02	1147 ± 24	1.20 ± 0.02	873 ± 28
2,4-TDI	1d	20.1 ±0.65	775 ± 6	4.40 ± 0.03	2635 ± 29
	2d	2.2 ± 0.03	2003 ± 37	3.08 ± 0.07	3516 ± 112
	3d	0.5 ± 0.02	1907 ± 61	0.23 ± 0.01	339 ± 15

In summary, the ultimate elongation of the materials is primarily controlled by the soft segment chain length, while the stress at break and the Young's moduli are mainly affected by the hard segment concentration and chemical structure. By using different soft segment chain lengths and varying the chemical structure of the hard segments a wide range of different mechanical properties were covered ranging from extremely soft to relatively stiff TPEs.

3.2.5. Morphological investigation

As it was shown in the previous chapters, hard segment domains have a strong influence on the material properties, a closer look on the morphology of these materials is of interest. Owed to a large difference of the solubility parameters of nonpolar PDMS $\delta = 15.5$ (J cm^{-3})$^{0.5}$ and the polar urea unit $\delta = 45.6$ (J cm^{-3})$^{0.5}$ microphase separation between the soft and the hard segment is present.[53,70] This is investigated in detail by SAXS and TEM of poly(urea-siloxane) **1a**.

Small angle X-ray scattering (SAXS)

Temperature dependent SAXS measurements of poly(urea-siloxane) **1a** were jointly conducted with Paul Reichstein, Macromolecular Chemistry I upon heating and cooling. Before each measurement the sample was equilibrated at the set temperature for 10 min. As can be seen in Figure 3.19 **(A)** a broad scattering signal is observed at 30 °C with a maximum scattering vector $q_{max} = 1.31$ nm^{-1}. This indicates a microphase separation between incompatible PDMS soft segments and urea hard segments, yet, without long-range order due to the absence of higher order reflections.[86] By heating the sample in steps to 120 °C, the signal intensity gradually decreases which is attributed to the disaggregation of the hard segment domains and the loss of microphase separation. Thus, at room temperature the hard segments are aggregated in an ordered form and are phase separated from the hydrophobic PDMS soft matrix, while upon heating they disaggregate and an isotropic homogenous melt is observed. By cooling the sample to 30 °C the signal intensity increases again confirming the aggregation and microphase separation of the hard segments (Figure 3.19 **(B)**).
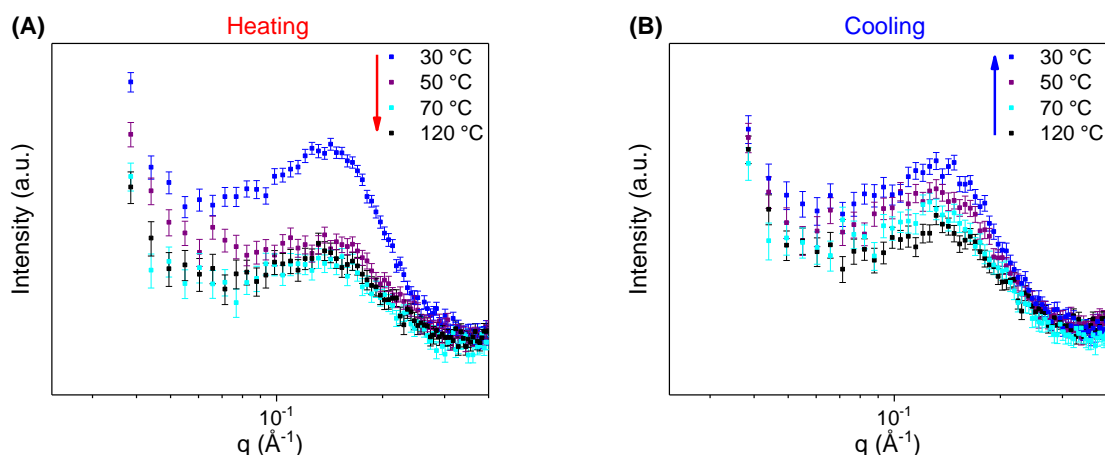
Figure 3.19: Temperature dependent SAXS measurements of poly(urea-siloxane) **1a**. **(A)** Upon heating, **(B)** upon cooling. The measurements were conducted in aluminum discs with a 1 mm hole, where the dry solution cast films are embedded. Samples were equilibrated at each temperature for 10 min prior measurement.

It is also obvious that the transition takes place over a broad temperature range and not at a distinct temperature which was already seen by temperature dependent FT-IR spectroscopy, DSC, rheology, and DMTA investigations. The initial intensity is not reached completely which is due to kinetic control of the hard segment aggregation. These SAXS data prove the thermoreversible behavior and microphase separation of the poly(urea-siloxane)s.

The interdomain spacing d, being an average periodic spacing length obtained within the copolymer morphology,[87] can be calculated from the q_{max} value according to equation **(3.3)**.

$$\mathrm{d}_{30\,°C} = \frac{2\pi}{\mathrm{q_{max}}} = 4.78\ \mathrm{nm} \qquad\qquad \textbf{(3.3)}$$

For poly(urea-siloxane) **1a** based on short chain PDMS and HMDI a spacing of 4.78 nm at 30 °C was determined. Yilgör *et al.* conducted SAXS measurements at room temperature on similar poly(urea-siloxane)s and reported interdomain spacings between $4 – 6$ nm. They showed that a slight increase of d is observed with increasing PMDS chain length. From these results and from calculations considering the bond angles between the atoms, they concluded that the end-to-end distance of the hard segments is too small to be directly correlated to the interdomain spacing. They suggest for d to be an average spacing length within the morphology.[53]

Transmission electron microscopy (TEM)

In addition to the SAXS measurements the morphology was also investigated by transmission electron microscopy (TEM). These measurements were jointly conducted with Carmen Kunert. Solution drop cast thin films from THF (10 mg mL^{-1}) were prepared and annealed at 60 °C for 15 min. Figure 3.20 shows TEM images of the poly(urea-siloxane) **1a** and **3a** based on HMDI with a short (M_n = 1513 g mol^{-1}) and a long chain PDMS (M_n = 4926 g mol^{-1}). In both cases circular structures embedded in the matrix are observed. The average diameter of the circular structure of **1a** is 51 ± 11 nm and 55 ± 22 nm for **3a**. The single circular objects differ slightly in size, corresponding to a small distribution of hard segment domain size. Comparing the two morphologies it can be seen that **3a** shows less circular domains than **1a**. This is owed to the lower concentration of the hard segments due to longer PDMS chain length and consequently a lower weight fraction of hard segments within the poly(urea-siloxane). Evaluating the area covered by the circular domains utilizing Image J, 7% and 4% for **1a** and **3a**, respectively was found which are in reasonable agreement with the calculated weight fractions.
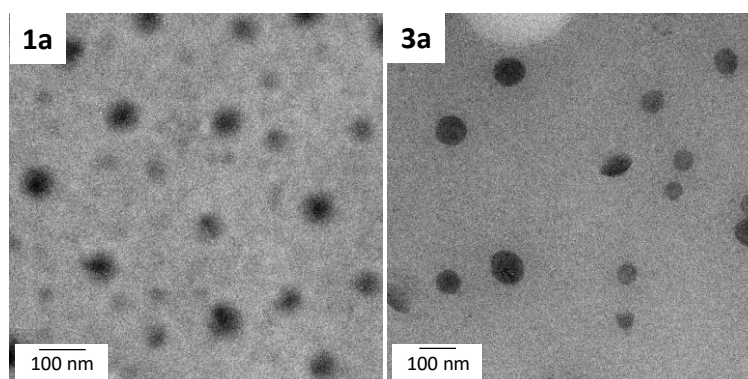
Figure 3.20: TEM images of solution drop cast thin films of poly(urea-siloxane) **1a** and **3a** based on HMDI (10 mg mL^{-1}, THF) after annealing at 60 °C for 15 min and cooling to room temperature.

As a final remark, it was shown by TEM that the urea hard segments of (AB)$_n$ segmented poly(urea-siloxane)s within thin solution cast films aggregate and microphase separate into domains with diameters up to about 90 nm.

3.2.6. Adjustment of the melt viscosity

An essential property for melt processing is the melt viscosity particularly in view of the applied extrusion-based additive manufacturing techniques. These need sufficient low melt viscosities to overcome back pressure issues within a setup and thus accommodate a homogenous and steady flow of the melt. On the one hand, the melt viscosity can be reduced by increasing the temperature, however this is restricted by the thermal stability of a material. On the other hand, the molecular weight of the copolymer can be reduced since it is proportional to the viscosity (cf. chapter 1.1). Due to the thermal stability of the (AB)n segmented poly(urea-siloxane) copolymers discussed in chapter 3.2.3 the copolymers cannot be heated higher than 140 °C for a prolonged time without irreversible crosslinking and property changes. Therefore, the molecular weight needs to be optimized in a defined manner to reduce the melt viscosity to ensure successful melt processing. In this respect poly(urea-siloxane)s **1a** and **3a** were modified regarding their molecular weight.

The polyaddition reaction follows the same procedure as in the syntheses described in Scheme 3.1, but with the difference that a small amount of benzylamine (Bz-NH$_2$) as monofunctional reagent is added to the PDMS-diamine solution at the beginning of the reaction (Scheme 3.3). The monofunctional reagent is responsible for a change in the stoichiometric ratio *r* resulting in a decreased molecular weight. The theoretical background of the molecular weight regulation is described in chapter 1.1.
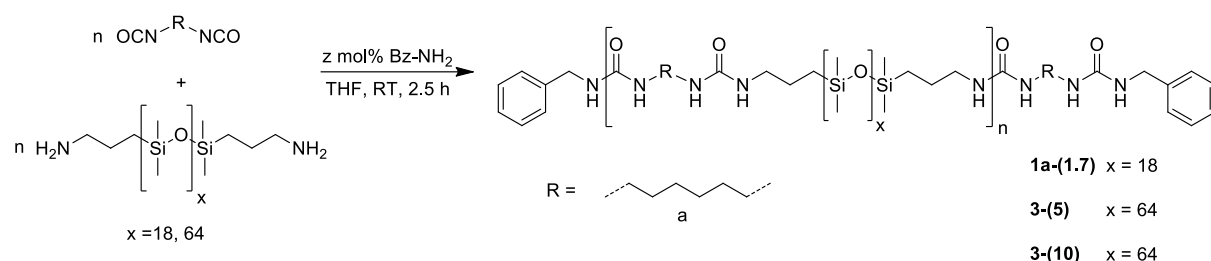
Scheme 3.3: Synthesis of molecular weight controlled (AB)n segmented poly(urea-siloxane) copolymers based on HMDI and PDMS-diamines. The degree of polymerization *n* is reduced by the addition of small amounts of benzylamine acting as monofunctional reagent.

In the following, the molecular weight controlled poly(urea-siloxane)s are denoted as before with the addition of the mol% of added benzylamine in parenthesis. For example, **1a-(1.7)** is based on the short chain PDMS (M$_n$ = 1513 g mol^{-1}, x = 18) and *1,6-hexamethylene diisocyanate* (HMDI) with 1.7 mol% benzylamine added to the reaction mixture to reduce the molecular weight.

The polymerization was also investigated by FT-IR spectroscopy to demonstrate the complete conversion of the diisocyanate by the absence of the NCO signal at 2270 cm^{-1}. The hydrogen bonding strength of **1a-(1.7)**, **3a-(5)**, and **3a-(10)** is not influenced by the addition of the monofunctional reagent. The reduction of the molecular weight was confirmed by SEC and is shown in Figure 3.21. It

can be seen that for both poly(urea-siloxane)s **1a** and **3a** the molecular weight was successively reduced due to the addition of the monofunctional reagent. The molecular weight distribution is unaltered monomodal with a dispersity of about 1.6.
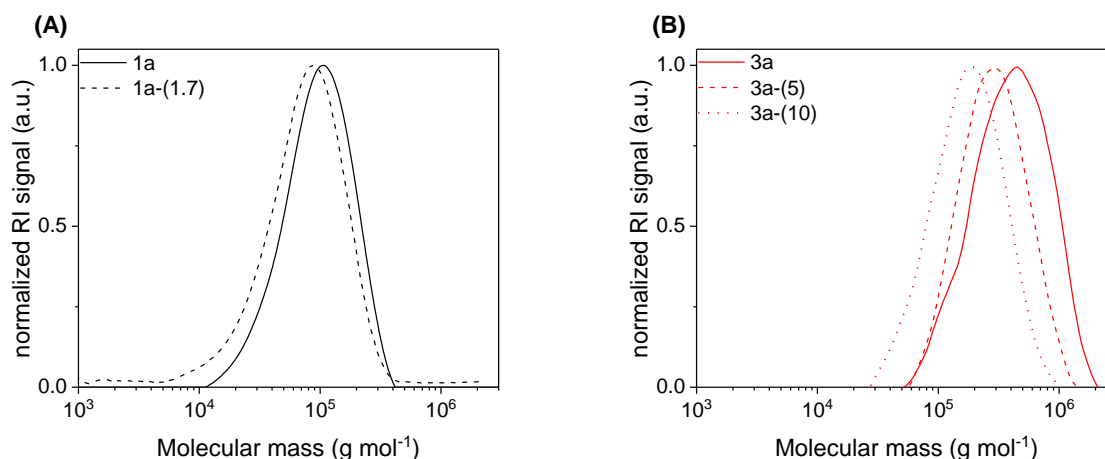
Figure 3.21: SEC curves of **(A)** molecular weight controlled poly(urea-siloxane) **1a** and **(B) 3a**. Owing to the addition of a small amount of the monofunctional reagent the molecular weight of **1a-(1.7)** and **3a-(5)** and **3a-(10)** was reduced, respectively. The SEC experiments were carried out with THF containing 0.25 wt.% tetrabutylammonium bromide as eluent. $\overline{M_n}$ and $\overline{M_w}$ were calculated based on a polystyrene calibration.

The SEC results of the molecular weight controlled poly(urea-siloxane)s are summarized in Table 3.9. The molecular weight of poly(urea-siloxane) **1a** was reduced from 73 kg mol^{-1} to 52 kg mol^{-1} by adding 1.7 mol% benzylamine which correlates to a reduction of the degree of polymerization *n* from 43 to 30. For the (AB)$_n$ segmented copolymer **3a** the molecular weight was reduced from 306 kg mol^{-1} to 238 kg mol^{-1} by adding 5 mol% benzylamine, while increasing the amount of monofunctional reagent to 10 mol% the molecular weight was even further reduced to 140 kg mol^{-1}, while the degree of polymerization was divided to more than half to n = 27. This is expected to have a significant influence on the melt viscosity of the material. The molecular weight reduction did not show an influence on the dispersity.

Table 3.9: SEC data of molecular weight controlled poly(urea-siloxane)s **1a** and **3a**.

Poly(urea-siloxane)	$\overline{M_n}$ [a] (kg mol^{-1})	$\overline{M_w}$ [a] (kg mol^{-1})	Đ [a]	n [b]
1a	73	115	1.6	43
1a-(1.7)	52	91	1.7	30
3a	306	491	1.6	58
3a-(5)	238	338	1.4	46
3a-(10)	140	213	1.5	27

[a] Determined by SEC, eluent: THF with 0.25 wt.% tetrabutylammonium bromide, $\overline{M_n}$ and $\overline{M_w}$ were calculated from polystyrene calibration. Đ = $\overline{M_w}$ / $\overline{M_n}$.
[b] Repeating unit *n* calculated from $\overline{M_n}$ determined by SEC.

An additional aim, next to the reduction of the melt viscosity, was to match the melt viscosities of **1a** and **3a** in view if simultaneous melt processing which is of great interest regarding the preparation of gradient materials from the melt which will be discussed in chapter 3.4. The influence of the optimized molecular weight on the melt viscosity was determined by isothermal rotational rheology measurements at 120 °C. Detailed experimental data are included in chapter 5.2. The molecular weight M_n and the melt viscosity at 120 °C $\eta_{melt\ 120\ °C}$ in dependency of the benzylamine content is graphically summarized in Figure 3.22. The melt viscosity of poly(urea-siloxane) **1a** decreases from 350 Pa·s to 70 Pa·s due to the addition of 1.7 mol% benzylamine. For **3a** the melt viscosity could be reduced from 630 Pa·s to 300 Pa·s and finally to 130 Pa·s after adding 5 and 10 mol% monofunctional reagent, respectively.
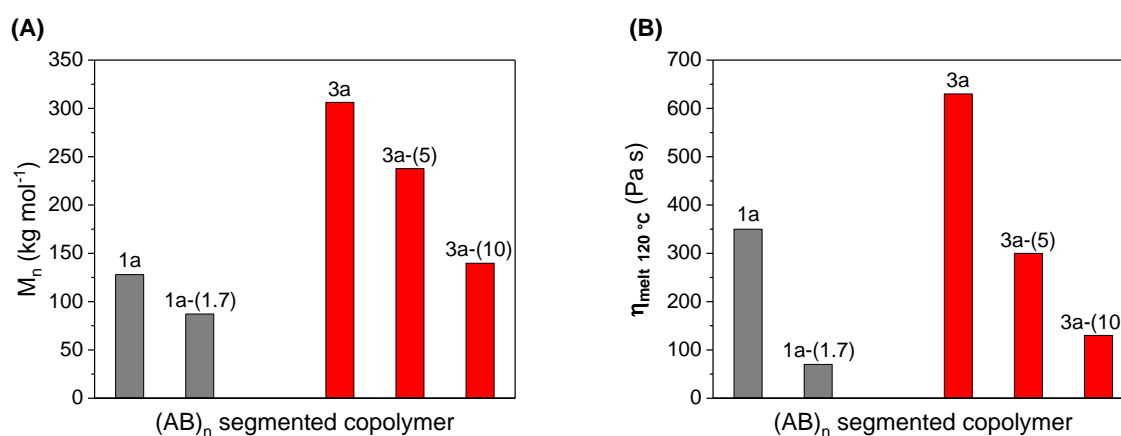
Figure 3.22: (A) Molecular weight of poly(urea-siloxane)s **1a** and **3a** with different amounts of the molecular weight regulator and **(B)** the melt viscosity determined with isothermal rheology measurements at 120 °C.

Rheology measurements of the molecular weight regulated poly(urea-siloxane)s show the same behavior as without regulation as shown in Figure 3.11 for **1a**. Upon cooling a steep increase of the storage and the loss modulus is observed due to the aggregation of the hard segments. A minor shift of the crossover temperatures T_{cross} was observed which is influenced by the different molecular weights. For poly(urea-siloxane) **1a** the crossover temperature increases about 5 °C with the addition of 1.7 mol% Bz-NH$_2$. While for **3a** a decreasing T_{cross} is observed with decreasing molecular weight. These results are summarized in Table 3.10. The crossover temperature of the 1st heating determined by DMTA in tension mode is also given.

Table 3.10: Crossover temperatures T_{cross} from a viscous to an elastic behavior upon cooling and heating are given as well as the melt viscosity determined at 120 °C of poly(urea-siloxane)s **1a** and **3a** with and without regulated molecular weights.

Poly(urea-siloxane)	T_{cross} (°C)[a] 1st cooling	T_{cross} (°C)[a] 2nd heating	T_{cross} (°C)[b] 1st heating	$\eta_{melt\ 120\ °C}$ (Pa·s)[c]
1a	55	70	75	350
1a-(1.7)	60	83	78	70
3a	80	123	63	630
3a-(5)	62	84	78	300
3a-(10)	61	82	76	130

[a] Determined by oscillating shear rheology measurements with a cooling/heating rate of 2 K min^{-1} and a frequency of 1Hz.
[b] Determined by DMTA in tension mode with a heating rate of 2 K min^{-1} and a frequency of 1 Hz.
[c] Isothermal continuous shear rheology measurements at 120 °C with a frequency of 0.5 Hz.

Tensile tests were conducted on the molecular weight regulated poly(urea-siloxane)s and compared with the non-regulated (AB)$_n$ segmented copolymers **1a** and **3a**. Detailed experimental data can be found in chapter 5.2. Representative stress-strain diagrams of **1a** and **3a** molecular weight regulated poly(urea-siloxane)s are shown in Figure 3.23. Comparing **1a** and **1a-(1.7)** only a marginal decreasing stress and strain at break is observed. While the stress and strain at break for the **3a** molecular weight regulated copolymers decreases significantly, which is due to a reduced copolymer chain length and less entangled chains. The strain at break decreases from 2593% to 2039% and finally to 1258% by adding 5 mol% and 10 mol% benzylamine, respectively.
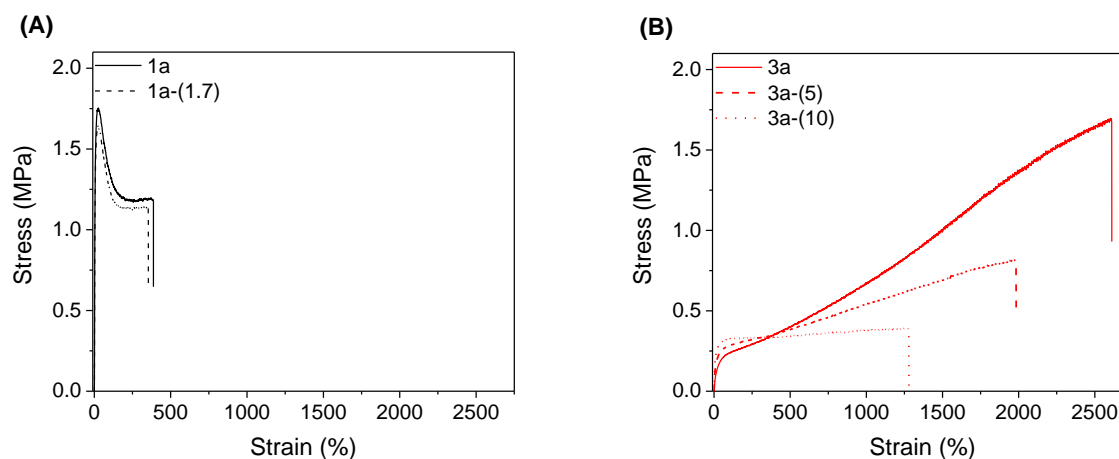
Figure 3.23: Stress-strain diagrams of **(A)** poly(urea-siloxane)s **1a** and **1a-(1.7)** based on short chain PDMS soft segment and of **(B)** poly(urea-siloxane)s **3a**, **3a-(5)**, and **3a-(10)** based on long chain PDMS soft segment. With increasing benzylamine content the strain at break and stress at break decrease due to lower molecular weight of the copolymers. Detailed experimental data can be found in chapter 5.2.

The mechanical properties determined from an average of ten specimens are given in Table 3.11. It can be seen that **1a-(1.7)** shows no significant change in the Young's modulus compared to **1a**. Whereas **3a** shows an increasing Young's modulus with the decreasing molecular weight in **3a-(5)** and **3a-(10)**. This can be explained by a reducing total chain length and keeping the hard segments at the same weight fraction results in a better formation of the physical network structure and in consequence a stiffer material with decreasing strain at break.

Table 3.11: Mechanical properties of poly(urea-siloxane)s **1a** and **1a-(1.7)** and **3a**, **3a-(5)**, and **3a-(10)**. An average of ten measurements is given. Detailed experimental data can be found in chapter 5.2.

Poly(urea-siloxane)	Young's modulus (MPa)	Strain at break (%)	Stress at break (MPa)	Toughness $(Jm^{-3}10^4)$
1a	36.6 ± 1.02	367 ± 15	1.23 ± 0.01	482 ± 19
1a-(1.7)	35.7 ± 1.4	321 ± 16	1.18 ± 0.04	415 ± 28
3a	1.1 ± 0.04	2593 ± 27	1.7 ± 0.02	2414 ± 56
3a-(5)	2.2 ± 0.06	2039 ± 50	0.84 ± 0.02	1137 ± 50
3a-(10)	3.2 ± 0.08	1258 ± 27	0.40 ± 0.01	451 ± 11

The Young's modulus in dependency of the benzylamine content is graphically summarized in Figure 3.24, showing the small changes of the Young's modulus due to the adjustment of the molecular weight of the (AB)$_n$ segmented copolymers. However, the large difference of Young's modulus between poly(urea-siloxane) **1a** and **3a** is influenced by the PDMS chain length and as clearly be seen is also present after regulation of the molecular weight.
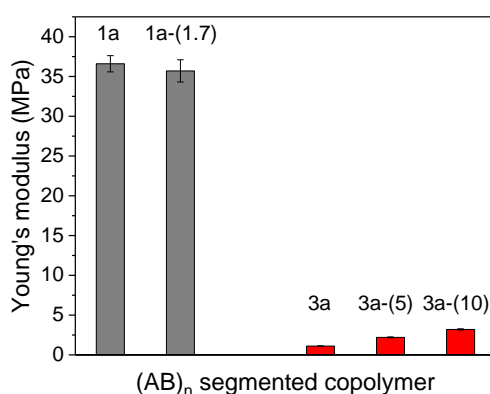
Figure 3.24: Young's moduli of poly(urea-siloxane)s **1a** and **3a** with different amounts of the molecular weight regulator. The significant difference of the Young's modulus between the two poly(urea-siloxane) systems is still present after changing the molecular weight resulting from the different chain length of the PDMS block.

It was shown that the melt viscosity of the (AB)$_n$ segmented poly(urea-siloxane) copolymers can efficiently and easily be modified by controlling the molecular weight while preserving the overall thermal and mechanical properties. Further, the melt viscosity of the (AB)$_n$ segmented poly(urea-siloxane)s can be adjusted to match similar orders of magnitude. This is important for gradient fabrication from the melt which will be discussed in chapter 3.4.

3.2.7. Conclusion of chapter 3.2.

Within this chapter hydrophobic (AB)$_n$ segmented poly(urea-siloxane) copolymers with different thermal and mechanical properties were designed, synthesized, and characterized concerning their thermal, mechanical, and morphological properties, providing a copolymer platform with a broad spectrum of properties for different additive manufacturing techniques from the melt.

Synthesis: Properties were tailored by varying the chain length of the soft segment and also the chemical structure of the hard segment to manipulate the intermolecular interaction strength. Thus, three PDMS-diamines with increasing chain length ranging from 1513 g mol^{-1} to 4926 g mol^{-1} and four different diisocyanate components (*1,6-hexamethylene diisocyanate*, *isophorone diisocyanate*, *4,4'-methylene bis(cyclohexyl isocyanate)*, and *toluene-2,4-diisocyanate*) were used. Latter differ in their chemical structure and range from linear, aliphatic to cycloaliphatic and aromatic. The (AB)$_n$ segmented copolymers were synthesized by a catalyst-free one-step polyaddition reaction in THF.

Material properties: The PDMS segment forms the soft matrix of the copolymer while the urea units form embedded aggregated, hydrogen bonded hard segment domains. These act as multiple physical crosslinks and mainly determine the mechanical properties next to the elastic properties being governed by the PDMS segment. The amorphous PDMS soft matrix determines the lower service temperature which is defined by the T_g of the copolymer at about -115 °C. The upper service temperature is defined at the crossover temperature T_{cross} from an elastic to a viscous behavior determined by rheology measurements and dynamic mechanical thermal analysis (DMTA). The crossover temperatures range from 55 °C to 137 °C for the different copolymers, only *1,6-hexamethylene diisocyanate* (HMDI) based poly(urea-siloxane)s show a distinct hysteresis upon cooling and heating, of about 30 °C. Above T_{cross} thermal processing is possible since the hard segment domains disassemble and form an isotropic melt. The thermal properties were found to differ in dependency of the type of hard segment and the chain length of the soft segment. It was shown by rheology that HMDI based poly(urea-siloxane)s exhibit a steep increase of moduli upon cooling which implies a fast solidification of the material. Whereas the other (AB)$_n$ segmented copolymers based on *isophorone diisocyanate*, *4,4'-methylene bis(cyclohexyl isocyanate)*, and *toluene-2,4-diisocyanate* only show a moderate increase of the shear storage and loss modulus over the entire cooling process. This implies a slower and less dominant solidification process. Regarding melt processing (AB)$_n$ segmented poly(urea-siloxane)s the thermal stability and the viscosity at 120 °C was investigated. Since urea units undergo back reactions at temperatures above 140 °C and irreversible, covalent crosslinking can result, the copolymers need to show adequate melt viscosities and stability below this critical temperature. Owed to the more complex structure of the *isophorone diisocyanate*, *4,4'-methylene bis(cyclohexyl isocyanate)*, and *toluene-2,4-diisocyanate* based hard segments the viscosities of these poly(urea-

siloxane)s were found to be at least ten times higher than for the *1,6-hexamethylene diisocyanate* based poly(urea-siloxane)s. Further the mechanical properties were determined by tensile tests and it was confirmed that the Young's modulus decreases with increasing soft segment chain length, yet the strain at break increases. To obtain more insight in the morphology, SAXS and TEM measurements were conducted. SAXS measurements showed for the $(AB)_n$ segmented copolymers a certain periodicity within the copolymer with a spacing length of 4.78 nm, however no defined morphology can be assigned. TEM images revealed domains being embedded in a matrix. Overall diameters of the urea hard segment domains were found up to 90 nm in size.

Adjustment of the melt viscosity: Other parameters like melt viscosity still play an important role in melt processing. Additionally, the molecular weight of two $(AB)_n$ segmented poly(urea-siloxane)s based on the shortest and the longest PDMS chain length was tailored to reduce the melt viscosity and to adjust the melt viscosities of both copolymers to match each. The melt viscosity determined at 120 °C was successfully reduced from 350 Pa·s to 70 Pa·s for the $(AB)_n$ segmented copolymer with the shortest PDMS chain length and from 630 Pa·s to 130 Pa·s for the one with the longest PDMS chain length by adding a defined amount of monofunctional reagent, benzylamine, to the reaction to offset the stoichiometry and the final molecular weight. The mechanical and thermal properties were not significantly influenced by the reduction of the molecular weight, solely the ultimate elongation was reduced owed to shorter polymer chains.

3.3. Melt electrospinning and extrusion-based additive manufacturing

3.3.1. Additive manufacturing techniques

Melt electrospinning

Electrospinning is a simple and versatile technique to fabricate randomly distributed fibers by inducing a fluid jet into an electrical field. Randomly nonwovens with quasi infinitely long fibers are collected in form of fiber membranes. Solution electrospinning was already discovered in 1897 by Rayleigh. The first patent was published in 1934 by Formhals.[88] Melt electrospinning was first introduced by Larrondo and Manley several years later in 1980s.[89–91] Using polymer melts instead of solutions makes it even more interesting since no additional solvent removal and ventilation system is necessary and on top the use of toxic solvents is excluded, making this approach much more environmentally friendly and less expensive. Also a mass loss by solvent evaporation is excluded resulting in a higher throughput rate.[92,93]

The general process of melt electrospinning is similar to solution electrospinning. A fluid (here a polymer melt) is extruded through a spinneret which has a high potential difference applied between the spinneret and the collector. The fluid forms first a pending drop which deforms into a Taylor cone at the needle tip. When the charges generated at the Taylor cone overcome the surface tension, an electrified, molten jet is directed towards the collector. This technique makes use of electrostatic forces dragging and thinning polymer fibers towards the collector instead of mechanical forces which are applied in common melt spinning techniques.[94] Electrostatic instabilities of the molten jet cause whipping, resulting in a chaotic fiber deposition. Instead of evaporation of the solvent in case of solution electrospinning, the polymer melt solidifies upon deposition. This can take place on the way towards or after fiber placement on the collector.[95]

Electrospun fibers either from solution or melt can be found in a wide range of applications, including membranes, filters, composites, biomimetic materials, drug-delivery systems, protective clothing, and scaffolds for tissue engineering.[14,94] Yet most of the research focuses on solution electrospinning while only a few report on melt electrospinning. This is owed to the fact that polymer melts are intrinsically nonconductive and poses a higher viscosity compared to solutions and thus thicker fibers are generated. Up to today, homogenous melt electrospun fibers with a diameter below one micron can be fabricated by increasing the electrical field strength and temperature.[14,96,97] Further studies concentrated on an increasing conductivity of the polymer melt to reduce the fiber diameter by adding conductive additives, such as antistatic agents, ammonium salts, sodium chloride or sodium oleate to the polymer melt.[98,99]

The physical instabilities induced by the electrical field influence size and geometry of the deposited fibers. The Rayleigh instabilities are axisymmetric and occur at low electrical field strength or at low viscosities. Yet this results in breakage of the jet and bead formation. These instabilities are suppressed

by high electrical fields. Next to that there are bending (axisymmetric) and whipping instabilities (non-axisymmetric) arising from charge-charge repulsion between the excess charges within the jet. These are responsible for thinning and elongation of the jet.[100] The morphology and fiber diameter of the electrospun fibers depend strongly on the one hand on the setup parameters such as applied high voltage, distance between needle tip to collector, flow rate, temperature, and inner needle diameter. On the other hand, intrinsic parameters like the electrical conductivity of the polymer, solidification behavior, surface free energy, and the viscosity are crucial.

The final fiber formation during the melt electrospinning process is based on a quite complex physical process which can be divided into four major steps:[12,101] (1) pendant droplet formation at the tip of the needle, (2) initiation of the melt jet, (3) elongation and thinning of the jet owed to electrical instabilities, and (4) solidification of the jet and final fiber fixation.[102] The physical process of the jet formation is initiated by a pendant drop formed at the needle tip as shown in Figure 3.25 **(A)**. Exposed to the electrical field the drop is elongated owed to repulsion of the induced charges **(B)**. At the Taylor cone **(C)** the melt jet is initiated, when the electrostatic charges overcoming the surface tension and the viscoelastic properties of the melt. This jet is accelerated towards the collector at a sufficient field strength.[96,97,103] Compared to solution electrospinning, the fibers resulting from melt electrospinning are thicker owed to higher viscosity.[92] In general, with increasing molecular weight of the polymer, chain entanglements increase causing an increasing resistance to elongation and stretching the fibers.[96] For highly viscous polymer melts, the jet is more likely extruded through the spinneret than electrospun since the jet stability increases.[103,104]
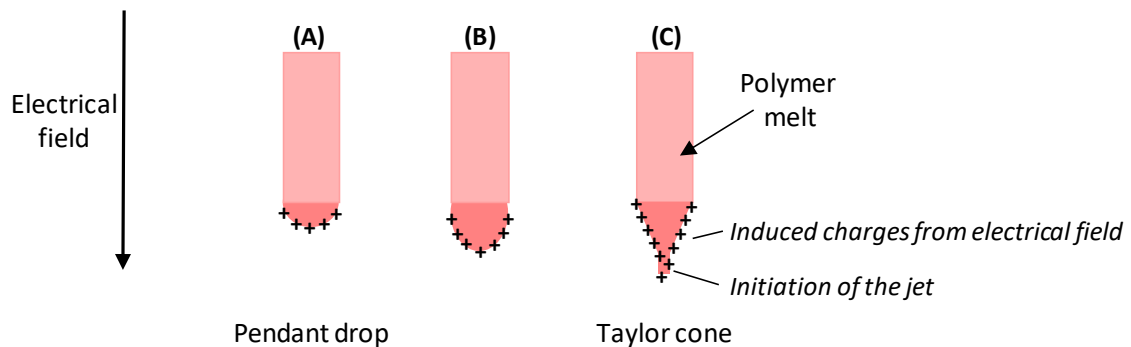
Figure 3.25: Schematic illustration of the Taylor cone formation and jet initiation. **(A)** Initially a pendant drop is formed at the needle tip which is **(B)** elongated due to repulsion of the induced charges from the electrical field. **(C)** In the last step the Taylor cone is formed and the melt jet is initiated, when overcoming the surface tension and the applied electrical field is high enough. [Adapted and printed with permission from [100]; © 2010 Elsevier]

Synthetic biomaterials such as silicone rubber and polyurethanes are of interest for different biomedical applications and medical use based on their properties. These include elasticity, excellent hydrolytic stability, tissue and blood compatibility, and resistivity to microorganisms and abrasion.[94,105] Up to today multiple research groups worked on the electrospinning behavior of polyurethane copolymers, yet in solution. Kang *et al.*[105] used an electrospun polyether-based TPU as non-degradable blood vessels since they are thermally stable in the body temperature range. Yilgor *et al.*[106] electrospun polyurethaneurea segmented copolymers based on poly(tetra-methylene oxide)glycol, a cycloaliphatic diisocyanate and an unsymmetrical chain extender from DMF solution. By varying the solution concentration, they were able to obtain fiber diameters in the range of 7 nm to 1.5 µm. Further they found that the morphology of the electrospun fibers strongly depends on the solution concentration and consequently on the viscosity as well as on the temperature.[106] Yilgor *et al.* showed by solution electrospinning of polydimethylsiloxane-urea copolymers from a THF/isopropanol solution followed by UV/ozone exposure a conversion of an hydrophobic surface into a hydrophilic one. They fabricated well-defined fibers with a diameter ranging from 1 µm to 7 µm. However, the fibers were not perfectly round more flatten.[107]

Knowing that all kinds of polymers were analyzed by solution electrospinning the amount of polymers being investigated by melt electrospinning is still limited. Polymers previously investigated by melt electrospinning include poly(ethylene), poly(propylene), poly(ethylene terephthalate), polyamides, polystyrene and poly(ethylene naphthalene) which were processed at high temperatures between 200 °C and 290 °C.[108] Dalton *et al.* reported melt electrospun poly(ethylene glycol-*block-ε*-caprolactone) fibers with melting points below 60 °C.[108] A biodegradable TPU based on poly(caprolactone) was melt electrospun and was found to form smooth, robust fibers without bead formation and having mechanical properties comparable to many native tissues.[109] Yet to the best of our knowledge there was so far no research on poly(urea-siloxane)s being melt electrospun.

Melt electrowriting (MEW)

Additive manufacturing (AM) describes techniques that build precise 3D constructs in a directed layer-by-layer material deposition process using computer-aided design (CAD) data.[16] They are achieving complex shapes and parts with high degree of automation, good accuracy, and reproducibility.[16] Melt electrowriting (MEW) is a relatively new additive manufacturing technique to melt fabricate 3D structures at least two magnitudes smaller than fused deposition modeling (FDM). It is also based on an extrusion process yet a high voltage is applied between the tip of the cannula and the collector plate which is the essential driving force to generate thinner fibers by electrostatically dragging them towards the collector plate. This allows a significant higher resolution while the resolution of FDM is limited by the nozzle size since it is solely an extrusion-based process.[24] Melt electrowriting bridges the gap between electrospinning and direct writing additive manufacturing techniques.[24] Albeit MEW is related to melt electrospinning, where small diameter fibers are induced by electrical instabilities and a chaotic fiber deposition takes place.[110]

In MEW a polymer melt is extruded through a spinneret and being charged due to an applied electrical field between the tip of the cannula and a collector. The jet formation is more or less analogous to the melt electrospinning process. Initially a pending drop is formed which deforms into the so called Taylor cone and by overcoming the surface tension the melt jet is induced. While electrospinning is based on electrical instabilities, MEW uses electrohydrodynamic stabilization of the molten jet to control the directed fiber deposition. In detail, MEW is based on a electrohydrodynamic process, where a molten jet is stabilized at low flow rates with an accelerating voltage, providing a predictable jet path. Using a moveable collector plate, allows a continuous direct writing and an accurate layer-by-layer fiber deposition with building heights to millimeters.[24,95,111–113]

In order to exclude buckling and coiling of the melt jet and reaching a straight and defined fiber deposition, the collector speed needs to be adjusted to the jet speed. This speed, when collector and jet are equal is defined as the critical translation speed (CTS) and is an important parameter for controlled fiber placement. In Figure 3.26 the fiber deposition in dependency of the jet s_J and collector speed s_C is shown schematically. It can be seen that at a stationary collector speed **(A)** coiling occurs owed to compression of the jet. This is reduced with increasing s_C **(B)**. At CTS **(C)**, straight fibers are deposited. With further increasing the collector speed **(D)** the fiber diameter can be further reduced by mechanical stretching. Nevertheless, the printing quality can suffer especially at the turning points due to an increasing lag of the jet. Thus, an optimal direct writing is obtained when the speed of the collector matches the jet speed as close as possible.[24]
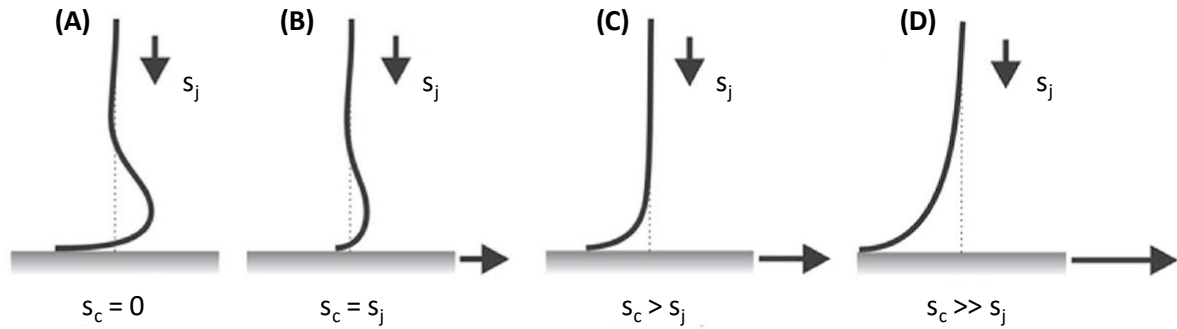
Figure 3.26: The shape of the melt electrospinning jet profile depends on the speed of the collector s_c relative to the jet speed s_j. [Adapted and printed with permission from [24]; © 2011 Wiley-VCH]

In Figure 3.27 distinct patterns are shown in dependency of the translation speed of the collector. **(A)** shows a straight fiber deposition owed to MEW printing at CTS, while the fibers in **(B)** to **(D)** are placed below the CTS showing increasing buckling owed to coiling of the jet on its way towards the collector.[113]
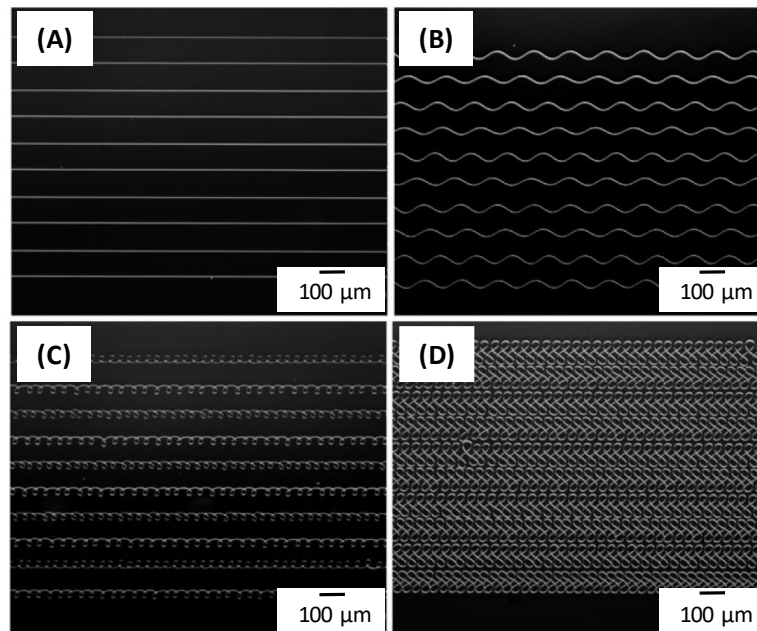
Figure 3.27: Different fiber deposition patterns depending on the jet speed relative to the collector speed, with it being **(A)** at and **(B-D)** below the critical translation speed (CTS). [Adapted and printed with permission from [113]; © 2016 Walter de Gruyter]

Direct writing of highly resolved 3D objects by applying a high voltage on a molten polymer jet requires several parameters to be adjusted. In comparison to extrusion based techniques, MEW uses an electrical field to further reduce the fiber diameter and thus the overall resolution of the 3D structure. To ensure a high printing quality, including uniform fiber diameters, accurate and unbroken fiber stacking, the mass flow rate from the spinneret onto the collector plate needs to be adjusted to exclude pulsing, which is defined as undesired sectional oscillation of the fiber diameter. It can be distinguished between three diameter instabilities: (1) temporary pulsing, (2) continuous pulsing and (3) regular long bead pulsing. Pulsing has also a negative effect on the fiber deposition when there is a change in

direction of the collector plate like turning. Further, the collector distance, spinneret size, electrical field strength, and environmental conditions influence the printing quality and need to be optimized.[113] Next to the instrumental parameters the material characteristics have also a significant influence on the printing accuracy and resolution of the 3D objects. The molecular weight is most critical, as it determines the melt viscosity of the material and being the major factor for the ability to extrude the polymer melt through the needle tip and overcoming back pressure.[113]

MEW permits the fabrication of 3D object such as scaffolds with defined designs in pore size, pore interconnectivity, or mechanical properties.[95] Since MEW is described as an additive manufacturing technology for tissue engineering, multiple medical polymers were processed and investigated. Including the benchmark material poly(ε-caprolactone) (PCL),[24,114–119] poly(lactide-*co*-glycolide),[120] poly(lactic acid),[121] PCL-*block*-poly(ethylene glycol),[97,122–125] photocurable poly(lactide-*co*-capro-lactone-*co*-acryloyl carbonate),[126] nondegradable poly(propylene),[97,127] poly(methyl meth-acrylate),[128] and water-soluble poly(2-ethyl-2-oxazoline).[129] PCL gained a lot of interest for MEW not only because of its biodegradable behavior but also from a processing perspective. PCL has a low melting temperature ($T_m = 58 \,°C$) as well as a slow thermal and hydrolytic degradation. Further its semi-crystalline character is advantageous for fast solidification upon cooling and a precise layer-by-layer deposition. However, this is also a drawback since the material is opaque, limiting applications where optical quality is required.

Still there is in general a challenge in fabricating higher 3D structures by MEW owed to repelling of newly deposited fibers on top of each other at a certain height. This leads to inaccurate fiber deposition and poor printing quality and is assigned to shielding and residual charges upon the previous deposited fibers.[119]

Fused deposition modeling (FDM)

Fused deposition modeling, as one of the cheapest and most popular AM technologies, is a solely extrusion based process. It is already commercially used in the fields of aerospace, automotive, and medical engineering only to name few. The basic principle is based on a polymer filament being transported to a liquefier were it melts before it is extruded through a nozzle onto a moveable collector plate. The fiber thickness is defined by the nozzle diameter and extrudate swell. FDM can fabricate 3D objects on the centimeter scale which means that a larger quantity of materials on the kilogram scale is necessary for manufacturing the filament, while MEW uses only few grams. Since no electrical field is applied and the melt is not charged, no defects owed to repulsion upon layer-by-layer fiber deposition are observed and building higher 3D objects is not restricted by this. Yet the spatial resolution is limited due to difficulties in extruding strands below 100 µm. Reducing the nozzle diameter and the filament diameter to the lower micron scale leads to a dramatic slowing of the FDM

process. Fabricating polymer filaments with diameters above 100 μm is a lot faster, though sacrificing smooth surfaces and an additional post-processing step might be necessary.[17] The fiber geometry is significantly influenced by material properties such as solidification behavior and stiffness. However, critical instrument parameters including nozzle temperature, nozzle path and speed, and the collector temperature govern the printing quality.[130] In order to print more complex 3D objects, supporting structures are necessary which can be printed in-situ utilizing a second printing head and be removed afterwards. The fiber diameter resulting from FDM is mainly determined by the nozzle diameter, yet it further extends after exiting the nozzle.[131] Polymer chains are statistically oriented, forming random coils in the molten state. Upon extruding them through a nozzle the mechanical stress leads to deformation and stretching of the polymer chains. Upon leaving the nozzle a relaxation process takes place called extrudate swell. This process is driven by entropy and releases the elastically stored energy of the stretched polymer chains by again randomly coiling. This process results in larger fiber diameters than the nozzle diameter itself.[131]

Typical FDM materials are thermoplastic polymers and in particular amorphous polymers such as acrylonitrile-butadiene-styrene (ABS), polyetherimide (PEI), acrylonitrile-styrene-acrylate-copolymers (ASA) and polyethylene terephthalate modified with glycol (PET-G). Semi-crystalline polymers are less popular due to warping and inaccuracy of the final 3D construct. Nevertheless, there are some commercial semi-crystalline polymers used for FDM such as poly(lactic acid) (PLA), polyamide 12 and poly(propylene).[20,132–135] TPEs such as polyurethanes are also commercially available for FDM. Yet they have a high shore hardness which corresponds to comparable tough and stiff materials. For example, a TPU filament from *SainSmart* has a shore A hardness of 95[136] and FlexLine from *Extrudr* being slightly softer with a shore A hardness of 88.[137] Further these TPUs are predominantly processed at extremely high temperatures (~ 200 °C). Owed to the difficulty in filament transportation towards the liquefier and a reduced printing quality of soft and elastic materials the product market is rather small.

FDM for commercial applications or only for material screening needs generally large quantities of material. Common filament spools are available with 0.5 kg and up. Thus it is not possible to investigate new classes of materials if they are only available on a small scale. At the chair Macromolecular Chemistry I at the University of Bayreuth Jin *et al.* developed a method for screening new FMD materials using small material quantities (8 – 20 g).[20] First they fabricated single filament rods instead of endless filament spools by compounding and injection molding. A special design of a printed square tube was developed to investigate the FDM performance as a function of the polymer type, material composition, and printing parameters. The 3D construct is based on a free-standing, open, square tube with cubic dimensions built up of single-line stacks. This tube can be used to evaluate the printing performance such as wrap deformation and interlayer bonding of new materials. An advantage of this method is material, time, and cost savings for the development of novel FDM materials.[20]

Thermoplastic elastomers are well known not only for their elastic properties at service temperature but also for their thermoreversible nature which allows processing from the melt with common techniques for thermoplastic polymers such as extrusion or injection molding. Within this chapter, the before described (AB)$_n$ segmented thermoplastic poly(urea-siloxane) copolymers will be melt processed into fibers. First *melt electrospinning* is utilized to determine the melt processability within an applied electrical field and the resulting fiber properties such as fiber geometry, fiber diameter, and fiber fusion will be analyzed. This is followed by two additive manufacturing techniques on different length scales *melt electrowriting* (MEW) and *fused deposition modeling* (FDM). The layer-by-layer fiber deposition and the influence of processing parameters on the printing quality will be investigated for these two methods. The aim is to fabricate accurate 3D objects with thin fiber diameters and perfect fiber fusion on two different length scales.

3.3.2. Melt electrospinning

Melt electrospinning setup

A schematic illustration of a melt electrospinning unit is shown in Figure 3.28. A 1 mL glass syringe containing the polymer is heated to the melt by an external electrical heater. The viscous polymer melt is transported with a constant flow rate to the needle tip by applying a defined pressure on the piston via a syringe pump. Initially a drop is formed at the needle tip before transforming into a Taylor cone induced by the applied high voltage between tip and collector. Overcoming the surface tension, a polymer jet is formed which is dragged towards the collector while whipping occurs. Chaotic distributed, solidified fibers are deposited on the collector.
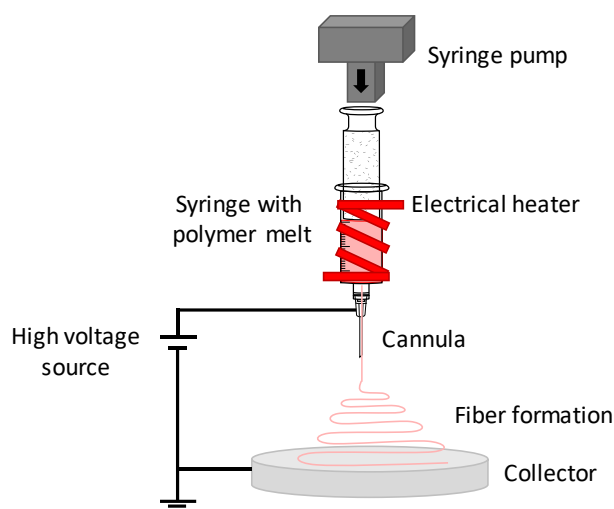
Figure 3.28: Schematic setup of a melt electrospinning unit containing a syringe pump and a heated glass syringe filled with the polymer melt. Upon applying a defined pressure on the syringe and a high voltage between cannula and collector a polymer jet is formed which moves randomly from the needle tip towards the collector.

For the $(AB)_n$ segmented copolymers a capillary cannula with an inner diameter of 600 µm is chosen. The viscosity of the melt has to ensure a sufficient and continuous flow rate through the capillary. Further the distance between tip and collector is essential since the solidification of the jet needs to be ensured before reaching the collector to avoid coalescence of molten fibers. The electrical field depends on the applied voltage and the needle tip to collector distance, which was kept constant at 3.7 cm, while the high voltage was varied between 10 and 27 kV, resulting in a field strength *E* of 2.7 to 7.3 kV cm^{-1}.

Material selection

The viscosity of the polymer melt plays a crucial factor on the melt flow rate and the final fiber diameter. Further a fast solidification of the polymer is advantageous to obtain homogenous round fibers which don't conglomerate into broad objects at the collector surface. Concluding from these requirements $(AB)_n$ segmented poly(urea-siloxane) copolymers based on *1,6-hexamethylene diisocyanate* (HMDI) are of great interest owing to their excellent steep increase of moduli upon

cooling going hand in hand with a rapid solidification. Hence, the poly(urea-siloxane) **1a** and **2a** are chosen as suitable candidates for melt electrospinning due to their complex viscosities determined at 100 °C of 370 Pa·s and 340 Pa·s, respectively. Poly(urea-siloxane) **3a** is not selected as a suitable candidate owed to its too high melt viscosity and particularly its self-healing characteristic. Self-healing could lead to an increase in merging and sticking of the fibers.

Results and discussion

*Melt electrospinning of **1a**: Influence of flow rate on fiber formation*
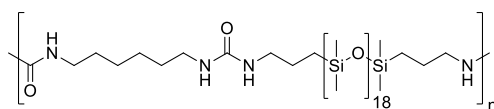
1a

First the processing temperature was determined in the melt electrospinning setup without applied electrical field at a flow rate of 100 µL h^{-1}. The copolymer was completely molten at 140 °C for 10 min and subsequently cooled to 60 °C. Increasing the temperature stepwise in 5 K steps the processing temperature was determined obtaining a homogenous and constant melt flow. The optimal processing temperature was found to be 100 °C for **1a**. Poly(urea-siloxane) **1a** was investigated by melt electrospinning concerning the fiber geometry, fiber diameter and fiber fusion in dependency of an increasing flow rate.

As can be seen in Figure 3.29 **1a** can be melt electrospun at 100 °C with an applied voltage of 20 kV (E = 5.4 kV cm^{-1}) and a *flow rate* of *100 µL h^{-1}*. Neither electrospraying nor breakage of the melt jet was observed during the whole process, implying an extremely stable process. Upon that process cooling and solidification of the melt jet occurs. If the jet solidifies more or less completely upon its way towards the collector the fibers are defined as solid state fibers. While if they are still in the molten state upon arrival at the collector, they are denoted in this thesis as molten fibers since the fibers show coalescence and a flattened geometry. For poly(urea-siloxane) **1a** only one category of fibers is observed, namely perfectly round fibers in the solid state. **1a** solidifies extremely fast which results in homogenous fibers with a round and uniform fiber diameter of 56.9 ± 3.7 µm. The small standard deviation is due to a constant melt jet and the fast solidification. For high quality and resolution of fiber placement, meaning uniform solid fibers with round fiber diameters are the aim. It is also noticeable that no beads are formed along the fibers. Yet no random fiber mats are obtained, instead the fibers are curled and stacked into height as seen in Figure 3.29 **(A)**. This can be explained by the relatively high viscosity of the polymer melt, preventing the melt jet from a high degree of whipping and a significant acceleration towards the collector. Further extremely smooth fiber surfaces without any cracks or other physical defects are obtained as can be seen in Figure 3.29 **(B)**. From solution electrospinning it is known that many cracks on the fiber surface are caused by solvent evaporation

which is faster on the surface than within the fiber core.[94] One major interest in melt electrospinning poly(urea-siloxane)s was the single fiber fusion which is essential for printing 3D structures with excellent bonding between the single fibers. As shown in magnification in Figure 3.29 **(C)** fiber fusion, maintaining the round fiber geometry, is observed. This is due to the physical crosslinks within the copolymer. Since these fibers are thermally processed, the hard segments disaggregate at elevated temperatures and upon fiber formation and fusion, the urea units re-aggregate and form physical crosslinks also between the interfaces resulting in well fused fibers with excellent bonding.
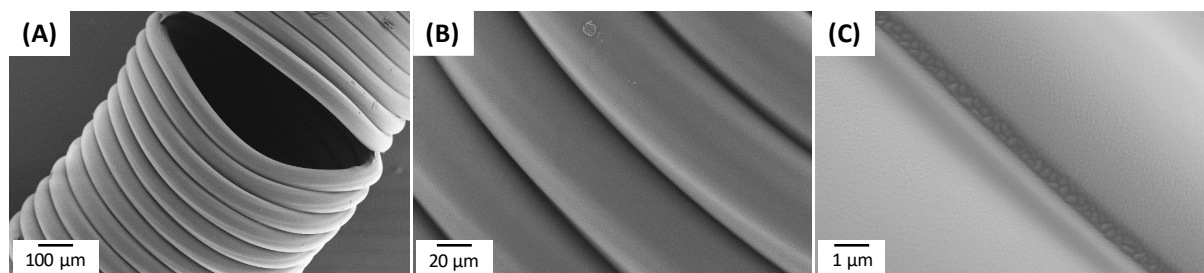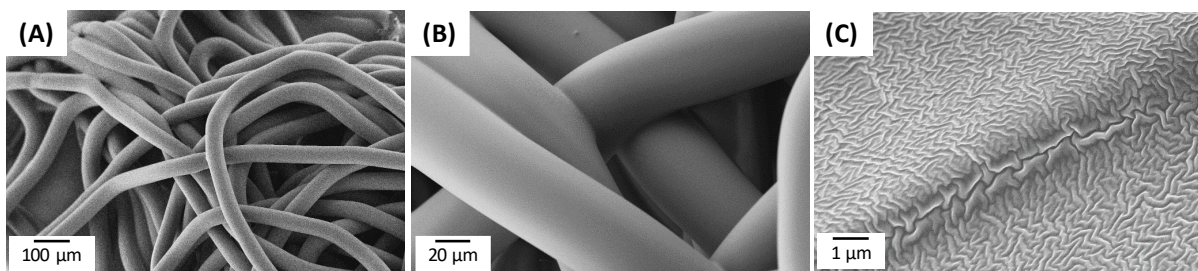

Figure 3.29: SEM images of electrospun fibers from poly(urea-siloxane) **1a** at different magnifications presenting perfectly round and uniform fibers **(A)** with a smooth fiber surface **(B)** and visualizing fiber fusion **(C)**. The highly viscous melt prevents a high degree of whipping and acceleration of the jet resulting in a more extrusion based process. Electrospinning conditions: 100 °C, 20 kV, 100 μL h^{-1}.

Applying a higher *flow rate* of *500 μL h^{-1}* while keeping the temperature at 100 °C and the applied voltage at 20 kV (E = 5.4 kV cm^{-1}) a similar behavior of fiber formation can be observed as can be seen in Figure 3.30. This is due to a more extrusion based process than electrospinning including whipping. Again the fibers form a curled and stacked object and not a random fiber mat **(A)** owed to the viscosity of the polymer melt. Since the fibers reach the collector in the solid state, ideally round and uniform, symmetric fibers are observed. The fibers also show a perfectly smooth surface as well as a good fiber fusion **(B)** and **(C)**. Owing to the increased flow rate and consequently a higher mass throughput, thicker polymer fibers with an average fiber diameter of 179.9 ± 5.5 μm are obtained which is about three times larger than at a flow rate of 100 μL h^{-1}. The small standard deviation confirms additionally the uniformity and homogeneity of the fibers due to the constant melt flow. Even at higher flow rates the melt jet remains constant without bead formation or jet breakage.
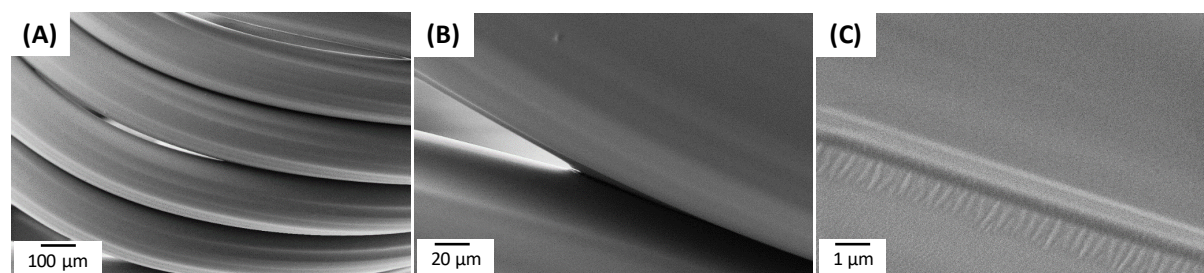

Figure 3.30: SEM images of electrospun fibers from poly(urea-siloxane) **1a** at different magnifications presenting perfectly round and uniform fibers **(A)** with a smooth fiber surface **(B)** and fiber fusion to a certain extent **(C)**. The highly viscous melt prevents a high degree of whipping and acceleration of the jet resulting in a more extrusion based process. Electrospinning conditions: 100 °C, 20 kV, 500 μL h^{-1}.

*Melt electrospinning of **2a**: Influence of applied voltage on fiber formation*
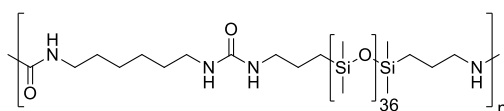
2a

Poly(urea-siloxane) **2a** possessing about twice the PDMS chain length as **1a** and an increased elasticity with a significantly lower Young's modulus, yet a larger strain at break was investigated concerning its potential for melt electrospinning. The optimal processing temperature was also found to be 100 °C with a viscosity of $\eta^*_{100\,°C}$ = 340 Pa·s. In Figure 3.31 SEM images of the resulting fibers melt electrospun at 100 °C with an *applied voltage* of *10 kV* (E = 2.7 kV cm^{-1}) and a flow rate of 100 μL h^{-1} are shown. As seen before for **1a**, round fibers with an extremely smooth surface and fiber fusion are obtained **(B)** and **(C)**. The melt jet shows also for **2a** a fast solidification upon its way towards the collector and reaching it in the solid state excluding any flattening of the fiber geometry. Yet less stacking in height is observed as was seen for the previous less flexible copolymer. Owed to its more elastic and softer properties the polymer melt is dragged towards the collector in a more random form. An average fiber diameter of 159.1 ± 13.5 μm without bead formation along the fibers was achieved. The melt jet was stable and constant throughout the whole electrospinning process, resembling more an extrusion process instead of electrospinning.
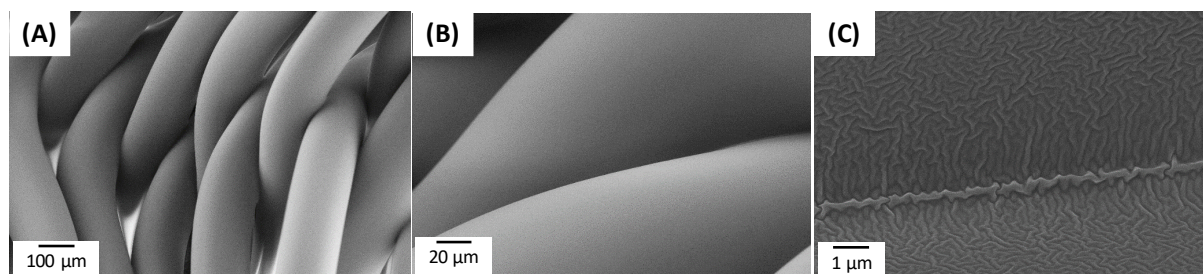
Figure 3.31: SEM images of electrospun fibers from poly(urea-siloxane) **2a** at different magnifications presenting perfectly round and uniform fibers **(A)** with a smooth fiber surface **(B)**. **(C)** visualizing an excellent fiber fusion. Electrospinning conditions: 100 °C, 10 kV, 100 μL h^{-1}.

For this poly(urea-siloxane) system the influence of an increasing applied high voltage in regard of fiber geometry, fiber diameter, and fiber fusion was investigated. By increasing the *applied voltage* to *20 kV* (E = 5.4 kV cm^{-1}) the fiber diameter could be reduced to 58.7 ± 3.0 μm which is in the same range as melt electrospun fibers of **1a** under the same conditions. This is owed to similar viscosities at 100 °C of **1a** ($\eta^*_{100\,°C}$ = 360 Pa·s) and **2a** ($\eta^*_{100\,°C}$ = 340 Pa·s), resulting in comparable flow rates. Besides, more random fiber distribution and less stacking in height is observed resulting from the more elastic behavior of the TPE and the increased impact of the higher applied voltage (Figure 3.32). Furthermore, a visual excellent fiber fusion and smooth surface is obtained.
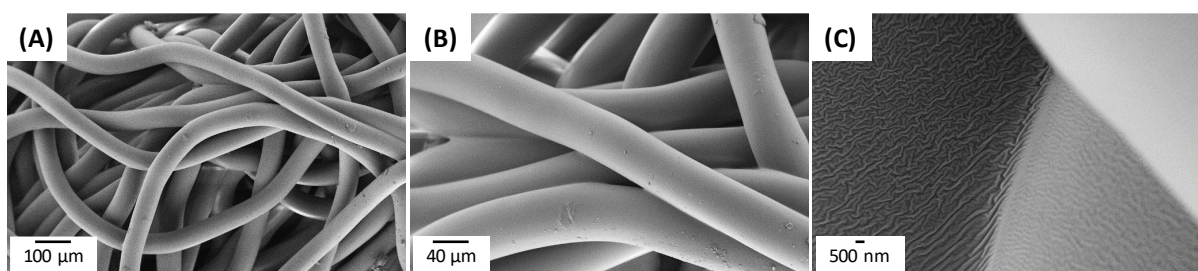
Figure 3.32: SEM images of electrospun fibers from poly(urea-siloxane) **2a** at different magnifications presenting perfectly round and uniform fibers **(A)** with a smooth fiber surface **(B)**. **(C)** visualizing an excellent fiber fusion. Electrospinning conditions: 100 °C, 20 kV, 100 µL h^{-1}.

Further increasing the *applied voltage* to *27 kV* (E = 7.3 kV cm^{-1}) and keeping the other parameters constant even thinner and randomly distributed fibers are obtained (Figure 3.33). During the whole processing time the melt jet remained constant without bead formation or even breakage of the melt jet. Which is again attributed to the materials viscosity, resembling still a more extrusion based process instead of electrospinning. The average fiber diameter amounts to 48.3 ± 1.8 µm. A visual excellent fiber fusion and smooth surface is still observed. 27 kV is the maximum applied voltage before arching and breakdown of the electrical field occurred.

Figure 3.33: SEM images of electrospun fibers from poly(urea-siloxane) **2a** at different magnifications presenting perfectly round and uniform fibers **(A)** with a smooth fiber surface **(B)** and an excellent fiber fusion **(C)**. Electrospinning conditions: 100 °C, 27 kV, 100 µL h^{-1}.

It was shown that (AB)$_n$ segmented poly(urea-siloxane) copolymers **1a** and **2a** based on *1,6-hexamethylene diisocyanate* (HMDI) and different PDMS chain length can be processed into fibers with an average fiber diameter ranging from 180 µm down to 48 µm via melt electrospinning. Varying the applied electrical field, the fiber diameter can be tuned in this range. Here an extrusion like process through the needle tip is present. It was further shown that constant melt jets without bead formation and / or breakage during processing were obtained. The material properties allow a more stacked construct formation, however, without repelling of single fibers owed to charge accumulations. This is a distinct feature for further processing the copolymers by extrusion-based layer-by-layer additive manufacturing methods. The fibers show a fiber fusion and homogenous, smooth fiber surfaces. Proceeding from these results it is expected that these poly(urea-siloxane) copolymers are an excellent material for extrusion-based additive manufacturing techniques such as melt electrowriting and fused deposition modeling. This will be discussed in the following chapters.

3.3.3. Melt electrowriting

Melt electrowriting setup

A general melt electrowriting unit is schematically shown in Figure 3.34 **(A)** as well as a photograph **(B)** of the actual setup. A 3 mL glass syringe equipped with a flat-tipped stainless steel cannula (inner diameter: 300 µm) is filled with polymer and heated by an electrical heater above the crossover temperature of the poly(urea-siloxane). Nitrogen pressure is used to generate a certain flow rate on the polymer melt to extrude it through the cannula. A positive high voltage is applied between the needle tip and the collector plate analogous to the melt electrospinning setup maintaining a distance of 8.5 mm which is significantly smaller than for melt electrospinning. The field strength of the applied electrical field was varied between 9.4 kV cm^{-1} and 14.1 kV cm^{-1}. The syringe can be moved in z-direction while the collector plate is no longer stationary as for the melt electrospinning experiments, it can be moved in x- and y-direction programmed previously with a software to direct write a distinct structure on a glass microscope slide.
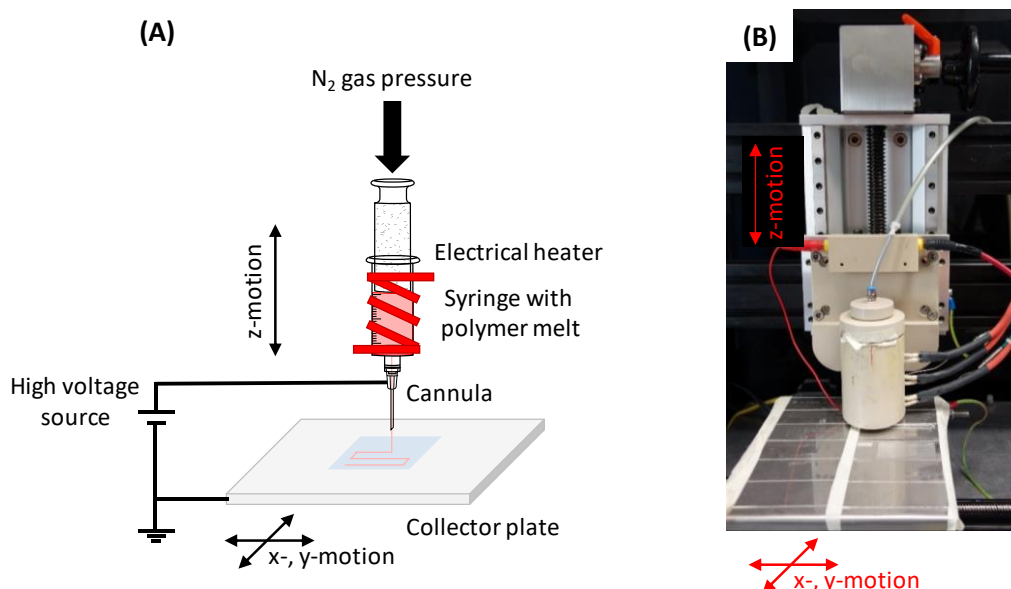
Figure 3.34: (A) Schematic setup of a melt electrowriting unit. Nitrogen pressure is applied on the heated syringe containing the polymer melt. Between the tip and the collector, a high voltage is applied dragging the formed polymer jet in a controlled way towards the collector. For accurate fiber deposition the collector speed in x- and y-direction is externally controlled. **(B)** shows a photograph of the MEW setup at the University of Würzburg utilized within this thesis.

Material selection

As known from other polymers, polymers used for MEW have to fulfill certain requirements. First they need to be melt processable and thermally stable over several hours since MEW processing can take place over at least 4 – 5 hours.[138] A sufficient melt viscosity and fast solidification is also important to ensure a homogenous melt jet and perfectly stacked round fibers resulting in a highly accurate 3D construct. Moreover, a good fusion between the fibers is advantageous since it improves the quality of the final construct by minimizing defects. As shown by melt electrospinning (AB)$_n$ segmented poly(urea-siloxane) copolymers can be processed into symmetrical, uniform fibers. The polymer melt can be influenced and stretched by an applied electrical field, forming a stable and constant melt jet. This airborne, extruded jet was stretched to equilibrium while the charges within the melt and the surface tension balance each other and owed to the high viscosity a predictable melt jet path was observed.[108] Based on the electrospinning experiments it was demonstrated that poly(urea-siloxane) **1a** showed a fast solidification upon deposition and fiber curling in height without repelling of charged fibers, whereas **2a** showed more randomly distributed fibers. For these reasons **1a** is chosen for MEW experiments.
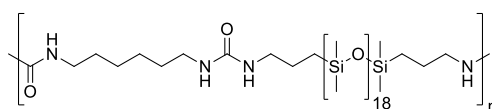
1a

Results and discussion

Thermal stability during melt electrowriting process

Essential for MEW is a thermal stability of the polymer for at least 4 – 5 h to achieve a sufficient printing time. During that period the polymer should neither degrade nor melt jet instabilities should emerge influencing the uniform fiber diameter. Poly(urea-siloxane) **1a** shows a thermal stability over several hours at temperatures lower than 140 °C as previously discussed by isothermal rheology measurements (chapter 3.2.3, Figure 3.17). Above that temperature within short time frames a dramatic increase in viscosity owed to chemically crosslinking is observed. Additionally, the fiber behavior with respect to diameter fluctuations was investigated over time. The average fiber diameter was monitored at optimum processing conditions (90 °C, 2.0 bar, 10.0 kV, 8.5 mm, 11.8 kV cm^{-1}) for 8 h. An average fiber diameter of 15.3 µm and a standard deviation of 0.1 µm was determined. No significant change nor a breakup of the electrified jet over time was observed demonstrating the thermal stability of the material and a constant flow rate at processing conditions over time (Figure 3.35).[85]
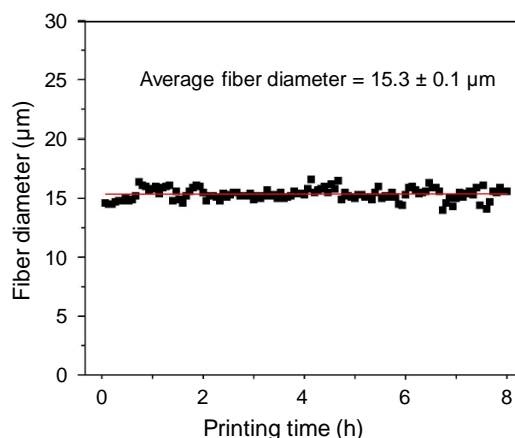
Figure 3.35: Fiber diameter in dependency of MEW printing time. The data points are fitted with a linear fit showing a gradient of 0.02, indicating no change in polymer melt properties and thermal stability over 8 h. Printing parameters: 90 °C, 2.0 bar, 10.0 kV, 11.8 kV cm^{-1}. [Reprinted with permission from [85]; © 2018 WILEY-VCH]

Influence of instrument parameters on single fiber formation

The variation of the average fiber diameter was determined by varying one instrument parameter at the time while keeping the others constant. In specific the influence of the heating temperature T, the feeding pressure p, and the applied voltage U are analyzed regarding the fiber diameter variation while maintaining a constant tip to collector distance of 8.5 mm.

Initially the lowest possible temperature T_{min} for MEW of poly(urea-siloxane) **1a** was determined. For this the copolymer was completely molten in the syringe for 10 min at 150 °C. The temperature was decreased to 60 °C and gradually elevated until T_{min} = 80 °C was reached. It was found that the most significant instrument parameter influencing the fiber diameters are the feeding pressure and the collector speed, while the applied voltage is tuned to minimize fiber pulsing, a common issue with MEW where the fiber diameter periodically fluctuates such as bead formation, resulting in poor placement and stacking accuracy.[113] Hence single MEW direct-writing layers were processed to investigate the influence of multiple instrument parameters on the printed fibers and to suppress fiber pulsing. The average fiber diameter was investigated as a function of heating temperature T, feeding pressure p and applied voltage U. Only one parameter was changed at a time in five equidistant steps as shown in Table 3.12, while the other parameters were kept constant at the optimum parameters (90 °C, 2.0 bar, 10.0 kV, 8.5 mm, 11.8 kV cm^{-1}).

Table 3.12: Investigated instrument parameters for MEW of poly(urea-siloxane) **1a**. While investigating one specific parameter (heating temperature, feeding pressure or applied voltage), the others were kept at the optimum parameters. The distance between tip and collector were maintained at 8.5 mm. The average fiber diameter is calculated from a total of 40 fibers.

Heating temperature (°C)	Feeding pressure (bar)	Applied voltage (kV)	Average fiber diameter (µm)
80			14.6 ± 0.5
85			15.0 ± 0.9
90	2.0	10.0	15.6 ± 0.5
95			16.5 ± 0.8
100			17.0 ± 0.9
	1.0		10.6 ± 0.6
	1.5		13.5 ± 0.5
90	2.0	10.0	15.3 ± 0.5
	2.5		16.9 ± 0.8
	3.0		17.0 ± 1.5
		8.0	17.8 ± 0.7
		9.0	16.5 ± 0.6
90	2.0	10.0	15.1 ± 0.4
		11.0	14.6 ± 0.6
		12.0	13.5 ± 0.7

Pulsing, defined as the undesired sectional oscillation of the fiber diameter, needs to be avoided to achieve homogenous fiber diameters and a good printing quality. This includes a straight fiber deposition as well as an accurate deposition at the turning points. This can be controlled by adjusting the fiber deposition flow rate and the feeding pressure.[113] The printing performance and the average fiber diameter $f_\varnothing$ was initially evaluated in 5 °C steps up to 20 °C above T_{min}. Figure 3.36 **(A)** shows the *average fiber diameter in dependency of the temperature T* which increases from 14.6 ± 0.5 µm to 17.0 ± 0.9 µm upon heating from 80 °C to 100 °C. This is owed to a decreasing melt viscosity and as a result an increasing throughput. The critical translation speed CTS which is defined as the minimum collector speed where straight fibers can be collected, as well as the deposition flow rate *dV/dt* show a linear correlation to the increasing temperature. The CTS, expressing the jet speed, increases from 1521 ± 108 mm min^{-1} at 80 °C to 3850 ± 364 mm min^{-1} at 100 °C since a low viscous melt is more accelerated towards the collector than a higher viscous melt jet. The deposition flow rate increases from 61 ± 5 mm^3 h^{-1} at 80 °C to 209 ± 23.5 mm^3 h^{-1} at 100 °C.

Further the *feeding pressure p* exhibits a direct *influence on the fiber diameter* as can be seen in Figure 3.36 **(B)**. By increasing the pressure from 1.0 bar to 3.0 bar in 0.5 bar steps the fiber diameter $f_\varnothing$ increases from 10.6 ± 0.6 µm to 19.5 ± 1.5 µm owed to a higher throughput. The standard deviation of the fiber diameter is increased at 3.0 bar as a consequence of fiber pulsing. For the CTS only minor changes are observed with increasing pressure, while the deposition fiber flow rate shows again a

linear dependency on the feeding pressure (appendix Figure A-6.14). Starting from 57 ± 4 mm^3 h^{-1} at 1.0 bar it linearly increases to 173 ± 19 mm^3 h^{-1} at 3.0 bar since the throughput increases. Thus, by varying the feeding pressure, the fiber diameter can be tuned between 10 – 20 µm.[85]

(A)

(B)

(C)
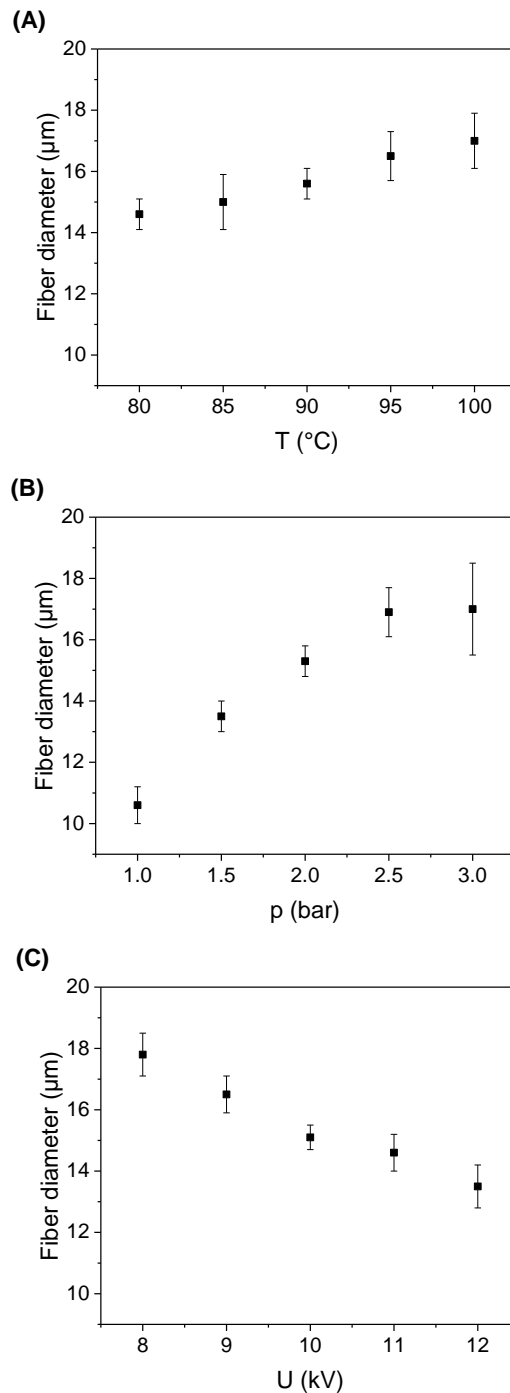
Figure 3.36: Influence of **(A)** temperature *T*, **(B)** feeding pressure *p* and **(C)** applied voltage *U* on the fiber diameter. Only one parameter was varied at a time the other parameters were kept at the optimum processing conditions: 90°C, 2.0 bar, and 10 kV. An increasing fiber diameter can be observed with increasing temperature and feeding pressure, while it decreases with increasing applied voltage.

Varying the applied voltage U, a decreasing fiber diameter with higher applied voltage can be observed since the electrical field is thinning the melt jet by accelerating towards the collector (Figure 3.36 **(C)**). The fiber diameter decreases from 17.8 ± 0.7 µm to 13.5 ± 0.7 µm with an applied voltage of 8.0 kV and 12.0 kV, respectively. Yet, the voltage cannot influence the deposition flow rate since the melt feed rate remains constant. Further, the voltage cannot be decreased below a critical value since a strong electrical field is necessary to introduce and maintain a Taylor cone and the electrohydrodynamically stable jet.[139] Neither can the voltage be increased above a critical value, leading to arching and thus to a breakdown of the electrical field. From experience it was found that a field strength of E ~ 10 – 20 kV cm^{-1} is a realistic maximum for MEW printing. The theoretical limit in air is E ~ 30 kV cm^{-1},[140] however, in real systems it is usually lower considering a humid environment. Interestingly, previously MEW processed polymers did not show a significant variation of the fiber diameter in dependency of the applied voltage. It is primarily tuned to control and minimize fiber pulsing.[85] Besides, the jet speed could be controlled by the voltage which increases with higher voltage while the deposition flow rate remains mostly constant. The investigated range of instrument parameters did neither show pulsing or long beading, nor other processing instabilities, classifying this material as an excellent candidate for MEW.[85]

Concluding from these results, the feeding pressure was tuned to control the fiber size of the printed structure. Whereas the fiber diameter and the jet speed were regulated by the applied voltage.

Fabrication of high resolution MEW printed 3D constructs

The resolution of direct-writing is affected in two ways. On the one hand, it is given by the resolution of the linear collector plate specifications, which is in this instance 1 µm. On the other hand, the accuracy of fiber stacking which is influenced by the copolymer properties, such as physical crosslinks, macromolecular entanglements, shear thinning, electrorheology, and conductivity. Figure 3.37 **(A-D)** shows a melt electrowritten 3D scaffold constructed from **1a** with 100 layers in total at the cross sections and 50 in x- and 50 in y-direction. The printing parameters were set at 90 °C, 2.0 bar, and 10 kV. The entire scaffold (17.5 · 17.5 mm^2) with square boxes of 1.0 · 1.0 mm^2 and a total height of about 360 µm shows an excellent fiber stacking accuracy as well as extremely homogenous fibers. This high accuracy was observed for the first time by MEW fabricated scaffolds. The benchmark system, PCL, was also reported to have highly accurate stacked fibers, although periodic defects, as repelled fibers, were obtained owed to charge accumulations on or in the fibers as the number of layers increase.[141] Other MEW printed polymers exhibit less accurate fiber stacking and homogeneity of fiber diameter.[126,129] Another outstanding feature of MEW processed **1a** is a lack of fiber sagging allowing a similar stacking height throughout the whole construct. Owed to the perfectly controllable MEW process with poly(urea-siloxane) **1a** and the rapid solidification upon cooling, a highly resolved 3D scaffold with a constant mesh size was fabricated. From an additive manufacturing perspective, **1a**

is very well suited for MEW and in some instances is superior to PCL, which is the current benchmark for this process.[85]

SEM investigations of the MEW printed scaffold also show homogenous and smooth fiber surfaces as presented in Figure 3.37 **(E-F)**. This is owed to the material properties but also to the controlled melt process since it was shown in literature that solution electrospun fibers show cracks and defects on the fiber surface due to solvent evaporation.
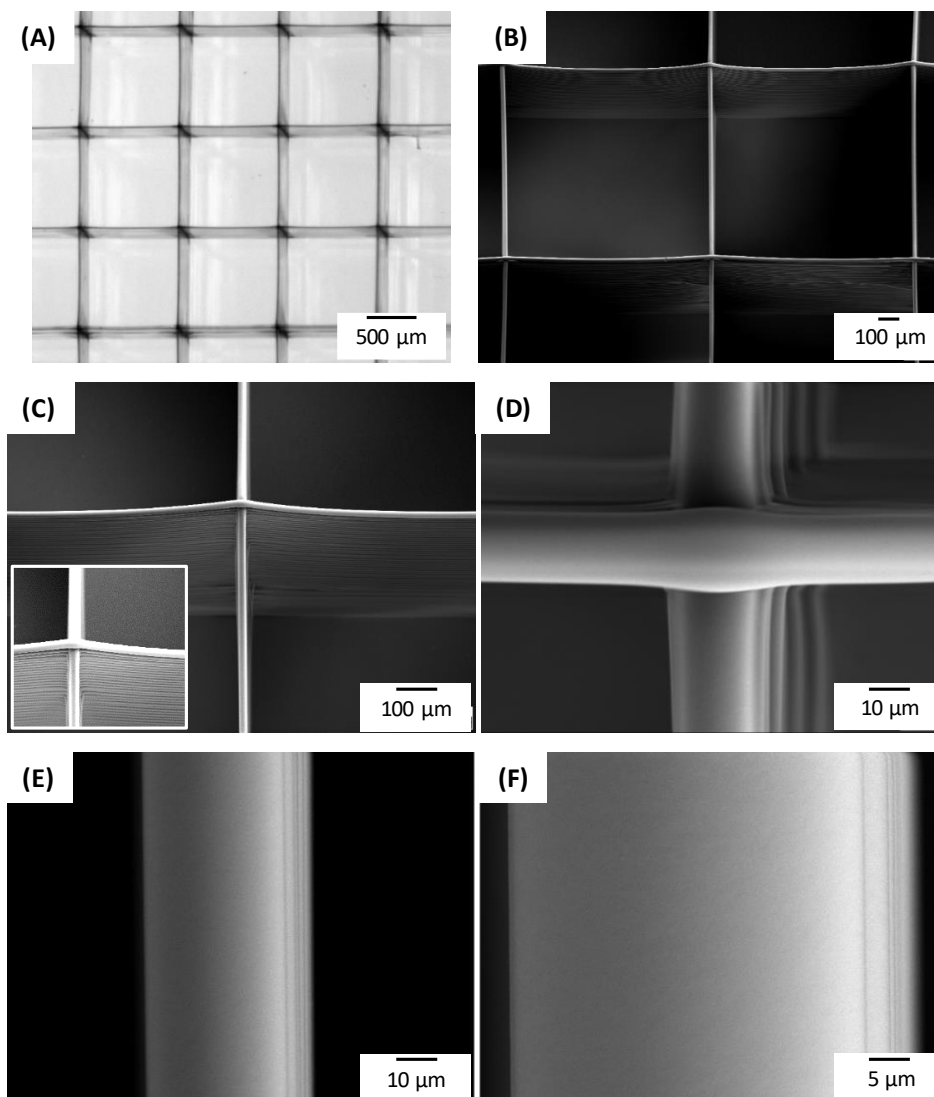
Figure 3.37: (A) Optical microscope image of MEW printed scaffold based on poly(urea-siloxane) **1a**. **(B-D)** SEM images of MEW printed scaffold and its magnification presenting highly precise fiber stacking on top of each other at the processing conditions 90 °C, 2.0 bar, 10 kV, 11.8 kV cm^{-1}. Constant fiber diameters, mesh width, and smooth fiber surface are observable. **(E-F)** depicts the smooth printed fiber surface. [Adapted and printed with permission from [85]; © 2018 WILEY-VCH]

In conclusion, it was shown that (AB)$_n$ segmented poly(urea-siloxane) **1a** is in some instances superior to the printing properties of the current benchmark material, PCL. No fiber sagging between the crossover points was observed which results in similar stacking height throughout the whole printing process. Additionally, extremely uniform fiber diameters and a high fiber placement and stacking accuracy without any fiber repelling was demonstrated. Finally, a defect-free and highly resolved 3D scaffold on the low micrometer scale was MEW printed.

3.3.4. Fused deposition modeling

Fused deposition modeling setup

FDM is another additive manufacturing method solely based on extrusion of the polymer melt. Here no additional thinning of the fiber, owed to an applied electrical field, is present. Hence, larger macroscopic 3D objects with fiber diameters above 100 µm can easily be fabricated. Schematically a fused deposition modeling (FDM) setup as shown in Figure 3.38 contains five major elements. A feeding system, a filament supply tube, a liquefier, a nozzle, and a collector plate. Commercial FDM setups use filament spools on a larger scale (> 0.5 kg). For testing new classes of material concerning their suitability for FDM, a setup was used developed at the Chair of Macromolecular Chemistry I, University of Bayreuth by Jin *et al.*[20] allowing processing on a small scale requiring only 8 - 20 g of material and single filament rods. These filament rods were fabricated by injection molding and are described in more detail in the following. The vertically aligned filament rod is transported to the liquefier by the feeding system assisted by a filament supply tube. Up to today, the 3D printing of elastic and extremely soft materials is challenging due to difficulties with feeding. The constant transportation by gear wheels of soft and flexible materials is restricted due to bending and yielding. Here the approach of Jin *et al.*[20] was followed and the filament supply tube was modified by shortening the length to about 5 cm to allow the transportation of softer filaments. Within the liquefier the filament melts and is extruded through the nozzle onto the collector plate. To obtain 3D constructs the collector plate can be moved in x, y-direction but also in z-direction. The printing parameters are controlled by an external software. It is known, using FDM the minimal fiber diameter is predominantly determined by the nozzle diameter.
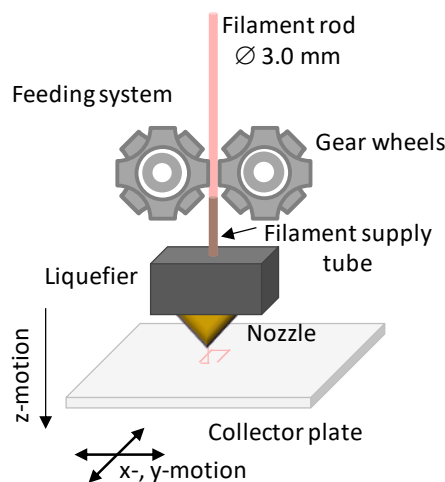
Figure 3.38: Schematic setup of the FDM unit. A filament rod is transported via a feeding system and a filament supply tube to a heated liquefier. The material melt is extruded through a nozzle onto an in x-, y- ,and z-axis moveable collector plate.

Material selection

A major challenge of FDM is the constant transportation of the filament rod towards the liquefier. Using a stiff material such as semi-crystalline or amorphous polymers with high T_g's, the filament rods can easily be transported to the liquefier by precise gripping of the gear wheels. If the material becomes more soft and elastic this step becomes more difficult due to bending and yielding. To overcome this problem, the distance between feeding system and liquefier, which is supported by the filament supply tube, is reduced to minimize the flexibility, bending and yielding of the filament rods. Nevertheless, the material needs a certain stiffness at room temperature for a constant transportation. Next to the setup restrictions a homogenous and low viscous polymer melt is needed for a constant and homogenous printing processes. Moreover, fast solidification is of advantage to achieve an accurate printing quality by the formation of uniform extrudates and accurate layer-by-layer fiber deposition. According to these requirements poly(urea-siloxane) **1a-(1.7)** was chosen.
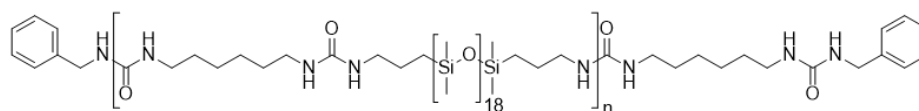
1a-(1.7)

With a Young's modulus of 35.7 ± 1.4 MPa at room temperature it is expected to be stiff enough for the feeding step. Further, the lower melt viscosity of 70 Pa·s at 120 °C of the molecular weight regulated poly(urea-siloxane) compared to the stoichiometric poly(urea-siloxane) **1a** ($\eta_{\text{melt, 120 °C}}$ = 350 Pa·s) is expected to allow a more homogenous and constant printing process. Poly(urea-siloxane)s **2a** and **3a** with Young's moduli from 1 to 5 MPa are too soft and elastic to be transported with this specific feeding system. The other poly(urea-siloxane)s based on i*sophorone diisocyanate* (IPDI), *4,4'-methylene bis(cyclohexyl isocyanate)* (mbCHDI), and *toluene-2,4-diisocyanate* (2,4-TDI), respectively, were excluded due to their high viscosities at elevated temperature and because of the lack of rapid solidification upon cooling.

Fabrication of filament rods

The filament rods of poly(urea-siloxane) **1a-(1.7)** were fabricated via injection molding. Only about 8 g of the copolymer is needed for the preparation of six filament rods of a length of 140 mm and a diameter of 3 mm. Following Jin's methods,[20] first the copolymer was cut into small pieces and compounded for 5 min under nitrogen atmosphere in a co-rotating twin-screw micro-compounder. The screw speed was set to 40 rpm at a temperature of 120 °C. The obtained homogenous polymer melt was discharged and directly transferred into the barrel of a miniature injection molding machine. It was injected into a metal mold containing a Teflon® tube with a total length of 140 mm and an inner diameter of 3.0 mm. The injection molding temperature was at 120 °C and the mold temperature was

set to 20 °C to achieve fast solidification of the polymer melt within the Teflon® tube. The injection pressure was set to 2.5 bar with a dwell time of 5 sec. After removing the Teflon® tube the filament rod was demolded by cutting the outer Teflon® tube (Figure 3.39). Using this injection molding technique well-defined and reproducible transparent filament rods with a smooth surface were obtained.
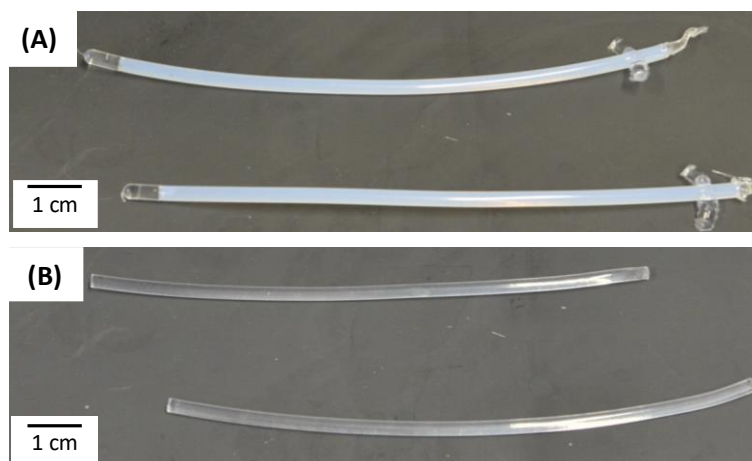
Figure 3.39: (A) Injection molded filament rods of the $(AB)_n$ segmented copolymer **1a-(1.7)** within Teflon® tubes. **(B)** Transparent filament rods after removing the Teflon® tubes. The cut rods had a total length of 140 mm and a diameter of 3 mm.

Results and discussion

For FDM a desktop twin-nozzle FFF 3D printer (3NTR, Italy) with a nozzle diameter of 450 μm was used. The extrusion temperature was set to 125 °C to guarantee a homogenous, low viscous melt while the collector temperature was kept at 30 °C, allowing a fast solidification of the printed fiber. A printing speed of 5 mm sec^{-1} was applied. A single line stacked square tube with a 1 cm · 1 cm cross section, a layer height of 200 μm, and an overall height of 5 cm was printed. The $(AB)_n$ segmented copolymer **1a-(1.7)** with a melt viscosity of $\eta_{\text{melt } 120\,°C} = 70$ Pa·s could be continuously extruded and deposited. The deposited line width is 650 μm and thicker than the nozzle diameter (450 μm). This owed to extrudate compression. The printed transparent 3D construct is shown in Figure 3.40. As seen in Figure 3.40 **(A)** a defect is obtained at half height due to feeding of single filament rods. This could be avoided by fusion of the single filament rods to one long filament at elevated temperatures. In Figure 3.40 **(B)** the accurate and homogenous printing quality can be seen in a larger magnification. Interestingly almost no warping is observed which is a common problem in FDM for semi-crystalline polymers owed to shrinkage induced by residual inner stress.[142] With increasing crystallinity, it is known that warp deformation increases and negatively influences the printing quality of a construct.[20] Fast solidification of the copolymer and its elastic properties is responsible for rendering a high quality 3D printed poly(urea-siloxane) construct.

(AB)$_n$ segmented poly(urea-siloxane) copolymers are a promising material for 3D printing with several positive characteristics. It was shown that a highly resolved transparent 3D structure on a centimeter scale based on a poly(urea-siloxane) copolymer was fabricated by FDM, whereas with MEW such structures can be fabricated on the µm scale. The fiber diameters by FDM (650 µm) are over ten times larger than for MEW (15 µm) however on both length scales an outstanding printing quality was achieved.
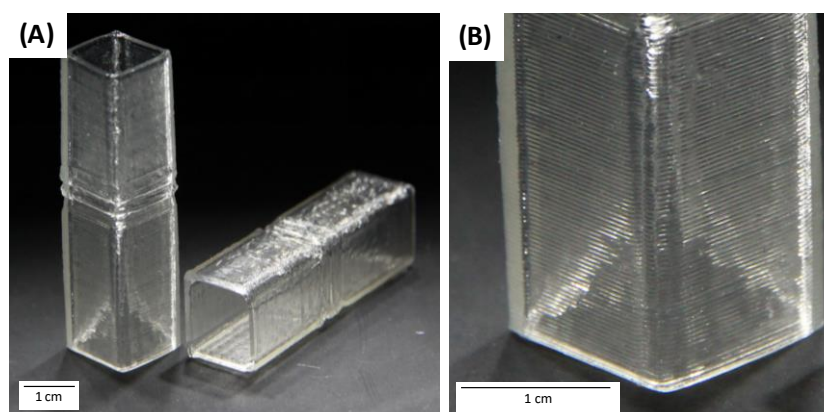
Figure 3.40: (A) Photograph of the (AB)$_n$ segmented copolymer **1a-(1.7)** 3D printed square tubes with a cross section of 1 cm · 1 cm and a total height of 5 cm. **(B)** Shows a more detailed view of the square tube demonstrating the accurate and homogenous line stacking without warping or shrinkage.

Mechanical characterization

The 3D printed single line stacked square tube was characterized concerning its mechanical properties via tensile tests. Therefor a 3D printed square tube with a cross section of 5 cm · 5 cm was cut into four single side wall pieces with a CO_2 laser cutter and dogbone specimens were punched out as 0° and 90° specimen depending on the orientation of the specimen relative to the stacked layers (Figure 3.41). In literature it is shown that the mechanical properties of the resulting 3D objects tend to be anisotropic since the fibers are strain-induced oriented by dragging and depositing on each layer The molecular orientation within the fiber can be induced by the FDM layer-by-layer process. Insufficient fusion of the single fiber strands between the layers results in weaker interlayer bonding which limits the mechanical properties. For FDM it was found that the anisotropy and the mechanical properties strongly depend on material and process parameters.[17,143–145]

The stress-strain diagrams of the 0°, 90° specimen, and the neat poly(urea-siloxane) **1a-(1.7)** bulk material are shown in Figure 3.41. Clearly it can be seen that the specimen orientation relative to the printing direction has a distinct effect on the ultimate elongation of the material. The specimen parallel to the printing orientation (0° specimen) shows an elongation up to 450% which is about 130% higher than for the neat bulk material. This implies that multiple stacked fibers improve the elongation if stretched into longitudinal direction. In literature it is stated that the highest mechanical properties are observed for 3D printed samples parallel to the printing direction.[143] However, the elongation of

the specimen perpendicular to the printing orientation (90° specimen) is six times shorter than the bulk material revealing a weaker bonding between the single stacked layers.
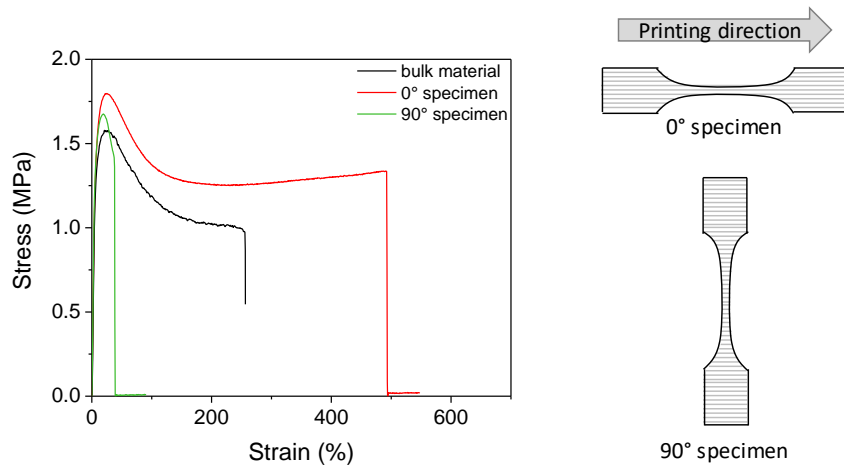
Figure 3.41: Stress-strain diagram of poly(urea-siloxane) **1a-(1.7)** (bulk material) in comparison to the 3D printed material tested as a 0° and a 90° specimen to the printing direction. Detailed experimental data are included in chapter 5.2.

These results show also that the single fibers are well fused since the material can be elongated in both directions and does not immediately rapture. Comparing to amorphous polymers, the fiber fusion and interlayer bonding is improved owed to the hydrogen bonded urea hard segments. These act in addition to entanglements as crosslinking points which enhance the interlayer bonding while amorphous polymers solely contain chain entanglements.[130]

This behavior is shown schematically in Figure 3.42. The urea units can rearrange at the interface to form new hard segment domains upon fiber placement owed to self-healing characteristics.[146] External stimuli such as temperature improves this self-healing process and interlayer bonding at the interface. Since the nozzle transfers a certain amount of heat to the fused fibers, thus the hydrogen bonds can re-aggregate at the interface and reinforce the layer-by-layer bonding.[145]
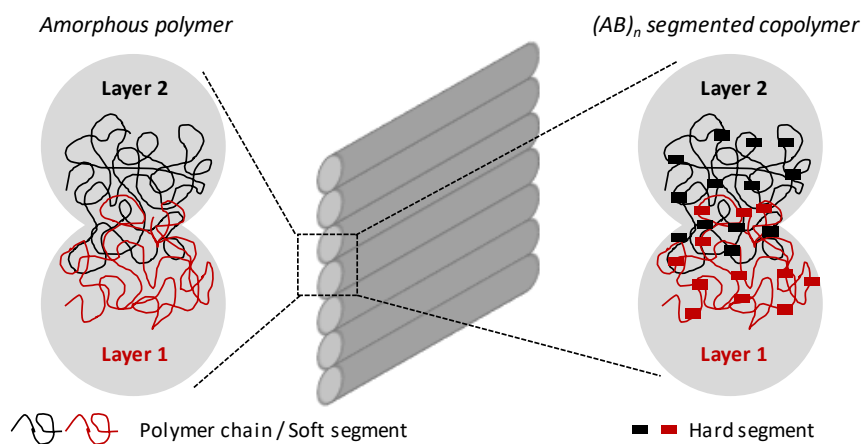
Figure 3.42: Comparing interlayer bonding of FDM printed single line fiber stacks of amorphous (left) and (AB)ₙ segmented copolymers (right). Interlayer bonding of amorphous polymers is solely based on chain entanglements while (AB)ₙ segmented copolymers additionally contain hard segments improving the bonding strength and fusion between the single layers.

The mechanical properties are summarized in Table 3.13. The Young's modulus is not significantly influenced by 3D printing or effected by the specimen orientation. The stress at break varies marginal, though it is highest for the 90° specimen which proves the fusion of the single fibers. However, the strain at break is much lower.

Table 3.13: Tensile properties of poly(urea-siloxane) **1a-(1.7)** as bulk material and after 3D-printing. The results of the 3D printed structures are given as 0° and 90° specimens, demonstrating the influence of the printing direction on the testing orientation. An average of five specimens is given. Detailed experimental data can be found in chapter 5.2.

	Bulk material	0° specimen	90° specimen
Young's Modulus (MPa)	35.7 ± 1.4	29.2 ± 0.74	34.8 ± 1.0
Strain at break (%)	321 ± 16	453 ± 47	38 ± 3.2
Stress at break (MPa)	1.18 ± 0.04	1.25 ± 0.06	1.46 ± 0.12
Toughness (Jm^{-3}10^{4})	415 ± 28	558 ± 53	57 ± 7

Concluding, it was shown that 3D structures with an accurate layer-by-layer stacking behavior can be fabricated by FDM using the (AB)$_n$ segmented poly(urea-siloxane) copolymer **1a-(1.7)**. Neither drawbacks such as shrinkage or warping were observed using this class of materials. Mechanical characterization of the 3D printed object revealed significantly improved strain properties along the printing direction.

3.3.5. Conclusion of chapter 3.3.

In this chapter melt processing of (AB)$_n$ segmented poly(urea-siloxane) copolymers into single fibers and 3D constructs is presented. Copolymers with hard segments based on *1,6-hexamethylene diisocyanate* (HMDI) were chosen owed to their material properties including low adjustable melt viscosity, fast solidification upon cooling and mechanical properties ranging from soft to stiff (Young's modulus: 1 MPa – 37 MPa).

Melt electrospinning was performed and the fiber formation, geometry, and uniformity as well as fiber fusion was investigated. It was found that the fiber diameter of poly(urea-siloxane)s processed fibers range from 57 μm to 180 μm depending on the utilized copolymer and processing parameters. Using (AB)$_n$ segmented copolymer **1a** with the shortest PDMS chain length (M$_n$ = 1513 g mol^{-1}, x = 18) and the highest hard segment content, randomly stacked objects were obtained while processing copolymer **2a** based on PDMS soft segment with a molecular weight of 2871 g mol^{-1} (x = 36) resulted in more randomly distributed objects with less stacking and piling in height due to a higher degree of whipping. This is explained by the decreasing Young's modulus of **2a** (E-modulus = 5 MPa) compared to **1a** (E-modulus = 37 MPa) as well as the increasing elasticity (strain at break: 1773% *vs.* 321%). Yet, due to the high viscosity of the copolymers electrospinning resembles more an extrusion based process. However, it was shown that perfectly round, symmetrical and uniform fibers were generated without any defects or bead formation (Figure 3.43 **(A)**).

Additive manufacturing techniques are of importance in biofabrication. Two material *extrusion-based AM* techniques namely *melt electrowriting (MEW)* and *fused deposition modeling (FDM)* were utilized to fabricate 3D constructs on different length scales. The instrument parameters and material properties were taken into account on the fiber formation and printing accuracy.

Melt electrowriting of poly(urea-siloxane) **1a** based on the shortest PDMS chain length and *1,6-hexamethylene diisocyanate* resulted in extremely homogenous and uniform fibers with an average fiber diameter of 10 – 20 μm depending on feeding pressure, applied voltage, and temperature utilizing a cannula inner diameter of 0.3 mm. The ideal processing parameters were determined to be 90 °C, 2.0 bar, and 10 kV (11.8 kV cm^{-1}). The fiber surface was found to be very uniform. MEW printing a scaffold with a cross section of 17.5 mm · 17.5 mm and a total thickness of 360 μm showed a good layer-by-layer stacking without defects and no fiber sagging between the crossing points which was shown for the first time in this high quality. The fibers already solidify upon their way towards the collector. It is remarkable that 50 layers in x- and 50 layers in y-direction resulting in 100 layers at the crossing points were printed without any charged induced defects such as repelling which is a widely known problem in literature and that each single round fiber was perfectly fused to the next layer (Figure 3.43 **(B)**). Poly(urea-siloxane) **1a** was shown to be an ideal candidate for MEW processes

comparable to the bench mark material PCL including the features stacking height, fiber placement accuracy, fiber smoothness, and control over fiber diameter by voltage. In some instances, such as optical properties, it even surpasses PCL.

Fused deposition modeling was used to fabricate a 3D construct on the cm-scale. First the FDM setup was optimized in regard to process a soft material with a low modulus. Therefor the filament supply tube located between feeding system and liquefier was shorten to allow a filament transportation with reduced bending and yielding as well as continuous feeding. Filament rods of molecular weight regulated poly(urea-siloxane) **1a-(1.7)** were fabricated by injection molding. This copolymer was used for FDM due to its lower melt viscosity ($\eta_{melt\ 120\ °C}$ = 70 Pa·s) compared to **1a**. A low viscosity is advantageous to reduce the fiber diameter since the fiber diameter strongly depends on the nozzle diameter and extrudate compression. A transparent, single line stacked square tube with a cross section of 1 cm · 1 cm, a layer height of 200 µm, a line width of 650 µm, and a total height of 5 cm was printed. The fiber diameter was found to be thicker than the nozzle diameter (450 µm) owed to extrudate compression. Also at a larger centimeter length scale, it was possible to print an accurate, defined and defect-free 3D construct (Figure 3.43 **(C)**). Using **1a-(1.7)** no warping during or after the printing process which is a common issue using semi-crystalline polymers, was observed. Mechanical characterization revealed an excellent elongation behavior along the printing orientation (0°) and a slightly reduced elongation perpendicular to the line stacking (90°) compared to the bulk material. The Young's modulus was not influenced by the printing process.

Melt electropsinning *Melt electrowriting* *Fused deposition modeling*
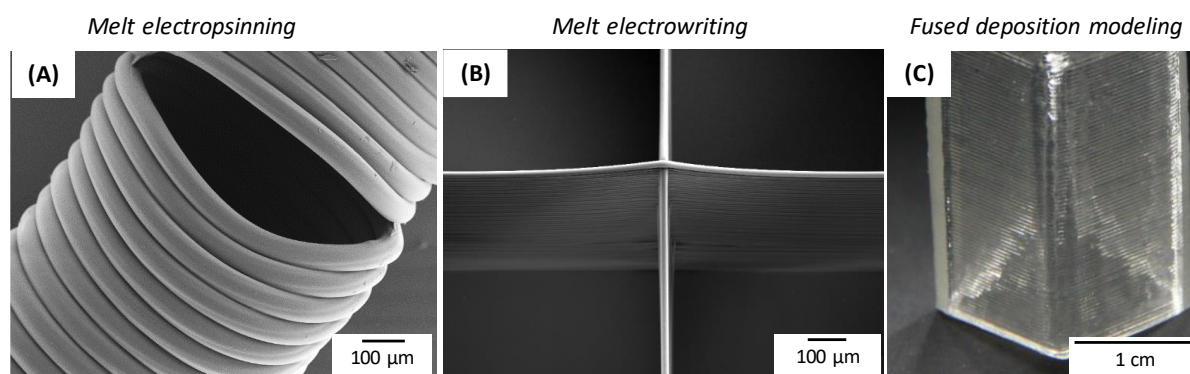
Figure 3.43: Melt processed constructs on the micrometer and centimeter scale with accurate layer-by-layer fiber deposition using melt electrospinning, melt electrowriting, and fused deposition modeling.

As a final remark, it was shown for the first time that (AB)$_n$ segmented poly(urea-siloxane) copolymers can be used for a wide range of thermal processing techniques in specific single fiber formation. Highly resolved and accurate layer-by-layer constructs could be printed on the micrometer and centimeter scale (Figure 3.43).

3.4. Melt processed gradient materials with continuously changing mechanical properties

3.4.1. Gradient materials

Polymer gradient materials are defined as materials which change their composition continuously along one axis and hence being characterized by at least one changing property such as mechanical, optical, morphological, or topological.[147,148] It has to be distinguished between gradient copolymer chains[149] and bulk polymer gradient materials. While the former is defined by a compositional gradient along a single polymer chain without macroscopic gradient properties, the latter are macroscopic gradient materials with a continuously changing composition along the entire sample and are in the focus of this thesis. Bulk polymer gradient materials inspired by nature contain a gradient structure found in natural materials such as mussel byssus or tendons, which are based on a mechanical property gradient mediating between soft tissue and stiff rocks and bones, respectively.[150] The requirements of such materials are challenging since they mediate between an enormous mismatch of a very soft tissue and a very hard and stiff material. These gradients are built up by a continuously varying composition with different stiffness. In the human body these complex multiphase systems are formed by dynamic interactions between cells, extracellular matrix, and tissue architecture.[151] In general, gradient materials can be classified into materials with different mechanical, surface or surface topological gradients. This concept can be transferred to bulk polymer gradient materials which give rise to a broad research field in regard of regenerative medicine. Bulk polymer gradient materials are in addition to that of great interest in the engineering field not least due to their outstanding properties in reducing stress concentrations at the interface and failure of the material.[152,153] To get a more detailed understanding of these properties, it must be distinguished between graded and gradient materials which are depicted in Figure 3.44. Graded materials **(A)** are characterized by a stepwise change along one axis joining discrete sectors together, while in gradient materials **(B)** a continuously changing composition along the whole specimen is present.[153,154]

Figure 3.44: It can be distinguished between **(A)** graded materials with a stepwise changing composition and **(B)** gradient materials with a continuously changing composition. Owed to the lack of interfaces, gradient material exhibit unique mechanical properties such as reduced stress concentration and high resistance. [Adapted and printed with permission from [147]; © 2012 Wiley-VCH]

A drawback of the stepwise changing properties in graded materials lays in the generated interfaces and layers. Bringing two materials into contact, the mismatch in their respective stiffness determines

the failure of the material.[153] Considering two joint materials A and B with different Young's moduli loaded tension, an additional stress, the radial stress σ_r, occurs at the interface (Figure 3.45 **(A)**). This interfacial stress increases with increasing degree of the modulus mismatch between both layers as shown in Figure 3.45 **(B)** and weakens the overall performance of the material, leading to deformation, cracking, and ultimate failure. In the contrary, a gradient material with a continuous changing Young's modulus along the axis shows unique mechanical properties such as reduced stress concentration, high resistance to contact deformation and damage and increased fracture toughness due to the lack of interfaces avoiding a focus of stress at any point **(C)**.[147,153] A continuously varying Young's modulus is expected to hinder crack propagation.[155] Besides engineering parts, such materials are of interest as substrates for cell growth studies since cell migration and proliferation is guided by the rigidity and stiffness of a material.[151] Controlling the stiffness of a material by generating a gradient in a defined Young's modulus range on a certain length scale, cell interactions can be studied which is of interest for tendon recovery, biofabrication, and regenerative medicine in general.[147,148,156]
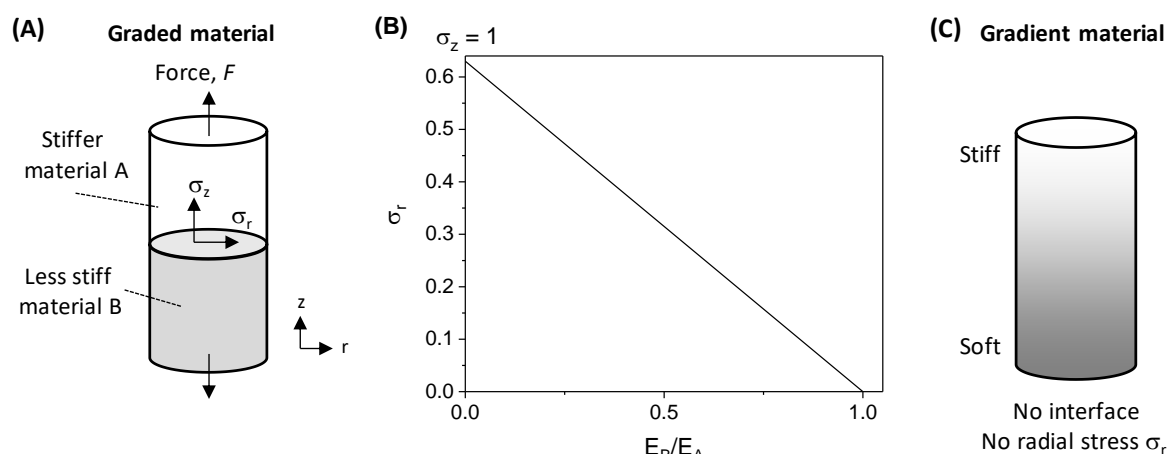
Figure 3.45: (A) shows a graded, bi-layer material with a difference in Young's modulus of material A and B ($E_A > E_B$). Applying a tension force to the material, an additional radial stress σ_r occurs at the interface being responsible for the graded material to fail under less load than a material with no change in stiffness. **(B)** The radial stress increases linearly with an increase in the difference of the Young's moduli of material A and B. The gradient material **(C)** with a continuous varying Young's modulus does not show an interface and consequently no additional radial stress. [Adapted and printed with permission from [153]; © 2004 American Chemical Society]

Macroscopic, longitudinal bulk polymer gradient materials with a mechanical gradient from soft to stiff were fabricated for the first time by Claussen *et al.* at the Chair of Macromolecular Chemistry I utilizing a high precision syringe pump setup and liquid pre-polymers.[156] Two components with different Young's moduli are simultaneously processed and mixed to a defined gradient composition along the entire sample. The pre-polymer components are low viscous at room temperature and can be processed under ambient conditions. However, they need an additional crosslinking step to preserve the gradient structure. This is achieved by a thermal- or photo-polymerization using catalysts or initiators. This results in an irreversible covalently crosslinked network with a gradient crosslink density. Claussen *et al.* investigated a variety of systems ranging from poly(dimethylsiloxane),

poly(urethane), poly(mercaptopropyl methyl siloxane) to poly(ether/ester acrylate). The different mechanical properties along the sample are obtained by different crosslink densities ranging from a low crosslink density corresponding to a soft material to a highly crosslinked one with higher Young's modulus.

The *poly(dimethylsiloxane)* system used is based on a thermal platinum-catalyzed hydrosilylation crosslinking reaction as illustrated in Figure 3.46. The viscosity of the high crosslink density component is 10.5 Pa·s while the low crosslink density component has a viscosity of 2.7 Pa·s. This allows an easy processing at room temperature using the syringe pump setup. Using these two materials, a gradient range of 0.2 MPa to 1.8 MPa could be achieved.[156]
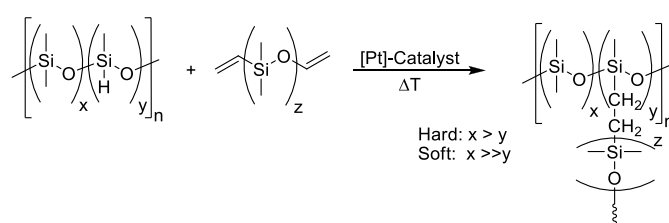
Figure 3.46: Chemical crosslinking of poly(dimethylsiloxane) system via Pt-catalyzed thermal polymerization. The mechanical gradient is generated adjusting different crosslink densities.[156]

Another elastomeric material Claussen *et al.* investigated is a *poly(urethane)* system with thermal crosslinking (Figure 3.47). Combining a tri-functional isocyanate with either an aliphatic linear short chain polyester polyol or an aliphatic highly branched short chain polyester polyol a low and a high crosslink density was obtained. This system resulted in a stiffness gradient from 6 MPa to 700 MPa.[148]
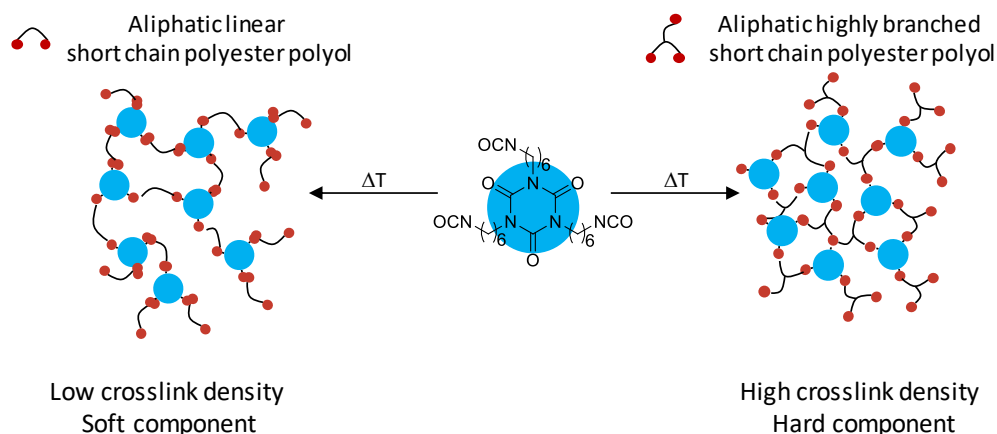
Figure 3.47: Polymer gradient material based on poly(urethane) chemistry covering a Young's modulus range of 6 MPa to 700 MPa. The different stiffness is adjusted by a low and a high crosslink density using either linear or highly branched polyester polyol in combination with a tri-functional isocyanate. [Reprinted with permission from [148]; © 2014 Elsevier]

Other systems such as *poly(mercaptopropyl methyl siloxane)* and *poly(ether/ester acrylate)* are based on UV crosslinking with Young's moduli ranging from 8 – 600 MPa and 10 – 1300 MPa, respectively.[148] Claussen *et al.* also fabricated mechanical *protein-based gradients with fibroin and gelatin* covering a modulus range of 160 – 550 MPa.[157]

Another research field concentrates on surface topography gradient materials. Claussen *et al.* introduced *controlled wrinkle surface gradients* by varying the substrates modulus.[158] Further topography gradient materials were investigated by Schedl *et al.* for the development of tunable optical gradients.[159–161] Yu *et al.* also demonstrated the formation of controlled surface patterns including folding and wrinkling using on elasticity gradient PDMS substrate. Such materials are expected to be beneficial in flexible electronics, optical devices, biological templates, and micro- and nanofluid channels.[162]

One drawback of these liquid pre-polymer based systems is their low viscosity upon processing which can undergo diffusion prior chemical crosslinking and influence the gradient structure even if a sufficient reactivity is given at room temperature. Further solution based systems may show shrinkage and surface defects due to solvent evaporation. However, since all these systems are based on covalent crosslinked materials either by thermal- or photo-polymerization using catalysts or initiators, none of them show self-healing properties which is an interesting feature in regard of mimic natural gradient materials and improved material strength.

Within this thesis the drawback of liquid pre-polymers and an additional chemical curing step will be addressed by fabricating a *macroscopic stiffness gradient from the melt* without initiators or catalysts. The goal is to generate a gradient with a continuously changing Young's modulus and fast solidification behavior upon cooling to solidify the gradient structure upon processing. $(AB)_n$ segmented poly(urea-siloxane) copolymers with different mechanical properties will be used owed to their thermoreversible nature and tunable mechanical properties. An additional benefit of these systems is the self-healing behavior due to hydrogen bonded urea units and the elasticity of the PDMS segment at room temperature with a T_g ~ -115 °C. Such polymer gradient materials processed from the melt are of interest as non-degradable supporting structures in biofabrication and tissue engineering owed to the biocompatibility, as well as resistance to microorganism of poly(urea-siloxane)s.[45]

3.4.2. Heated syringe pump setup

For the melt fabrication of a macroscopic poly(urea-siloxane) longitudinal gradient on a centimeter scale with a continuously increasing Young's modulus a heated mid-pressure syringe pump setup was developed as shown in Figure 3.48 which was designed and installed jointly with Dr. Reiner Giesa. Two components A and B with different E-moduli are filled in two separate heated, stainless steel syringes being connected to a static mixer via heated metal capillaries. The heated static mixer is chosen to allow a sufficient and homogeneous mixing of both components during processing. This was demonstrated in the scope of my master thesis.[138] The mixed polymer melt is extruded into a Teflon® mold ($14 \cdot 1 \cdot 0.1$ cm³) by applying a flow profile via an external software. For a uniform filling of the mold the platform is moved in x-direction with a continuous and synchronized to the flow profile speed. Each part within the setup can be heated individually up to 200 °C.
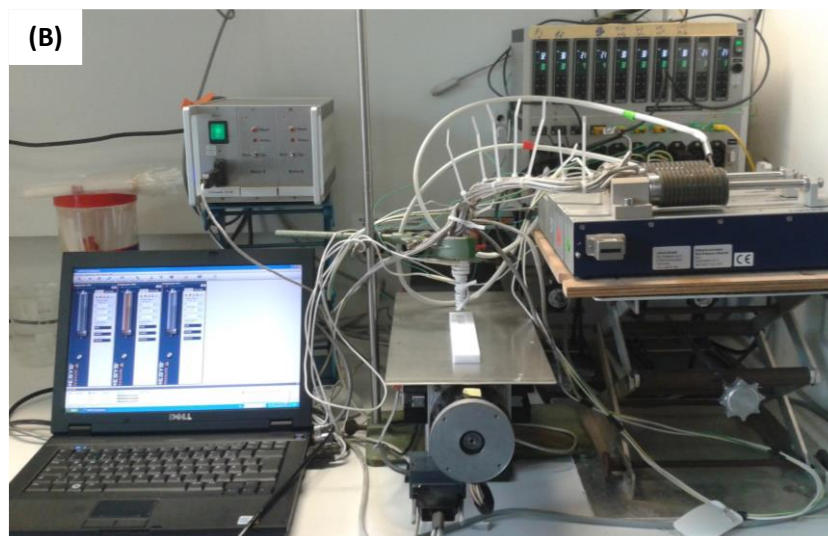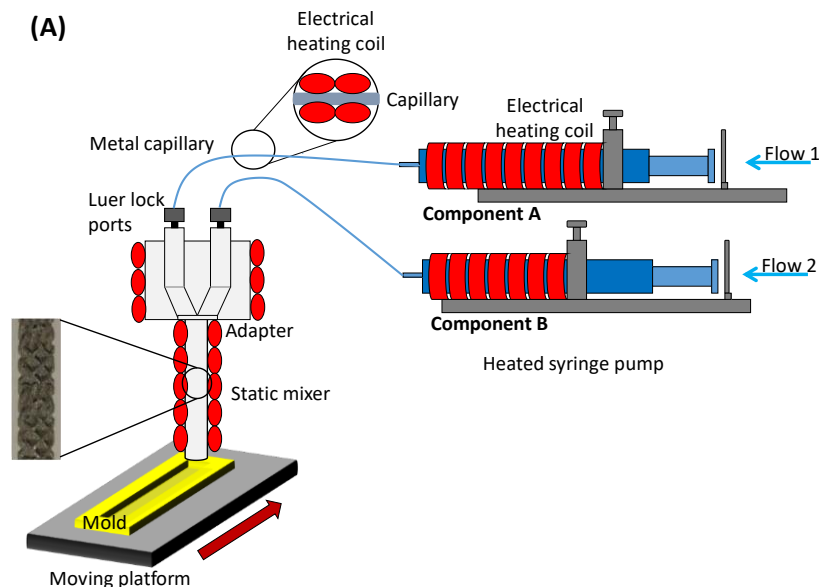
Figure 3.48: (A) Schematic heated syringe pump setup. The heated metal syringes, capillaries, the mixing head with the static mixer are heated by external electrical temperature controllers. The Teflon® mold is fixed on a linearly moving platform which is controlled by a software. For the fabrication of a gradient a flow profile is applied regulating the dosing units occupying two different components. **(B)** Shows the photograph of the actual setup used for the fabrication of the polymer gradient.[138]

3.4.3. Material selection

Melt fabrication of a polymer gradient with a continuously varying Young's modulus involves a variety of requirements which need to be fulfilled concerning the selection of material. First these materials need to be melt processable with a certain solidification behavior upon cooling to maintain the final gradient structure and minimize additional diffusion of the components after processing. Further a sufficient low melt viscosity and thermal stability must be given during the whole fabrication process. In regard of fabricating a gradient with a continuously changing Young's modulus, two materials with a significant difference in their Young's moduli are required. Owed to these demands, the (AB)$_n$ segmented poly(urea-siloxane) copolymers **1a-(1.7)** with a Young's modulus of 35.7 ± 1.4 MPa and **3a-(10)** with a Young's modulus of 3.2 ± 0.08 MPa are selected.
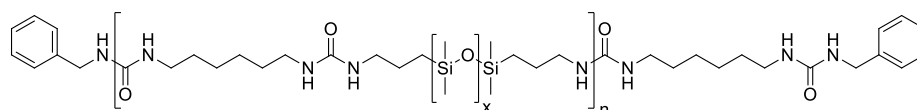
1a-(1.7) (x = 18) / **3a-(10)** (x = 64)

These are further selected due to their sufficient solidification upon cooling which is due to the linear, aliphatic structure of the *1,6-hexamethylene diisocyanate* based hard segment. In addition, these two copolymers are chosen due to their low and comparable melt viscosities at 120 °C of 70 Pa·s for **1a-(1.7)** and 130 Pa·s for **3a-(10)**. This is an important feature in order to allow a steady flow rate and homogenous mixing of both components. The (AB)$_n$ segmented copolymers **1a** and **3a** without molecular weight regulation were found to be highly viscous at processing temperatures with melt viscosities at 120 °C of 400 Pa·s and 730 Pa·s. This resulted in a too high back pressure in the capillaries and no continuous melt flow and homogenous mixing of both components could be ensured. Increasing the processing temperature to further reduce the melt viscosity was not an optimum due to the limited thermal stability of the copolymers as discussed in chapter 3.2.3. (AB)$_n$ segmented poly(urea-siloxane) copolymers based on *isophorone diisocyanate* (IPDI), *4,4'-methylene bis(cyclohexyl isocyanate)* (mbCHDI), and *toluene-2,4-diisocyanate* (2,4-TDI) hard segments were not selected due to their very high melt viscosities compared to the HMDI based poly(urea-siloxane)s and their slower solidification behavior upon cooling compared to HMDI based copolymers.

3.4.4. Melt processing of gradient materials

Component A represents the softer component, **3a-(10)** while component B corresponds to the stiffer poly(urea-siloxane) **1a-(1.7)**. For optical visualization and characterization of the gradient structure a UV-active dye, Lumogen$^\circledR$ Red F300 (Figure 3.49 **(C)**) is added to the soft component prior processing. Both components were filled into the syringes at room temperature and heated up to 130 °C and 120 °C, respectively for 10 min before processing to obtain a homogenous melt and remove air bubbles. Component A was heated 10 °C higher to additionally decrease the melt viscosity which is slightly higher ($\eta_{\text{melt 120 °C}}$ = 130 Pa·s) than for component B ($\eta_{\text{melt 120 °C}}$ = 70 Pa·s). The capillaries and the syringes were set to the same temperatures of 130 °C and 120 °C, respectively. The temperature of the mixing head and the static mixer was increased to 140 °C to ensure a uniform and constant melt flow. The Teflon$^\circledR$ mold was pre-heated at 160 °C in an oven and placed into the setup before processing. This ensures a uniform filling of the mold. The used temperatures assigned to each component within the syringe pump setup are shown in Figure 3.49 **(A)**. Moreover, the applied flow profile is shown in Figure 3.49 **(B)**. To generate a gradient structure a continuously changing flow profile needs to be applied. In this specific case poly(urea-siloxane) **3a-(10)** was initially added at a constant flow of 25 µL s^{-1} and is continuously decreased to 0 µL s^{-1} after 52 sec. The stiffer component B, **1a-(1.7)**, was added the opposite way. Simultaneously the platform was steadily moved with a constant velocity of 1.25 mm sec^{-1}. Before fabrication and starting the flow profile the static mixer is filled completely with component A. Thus, applying the flow profile, a plateau of component A is expected at the beginning of the gradient due to the filled dead volume of the static mixer.
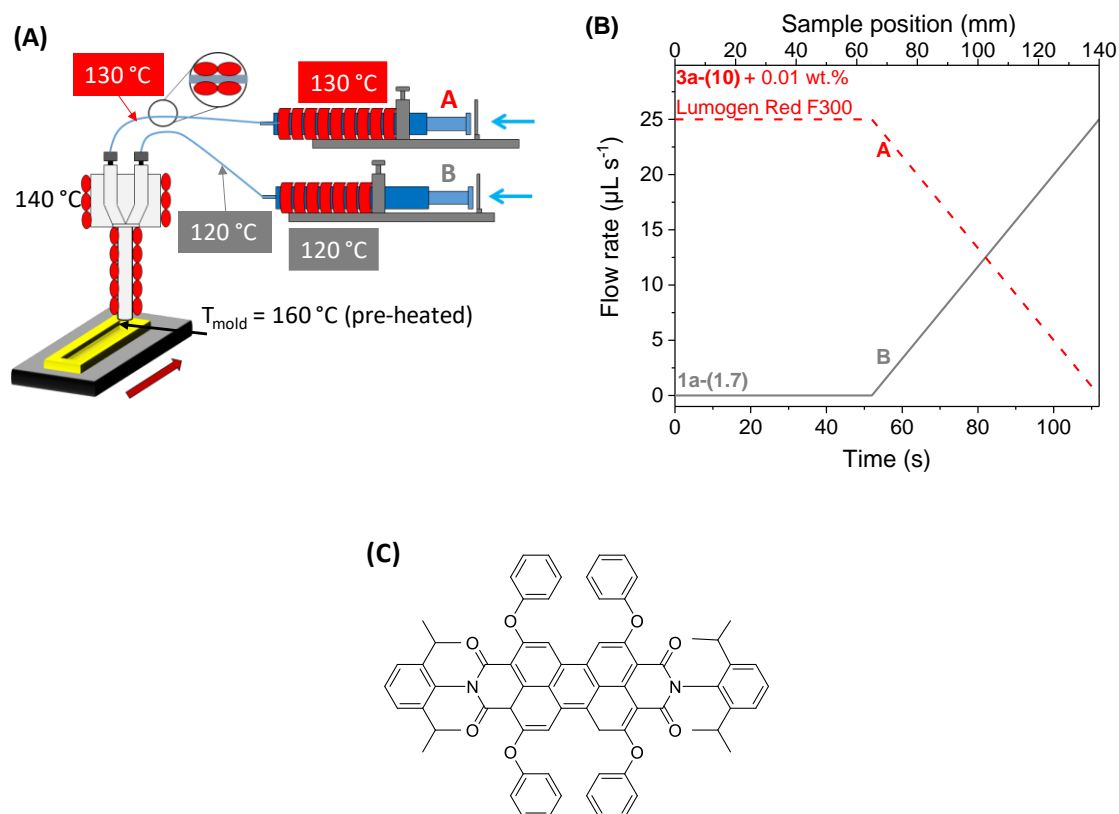
Figure 3.49: (A) Applied temperatures of each component during the melt gradient preparation process. **(B)** Applied flow profile as a function of processing time and sample position for the fabrication of the polymer gradient from the melt using **1a-(1.7)** as the hard component and **3a-(10)** as the soft component. **(C)** The dye Lumogen® Red F300 with an absorption maximum at 575 nm is added to the soft component to optically visualize the gradient.

Both poly(urea-siloxane)s with optimal molecular weight are easily processed by the heated syringe pump setup. The reduction of the molecular weight and thus the melt viscosity enabled to overcome high back pressure and blocked capillaries within the setup allowing a constant melt flow. For optical visualization of the gradient structure the dye Lumogen® Red F300 was added to the soft component (Figure 3.50). It can be seen that a color gradient from deep red to transparent is obtained caused by the continuous addition of the soft component A and the stiff component B. The color gradient represents the decreasing amount of **3a-(10)** along the longitudinal specimen axis.
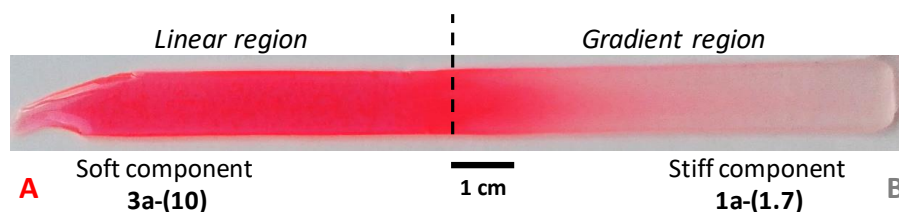
Figure 3.50: Melt processed polymer gradient from the soft component A (**3a-(10)**) to the stiffer component B (**1a-(1.7)**) being optically visualized.

Several polymer gradients of this type were fabricated from the melt to demonstrate the reproducibility of this technique.

3.4.5. Optical and mechanical characterization

An optical and mechanical analysis of the melt fabricated gradient was conducted to verify the continuous gradient structure. Therefor the gradient was characterized by UV-Vis spectroscopy due to the absorption maximum at 575 nm of the dye Lumogen® Red F300. The absorption maximum at 575 nm in dependency of the sample position of the gradient is shown in Figure 3.51. As it can be seen the absorption shows initially a plateau. After about 60 mm the absorption maximum at 575 nm continuously decreases to almost zero absorption owing to the increasing amount of component B (**1a-(1.7)**) and decreasing amount of A (**3a-(10)**).

The Young's moduli along the gradient specimen were determined via non-destructive tensile tests using a video extensometer. For the first time this technique was applied in this thesis to determine the Young's moduli along the gradient axis without destruction of the gradient. So far only compression tests were applied on specimen punched out along the gradient axis. The automated video extensometer records a video of the sequence being tensile tested (between two distinct positions being marked by black dots) and evaluates the stress-strain dependency to calculate the Young's modulus from the initial slope. The material is only strained within the linear elastic regime up to 0.04%. The results are included in Figure 3.51 presenting the Young's modulus in dependency of the sample position. First a plateau at low moduli values (5 MPa) is observed while after about 60 mm the Young's modulus continuously increases to about 40 MPa showing the gradient structure from the soft poly(urea-siloxane) **3a-(10)** to the stiffer **1a-(1.7)** in agreement with the UV-Vis characterization. The aim to fabricate a macroscopic gradient on the cm-scale from the melt with a continuous increasing Young's modulus was achieved with a total gradient length of about 70 mm and a variation of the Young's modulus from 5 MPa to 40 MPa.
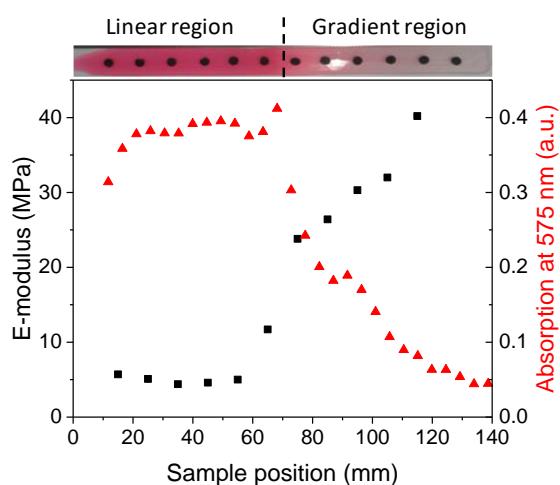
Figure 3.51: Young's moduli and absorption of the dye as a function of the sample position. The Young's modulus of the polymer gradient shows initially a steady plateau which then increases continuously while the absorption shows the opposite behavior. Detailed experimental data can be found in chapter 5.2.[163]

Demonstrating the reproducibility of the melt gradient fabrication and investigating the influence of the melt viscosities of the polymers on the final gradient structure, the fabrication process was applied in the opposite way. Applying the flow profile by changing the sequence of addition of component A and B results in a slightly steeper gradient structure. The flow profile as well as the optical characterization and the Young's modulus in dependency of the sample position can be seen in Figure 3.52. All other processing parameters were kept constant. Initially a plateau over 80 mm with no absorption is observed based on the neat **1a-(1.7)**, followed by a steep but continuous increase of absorption which is observed due to the continuously added softer component, **3a-(10)**. The Young's moduli further confirmed the gradient structure by starting with a plateau at about 40 MPa, followed by a decreasing moduli along the sample axis. A total gradient length of 60 mm is obtained which is 10 mm shorter than the first fabricated gradient. This is due to a slightly higher melt viscosity of the soft component **3a-(10)** ($\eta_{melt\ 120\ °C}$ = 130 Pa·s) compared to the hard component **1a-(1.7)** ($\eta_{melt\ 120\ °C}$ = 70 Pa·s) which results in a small difference in the melt flow rate.
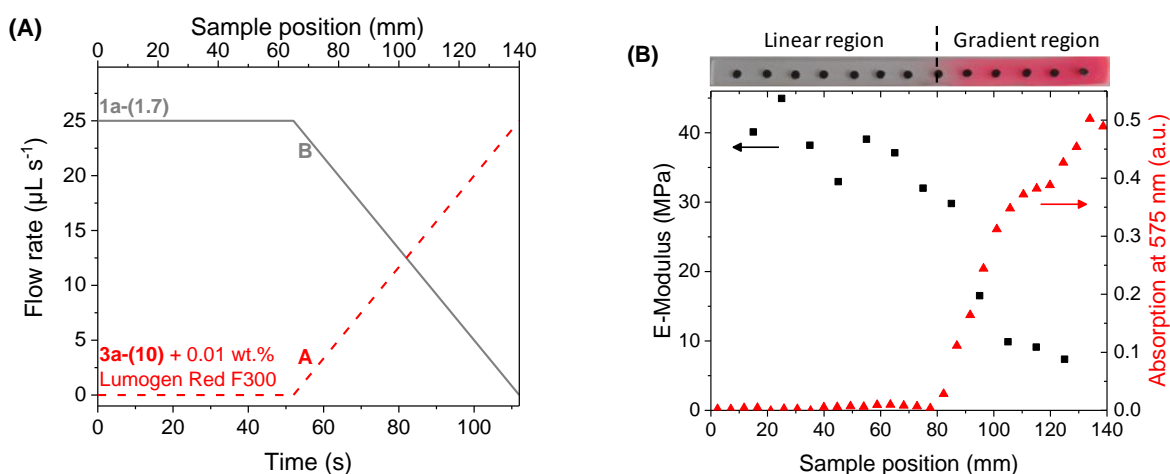
Figure 3.52: (A) Applied inverse flow profile in dependency of processing time and sample position for the fabrication of a poly(urea-siloxane) gradient from the melt. Using **1a-(1.7)** as the hard and **3a-(10)** as the soft component. The dye Lumogen® Red F300 is added to the soft component to optically visualize the gradient. **(B)** Young's moduli and absorption of the dye as a function of the sample position. The polymer gradient shows initially a plateau of the Young's moduli which then decreases continuously while the absorption simultaneously increases.

3.4.6.   Conclusion of chapter 3.4.

It was shown that *macroscopic gradient materials* were *melt fabricated* from (AB)$_n$ segmented poly(urea-siloxane)s based on *1,6-hexamethylene diisocyanate* utilizing a heated syringe pump setup. Adjusted melt viscosities were necessary for a constant melt processing. Molecular weight regulated copolymers **1a-(1.7)** ($\eta_{melt\,120\,°C}$ = 70 Pa·s) and **3a-(10)** ($\eta_{melt\,120\,°C}$ = 130 Pa·s) based on the shortest and longest PDMS chain length were employed due to their similar melt viscosities and their different mechanical properties. The gradient structure was optically and mechanically characterized by UV-Vis spectroscopy and non-destructive tensile testing proving the continuously variation of composition and properties along the longitudinal axis. An overall gradient regime of 70 mm with a Young's modulus ranging from 5 MPa to 40 MPa was obtained. This corresponds to an increasing weight fraction of the urea hard segments along the gradient axis which is correlated to the physical crosslink density (Figure 3.53).
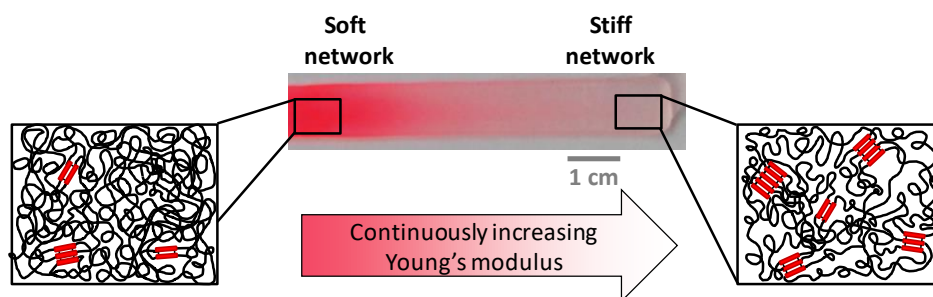
Figure 3.53: Melt processed poly(urea-siloxane) gradient with a continuously increasing Young's modulus. Starting from the soft network based on molecular weight regulated poly(urea-siloxane) **3a-(10)** it continuously change over to the stiffer network based on **1a-(1.7)**. The varying Young's moduli are obtained due to an increasing amount of urea hard segments and shorter PDMS chain length upon continuously increasing the hard component and simultaneously decreasing the soft component.

In addition, it was shown that the gradient can be reproducibly fabricated from the melt and by applying a reverse flow profile an even steeper gradient regime of 60 mm can be generated due to a small deviation of the melt viscosities of the two components. Owed to the sufficient fast solidification of the poly(urea-siloxane)s based on *1,6-hexamethylene diisocyanate* (HMDI) hard segments the gradient structure is fixed during processing eliminating additional diffusion of both components.

3.5. Thermoplastic elastomer foams

3.5.1. Polymer foams

Polymer foams are materials containing voids surrounded by a dense polymer matrix. They have low density and are lightweight materials which make them perfect candidates in a variety of applications such as insulation, cushion, and as absorbents. Well known polymers used for foam applications are poly(urethane), polystyrene, poly(ethylene), poly(propylene), poly(vinyl chloride), and poly(carbonate). Polymer foams can be classified according to their cell structure into open cell or closed cell foams (Figure 3.54). Within open cell foams **(A)** the cells are interconnected with each other resulting in more flexible foams. Closed cell foams **(B)** show isolated cells which are surrounded by a cell wall. In general, closed cell foams have better insulation properties owed to lower permeability and higher compression strength at a higher foam density compared to open cell foams.[164,165]
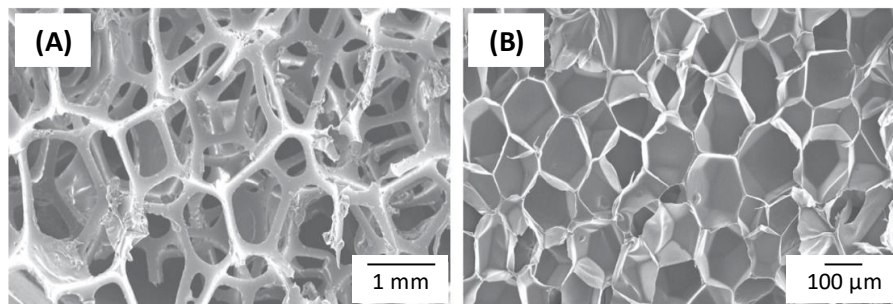
Figure 3.54: Comparison of **(A)** open cell and **(B)** closed cell foam structure. [Reprinted with permission from [165]; © 2015 Elsevier]

Polymer foams were further classified by Lee according to cell density and cell size into four major groups namely *conventional*, *fine-celled*, *microcellular*, and *nano cellular foams*.[166,167] The corresponding cell size and cell density ranges are listed in Table 3.14.

Table 3.14: Classification of polymer foams according to cell density and cell size.[166]

Foam type	Cell size (μm)	Cell density (cells cm^{-3})
Conventional	> 300	< 10^6
Fine-celled	10 – 300	$10^6 – 10^9$
Microcellular	0.1 – 10	$10^9 – 10^{15}$
Nano cellular	< 0.1	> 10^{15}

Foaming processes

It can be distinguished between *continuous*, *semi-continuous*, and *discontinuous foaming processes*. Extrusion foaming process belongs to the first process due to the continuous feeding of the extruder. Foam injection molding is known as a semi-continuous process due to demolding.[165,168] On the other hand, a discontinuous foaming process is characterized by sequential foaming like it is typical for batch foaming. This technique is often used for screening the foaming ability of new materials. A foaming process can be divided into three steps. First the polymer in its molten state is saturated with a physical

blowing agent at a sufficiently high pressure and defined temperature. The temperature is chosen according to the polymer glass transition and melting temperature. The second step introduces a thermodynamic instability into the saturated polymer melt/gas mixture. This can be achieved either by a sudden pressure drop or abrupt increase of temperature. Then a phase separation of the mixture occurs which introduces cell nucleation owing to a decreasing solubility of the blowing agent. The third and last step comprises of cell growth and stabilization due to gas diffusion from the polymer matrix into the nucleated cells. Finally, the cell morphology is stabilized by cooling. Cell stabilization depends on the melt strength of the polymer as well as the cell growth stress.[165] The final foam morphology and properties are affected by the polymer matrix crystallinity, melt strength, and gas solubility. Moreover, the saturation conditions such as temperature, pressure, and time have a large impact and need to be fine-tuned for every system.[164,169]

The batch foaming processes which is used in this thesis can be divided into two methods, the *pressure-induced* and the *temperature-induced batch foaming*. The temperature-induced batch foaming process is a two-step process. In the first step the specimens are saturated with gas at moderate temperatures until an equilibrium is reached followed by placing the saturated samples into a hot oil bath at a specific temperature and for a certain time period to induce the cell nucleation and growth. The pressure-induced batch foaming process is a one-step process in which the specimens are saturated with the blowing agent at a defined temperature and at a certain pressure for a distinct time period before abruptly releasing the pressure and inducing the cell nucleation and growth.[165,170]

Blowing agents

An essential component of polymer foaming is the blowing agent which introduces gas into the material thus driving the void formation of the resulting porous structure. This can be either realized through a chemical reaction (*chemical blowing agent*) or achieved by physically incorporating gas into the polymer matrix (*physical blowing agent*). Further microspheres can be used as propellants. Chemical blowing agents are defined as organic or inorganic compounds carrying out a decomposition reaction above a certain temperature resulting in gaseous and solid components. A common example for a chemical blowing agent is the reaction of water with an isocyanate releasing CO_2, being an efficient method to foam commercially polyurethane foams. Physical blowing agents influence the physical state of the host polymer matrix upon temperature or pressure change. Common physical blowing agents include volatile organic compounds, compressed gases or gases in the supercritical state such as N_2 and CO_2.[164] The advantage of gases are their non-flammable, inert, and environmentally friendly properties. Besides, physical blowing agents are beneficial due to their higher gas dosing possibility compared to chemical blowing agents and the closed-cell structure of the final

foams. Depending on the amount of physical blowing agent being loaded to the material the foam morphology can be influenced. Within this thesis the focus is solely on CO_2 as physical blowing agent.

Cell Nucleation and stabilization

Since cell nucleation and stabilization are major steps during the foam process and governing the final foam morphology it will be discussed in more detail in the following. A completely saturated polymer melt can be foamed as the gas solubility decreases upon either a sudden temperature increase or pressure drop. The polymer-gas mixture forms small bubbles in order to restore a low-energy stable state. Cell nucleation can be classified according to the classical nucleation theory into two types: *Homogenous* and *heterogeneous nucleation*. Homogenous cell nucleation occurs within a uniform polymer-gas mixture, while the heterogeneous cell nucleation is assisted by heterogeneous nucleating sites such as nucleating agents or impurities reducing the free energy, which is necessary to form bubbles with a critical radius. For a homogenous nucleation the free energy reaches a high-energy maximum before it decreases (Figure 3.55). This correlates to an increasing cell radius *R* which equals the critical radius *r** at the high-energy maximum. Below the critical radius (R < r*) the nucleus collapses since it is thermodynamically instable while above (R > r*) it grows and forms a stable bubble.[165,171,172] Thus, the foaming parameters need to be adjusted that initially stable cell nuclei can be formed followed by bubble growth and formation of a stable cell structure. Within this thesis only homogenous nucleation is considered.

Figure 3.55: The free energy is plotted as a function of cell nucleation and growth. The formed bubbles need to exceed the critical radius *r** to grow, while nuclei with smaller radii than *r** collapse. A homogenous cell nucleation requires a larger free energy to overcome the *r** than a heterogeneous cell nucleation which is assisted by heterogeneous nucleating sites such as nucleating agents. [Reprinted with permission from [165]; © 2015 Elsevier]

Polyurethane (PU) foams were invented by Dr. Otto Bayer in the 1940's.[173] The main ingredients for PU foams are a polyol, isocyanate, catalyst, and a blowing agent. By controlling the amount of water and blowing agent the final foam density can be controlled. Thereby it can be distinguished between flexible and rigid foams. Polyurethane foams show outstanding mechanical properties and are widely used in the automotive industry, as acoustical parts, furniture, insulation, and many others.[173] Poly(urethane-urea) foams are also promising materials for biomedical applications due to their versatility, toughness, durability, and biocompatibility.[174] In general, it can be distinguished between biostable and biodegradable foams for tissue engineering applications. The former are interesting as stable materials with low protein adhesion in blood-contact applications while the latter support and promote cell attachment and proliferation on tissue engineering scaffolds.[175,176] Such lightweight polymeric foams are tailored regarding a low foam density resulting from a high density reduction and small cell sizes while maintain a high toughness.[8,174]

Silicon foams described in literature are known for their good high- and low temperature stability, however suffering from poor mechanical properties and relatively high foam densities. Combining these two classes of materials, Wacker describes in patents the formation of mechanical stable silicone based polyurethane foams using chemical blowing agents.[177–179] The foam is generated in situ while an excess of isocyanate reacts with an amine and with water molecules forming CO_2, acting as chemical blowing agent. The isocyanate further reacts with hydroxyl terminated PDMS resulting in urethane units and a covalently crosslinked network. This foaming process is based on two simultaneously proceeding reaction, the blowing reaction and the gelation reaction which crosslinks and stabilizes the foam structure. Increasing the amount of water creates more urethane hard segments and increases the matrix toughness. The drawback of these foams are that unreacted silicon molecules syneresis over time as well as the use of a catalysts.[178,179]

Within this chapter catalyst-free *thermoplastic elastomer foams based on (AB)ₙ segmented poly(urea-siloxane)s* will be presented. These are envisioned as materials for biostable, non-degradable foams in biofabrication due to their inert and biocompatible nature. Structure-property relationships of these polymers on the foam morphology and mechanical properties will be investigated utilizing a pressure-induced batch foaming process. The goal is the fabrication of elastomeric, soft foams with a low foam density and a homogenous, uniform cell structure on the low micrometer scale with a comparable high compression modulus. The influence of the chemical structure of the poly(urea-siloxane)s depending on different soft segment chain lengths and a variation of hard segments on foam morphology, expansion ratio, and form stability is discussed. From these results the most promising poly(urea-siloxane) is selected and the influence of varying foaming parameters on the final foam properties is investigated.

3.5.2. Pressure-induced batch foaming process

The batch foaming experiments within this thesis were conducted at the Chair of Polymer Engineering at the University of Bayreuth (Prof. Volker Altstädt) utilizing a pressure-induced batch foaming process. The setup is shown in Figure 3.56. The specimen is placed into a high pressure autoclave and saturated with CO_2, the physical blowing agent, at a certain temperature and pressure which are set by external controllers.
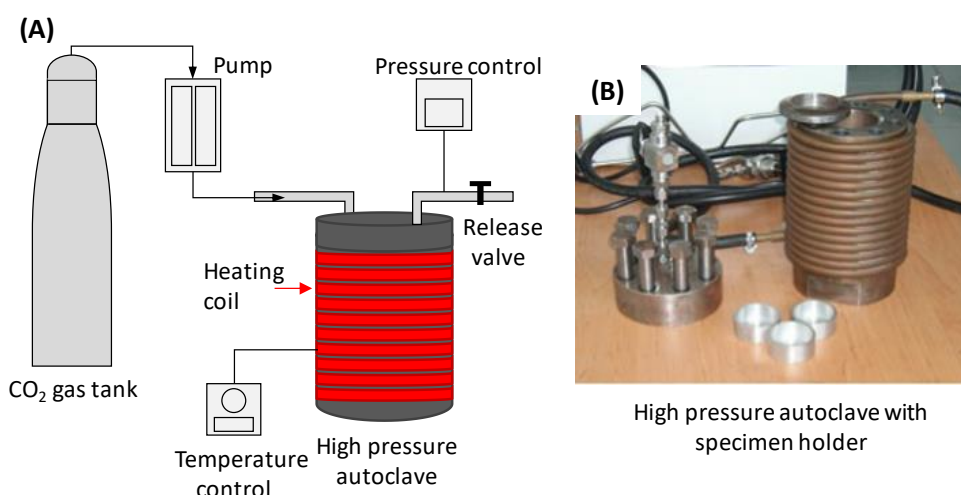
Figure 3.56: (A) Schematic setup of the pressure-induced batch foaming process. A CO_2 gas tank is connected via a pumping system to a heated autoclave. The pressure and temperature are set via two external controllers. The pressure of the autoclave can be abruptly released via a release valve, resulting in foaming the samples within the autoclave. **(B)** shows a photograph of the high pressure autoclave with its specimen holders.

Batch foaming is a discontinuous foaming process. With this specific setup five samples can be foamed simultaneously. A schematic illustration of the specimen holders is shown in Figure 3.57 containing as example the transparent, circular specimen of **1a-(1.7)** with a diameter of 25 mm. The foaming is induced by an abrupt pressure drop to atmospheric pressure resulting in thermodynamic instabilities and consequently cell nucleation, growth, and stabilization. The final cell structure is obtained by cooling the samples in air, the so called post foaming.
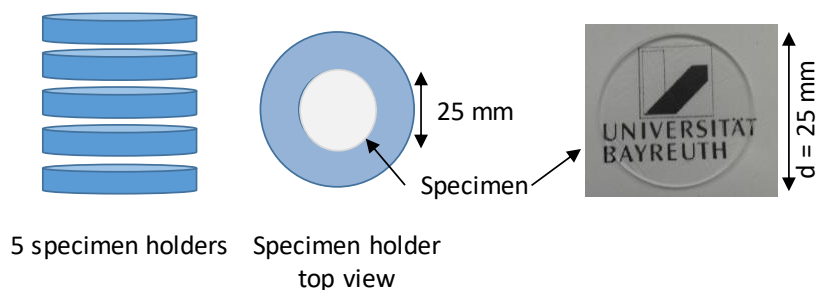
Figure 3.57: Schematic illustration of specimen holders (front and top view) and the dry, transparent solution cast specimen (**1a-(1.7)**) with a diameter of 25 mm and a thickness of 0.5 – 1 mm.

3.5.3. Material selection

Poly(urea-siloxane)s based on the symmetric, aliphatic *1,6-hexamethylene diisocyanate* (HMDI) and the asymmetric, cycloaliphatic *isophorone diisocyanate* (IPDI) hard segments with different soft segment PDMS chain length of M_n = 1513, 2871, and 4926 g mol^{-1} (x = 18, 36, 64) are selected. First their ability of forming stable foams will be investigated. Then structure-property-relationships between the different foamed morphologies, cell sizes, cell density, and the compression modulus in dependency of varied saturation parameters such as time, temperature, and pressure will be analyzed. (AB)$_n$ segmented poly(urea-siloxane) copolymers based on HMDI are selected owed to their fast solidification upon cooling which correlates to the steep increase of shear moduli and viscosity upon cooling demonstrated by rheology (chapter 3.2.3). These copolymers are expected to have a sufficient form stability and melt strength upon saturation and expansion of the specimen with the physical blowing agent below or close to T_{cross}. In detail the copolymers **1a-(1.7)**, **2a**, and **3a-(5)** are investigated concerning their foam behavior and properties in dependence of an increasing soft segment chain length. Next to these poly(urea-siloxane)s **1b**, **2b**, and **3b** based on *isophorone diisocyanate* (IPDI) with increasing PDMS chain length are investigated. They are selected due to their significant weaker mechanical properties. Rheology measurements did not show a steep increase of shear moduli or viscosity upon cooling as observed for HMDI based poly(urea-siloxane)s, instead a moderately increase was observed. However, the viscosity below T_{cross} is in the similar range and allows the assumption of a sufficient melt strength upon saturation close to T_{cross}. The chemical structure of the selected poly(urea-siloxane)s are depicted in Figure 3.58.
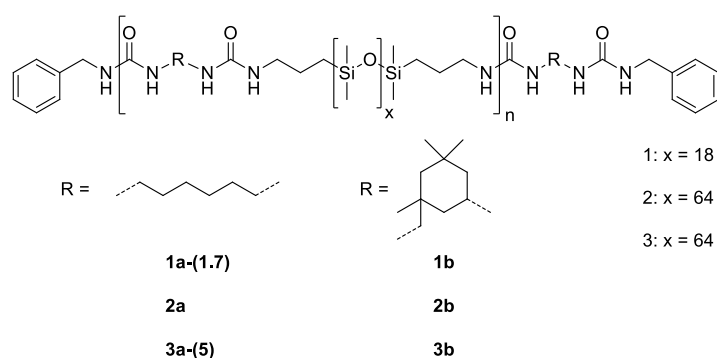
Figure 3.58: Chemical structure of the (AB)$_n$ segmented poly(urea-siloxane) copolymers selected for the pressure-induced batch foaming process based on *1,6-hexamethylene diisocyanate* (HMDI) (**1a-(1-7)**, **2a**, **3a-(5)**) and *isophorone diisocyanate* (IPDI) (**1b**, **2b**, **3b**). The copolymers differ in the PDMS chain length and the chemical structure of the hard segment.

First the different (AB)$_n$ segmented poly(urea-siloxane) copolymers are investigated concerning their cell morphology, cell size, cell density, and compression modulus in comparison to the neat polymer as bulk material. Concluding from these structure-property results a systematic analysis of the influence of the saturation parameters (time, temperature, pressure) on the foam properties is conducted.

3.5.4. Structure-property relationship of foam properties

Fabrication of specimen prior foaming

Transparent circular specimen for the pressure-induced batch foaming process with a diameter of 25 mm and a thickness of 0.5 to 1 mm were punched out of the dried polymer films obtained after solution casting. An example is shown in Figure 3.57.

Pressure-induced batch foaming of poly(urea-siloxane) based on 1,6-hexamethylene diisocyanate as hard segment and the shortest PDMS chain length

The first experiments were conducted with the copolymer **1a-(1.7)** based on *1,6-hexamethylene diisocyanate* (HMDI) and the shortest PDMS segment. Initially the saturation temperature for the pressure-induced batch foaming process was chosen close to the crossover temperature T_{cross} (1st heating) of 78 °C which was determined by DMTA as the transition from an elastic to a viscous behavior upon heating. At this temperature the material can sufficiently take up the blowing agent while preventing the specimen from melting. Rheology measurement discussed in chapter 3.2.6 implying a suitable melt strength due to a high viscosity of 12640 Pa·s at T_{cross} stabilizing the specimen shape and preventing it from collapsing or over expansion upon foaming. Copolymer **1a-(1.7)** was first saturated with CO_2 at a pressure of 100 bar for 30 min at 60 °C and 70 °C, followed by a sudden pressure drop. Upon pressure release cell nucleation and cell growth is initiated. The final cell morphology is stabilized upon cooling to room temperature. The specimen expanded in all dimensions while maintaining the overall specimen shape. The obtained cell morphologies can be seen in Figure 3.59. A closed and extremely inhomogeneous cell morphology was observed in both cases.
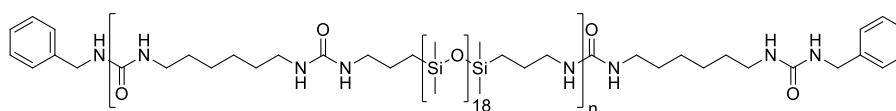
1a-(1.7)
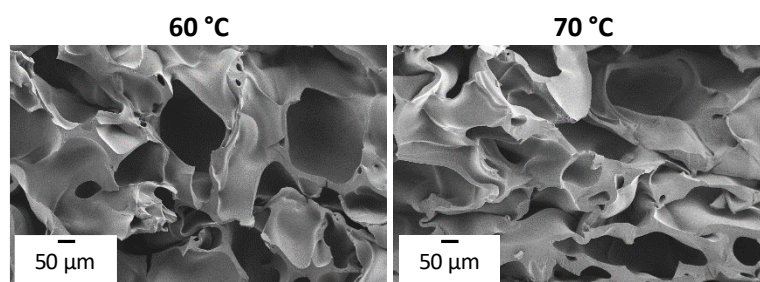
Figure 3.59: Foam morphologies of poly(urea-siloxane) foams based on **1a-(1.7)** saturated with CO_2 at 100 bar for 30 min at a temperature of 60 °C and 70 °C.

Variation of saturation temperature: Analyzing SEM images utilizing the software Image J and assuming spherical cells allows the calculation of the cell size. Detailed experimental data are included in chapter 5.2. The cell size was determined in dependency of the saturation temperature and is shown in Figure 3.60 **(A)**. The cell morphology shows an inhomogeneous cell size distribution, which is confirmed by the large standard deviation. The poly(urea-siloxane) foam saturated at 60 °C shows cell sizes ranging from 60 to 230 μm while the distribution decreases slightly for 70 °C, ranging from 53 to 210 μm.
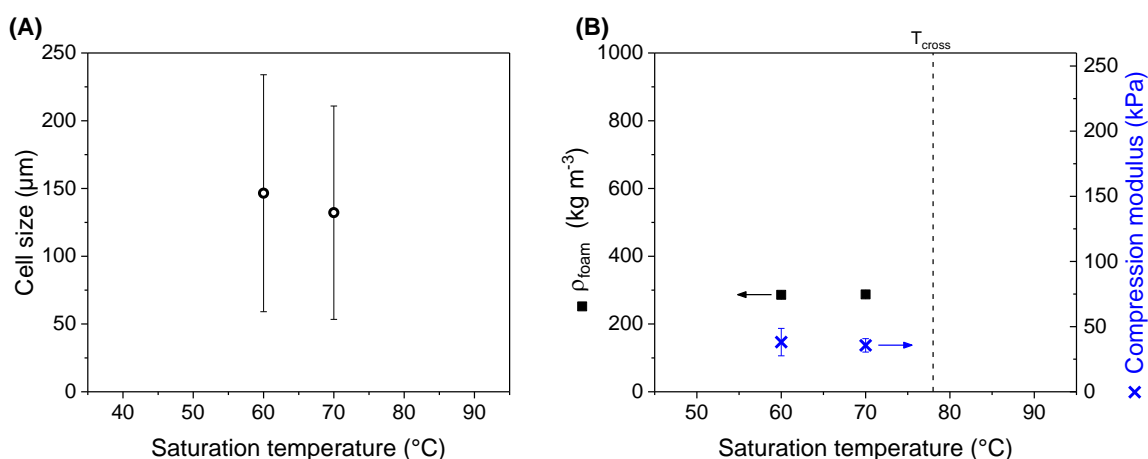
Figure 3.60: (A) Cell size, **(B)** foam density, and compression modulus of poly(urea-siloxane) foams based on **1a-(1.7)** foamed at two different saturation temperatures 60 °C and 70 °C. Other saturation conditions: CO_2 at 100 bar for 30 min.

Taking a closer look at the foam density (Figure 3.60 **(B)**) it can be seen that they are similar for 60 °C and 70 °C at 286 kg m^{-3} and 287 kg m^{-3}, respectively. This is equivalent to a density reduction of 72% compared to the neat poly(urea-siloxane) material with a bulk density of 1017 kg m^{-3}. For a closer insight into the mechanical properties of the foamed specimen compression tests have been conducted. The compression modulus was determined from the initial slope of the stress-displacement curve and is given as an average of at least four measurements. The compression moduli are shown in Figure 3.60 **(B)**. The compression modulus of the foam saturated at 60 °C is slightly larger (38 kPa) than the one saturated at 70 °C (36 kPa). This can be explained by the similar cell sizes and foam density since the mechanical properties are in general proportional to the foam densities.[8] The larger standard deviation is due to a larger standard deviation of the cell size. Nevertheless, in comparison to the neat bulk material (525 kPa) a significant reduction of about 93% of the compression modulus was achieved. Additionally, the cell density, corresponding to the cells per unit volume, was determined. The density is the same for both foams ($9 \cdot 10^5$ cells cm^{-3}), classifying them as fine-celled foams. All results are summarized in Table 3.15.

Table 3.15: Morphological properties, foam density, and compression modulus of poly(urea-siloxane) foams based on **1a-(1.7)** foamed at two different saturation temperatures. Other saturation conditions: CO_2 at 100 bar for 30 min.
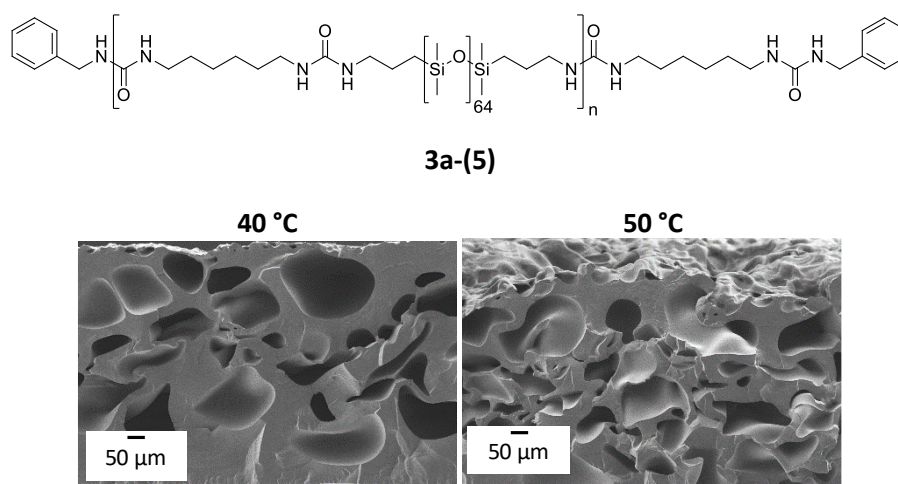
Material	Saturation temperature (°C)	Cell size (µm)	Density (kg m^{-3})	Density reduction (%)	Cell density (cells cm^{-3})	Compression modulus (kPa)
bulk	-	-	1017 ± 15	-	-	525 ± 70
1a-(1.7)	60	147 ± 87	286 ± 7	72	$9.1 \cdot 10^5$	38 ± 11
	70	132 ± 79	287 ± 7	72	$9.0 \cdot 10^5$	36 ± 5

Variation of saturation pressure: For more insight into the foam formation and properties of this material, especially concerning cell size, the saturation pressure was varied while keeping the saturation time and temperature constant at 30 min and 70 °C. The foam morphologies of the poly(urea-siloxane) saturated at 100, 120 and 180 bar are depicted in Figure 3.61. As can be seen, the cell size decreases dramatically upon increasing the saturation pressure. In magnification it is illustrated that the cell sizes are simultaneously becoming more and more homogenous in size and shape. Applying higher saturation pressures, more physical blowing agent is taken up by the specimen and increasing the nucleation rate upon pressure drop, resulting in a larger amount of smaller cells as well as an increased homogeneity.
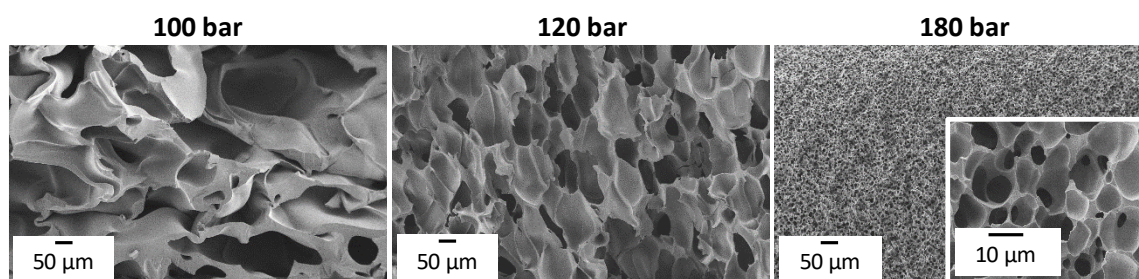
Figure 3.61: Foam morphologies of poly(urea-siloxane) foams based on **1a-(1.7)** saturated with CO_2 at 70 °C for 30 min at different pressures.

A more detailed analysis of the cell size reveals that a more homogenous cell size is formed reflected by its dramatically decreasing standard deviation (Figure 3.62 **(A)**). Upon increasing the pressure from 100 to 120 and finally to 180 bar the cell size decreases from 132 µm to 61 µm and finally to 7 µm, which is almost 20 times smaller. Increasing the pressure leads to an increase uptake of the blowing agent and more nucleation sites upon pressure drop, resulting in an increased amount of smaller cells.
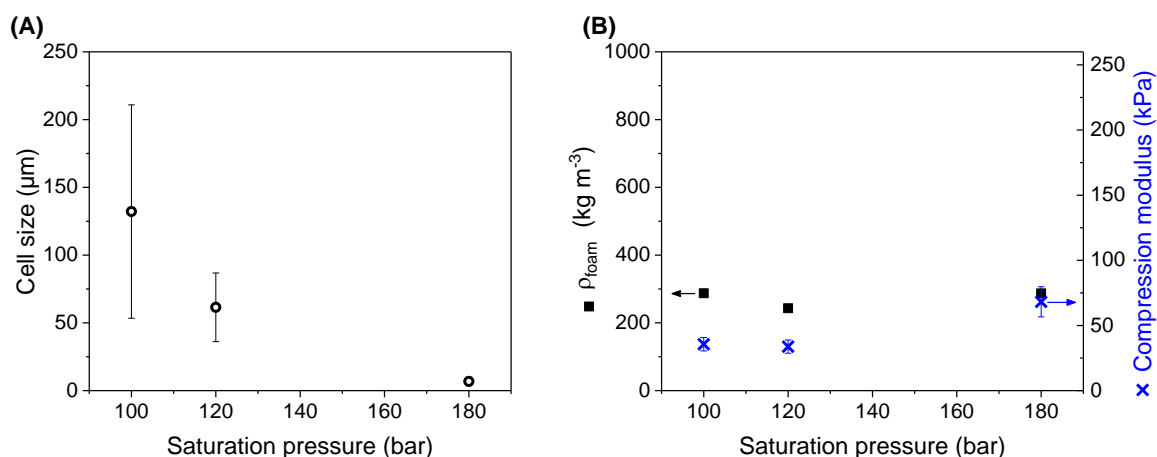
Figure 3.62: (A) Cell size, **(B)** foam density, and compression modulus of poly(urea-siloxane) foams based on **1a-(1.7)** foamed at different saturation pressures. Other saturation conditions: CO_2 at 70 °C for 30 min.

The difference in foam density of the single foams is less pronounced as can be seen in Figure 3.62 **(B)**. It ranges from 243 to 287 kg m^{-3} which corresponds to a density reduction of 72 to 76%. The compression moduli show an inverse behavior to the cell size. With increasing saturation pressure the compression modulus increases. Though a compression modulus of 68 kPa, corresponding to a reduction of 87%, is indicative of a soft poly(urea-siloxane) foam.

The data are summarized in Table 3.16 including the cell density which is significantly increased upon increasing saturation pressure owed to a growing amount of nuclei. For 100 bar a cell density of $9.0 \cdot 10^5$ cells cm^{-3} was obtained while it increased to $1.3 \cdot 10^7$ cells cm^{-3} at 120 bar and to $8.6 \cdot 10^9$ cells cm^{-3} at 180 bar. The foam saturated at 180 bar can consequently be classified as a microcellular foam while the other ones are fine-celled foams. Increasing cell numbers and decreasing size, goes along with an increased foam density and thus again with an increasing compression modulus. These results show a high potential of **1a-(1.7)** to fulfill the goal to fabricate soft foams with cell sizes on the low micrometer scale with a high density reduction while maintaining a certain toughness.

Table 3.16: Morphological properties, foam density, and compression modulus of poly(urea-siloxane) foams based on **1a-(1.7)** foamed at different saturation pressures. Other saturation conditions: CO_2 at 70 °C for 30 min.

| Material	Saturation pressure (bar)	Cell size (µm)	Density (kg m^{-3})	Density reduction (%)	Cell density (cells cm^{-3})	Compression modulus (kPa)
bulk	-	-	1017 ± 15	-	-	525 ± 70
1a-(1.7)	100	132 ± 79	287 ± 7	72	$9.0 \cdot 10^5$	36 ± 5
	120	61 ± 25	243 ± 4	76	$1.3 \cdot 10^7$	34 ± 5
	180	7 ± 3	287 ± 4	72	$8.6 \cdot 10^9$	68 ± 12

Pressure-induced batch foaming of poly(urea-siloxane) based on 1,6-hexamethylene diisocyanate as hard segment and the medium PDMS chain length

In contrast to the copolymer **1a-(1.7)** discussed before, the poly(urea-siloxane) **2a** has an increased soft segment chain length. Poly(urea-siloxane) **2a** with the medium PDMS chain length with a molecular weight of M_n = 2871 g mol^{-1} (x = 36) and *1,6-hexamethlyene diisocyanate* as hard segment is a softer and more elastic material with a lower compression modulus of 335 kPa than to **1a-(1.7)** with 525 kPa. This is owed to a decreasing weight fraction of the hard segments. For foaming the specimen was saturated at 100 bar for 30 min at 70 °C, which is close to T_{cross} (1st heating) of 72 °C. These saturation parameters resulted in a foamed material with a density reduction of only 21%. Therefore, the specimen was saturated under the same conditions but at 80 °C. The density reduction was almost doubled by increasing the temperature but going along with an inhomogeneous cell size distribution, an average cell size of 73 ± 40 µm and a low volume expansion. A SEM image of the foam morphology is depicted in Figure 3.63. By applying a higher saturation temperature of 90 °C, the specimens lose their overall geometry due to over expansion of the material. This is due to the decreased weight fraction of hard segments within the copolymer decreasing the mechanical strength and reducing the melt strength.

2a

80 °C

50 µm
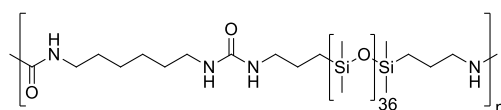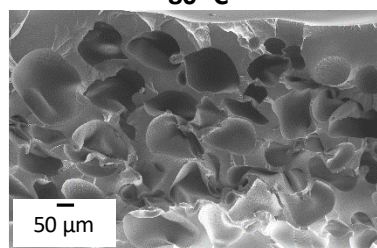
Figure 3.63: Foam morphology of poly(urea-siloxane) foam based on **2a** saturated with CO_2 at 100 bar and 80 °C for 30 min.

The foam density δ_{foam} in dependency of the saturation temperature is shown in Figure 3.64. The foam density is 740 kg m^{-3} for the poly(urea-siloxane) foam saturated at 70 °C and decreases to 572 kg m^{-3} for a saturation temperature of 80 °C. However, this is equivalent to a density reduction of 21% and 39%, respectively. The compression modulus shows the same trend. With increasing temperature, a decreasing modulus is obtained. The foam saturated at 80 °C shows a compression modulus of 32 kPa which is slightly lower than the poly(urea-siloxane) **1a-(1.7)** foam saturated at 70 °C (36 kPa).
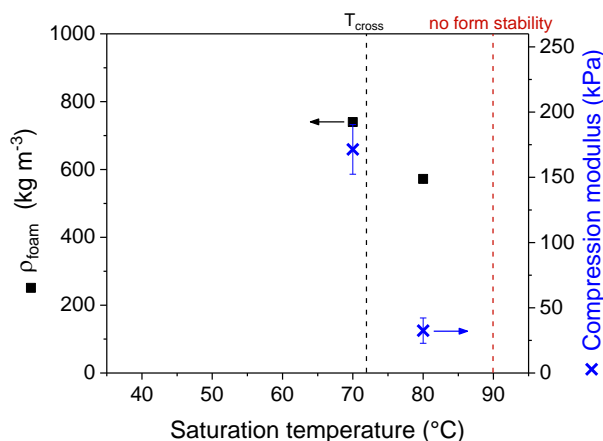
Figure 3.64: Foam density and compression modulus of poly(urea-siloxane) foams based on **2a** foamed at two different saturation temperatures of 70 and 80 °C. At 90 °C the specimen over expands upon the foaming process and loses its shape. Other saturation conditions: CO_2 at 100 bar for 30 min.

The results of the pressure-induced batch foaming of poly(urea-siloxane) **2a** are summarized in Table 3.17. The cell density of the **2a** foam saturated at 80 °C was determined to be $1.8 \cdot 10^6$ cells cm^{-3} classifying it as a fine-celled foam.

Table 3.17: Morphological properties, foam density, and compression modulus of poly(urea-siloxane) foams based on **2a** foamed with two different saturation temperatures. Other saturation conditions: CO_2 at 100 bar for 30 min.

Material	Saturation temperature (°C)	Cell size (µm)	Density (kg m^{-3})	Density reduction (%)	Cell density (cells cm^{-3})	Compression modulus (kPa)
bulk	-	-	936 ± 65	-	-	335 ± 19
2a	70	n.d.[a]	740 ± 7	21	n.d.[a]	171 ± 19
	80	73 ± 40	572 ± 7	39	$1.8 \cdot 10^6$	32 ± 9

[a] Not determined.

Poly(urea-siloxane) **2a** can be foamed, yet the extend of foaming including volume expansion and density reduction, is not as high as was observed for poly(urea-siloxane) foams based on **1a-(1.7)**. This is owed to the chemical structure of the TPE which has a diluted weight fraction of hard segments compared to **1a-(1.7)**. Thus the melt strength decreases. Further the overall material mechanical strength is weaker, resulting in an uncontrolled expansion of the specimen and loss of specimen geometry upon pressure drop and volume expansion at elevated temperatures.

Pressure-induced batch foaming of poly(urea-siloxane) based on 1,6-hexamethylene diisocyanate as hard segment and the longest PDMS chain length

To complete the series of poly(urea-siloxane) foams based on *1,6-hexamethylene diisocyanate* as hard segment, the $(AB)_n$ segmented copolymer **3a-(5)** with the longest soft segment chain length (M_n = 4926 g mol^{-1}, x = 64) and lowest hard segment content is investigated concerning its foaming behavior and foam properties. The compression modulus of the neat material is almost 4-fold smaller (142 kPa) than for **1a-(1.7)** (525 kPa). The specimens were saturated at 100 bar for 30 min at 40 °C and 50 °C. Specimen being saturated at 60 °C lost their shape upon pressure release owing to a too low melt strength even though the crossover temperature is above 60 °C (T_{cross} (1st heating) = 78 °C). The cell morphology of the foams are shown in Figure 3.65. As already observed for **2a** the foamed specimens show a low volume expansion. Relatively large closed cells with thick cell walls were obtained. A slightly decrease with increasing saturation temperature was observed. Owed to the lower saturation temperatures, less CO_2 was uptaken, resulting in fewer cell nuclei and consequently poor foaming. The efficient saturation with the blowing agent is affected by the soft and elastic material properties. Lower hard segment content decreases the melt strength at higher temperatures. The soft material tends to over expansion due to decreasing mechanical strength which is mainly determined by the hard segment weight fraction, consequently restricting the blowing agent uptake and the cell nucleation.

3a-(5)

Figure 3.65: Foam morphologies of poly(urea-siloxane) foams based on **3a-(5)** saturated with CO_2 at 100 bar for 30 min at different temperatures of 40 °C and 50 °C.

The cell size as a function of the saturation temperature is shown in Figure 3.66 **(A)**. The cell size decreases from 99 μm to 71 μm upon increasing the temperature. Nevertheless, the distribution is extremely inhomogeneous resulting in a large standard deviation. The foam density, shown in Figure 3.66 **(B)**, also decreases from 632 kg m^{-3} to 534 kg m^{-3} with increasing saturation temperature. For the compression modulus the same trend is observed, with moduli decreasing slightly from 85 kPa to 81 kPa.
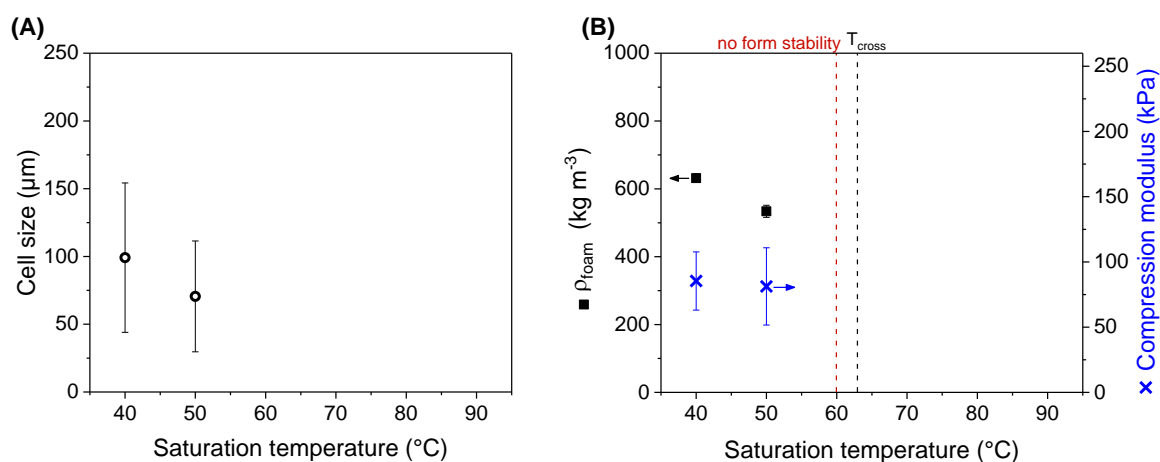
Figure 3.66: (A) Cell size, **(B)** foam density, and compression modulus of poly(urea-siloxane) foams based on **3a-(5)** foamed at two different saturation temperatures of 40 and 50 °C. At 60 °C the specimen over expands upon the foaming process and loses its shape. Other saturation conditions: CO_2 at 100 bar for 30 min.

The morphological properties, foam and cell density as well as the compression modulus are summarized in Table 3.18. In summary, the foams based on **3a-(5)** can be expanded up to a density reduction of 45%. Applying a higher saturation temperature did not result in a higher density reduction due to a too low melt strength and loss of form stability upon pressure release. However, these foams can also be classified as fine-celled foams.

Table 3.18: Morphological properties, foam density, and compression modulus of poly(urea-siloxane) foams based on **3a-(5)** foamed at two different saturation temperatures. Other saturation conditions: CO_2 at 100 bar for 30 min.

Material	Saturation temperature (°C)	Cell size (μm)	Density (kg m^{-3})	Density reduction (%)	Cell density (cells cm^{-3})	Compression modulus (kPa)
bulk	-	-	973 ± 8	-	-	142 ± 25
3a-(5)	40	99 ± 55	632 ± 12	35	$3.7 \cdot 10^5$	85 ± 22
	50	71 ± 41	534 ± 18	45	$1.4 \cdot 10^6$	81 ± 30

These results of the (AB)$_n$ segmented poly(urea-siloxane) copolymers revealed that the hard segment weight fraction and the resulting melt strength have a significant impact on the foam properties and the overall form stability. The higher the hard segment weight fraction, the smaller the cell sizes can be generated going along with an increasing density reduction and comparably high compression moduli.

Pressure-induced batch foaming of poly(urea-siloxane)s based on isophorone diisocyanate as hard segment

(AB)$_n$ segmented poly(urea-siloxane) copolymers **1b**, **2b**, and **3b** based on *isophorone diisocyanate* (IPDI) and different soft segment chain length show a significantly lower Young's modulus with a higher stress at break compared to HMDI based poly(urea-siloxane)s resulting in even softer material properties. The crossover temperatures upon 1st heating determined by dynamic mechanical thermal analysis ranging from 62 °C to 72 °C. Upon cooling a moderately increasing storage and loss modulus is obtained as shown by oscillating rheology measurements (chapter 3.2.3). In comparison, the HMDI based copolymers (**1a-(1.7)**, **2a**, **3a-(5)**) possess a steep increase of moduli. This behavior has a significant impact on the solidification behavior of the material and is expected to influence the foam stability and properties. IPDI based TPEs were saturated at 120 bar for 30 min at 60 °C, 70 °C, and 80 °C. The saturation pressure was chosen because a more homogenous cell size distribution and smaller cells were obtained at higher pressures than at 100 bar as shown by **1a-(1.7)** system. SEM images of the foam morphologies of the poly(urea-siloxane) with increasing PDMS chain length (**1b**, **2b**, **3b**) saturated at 120 bar for 30 min at 80 °C are shown in Figure 3.67.

1: x = 18
2: x = 36
3: x = 64

1b   **2b**   **3b**

50 µm   10 µm   50 µm   10 µm   50 µm   10 µm
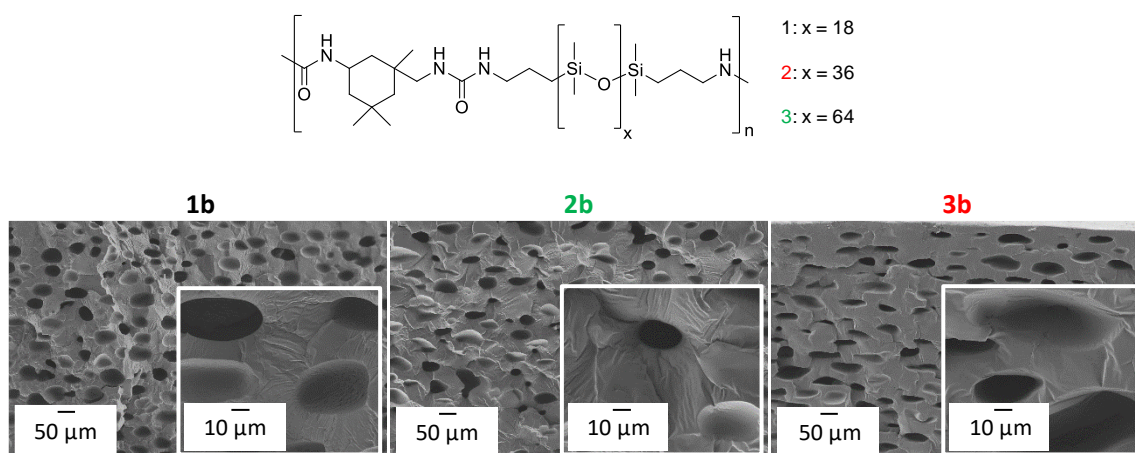
Figure 3.67: Foam morphologies of poly(urea-siloxane) foams based on **1b**, **2b**, and **3b** and inserted magnifications. Saturation conditions: CO_2, 80 °C, 120 bar for 30 min.

It can be seen that the specimens are not foamed to a complete extend indicated by the thick cell walls. This demonstrates an insufficient volume expansion and highly restricted cell growth. The cell size range from 20 to 36 µm and do not significantly change with increasing PDMS chain length as depicted in Figure 3.68 **(A)**. According to cell size and cell density they can be classified as fine-celled foams.
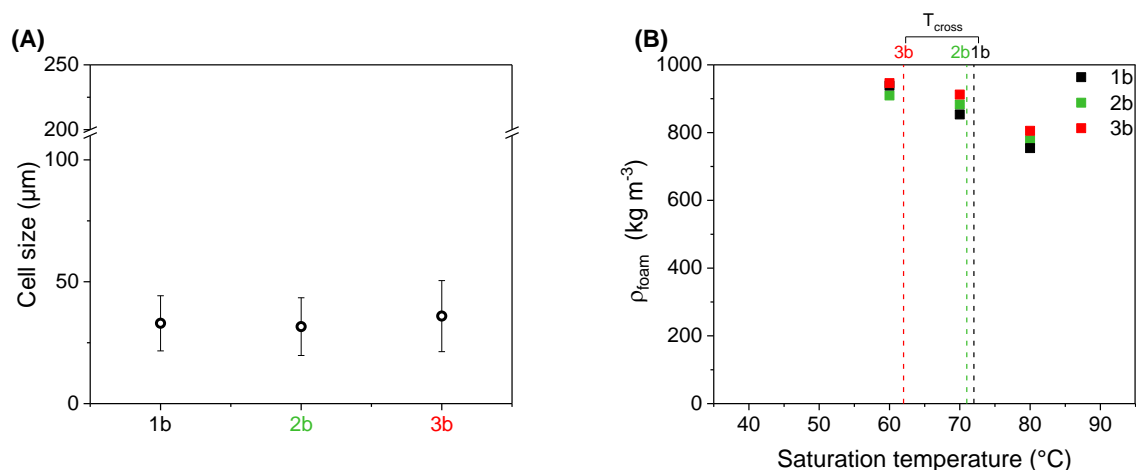
Figure 3.68: (A) Cell sizes of *isophorone diisocyanate* based poly(urea-siloxane) foams based on **1b**, **2b**, and **3b**, saturated with CO_2 at 120 bar and 80 °C for 30 min. **(B)** Foam density as a function of the saturation temperature of poly(urea-siloxane) foams **1b**, **2b**, and **3b**. Other saturation conditions: CO_2 at 120 bar for 30 min.

The foam density in dependency of the saturation temperature is shown in Figure 3.68 **(B)**. Considering the bulk material density of about 990 kg m^{-3} it can be seen that the density reduction is quite low at 60 °C and 70 °C. Even at a saturation temperature of 80 °C only a density reduction of about 20% was realized for the three poly(urea-siloxane)s. Compared to **1a-(1.7)** a smaller average cell size was obtained hence resulting in a density reduction of only 14%. An observation of these (AB)$_n$ segmented poly(urea-siloxane) copolymers based on IPDI is that after few weeks storing the specimens at ambient conditions they lose their foam structure and appear again as the original transparent specimens. This is owed to their self-healing ability and to elastic characteristics influenced by their chemical structure.[83,180] Storing the material at ambient temperature it tends to creep, re-arrange hydrogen bonding at the interfaces and consequently cannot stabilize the poor foam morphology resulting in a reverse process. Hence, no compression tests were conducted.

The morphological and density properties of poly(urea-siloxane) foams based on **1b**, **2b**, and **3a** are summarized in Table 3.19. In conclusion, it was shown that (AB)$_n$ segmented poly(urea-siloxane) copolymers can be foamed by a pressure-induced batch foaming process. However, the design of the copolymers has a large impact on the final foam morphology and quality.

Table 3.19: Morphological properties and foam density of poly(urea-siloxane) foams **1b**, **2b**, and **3b** based on IPDI and different PDMS chain length foamed at different saturation temperatures. Other saturation conditions: CO_2 at 120 bar for 30 min.

Material	Saturation temperature (°C)	Cell size (μm)	Density (kg m^{-3})	Density reduction (%)	Cell density (cells cm^{-3})
bulk	-	-	997 ± 11	-	-
	60	n.d.[a]	939 ± 6	6	n.d.[a]
1b	70	20 ± 8	854 ± 15	14	$8.5 \cdot 10^6$
	80	33 ± 11	754 ± 9	24	$6.8 \cdot 10^6$
bulk	-	-	986 ± 8	-	-
	60	n.d.[a]	909 ± 24	8	n.d.[a]
2b	70	n.d.[a]	883 ± 36	10	n.d.[a]
	80	32 ± 12	778 ± 18	21	$3.4 \cdot 10^6$
bulk	-	-	978 ± 7	-	-
	60	n.d.[a]	946 ± 28	3	n.d.[a]
3b	70	n.d.[a]	912 ± 21	7	n.d.[a]
	80	36 ± 15	805 ± 6	18	$3.4 \cdot 10^6$

[a] Not determined.

The most promising TPE foam is based on poly(urea-siloxane) **1a-(1.7)**. A density reduction of 76%, which the other systems could not reach, was obtained by saturating the specimen with CO_2 at 120 bar and 70 °C for 30min. Further different foam morphologies and mechanical properties depending on the saturation conditions could be obtained. These ranged from large cell sizes (~ 150 μm) to small cell sizes of 7 μm and compression moduli of about 35 to 68 kPa. The foam quality decreased with longer PDMS chains within the poly(urea-siloxane)s based on HMDI. The materials showed less melt stability upon saturation and lose their form stability upon pressure release which is due to an increased elasticity and less strength provided by a lower hard segment weight fraction. Also (AB)$_n$ segmented poly(urea-siloxane)s based on IPDI were foamed. Using a saturation temperature close to the crossover temperature to maintain a high melt strength resulted in poor density reduction owed to the increased elastic properties of the material compared to the HMDI based poly(urea-siloxane)s. Only about 20% density reduction was achieved in combination with cell sizes of about 30 μm and thick cell walls. Furthermore, after storing the foamed specimen at ambient conditions for few weeks they transform back into their original shape owed to self-healing and creep behavior.

From these results it can be concluded that (AB)$_n$ segmented poly(urea-siloxane) copolymers based on **1a-(1.7)** are the most promising class for the pressure-induced batch foaming process to cover multiple foam morphologies, foam densities, and mechanical properties depending on the saturation conditions. In the following the influence of varying processing parameters on the foam morphology and mechanical properties of **1a-(1.7)** is investigated in detail.

3.5.5. Detailed investigation of the foaming behavior of one selected copolymer

The influence of saturation temperature and pressure on the foam morphology as well as the compression modulus are investigated in more detail for the $(AB)_n$ segmented poly(urea-siloxane) copolymer **1a-(1.7)**. This copolymer is based on short chain PDMS soft segment ($M_n = 1513$ g mol^{-1}, $x = 18$) and *1,6-hexamethylene diisocyanate* (HMDI) hard segment. The screening experiments revealed that this material exhibits the highest melt strength and stability upon the foaming process.
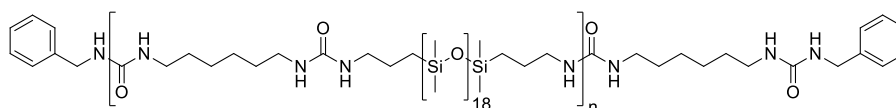
1a-(1.7)

Fabrication of specimen prior foaming

Circular plate specimens were fabricated by injection molding to exclude any potential trapped solvent residuals and to realize more meaningful results regarding future extrusion or injection molding foaming processes. The copolymer was molten at 120 °C within a twin-screw micro-compounder at 40 rpm for 5 min. The melt was discharged, directly transferred into the barrel of the injection molding machine and injected into a metal mold with a circular cavity with a diameter of 27 mm and a thickness of 1 mm. The melt was kept at 120 °C during injection whereas the mold was set to a temperature of 20 °C. The injection / holding pressure was set to 2.5 bar for 5 sec. The transparent specimens could easily be removed from the mold. The specimen did not show any anisotropy by optical light microscopy between two crossed polarizers. As for amorphous and semi-crystalline polymers the injection molding may cause an anisotropic effect within the specimen. This may have a significant effect on the foamed sample such as deformation. In other cases, this effect can be erased by annealing the specimen prior foaming. As for the poly(urea-siloxane) no additional treatment was necessary and the specimen were used as received after injection molding.

Pressure-induced batch foaming of poly(urea-siloxane) 1a-(1.7)

Figure 3.69 shows the neat injection molded poly(urea-siloxane) **1a-(1.7)** specimen. Thermoplastic elastomers are distinguished by their elastic properties which can also be observed in the pressure-induced batch foaming process. Right after the pressure drop (0 min) a complete white specimen with extended dimensions is observed. However, within a few minutes the specimen dimensions shrink. This shrinkage is about 12% of the foamed specimen. After 10 min the foamed specimen is completely stabilized and no further dimension change is observed. In total an expansion of approximately 30% in x-/y-direction compared to the original specimen was achieved. This shrinkage upon foaming is known from literature for TPEs owed to their high elasticity even at low temperatures.[181]

bulk | **0 min** | **2 min** | **10 min**

1 cm
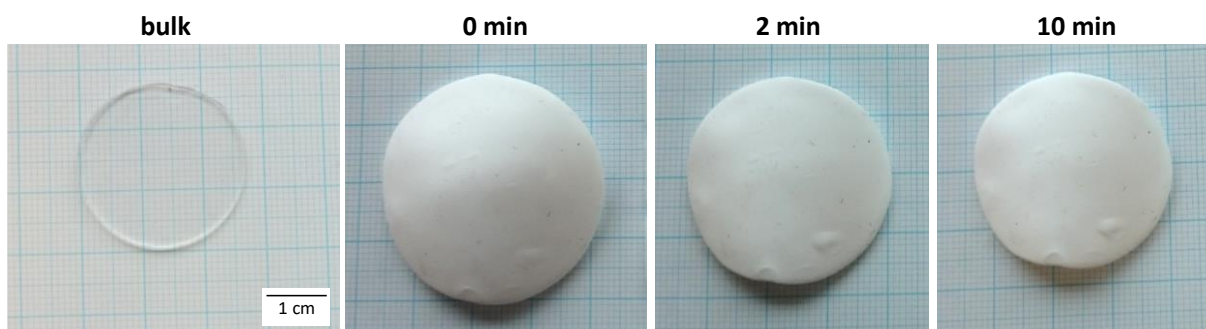
Figure 3.69: Photographs of neat injection molded poly(urea-siloxane) **1a-(1.7)** and the foamed samples directly after pressure drop (0 min), after 2 min and 10 min. The sample increases in all dimensions upon foaming and shrinks about 12% within the first 2 min after the pressure drop before reaching a stable state after 10 min. Saturation conditions: CO_2 at 150 bar and 50 °C for 30 min.

Variation of saturation time: First the influence of the saturation time *t* was analyzed concerning cell size, cell density, foam density, and the compression modulus. The poly(urea-siloxane) was saturated with CO_2 at 180 bar and 70 °C for 15, 30, and 60 min. The saturation pressure was chosen because of the previously discussed increased homogenous cell size distribution and a decreased standard deviation to determine an ideal saturation time. The resulting closed-cell morphologies as function of time are depicted in Figure 3.70.

15 min | **30 min** | **60 min**

2 µm | 2 µm | 2 µm
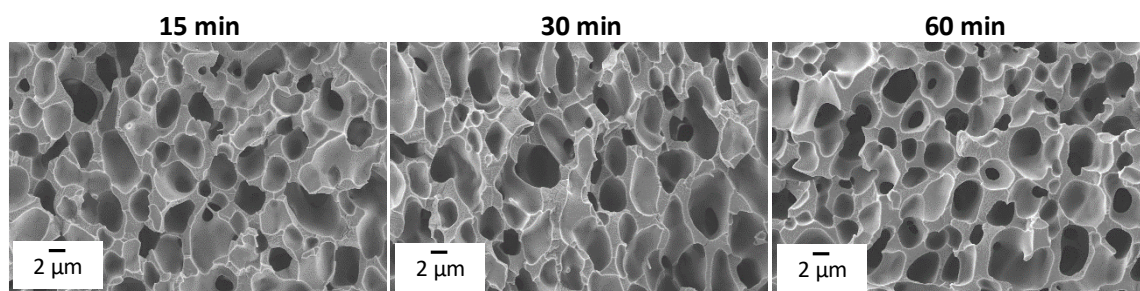
Figure 3.70: Foam morphologies of poly(urea-siloxane) foams based on **1a-(1.7)** saturated with CO_2 at 180 bar at 70 °C and different saturation times.

Comparing the cell sizes, it is obvious that the saturation time has no significant influence on the cell size. For all saturation times an average cell size of about 3 µm was determined (Figure 3.71 **(A)**).
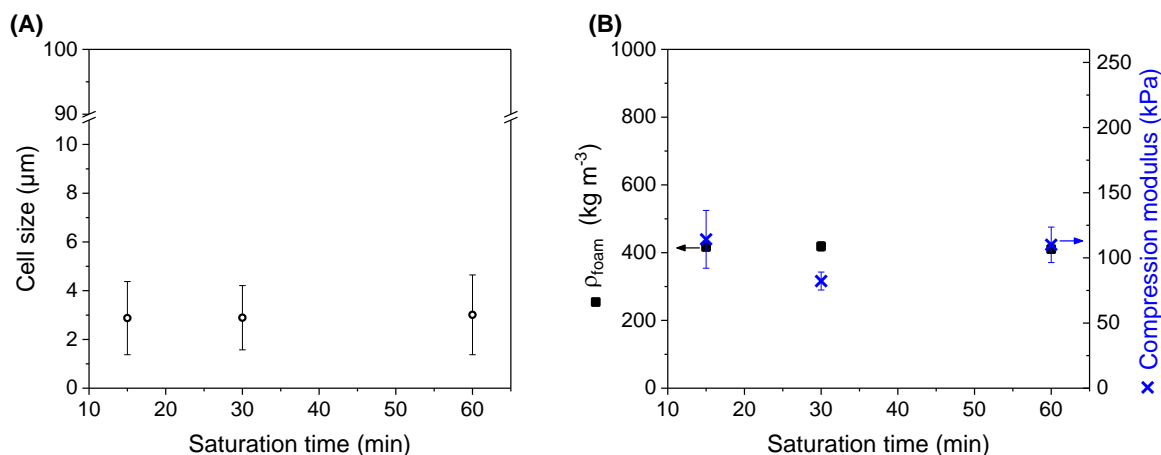
Figure 3.71: (A) Cell size, **(B)** foam density, and compression modulus of poly(urea-siloxane) foams based on **1a-(1.7)** foamed at different saturation times. Other saturation conditions: CO_2 at 180 bar at 70 °C.

Figure 3.71 **(B)** summarizes the foam density and the compression modulus as function of the saturation time. The time also has no significant influence on the foam density which is about 415 kg m^{-3}, resulting in a density reduction of 58%. The saturation time has also a small impact on the compression modulus. The lowest compression modulus was measured after saturating the sample with CO_2 for 30 min.

The morphological properties, foam and cell density, and compression modulus are summarized in Table 3.20. The cell density also shows a slight difference in dependency of the saturation time. After 30 min saturation the highest cell density with $5.1 \cdot 10^{10}$ cells cm^{-3} was observed. Concluding from these results owing to a small cell size and distribution as well as a high cell density a saturation time of 30 min is used as standard parameter in the following.

Table 3.20: Cell size, foam density, and compression modulus of poly(urea-siloxane) foams based on **1a-(1.7)** foamed at different saturation times. Other saturation conditions: CO_2 at 180 bar at 70 °C.

Material	Saturation time (min)	Cell size (µm)	Density (kg m^{-3})	Density reduction (%)	Cell density (cells cm^{-3})	Compression modulus (kPa)
bulk	-	-	1002 ± 5	-	-	554 ± 48
	15	2.9 ± 1.5	417 ± 7	58	$4.0 \cdot 10^{10}$	114 ± 22
1a-(1.7)	30	2.9 ± 1.3	419 ± 13	58	$5.1 \cdot 10^{10}$	82 ± 7
	60	3.0 ± 1.6	410 ± 7	59	$3.9 \cdot 10^{10}$	110 ± 14

Variation of saturation temperature and pressure: In the following the influence of the saturation temperature *T* and saturation pressure *p* on the foam morphology and mechanical properties are studied. The saturation temperature is varied from 25, 40, 50, 60 to 70 °C whereas the saturation pressure is increased from 100, 120, 150 to 180 bar. The saturation time was kept constant at 30 min for all experiments. *T* was chosen below the crossover temperature determined by oscillating shear rheology (T_{cross} (2nd heating) = 83 °C) to ensure a high viscosity, melt strength, and material stability upon pressure drop and foaming to prevent over expansion.

Influence of increasing saturation temperature at a CO_2 pressure of 100 bar

First the influence of increasing saturation temperature at 100 bar was studied. As can be seen in Figure 3.72 at temperatures between 25 and 50 °C small cells with an average cell size ranging from 1.5 to 6.9 µm are obtained. At higher temperatures larger cells with average cell sizes ranging from 28 to 50 µm are obtained going along with an inhomogeneous cell size distribution.
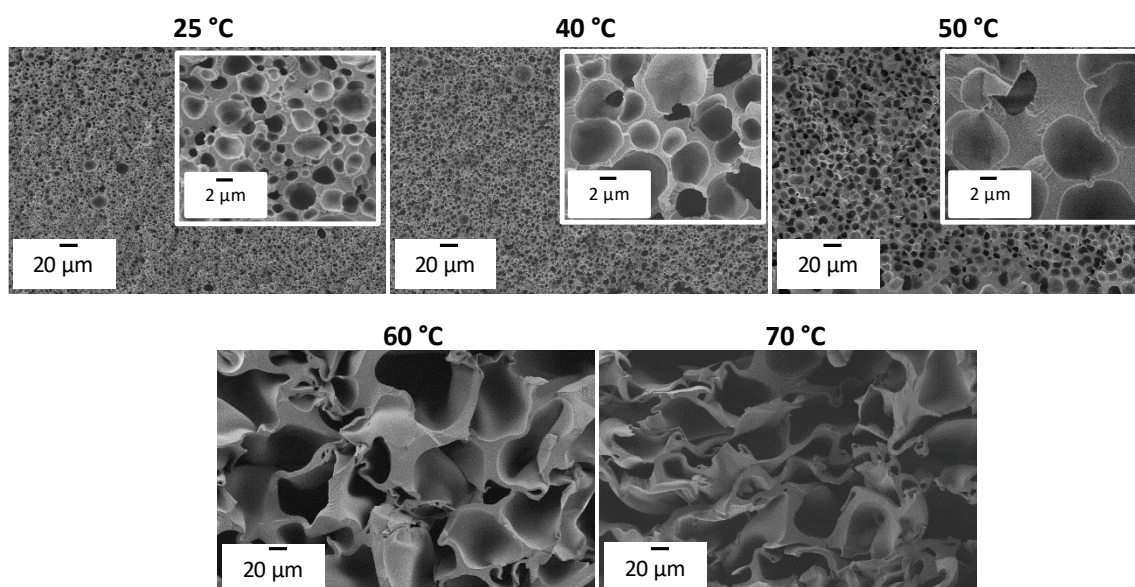
Figure 3.72: Dependence of the foam morphologies on the saturation temperature of poly(urea-siloxane) foams based on **1a-(1.7)** saturated with CO_2 at 100 bar for 30 min.

The cell sizes in dependency of the saturation temperature are shown in Figure 3.73 **(A)**. It can be seen that at temperatures well below the crossover temperature small and relatively homogenously distributed cell sizes are obtained. However, few single larger cells are included within the morphology. At temperatures closer to the crossover temperatures, the cell sizes suddenly increase almost about a factor of ten and show an extremely inhomogeneous cell size distribution indicated by a large standard deviation. This is due to a decreasing melt viscosity facilitating the gas expansion while maintaining the overall specimen shape. Yet the cell nucleation is extremely inhomogeneous resulting in such an uneven morphology.
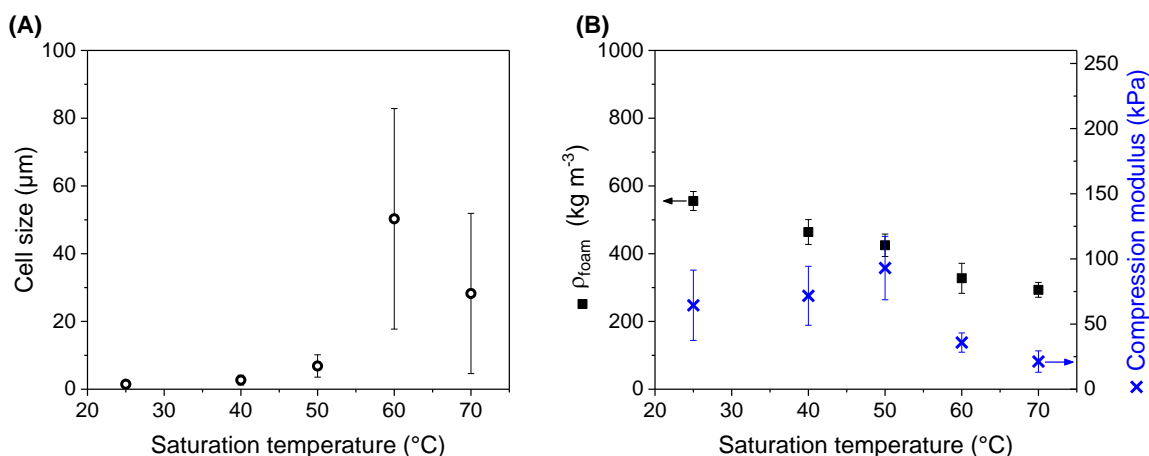
Figure 3.73: (A) Cell size, **(B)** foam density, and compression modulus of poly(urea-siloxane) foams based on **1a-(1.7)** foamed at different saturation temperatures. Other saturation conditions: CO_2 at 100 bar for 30 min.

The foam density on the other hand continuously decreases with increasing saturation temperature (Figure 3.73 **(B)**). The lowest foam density of 293 kg m^{-3} was observed for 70 °C which corresponds to a density reduction of 71%. The highest foam density (556 kg m^{-3}) obtained at a saturation temperature of 25 °C is still equivalent to a density reduction of 45%. Moreover, in Figure 3.73 **(B)** the compression modulus in dependency of the saturation temperature is plotted. An inverted behavior in comparison to the cell size can be observed. The foams with smaller cell sizes show a larger compression modulus (64 – 93 kPa) while the foams saturated at 60 °C and 70 °C show a decreased compression modulus of 36 kPa and 21 kPa, respectively, owed to larger cell sizes and a reduced foam density. These results indicate that even at lower temperatures CO_2 is uptaken into the specimen allowing a closed cell foam structure to be formed. Yet the expansion ratio increases significantly with increasing saturation temperatures.

The cell sizes, foam densities, and compression moduli are summarized in Table 3.21. The cell density is again influenced by the cell size and is in the range of $5.3 \cdot 10^{10}$ cells cm^{-3} for temperatures up to 50 °C and decreases by three orders of magnitude ($4.6 \cdot 10^7$ cells cm^{-3}) for higher saturation temperatures. Classifying the former as microcellular and the latter as fine-celled polymer foams.

Table 3.21: Morphological properties, foam density, and compression modulus of poly(urea-siloxane) foams based on **1a-(1.7)** foamed at different saturation temperatures. Other saturation conditions: CO_2 at 100 bar for 30 min.

Material	Saturation temperature (°C)	Cell size (µm)	Density (kg m^{-3})	Density reduction (%)	Cell density (cells cm^{-3})	Compression modulus (kPa)
bulk	-	-	1002 ± 5	-	-	554 ± 48
	25	1.5 ± 1.0	556 ± 28	45	$6.8 \cdot 10^{10}$	64 ± 27
	40	2.7 ± 1.5	464 ± 37	54	$5.3 \cdot 10^{10}$	72 ± 23
1a-(1.7)	50	6.9 ± 3.3	425 ± 33	58	$3.4 \cdot 10^9$	93 ± 24
	60	50.3 ± 33	328 ± 44	67	$1.0 \cdot 10^7$	36 ± 7
	70	28.3 ± 24	293 ± 22	71	$4.6 \cdot 10^7$	21 ± 8

Influence of increasing saturation temperature at a CO$_2$ pressure of 120 bar

Next the saturation pressure is increased to 120 bar while varying the saturation temperature again from 25 °C to 70 °C. The resulting foam morphologies are shown in Figure 3.74. It is conspicuous that with increased saturation pressure the cell sizes decrease due to higher CO$_2$ uptake. However, they increase with increasing saturation temperature which is owed to a decreasing viscosity of the specimen facilitating the gas expansion.
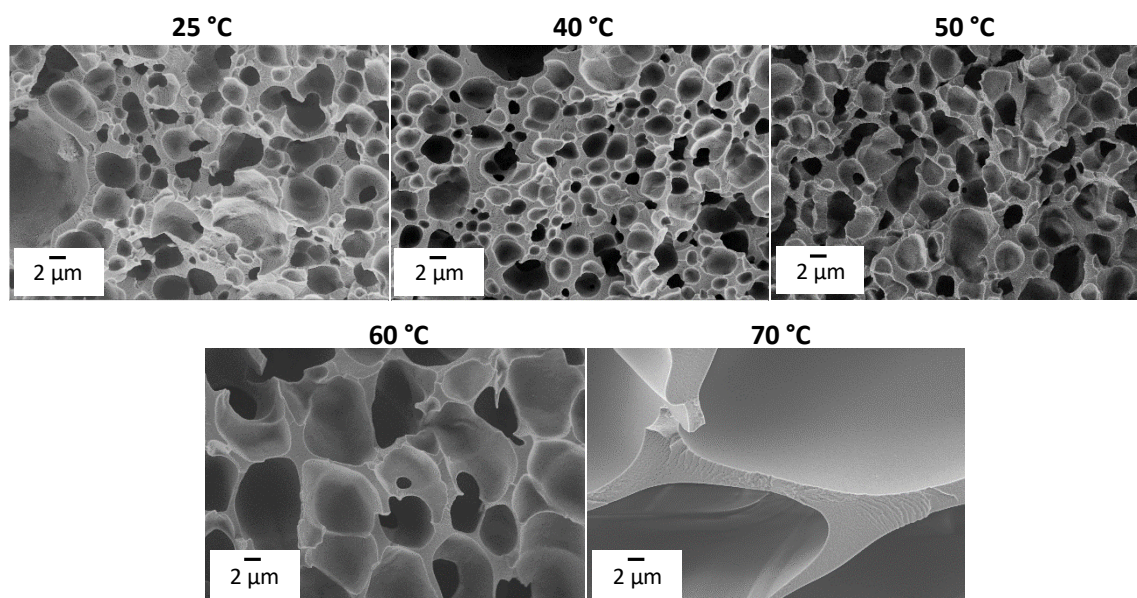
Figure 3.74: Dependence of the foam morphologies on the saturation temperature of poly(urea-siloxane) foams based on **1a-(1.7)** saturated with CO$_2$ at 120 bar for 30 min.

The cell size in dependency of the saturation temperature is shown in Figure 3.75 **(A)**. At 25 °C cells with a diameter of about 2 µm were obtained showing a relative large standard deviation of ±1.5 µm due to some single larger cells. Increasing the temperature to 60 °C the cell size increase to 6 µm and further increase to 25 µm at a saturation temperature of 70 °C. Yet the standard deviation increased significantly owed to an inhomogeneous cell size distribution. A similar trend as for 100 bar is observed which is again owed to the more efficient expansion upon higher temperatures due to a weaker polymer melt strength, resulting in larger cells.
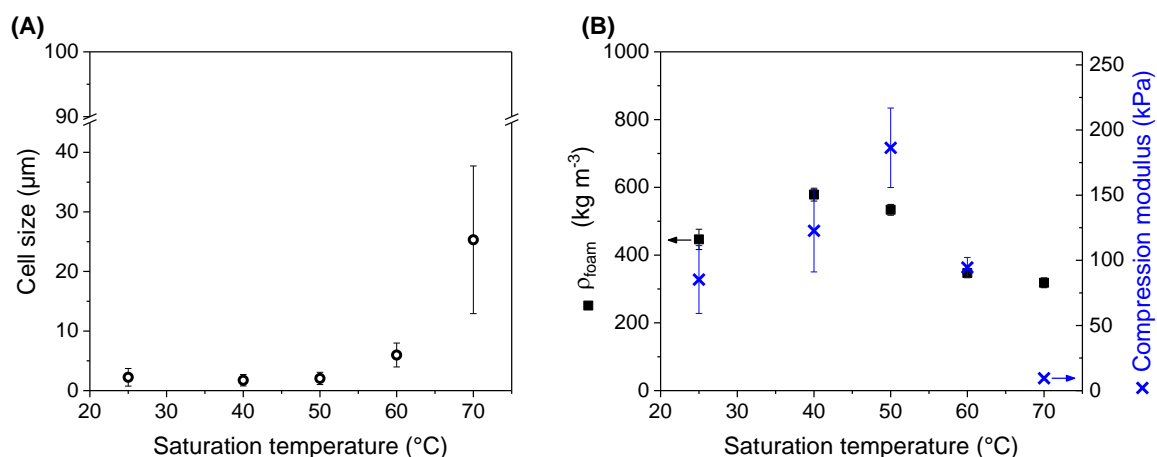
Figure 3.75: (A) Cell size, **(B)** foam density, and compression modulus of poly(urea-siloxane) foams based on **1a-(1.7)** foamed at different saturation temperatures. Other saturation conditions: CO_2 at 120 bar for 30 min.

The foam density in dependency of the saturation temperature increases initially up to 40 °C, then decreases with increasing temperature (Figure 3.75 **(B)**). At temperatures significantly lower the crossover temperature the foam density ranges between 446 kg m^{-3} and 534 kg m^{-3} corresponding to a density reduction of 42 – 55%. While applying saturation temperatures closer to T_{cross} the foam density decrease to about 320 kg m^{-3} which is equivalent to a density reduction of 68%. In Figure 3.75 **(B)** the compression modulus in dependency of the saturation temperature is shown. A minimum compression modulus of 10 kPa was observed applying a saturation temperature of 70 °C. While the largest compression modulus (186 kPa) was obtained for the poly(urea-siloxane) foam saturated at 50°C going along with small cell sizes of 2 µm. These results correlate well with the cell size and foam density.

In conclusion the cell sizes, foam densities, and compression moduli of the poly(urea-siloxane) foams saturated at 120 bar for 30 min are shown in Table 3.22. The cell density decreases with increasing saturation temperature from about $1 \cdot 10^{11}$ cells cm^{-3} to $2 \cdot 10^8$ cells cm^{-3} owed to an increasing cell size showing again the fabrication of microcellular to fine-celled polymer foams.

Table 3.22: Morphological properties, foam density, and compression modulus of poly(urea-siloxane) foams based on **1a-(1.7)** foamed at different saturation temperatures. Other saturation conditions: CO_2 at 120 bar for 30 min.

Material	Saturation temperature (°C)	Cell size (µm)	Density (kg m^{-3})	Density reduction (%)	Cell density (cells cm^{-3})	Compression modulus (kPa)
bulk	-	-	1002 ± 5	-	-	554 ± 48
	25	2.2 ± 1.5	446 ± 30	55	$5.9 \cdot 10^{10}$	85 ± 26
	40	1.7 ± 1.0	579 ± 19	42	$1.2 \cdot 10^{11}$	123 ± 32
1a-(1.7)	50	2.0 ± 1.0	534 ± 16	47	$1.1 \cdot 10^{11}$	186 ± 31
	60	6.0 ± 2.0	347 ± 14	65	$7.7 \cdot 10^9$	95 ± 8
	70	25.3 ± 12.4	318 ± 15	68	$2.2 \cdot 10^8$	10 ± 1

Influence of increasing saturation temperature at a CO_2 pressure of 150 bar

By increasing the saturation pressure even further to 150 bar the total cell size can be additionally reduced as can be seen in Figure 3.76. As well as an increased homogenous morphology is obtained.
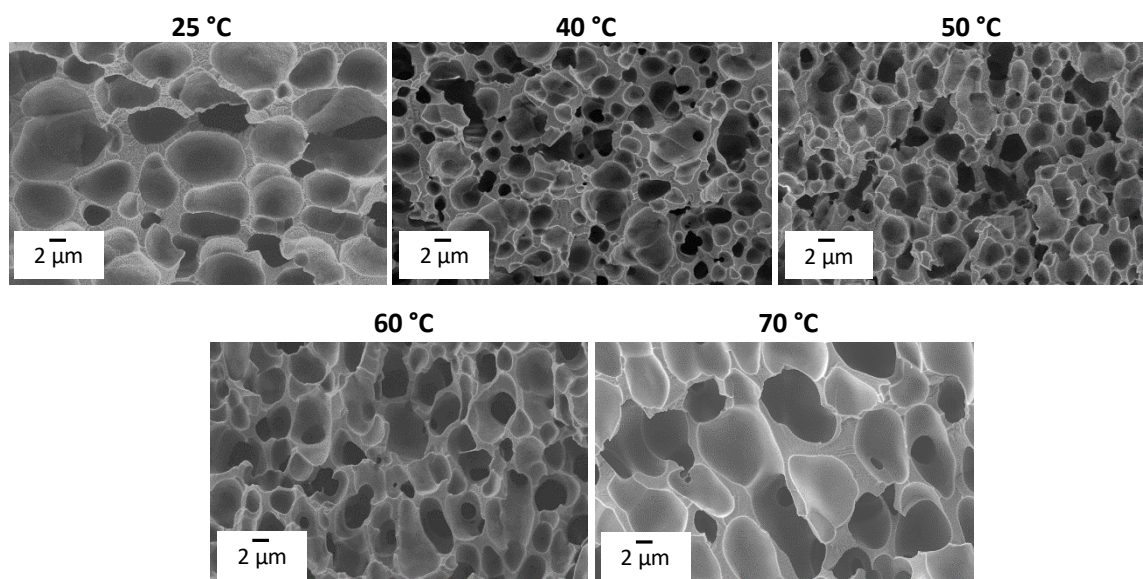
Figure 3.76: Dependence of the foam morphologies on the saturation temperature of poly(urea-siloxane) foams based on **1a-(1.7)** saturated with CO_2 at 150 bar for 30 min.

The cell size in dependency of the saturation temperature is shown in Figure 3.77 **(A)**. At 25 °C a cell size of 3.9 μm is obtained which decreases to 1.8 μm at a saturation temperature of 40 °C and then increases sequentially up to 5.1 μm with increasing *T*. Higher *p* again reduces the cell size as shown before due to an increasing CO_2 uptake. While upon temperature increase the material becomes softer, facilitating the volume expansion.
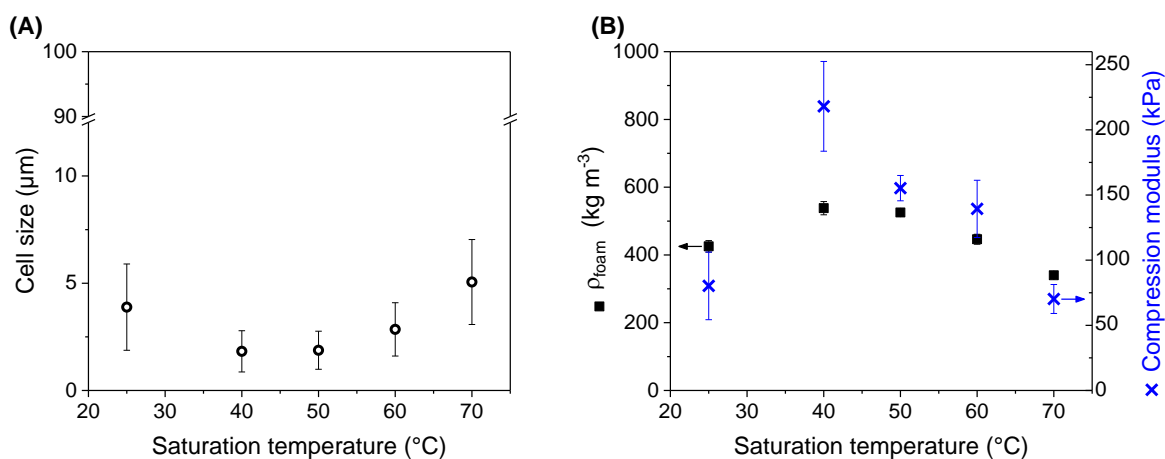
Figure 3.77: (A) Cell size, **(B)** foam density, and compression modulus of poly(urea-siloxane) foams based on **1a-(1.7)** foamed at different saturation temperatures. Other saturation conditions: CO_2 at 150 bar for 30 min.

The foam density shows the inverted behavior compared to the cell size in dependency of the saturation temperature (Figure 3.77 **(B)**). The lowest foam density obtained at a saturation pressure of 150 bar was 340 kg m^{-3} at a saturation temperature of 70 °C, corresponding to a density reduction of 66%. The compression modulus in dependency of the saturation temperature shows the same trend as the foam density which is owed to larger cell diameters. At T = 70 °C a compression modulus of 70 kPa was determined. The highest compression modulus determined at a saturation pressure of 150 bar is 218 kPa which was saturated at 40 °C and showing the smallest average cell size.

The morphological results, foam and cell density as well as compression modulus are summed up in Table 3.23. The cell density significantly increased in comparison to the poly(urea-siloxane) foams saturated at 100 bar and 120 bar, respectively. Even at a higher saturation temperature of 70 °C the cell density is still $1.1 \cdot 10^{10}$ cells cm^{-3}, classifying them all as microcellular foams. Yet this is also a reason for the increased compression modulus compared to the previous foamed systems.

Table 3.23: Morphological properties, foam density, and compression modulus of poly(urea-siloxane) foams based on **1a-(1.7)** foamed at different saturation temperatures. Other saturation conditions: CO_2 at 150 bar for 30 min.

Material	Saturation temperature (°C)	Cell size (µm)	Density (kg m^{-3})	Density reduction (%)	Cell density (cells cm^{-3})	Compression modulus (kPa)
bulk	-	-	1002 ± 5	-	-	554 ± 48
	25	3.9 ± 2.0	425 ± 17	58	$1.4 \cdot 10^{10}$	80 ± 26
	40	1.8 ± 1.0	538 ± 20	46	$1.2 \cdot 10^{11}$	218 ±34
1a-(1.7)	50	1.9 ± 0.9	525 ± 11	48	$1.3 \cdot 10^{11}$	155 ± 10
	60	2.8 ± 1.2	446 ± 15	55	$7.3 \cdot 10^{10}$	139 ± 22
	70	5.1 ± 2.0	340 ± 9	66	$1.1 \cdot 10^{10}$	70 ± 11

Influence of increasing saturation temperature at a CO$_2$ pressure of 180 bar

The influence of the saturation pressure on foam morphology, cell size, foam density, and compression modulus is completed by analyzing the effect of 180 bar. Figure 3.78 shows the different foam morphologies in dependency of the saturation temperatures. It can be seen that at 25 °C an inhomogeneous foam morphology with extremely large and small cells and comparable thick cell walls is obtained.
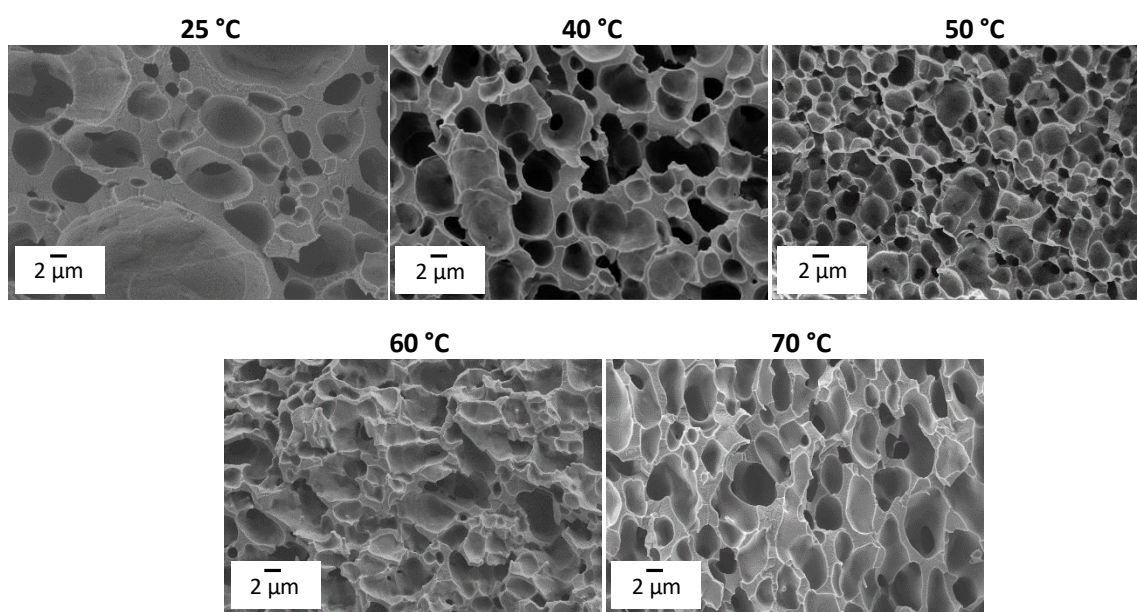
Figure 3.78: Dependence of the foam morphologies on the saturation temperature of poly(urea-siloxane) foams based on **1a-(1.7)** saturated with CO$_2$ at 180 bar for 30 min.

The cell sizes decrease with increasing saturation temperatures and reach a minimum at 60 °C with 1.6 µm before increasing slightly again. At 70 °C a cell diameter of 2.9 µm is obtained (Figure 3.79 **(A)**).
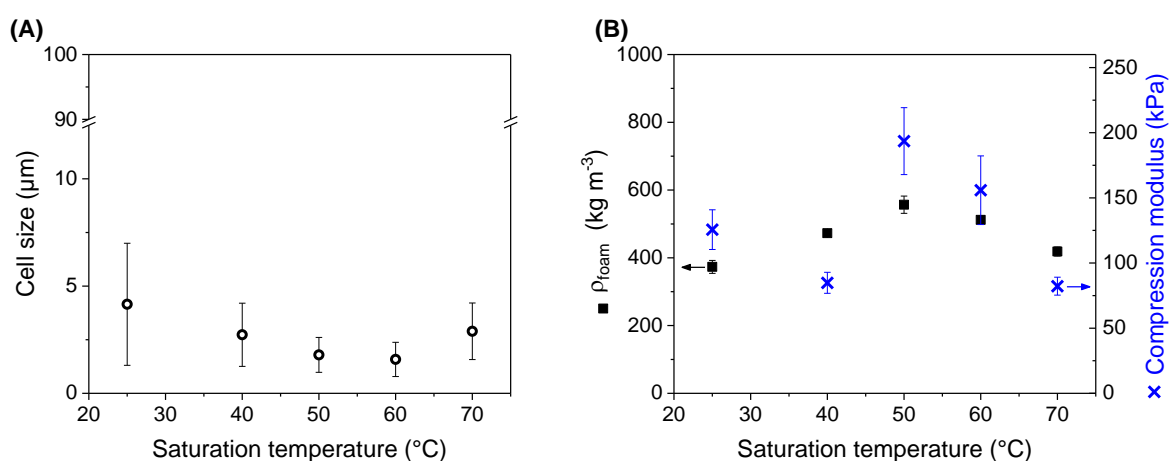
Figure 3.79: (A) Cell size, **(B)** foam density, and compression modulus of poly(urea-siloxane) foams based on **1a-(1.7)** foamed at different saturation temperatures. Other saturation conditions: CO$_2$ at 180 bar for 30 min.

The foam density initially increases up to 50 °C, then decreases which correlates again with the cell size. Even due to an inhomogeneous cell size distribution the lowest foam density of 373 kg m^{-3} was obtained at a saturation temperature of 25 °C which corresponds to a density reduction of 63% which is due to the larger cell size. With decreasing cell size, the foam density increases owed to denser material properties. At 70 °C the foam density is also low with 419 kg m^{-3}, being equivalent to 58% density reduction. In Figure 3.79 **(B)** the compression modulus in dependency of the saturation temperature is shown. The same trend as for the foam density is observed. A softer material is obtained with a lower foam density and a lower compression modulus, while a denser material shows a stiffer behavior with a higher compression modulus.

The data of the cell sizes, foam densities, and compression moduli are summarized in Table 3.24. The cell density increases slightly in comparison to the poly(urea-siloxane) foams saturated at 150 °C, thus can be classified as microcellular polymer foams.

Table 3.24: Morphological properties, foam density, and compression modulus of poly(urea-siloxane) foams based on **1a-(1.7)** foamed at different saturation temperatures. Other saturation conditions: CO_2 at 180 bar for 30 min.

Material	Saturation temperature (°C)	Cell size (μm)	Density (kg m^{-3})	Density reduction (%)	Cell density (cells cm^{-3})	Compression modulus (kPa)
bulk	-	-	1002 ± 5	-	-	554 ± 48
	25	4.2 ± 2.8	373 ± 19	63	$1.1 \cdot 10^{10}$	126 ± 15
	40	2.7 ± 1.5	473 ± 9	53	$6.0 \cdot 10^{10}$	85 ± 8
1a-(1.7)	50	1.8 ± 0.8	557 ± 26	44	$1.2 \cdot 10^{11}$	194 ± 26
	60	1.6 ± 0.8	512 ± 12	49	$2.0 \cdot 10^{11}$	156 ± 26
	70	2.9 ± 1.3	419 ± 13	58	$5.1 \cdot 10^{10}$	83 ± 7

To conclude, (AB)$_n$ segmented poly(urea-siloxane) **1a-(1.7)** can form fine-celled or microcellular closed cell foams with cell sizes between 1.5 μm and 50 μm depending on the saturation parameters (t, T, p). They all can be classified as soft, elastic polymer foams with compression moduli ranging from 10 kPa to 218 kPa. Furthermore, it was shown that the average cell size decrease with increasing saturation pressure while the homogeneity increased. Cell sizes smaller 2 μm with a total density reduction of almost 50% could be obtained going along with the highest achieved compression modulus of 218 kPa. The lowest foam density with 293 kg m^{-3} was reached with a saturation pressure of 100 bar for 30 min at 70 °C, corresponding to a total density reduction of 71% and an average cell size of 28 μm. The lowest compression modulus of 10 kPa, corresponding to a density reduction of 68% and an average cell size of 25 μm was determined at a saturation pressure of 120 bar and 70 °C. Applying different saturation pressures and temperatures a variation of different foam morphologies and mechanical properties could be realized. Depending on the application the foam properties and requirements can be fine-tuned using optimized (AB)$_n$ segmented poly(urea-siloxane)s and vary the process parameters.

118

In addition, it was shown that the specimen preparation has also an impact on the resulting foam properties as illustrated in Figure 3.80. Using specimen without thermal pre-treatment (solution cast) larger average cell sizes with large standard deviation are obtained compared to the specimen being prepared by injection molding **(A)**. Yet the foam density is lower for the solution cast specimen while the cell density shows the opposite behavior **(B)**. The compression modulus was found to be smaller for the injection molded specimen **(C)**. This can be explained by a more thermally controlled kinetic process of hard segment aggregation upon injection molding compared to the aggregation from solution upon solvent evaporation, since the hard segment domains are the major crosslinking points within the TPE being responsible for melt strength and the final foam quality. This again leads to a thermodynamic stable polymer morphology in which homogenously distributed cell nuclei can be introduced. Thus, foams fabricated by injection molded specimens are more interesting since the properties correlate more realistically with future extrusion or injection molding foaming.
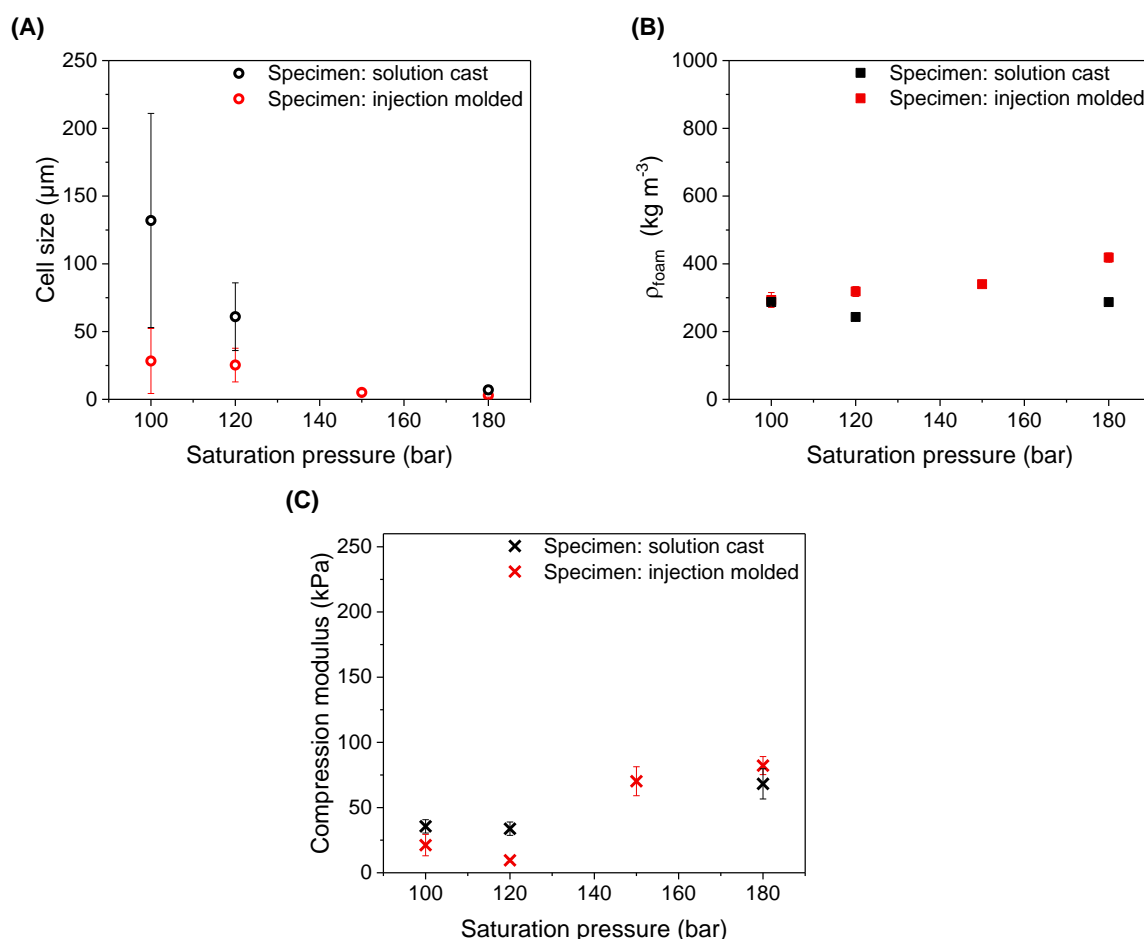
Figure 3.80: (A) Cell size, **(B)** foam density, and **(C)** compression modulus in dependency of saturation pressure of poly(urea-siloxane) foams based on **1a-(1.7)**. Other saturation conditions: CO_2 at 70 °C for 30 min. Comparing the influence of different specimen preparation: solution cast *versus* injection molded.

3.5.6. Conclusion of chapter 3.5.

Within this chapter (AB)$_n$ segmented poly(urea-siloxane) copolymers were investigated concerning their *foam forming ability* utilizing a pressure-induced batch foaming process. The material properties were modified by varying the soft segment chain length and the chemical structure of the hard segments to fabricate polymer foams with different properties including small cell sizes on the low micrometer scale and comparable high compression moduli.

In screening experiments *1,6-hexamethylene diisocyanate* (HMDI) and *isophorone diisocyanate* (IPDI) based poly(urea-siloxane)s with different PDMS soft segment chain length were investigated. It was found that IPDI based copolymers are not suitable candidates for TPE foams. On the contrary, poly(urea-siloxane)s with HMDI as hard segment can be foamed. It was found that the soft segment chain length and consequently the hard segment weight fraction have a significant influence on the foamability and foam properties. With increasing PDMS chain length the foam quality is reduced. This involves an increasing heterogeneity of the cell morphology, thicker cell walls, less density reduction only up to 40% with a cell density of $1 \cdot 10^6$ cells cm^{-3} and limited shape stability.

Detailed investigations of the foaming behavior of the best candidate, the molecular weight regulated poly(urea-siloxane) **1a-(1.7)** with the shortest PDMS chain length ($M_n = 1513$ g mol^{-1}, x = 18) and HMDI as hard segment were conducted. The morphological and mechanical properties were shown to be adjustable by varying the saturation parameters including time, temperature, and pressure as illustrated in Figure 3.81.
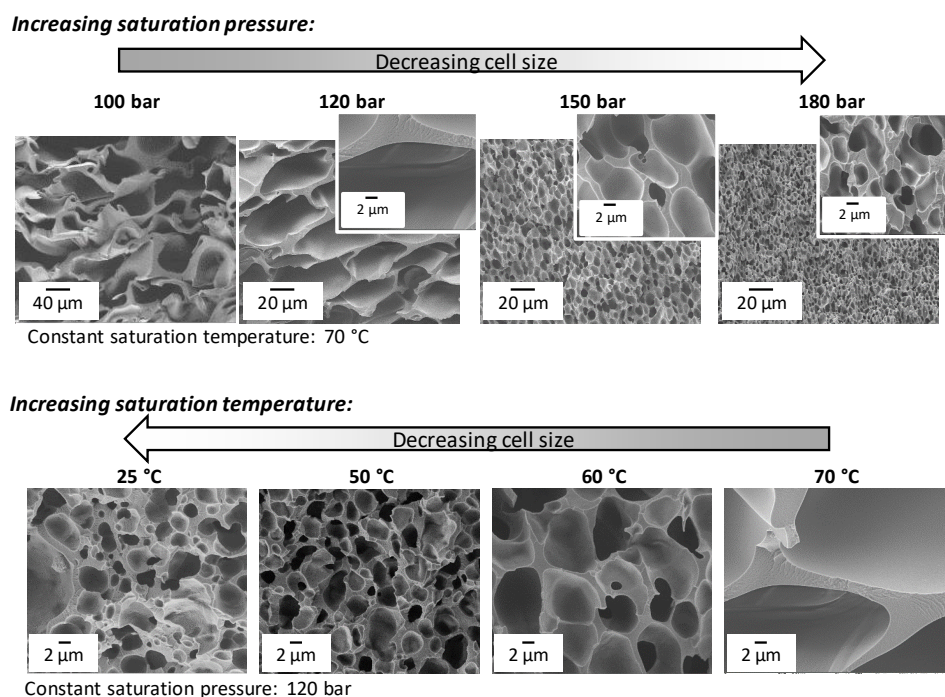
Figure 3.81: Foam morphologies of (AB)$_n$ segmented poly(urea-siloxane) **1a-(1.7)** based on short chain PDMS soft segments and *1,6-hexamethylene diisocyanate* hard segments. The cell size can be varied by changing either the CO_2 saturation pressure or temperature. Increasing pressure results in a decreasing cell size (top) while increasing temperature leads to an increase in cell size (bottom).

It was found that the optimum saturation time is 30 min to allow a uniform cell morphology to form through the whole sample and to obtain the lowest cell size. It was shown that by increasing the saturation pressure at a constant temperature the cell sizes become smaller and more homogenous. While with increasing saturation temperature at a constant pressure the cell sizes increased due to softening of the material.

Varying the saturation conditions, it was possible to prepare fine-celled to microcellular foams. Cell sizes ranging from 1.5 µm to 50 µm and cell densities ranging from $1.0 \cdot 10^7$ cells cm^{-3} to $1.3 \cdot 10^{11}$ cells cm^{-3} were obtained. In total a maximum density reduction of 71% was achieved and a minimum compression modulus of 10 kPa which corresponds to a reduction of 98% compared to the bulk material compression modulus. The highest compression modulus obtained was determined to be 218 kPa which corresponds to a reduction of 60% and an average cell size of 1.8 µm. In regard of fabricating biostable, non-degradable foams with small cell sizes and comparable high compression moduli as the scope of this thesis, saturation conditions of 150 bar and 40 °C are the first choice.

Concluding from these results it was shown that (AB)$_n$ segmented poly(urea-siloxane) copolymers provide a class of materials to fabricate soft and elastic polymer foams with adjustable properties including high density reduction, cell sizes on the low micrometer scale, and a homogenous and uniform foam structure. Utilizing *1,6-hexamethylene diisocyanate* hard segments, it was shown that the cellular structure is stabilized rapidly due to the relatively fast aggregation of the linear, aliphatic urea units upon cooling. However, the selection of soft segment is essential to obtain stable foam morphologies.

4. Amphiphilic (ABAC)$_n$ segmented poly(urea-siloxane) copolymers combining hydrophobic and hydrophilic segments

4.1. Physically and chemically crosslinked poly(ethylene glycol) based hydrogels

Poly(ethylene glycol) (PEG) based chemical or physical crosslinked polymers are known as perfect components for hydrogels due to their capability to absorb large amounts of water. However, for PEG hydrogels with physical crosslinks supramolecular self-assembly in water solely based on hydrogen bonding is impeded since intermolecular H-bonding competes with water molecules. This can be for example prevented by shielding the H-bonds from water by introducing a hydrophobic spacer. By incorporation of alkyl spacers between PEG segments and H-bonding segments non-polar local domains are introduced. This enhances the intermolecular interactions and hydrogen bonding formation.

In the following an overview of (AB)$_n$ segmented copolymers based on PEG and urea segments used as hydrogels known in literature is given. Sijbesma *et al.* introduced (AB)$_n$ segmented PEG-bisurea copolymers as injectable hydrogels which are stable in water.[182] To prevent the PEG segment (M_n = 8 or 20 kg mol^{-1}) to interfere with the hydrogen bonding units, hydrophobic alkyl spacers with ten methylene groups were incorporated between the urea and PEG segments (Figure 4.1).
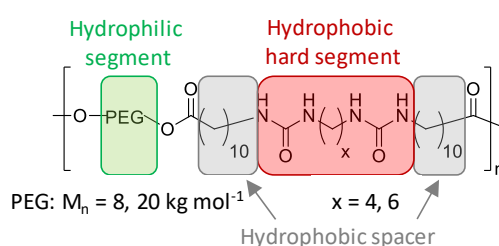
Figure 4.1: Chemical structure of (AB)$_n$ segmented PEG-bisurea copolymers which form stable hydrogels in water and can be used as injectable hydrogels. The hydrophobic alkyl spacers with ten methylene groups shields the PEG segments from interactions with the hydrogen bonding units.[182]

Cui *et al.*[183,184] investigated the synergistic effect between H-bonding and hydrophobic shielding effect and found that longer alkyl spacers enhance this effect (Figure 4.2). Stronger hydrogen bonds, such as urea compared to urethane, are of advantage due to the bidentate versus monodentate interactions. A long hydrophobic spacer of twelve methylene groups incorporated between urea and PEG segments with a molecular weight of 4 kg mol^{-1} yielded in an elastic and tough hydrogel with a water content up to 84 wt.%. These materials were further electrospun from a methanol solution into nanofibers. Shorter hydrophobic alkyl spacers, however, led to fragile and brittle hydrogels.
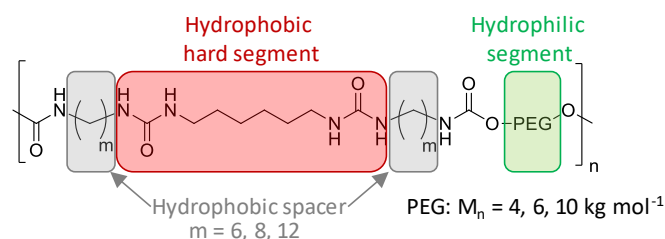
Figure 4.2: Chemical structure of a polyurethane-urea segmented copolymer which forms supramolecular hydrogels. Hydrophobic alkyl spacers shield the H-bonds from water, forming non-polar local domains enhancing the hydrogen bonding interactions, resulting in tough hydrogels.[183,184]

Another approach to improve the mechanical strength and water insolubility of PEG based hydrogels is the incorporation of multiple urea units within the backbone of a polyurethane-urea copolymer introduced by Guo *et al*. These multiple urea units range from 5, 6, 9, 12 to 15 urea units within one repetition unit linked via *isophorone diisocyanate* units and urethane units (Figure 4.3). A PEG with a molecular weight of 2 kg mol^{-1} was used here.[185]
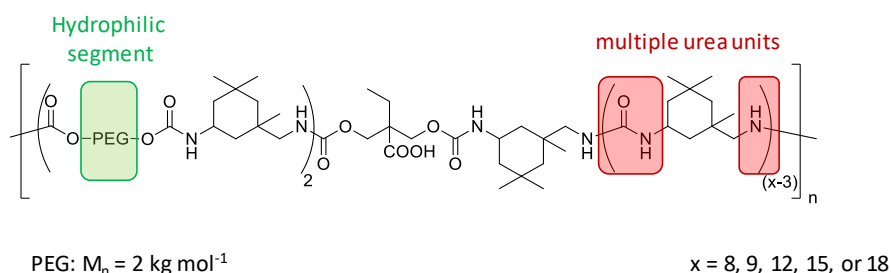
Figure 4.3: Chemical structure of the polyurethane-urea copolymer with multiple urea units being linked via *isophorone diisocyanate* and urethane units.[185]

Also the addition of more secondary self-complementary interactions, such as 2-ureido-4 [1H]-pyrimidinone (UPy), was investigated in the research group of Meijer.[37] Combining PEG with urethane, urea, and UPy units result in tough hydrogels. Nevertheless also the UPy units need to be shielded by a short hydrophobic spacer of a length of five methylene groups (Figure 4.4 **(A)**) resulting in tough hydrogels with a water content up to 86% using PEG with a molecular weight of 6 and 10 kg mol^{-1}. The semi-crystalline PEG domains become amorphous upon water absorption as shown by DSC. At the same time the hydrophobic hard segments reinforce the hydrogel network by strong H-bonding interactions which are protected from competing interactions with water molecules as schematically illustrated in Figure 4.4 **(B)**.
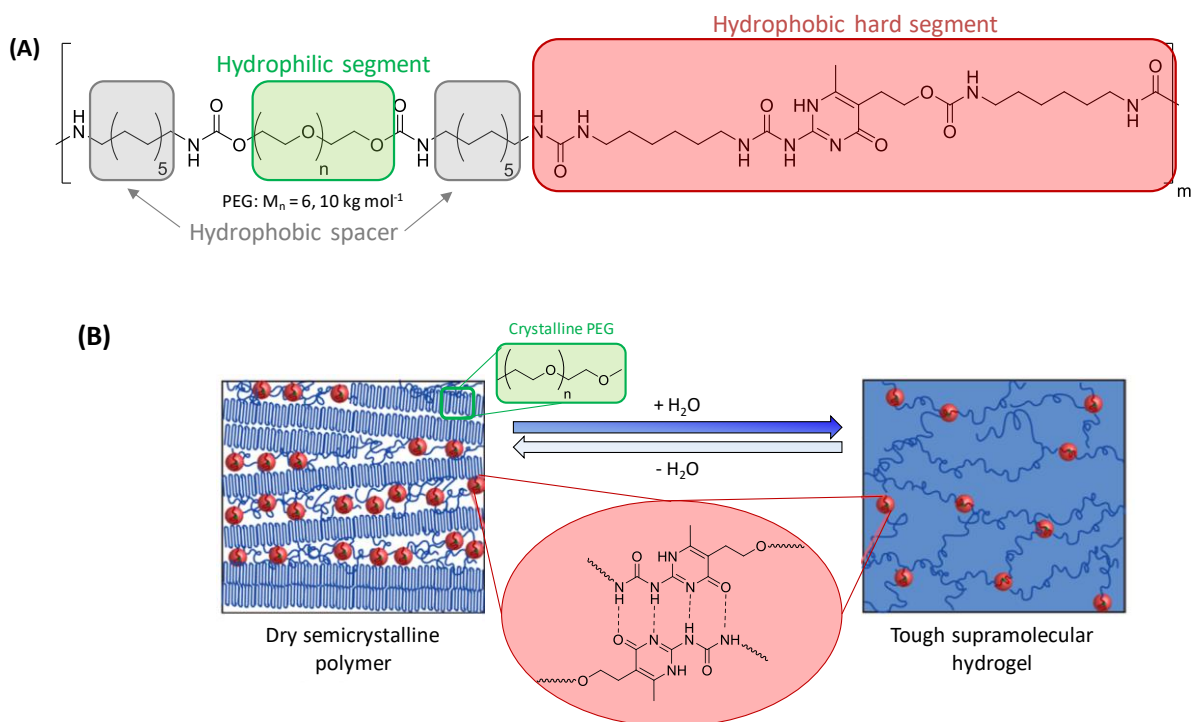
Figure 4.4: (A) Chemical structure of PEG based hydrogel with incorporated UPy units and hydrophobic alkyl spacers. **(B)** Illustration of dry semi-crystalline PEG-UPy chain-extended polymer morphology and its reversible transition into a supramolecular hydrogel upon water uptake. The quadruple H-bonding interaction between the UPy segments reinforce the network in the swollen state. [Adapted and printed with permission from [37]; © 2014 American Chemical Society]

All of these systems have in common that a sufficient shielding effect by a hydrophobic spacer is needed to prevent the hydrogel from falling apart and dissolution in water.

Within our research group J. Mechau investigated (AB)$_n$ segmented Jeffamine-urea copolymers with a variation of soft and hard segments (Figure 4.5 **(A)**).[186] These materials are designed regarding melt processing by melt electrowriting and allow the fabrication of 3D scaffolds. This is of interest for biofabrication applications. Figure 4.5 **(B)** shows a 3D scaffold prepared by melt electrowriting. By adjusting the chemical structure, hydrogels were prepared which are fragile and brittle and dissolve slowly over time in water.
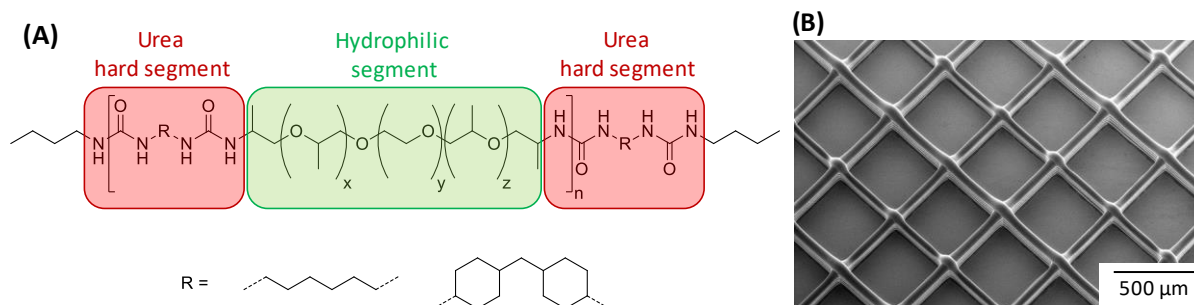
Figure 4.5: (A) General chemical structure of (AB)$_n$ segmented Jeffamine-urea copolymers. These copolymers can be melt processed into 3D scaffolds by melt electrowriting **(B)**.[186]

Kinning *et al.*[187] synthesized poly(dimethlysiloxane)-poly(propylene oxide)-urea copolymers and investigated their bulk, surface, and interfacial properties. The PDMS content within these systems was kept constantly at 25 wt.% while varying the poly(propylene oxide) (PPO) and hard segment content. Combining PDMS and PPO resulted in distinct improvements in the Young's modulus, tensile strength, and ultimate elongation. A phase separated morphology wherein PDMS forms spherical domains (~20 nm) surrounded by a continuous PPO and urea hard segment mixed matrix was visualized by transmission electron microscopy (TEM). Investigating the surface and interface properties of these materials they discovered a 1.5 – 2.0 nm thick layer of silicone soft segments at the surface which rearrange upon contact with water.[187]

Wilkes *et al.* studied the influence of the solid state structure-property behavior of poly(urea-siloxane)s with incorporated PPO units. These copolymers contained PDMS with a molecular weight of 3200 or 7000 g mol^{-1} and a hard segment content of 10 – 35 wt.% which are based on *4,4'-methylene bis(cyclohexyl isocyanate)*. PPO segments with a molecular weight of 450 or 2000 g mol^{-1} were used. It was found that these copolymers undergo microphase separation and show improved tensile properties due to inter-segmental hydrogen bonding of PPO units with urea units and the formation of a gradient interphase between the hard domains and the soft matrix.[188]

Li *et. al.* investigated amphiphilic polyurethane elastomers which were synthesized by a two-step polyaddition based on *isophorone diisocyanate* and 1,4-butanediol as hard segments and a mixture of dihydroxyl terminated PDMS (M_n = 2000 g mol^{-1}) and PEG (M_n = 1000 g mol^{-1}) soft segments. They investigated the mechanical and thermal properties. Further they demonstrated the tunable oxygen permeability and water vapor transmission rate of these copolymers by varying the built-in ratio of the diol components. These copolymers were found to exhibit excellent antibacterial efficacy along with cytocompatibility making them favorable for biorelated applications.[189]

Tew *et al.*[39,190] followed a different approach by chemically crosslinking a PEG system to control toughness and water uptake of the hydrogel. Here, a hydrophilic norbornene end-functionalized PEG and a hydrophobic norbonene end-functionalized PDMS were covalently crosslinked by thiolene click chemistry (Figure 4.6).[39,190]
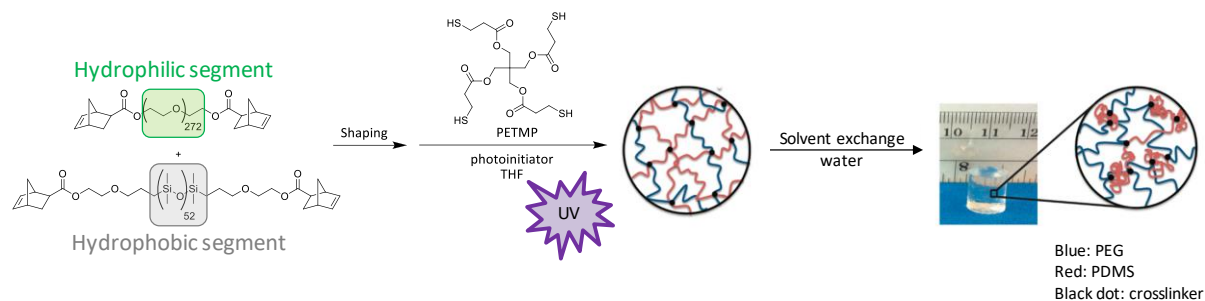
Figure 4.6: Synthesis and swelling of chemically crosslinked PEG/PDMS hydrogels. Norbornene end-functionalized PEG and PDMS are chemically crosslinked via thiol click-chemistry. By swelling in water the hydrophilic PEG block swells while the hydrophobic PDMS block collapse in an unswollen form. [Adapted and printed with permission from [190]; © 2012 American Chemical Society]

The polar PEG matrix governs the swelling capacity while the mechanical strength of the hydrogel is determined by the PDMS component and the microphase separation between PDMS and PEG segments.[39] They demonstrated high resilience hydrogels which can undergo reversible deformation without energy loss as well as the tunability of hydrogel properties by varying the PEG and PDMS composition.[190] Two drawbacks of this system are the lack of self-healing after the crosslinked network is damaged and the shaping step prior crosslinking excluding thermal processing of the crosslinked material. Nevertheless, these systems may contain residual thiol units and initiator fragments which may be toxic in regard to biofabrication.

Within this thesis the concept of Tew *et al.* will be further enhanced by synthesizing (ABAC)$_n$ segmented amphiphilic copolymers with statistically distributed hydrophobic PDMS (B) and hydrophilic PEG (C) segments. To obtain a material which is melt processable hydrogen bonding urea units (A) will be incorporated to generate physical crosslinks instead of chemical crosslinks. The aim is to provide a new class of mechanical stable hydrogels which can be used for additive manufacturing.

4.2.   Synthesis, characterization of amphiphilic copolymers and their hydrogel properties

Within the following the concept of amphiphilic, physically crosslinked (ABAC)$_n$ segmented copolymers is introduced. In addition to the hydrophobic PDMS segments (B) shown in black and the urea hard segments (A) shown in red, hydrophilic PEG containing segments (C) shown in green are incorporated (Figure 4.7). The PDMS and PEG segments are statistically incorporated. These (ABAC)$_n$ segmented copolymers are a modification towards amphiphilic hydrogels based on the in chapter 3.2 discussed hydrophobic (AB)$_n$ segmented poly(urea-siloxane)s by incorporating additional hydrophilic segments. These materials are designed to allow tuning of the hydrogel properties including water uptake and mechanical stability of the gels. At room temperature (Figure 4.7, center) the urea units are aggregated via hydrogen bonds and are distributed in an amorphous PDMS and PEG matrix. Depending on the PEG molecular weight the PEG phase can be either amorphous or semi-crystalline. In the swollen state (left) a selective water uptake occurs in the hydrophilic PEG containing segment while the hydrophobic PDMS segment will phase separate due to the incompatibility of the PDMS and PEG segments. On the other hand, since these materials are still based on physical crosslinks introduced by hydrogen bonded bisurea units, they are expected to form a processable, isotropic melt upon heating after disaggregation of the urea units (right).
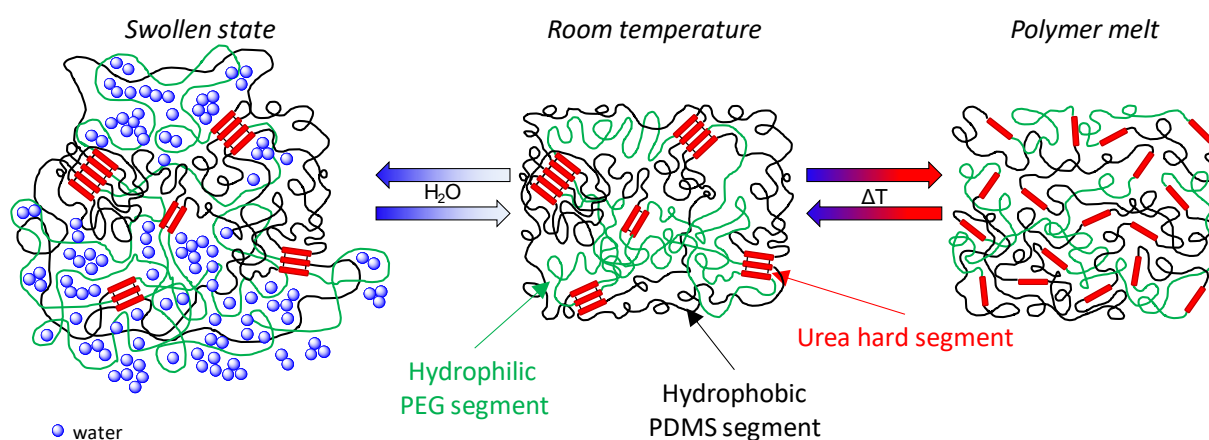
Figure 4.7: Schematic illustration of the (ABAC)$_n$ segmented amphiphilic, physically crosslinked copolymers. At room temperature (center) the urea units aggregate into hard segment domains (red bars) which are randomly distributed in the soft segment matrix. These consist of hydrophilic PEG (green) and amorphous, hydrophobic PDMS (black) segments. Upon storing in water (left) it partially swells depending on the amount of hydrophilic PEG and its chain length. In detail the hydrophilic PEG segments extend due to water absorption, whereas the PDMS remains unaffected because of its hydrophobic character. Intact physical crosslinks and phase separated PDMS and PEG segments, prevent the hydrogel from falling apart. Upon heating the amphiphilic copolymer (right), the hard segments disaggregate and the material becomes a processable melt.

The amphiphilic nature of these copolymers allows fine-tuning of hydrogel properties by simply varying the chain length of the hydrophilic segment but additionally, and more pronounced, by adjusting the ratio of hydrophobic and hydrophilic segments. PDMS is incorporated to improve the mechanical properties due to microphase separation of the hydrophobic PDMS and hydrophilic PEG segments and

to influence the swelling capacity of the hydrogel. Due to the selection of PDMS, PEG and urea segments these materials should be biocompatible.

Within this chapter this new class of amphiphilic, physically crosslinked copolymers will be synthesized and thoroughly characterized concerning their material and hydrogel properties. Short chain diamino terminated PDMS with a molecular weight of about 1500 g mol^{-1} and *1,6-hexamethylene diisocyanate* (HMDI) are selected as hydrophobic soft and hard segments, since poly(urea-siloxane) **1a** featured excellent mechanical strength and a rapid solidification upon cooling as discussed within chapter 3.2. The molecular weight of the hydrophilic diamino terminated PEG is varied using molecular weights of 1.2 kg mol^{-1} (1k), 2.2 kg mol^{-1} (2k) and 4.0 kg mol^{-1} (4k). In addition, the built-in ratio of hydrophobic PDMS and hydrophilic PEG segment is varied. Furthermore, a commercially available PEG based derivate with telechelic poly(propylene oxide) (PPO) segments and terminal amine groups (Jeffamine ED 900, M_n = 894 g mol^{-1}) is incorporated. The main material focus is on the thermal and rheological properties which are of importance regarding melt processing, as well as on the hydrogel properties and the correlation between water uptake and gel stability.

4.2.1. Synthesis

Synthesis of (ABAC)$_n$ segmented copolymers with PEG segments of different length

The synthesis of amphiphilic copolymers is based on the polyaddition reaction of a diisocyanate with a hydrophobic PDMS-diamine and a hydrophilic PEG-diamine, whereby a urea unit is formed. Mechanical and hydrogel properties will be investigated as function of different ratios of the hydrophobic PDMS and hydrophilic PEG content. Moreover, the chain length of the PEG-diamine is varied to analyze the influence on the water uptake of the systems as well as the melt behavior.

The synthesis of the (ABAC)$_n$ segmented copolymers is shown in Scheme 4.1. PEG-diamines were synthesized via an amination of a dihydroxy terminated PEG in our group with a molecular weight of 1223 (y = 26), 2191 (y = 48), and 3961 g mol^{-1} (y = 88) (determined by potentiometric amine end group titration). They are denoted in the following as PEG$_{1k}$, PEG$_{2k}$ and PEG$_{4k}$. The synthetic procedure is included in chapter 5.4.1. In addition, the commercial available PDMS-diamine with the shortest chain length (M_n = 1513 g mol^{-1}, x = 18) and the aliphatic *1,6-hexamethylene diisocyanate* (HMDI) are employed for the synthesis of the (ABAC)$_n$ segmented copolymers. As discussed in chapter 3 and 3.3 (AB)$_n$ segmented copolymers based on these two monomers show mechanical stability, excellent melt processing properties and fast solidification upon cooling which is also desirable for the (ABAC)$_n$ segmented copolymers. The degree of polymerization of the (ABAC)$_n$ segmented copolymers was regulated with a small amount of benzylamine (Bz-NH$_2$) serving as monofunctional reagent to control the molecular weight with respect to melt processability. During the reaction the isocyanate conversion was analyzed by FT-IR spectroscopy. After the reaction was completed the reaction solution was cast into Teflon$^\circledR$ molds and the solvent (THF) was evaporated under ambient conditions.
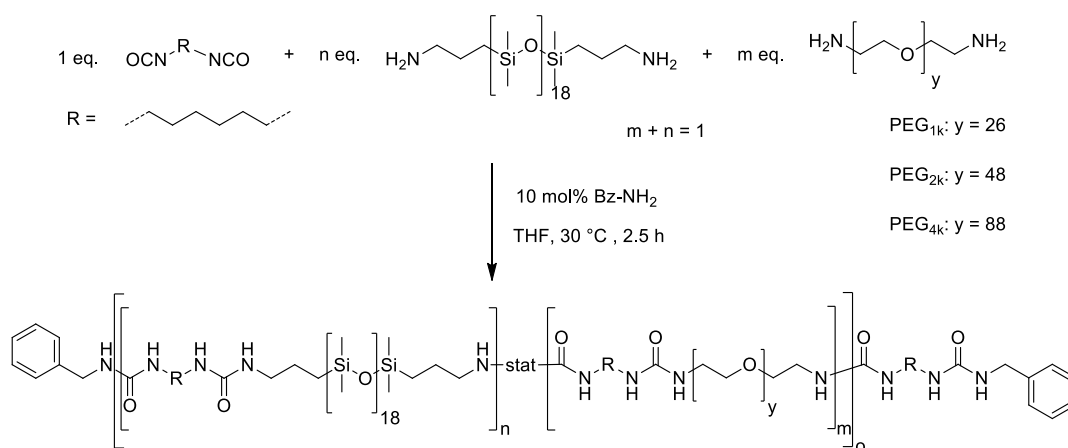
Scheme 4.1: Synthesis of (ABAC)$_n$ segmented **PDMS-PEG$_{1k, 2k, 4k}$** copolymers. The synthesis is based on the PDMS-diamine with a molecular weight of 1513 g mol^{-1} (x = 18) and three different PEG-diamines with molecular weights of about 1.2 kg mol^{-1} (y = 26), 2.2 kg mol^{-1} (y = 48) and 4.0 kg mol^{-1} (y = 88) and *1,6-hexamethylene diisocyanate* (HMDI). Copolymers with different ratios of PDMS-diamine to PEG-diamine were synthesized (Table 4.1).

Transparent films were obtained for all PDMS-PEG$_{1k}$ copolymers. The film of **PDMS-PEG$_{2k}$ (85/15)** is transparent, whereas with higher PEG$_{2k}$ content (> 57 wt.%) the films turned turbid. With PEG$_{4k}$ films

are also turbid due to crystallization of the PEG chains. Except at an 8 wt.% PEG_{4k} content, the film appears transparent due to the majority of the amorphous PDMS phase.

Synthesis of (ABAC)$_n$ segmented copolymers with Jeffamine ED 900

In addition, a commercial available PEG-derivate flanked with PPO-diamine units on each side, Jeffamine ED 900, with a molecular weight of M_n = 894 g mol^{-1} (determined by potentiometric amine end group titration) was used as hydrophilic soft segment. Jeffamine ED 900 was selected because it is more difficult to crystallize (T_m = 22.7 °C) in contrast to the PEG-based system of similar length (T_m = 42 °C). The polyaddition reaction (Scheme 4.2) is conducted analogous to the before presented synthesis based on PEG-diamines, with the only exception of an increased reaction time of four hours (Scheme 4.2).
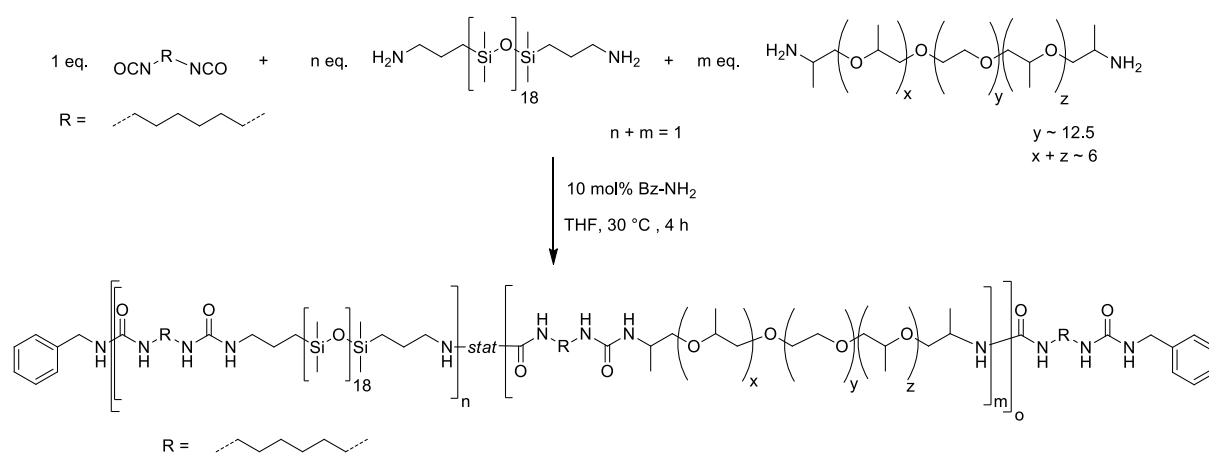
Scheme 4.2: Synthesis of amphiphilic, physically crosslinked **PDMS-Jeffamine** copolymers. The polyaddition is based on the PDMS-diamine with a molecular weight of 1513 g mol^{-1} (x = 18), Jeffamine ED 900 (M_n = 894 g mol^{-1}) and *1,6-hexamethylene diisocyanate* (HMDI). Copolymers with different ratios of PDMS-diamine to Jeffamine ED 900 were synthesized (Table 4.1).

After evaporation of the solvent transparent elastic films were obtained. Yet the amphiphilic copolymer based on the highest Jeffamine content (78 wt.%) appears slightly turbid.

Nomenclature: In the following the amphiphilic copolymers are denoted as **PDMS-PEG$_y$ (n/m)** or **PDMS-Jeffamine (n/m)**. **PDMS** representing the PDMS-diamine with the shortest chain length (M_n = 1513 g mol^{-1}, x = 18) and **PEG$_y$** represents the used PEG-diamines PEG_{1k} (y = 26), PEG_{2k} (y = 48) or PEG_{4k} (y = 88) while **Jeffamine** stands for Jeffamine ED 900. **(n/m)** indicates the built-in ratio of PDMS to PEG or PDMS to Jeffamine given in wt.%. As an example, **PDMS-PEG$_{1k}$ (93/7)** describes the (ABAC)$_n$ segmented amphiphilic copolymer based on *1,6-hexamethylene diisocyanate* (HMDI), the PDMS-diamine (M_n = 1513 g mol^{-1}) and PEG_{1k} with a built-in ratio of 93 wt.% PDMS to 7 wt.% PEG_{1k}.

4.2.2. Characterization

The copolymers based on the different PEG-diamines were synthesized with three different feed-ratios of PDMS to PEG, namely 90/10, 50/50 and 10/90 (mol%/mol%). The built-in ratios were determined via ^{1}H-NMR spectroscopy and are summarized in Table 4.1. In all cases the built-in ratios are in good agreement with the feed-ratios. The built-in ratio of the amphiphilic copolymer **PDMS-PEG$_{1k}$ (10/90)** could not be determined due to insolubility in CDCl$_3$. ^{1}H-NMR spectra of **PDMS-PEG$_{1k}$ (59/41)**, **PDMS-PEG$_{2k}$ (43/57)**, **PDMS-PEG$_{4k}$ (30/70)** and **PDMS-Jeffamine (62/38)** are depicted in the appendix (Figure A-6.17 – Figure A-6.20). All proton signals are in agreement with the copolymer structure.

Table 4.1: Feed- and built-in ratios (PDMS/PEG) of amphiphilic copolymers based on *1,6-hexamethylene diisocyanate* (HMDI) determined by ^{1}H-NMR as well as the SEC results.

Copolymer	Feed-ratio (mol%)	Built-in ratio[a] (mol%)	Built-in ratio[a] (wt.%)	$\overline{M_n}$ [b] (kg mol^{-1})	$\overline{M_w}$ [b] (kg mol^{-1})	Đ[b]
PDMS-PEG$_{1k}$	100/0[c]	100/0	**100/0**	73	115	1.6
	90/10	91/9	**93/7**	44	79	1.8
	50/50	54/46	**59/41**	52	225	4.3
	10/90	n.a.[d]	n.a.[d]	n.a.[e]	n.a.[e]	n.a.[e]
	0/100	0/100	**0/100**	n.a.[e]	n.a.[e]	n.a.[e]
PDMS-PEG$_{2k}$	100/0[c]	100/0	**100/0**	73	115	1.6
	90/10	89/11	**85/15**	17	43	2.5
	50/50	52/48	**43/57**	64	190	3.0
	10/90	16/84	**12/88**	77	253	3.3
	0/100	0/100	**0/100**	59	251	4.2
PDMS-PEG$_{4k}$	100/0[c]	100/0	**100/0**	73	115	1.6
	90/10	90/10	**77/23**	44	81	1.8
	50/50	53/47	**30/70**	52	73	1.9
	10/90	21/79	**9/91**	104	237	2.3
	0/100	0/100	**0/100**	23	49	2.1
PDMS-Jeffamine	100/0[c]	100/0	**100/0**	73	115	1.6
	90/10	87/13	**92/8**	35	61	1.8
	50/50	49/51	**62/38**	31	56	1.8
	10/90	14/86	**22/78**	47	68	1.5
	0/100	0/100	**0/100**	30	51	1.7

[a] The built-in ratio of PDMS/PEG was determined from ^{1}H-NMR spectra based on the integrals of the signal at 3.65 ppm and 0.08 ppm. The calculation is included in the appendix 6 (equation **(6.1)** and **(6.2)**).
[b] Determined by SEC, eluent: THF with 0.25 wt.% tetrabutylammonium bromide, $\overline{M_n}$ and $\overline{M_w}$ were calculated based on a polystyrene calibration. Đ = $\overline{M_w}$ / $\overline{M_n}$.
[c] The copolymers **PDMS-PEG$_{1k, 2k, 4k}$ (100/0)** and **PDMS-Jeffamine (100/0)** are the same as **1a** from chapter 3.2.
[d] Insufficient solubility in CDCl$_3$ for ^{1}H-NMR.
[e] Insufficient solubility in THF with 0.25 wt.% tetrabutylammonium bromide for SEC.

FT-IR spectroscopy

The FT-IR spectra of **PDMS-Jeffamine (92/8)** and **PDMS-Jeffamine (22/78)** are plotted in Figure 4.8. The complete conversion of the diisocyanate is quantified by the absence of the NCO vibration at 2270 cm^{-1}. The N-H and C=O signals confirm the formation of the urea unit. All signals are assigned to respective vibrations which correspond to the signals described in chapter 3.2.2. Additionally, the C-O-C vibration at 1088 cm^{-1} of the PEG block is observed. Depending on the built-in ratio of PDMS to Jeffamine the intensities of the C-O-C and Si-O-Si vibration change.
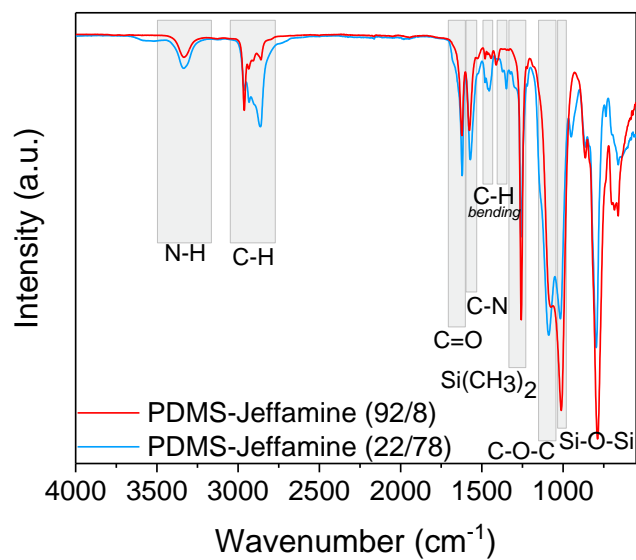
Figure 4.8: FT-IR spectra of **PDMS-Jeffamine (92/8)** and **PDMS-Jeffamine (22/78)**. Signals are assigned to the vibrations typical for the urea units. The ratio of the C-O-C and Si-O-Si vibrations change with varying amounts of PDMS to Jeffamine.

Analyzing the strength of the hydrogen bond interactions reveals information about the kind and extend of the hydrogen bonding between the copolymer chains. Completely free and disordered hydrogen bonding N-H and C=O vibration exhibit characteristic wavenumbers at 3450 cm^{-1} and 1690 cm^{-1}, respectively. Weak H-bonding shift to higher wavenumbers, 3350 cm^{-1} and 1640 cm^{-1}. Strong H-bonded units are typically at 3325 cm^{-1} and 1615 cm^{-1} for N-H and C=O vibration.[76] The characteristic wavenumbers of all amphiphilic copolymers are listed in Table 4.2 identifying them all as hydrogen bonded. While the amphiphilic copolymers based on PDMS-PEG$_{1k}$ show a slightly increased hydrogen bonding strength with increasing PEG content, the two systems with longer PEG chain length, PDMS-PEG$_{2k}$ and PDMS-PEG$_{4k}$, show weaker hydrogen bonding with increasing PEG content. The copolymers behave differently depending on the PEG chain length. PDMS-PEG$_{1k}$ copolymers feature a comparable shorter PEG chain length resulting in a higher overall urea content, with an increasing chance that the urea units can form multiple hard segment domains explaining the stronger hydrogen bonding with increasing PEG$_{1k}$ content. With increasing PEG chain length (PEG$_{2k, 4k}$) the urea units are diluted and the chance of forming hydrogen bonding is reduced. Owed to a decreasing probability the total hydrogen bonding strength decreases slightly, too. The PDMS-Jeffamine systems show like PDMS-PEG$_{1k}$ slightly increased hydrogen bonding strength with increasing

134

Jeffamine content. This is also due to the higher urea content within the system. However, the hydrogen bonding strength is slightly weaker compared to PDMS-PEG$_{1k}$ copolymers. This may be explained by the steric hindrance induced by the PPO units.

Table 4.2: Wavelength of N-H and C=O vibrations determined by FT-IR giving an insight to the hydrogen bonding strength of the (ABAC)$_n$ segmented copolymers. The vibrations of free hydrogen bonding units can be assigned to 3400 cm^{-1} for υ_{N-H} and to 1690 cm^{-1} for $\upsilon_{C=O}$. The υ_{N-H} is between 1615 – 1640 cm^{-1} and $\upsilon_{C=O}$ between 3325 – 3350 cm^{-1} for hydrogen bonded units. Stronger H-bonding shift to lower wavenumbers while weaker ones shift to higher wavenumbers.

PDMS-PEG$_{1k}$			PDMS-PEG$_{2k}$		
PEG$_{1k}$ content (wt.%)	υ_{N-H}[a] (cm^{-1})	$\upsilon_{C=O}$[a] (cm^{-1})	PEG$_{2k}$ content (wt.%)	υ_{N-H}[a] (cm^{-1})	$\upsilon_{C=O}$[a] (cm^{-1})
0	3334	1625	0	3334	1625
7	3333	1624	15	3335	1624
41	3336	1622	57	3339	1626
90[b]	3337	1621	88	3342	1619
100	3336	1618	100	3366	1643

PDMS-PEG$_{4k}$			PDMS-Jeffamine		
PEG$_{4k}$ content (wt.%)	υ_{N-H}[a] (cm^{-1})	$\upsilon_{C=O}$[a] (cm^{-1})	Jeffamine content (wt.%)	υ_{N-H}[a] (cm^{-1})	$\upsilon_{C=O}$[a] (cm^{-1})
0	3334	1625	0	3334	1625
23	3334	1624	8	3334	1623
70	3341	1629	38	3333	1621
91	3365	1644	78	3335	1621
100	3367	1644	100	3337	1620

[a] FT-IR spectroscopy of dry, solution cast films utilizing the ATR unit.
[b] Theoretical PEG content due to insufficient solubility for ^{1}H-NMR.

Size exclusion chromatography

In Figure 4.9 the SEC chromatograms of the *PDMS-Jeffamine copolymers* are depicted after synthesis and after purification by extraction in water. Reference material **PDMS-Jeffamine (100/0)**, equivalent to **1a**, was already discussed in chapter 3.2.2. The PEG-urea polymers **PDMS-PEG$_{2k}$ (0/100)**, **PDMS-PEG$_{4k}$ (0/100)** and **PDMS-Jeffamine (0/100)** were purified by dialysis in DI water and water soluble low molecular weight residuals such as unreacted PEG-diamines and oligomers removed. After this purification step a monomodal molecular weight distribution is observed. The results of the purified amphiphilic copolymers are summarized in Table 4.1. With increasing PEG content, the molecular weight increases due to a higher molecular weight of the PEG-diamine compared to the PDMS-diamine assuming a similar degree of polymerization. Also with increasing PEG chain length the overall molecular weight increases owed to the higher molecular weight of the PEG-diamine compared to PDMS-diamine. Only for copolymer **PDMS-PEG$_{1k}$ (10/90)** and its reference material **PDMS-PEG$_{1k}$ (0/100)** no SEC data could be measured due to the insolubility in THF. However, PDMS-Jeffamine copolymers show a lower molecular weight even with higher Jeffamine content ranging from

35 kg mol^{-1} to 47 kg mol^{-1} for **PDMS-Jeffamine (92/8)** and **PDMS-Jeffamine (22/78)**, respectively. The dispersity *Đ* is also quite narrow with 1.8 for PDMS-Jeffamine copolymers. For the nine PDMS-PEG$_{1k, 2k, 4k}$ copolymers the dispersities increase in the range from Đ = 1.8 to Đ = 4.3 and significantly broader molecular weight distributions are obtained. This is due to the molecular weight distribution of the PEG-diamine starting material possessing a rather broad and bimodal distribution with a small shoulder at the double molecular weight. In contrast Jeffamine ED 900 has a narrow, monomodal distribution with Đ = 1.2.
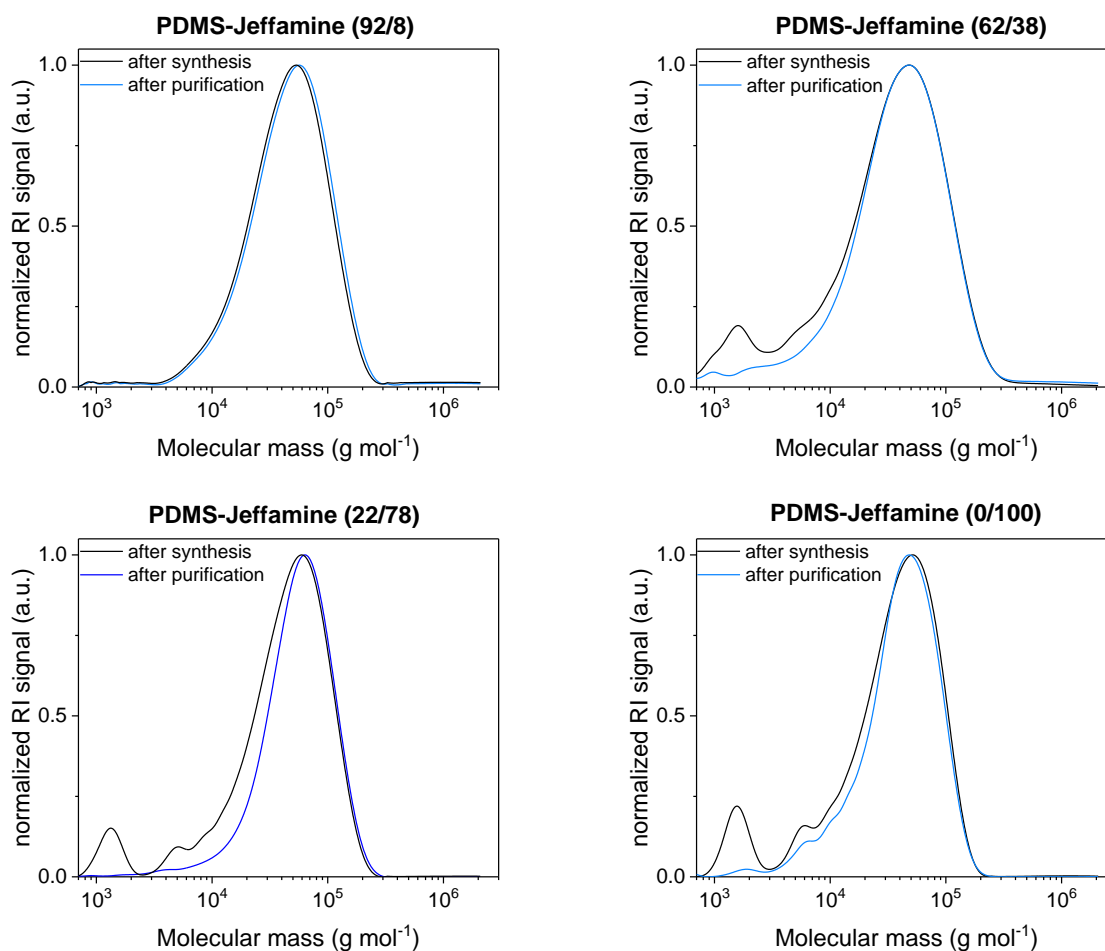
Figure 4.9: SEC chromatograms after synthesis (black) and after purification (blue) of PDMS-Jeffamine copolymers with different built-in ratios of 92/8, 62/38 and 22/78 (wt.%/wt.%) and its reference material **PDMS-Jeffamine (0/100)**. Traces of low molecular weight side products and monomer residuals were removed by water extraction. The reference material **PDMS-Jeffamine (0/100)** was purified by dialysis in DI water.

4.2.3. Thermal properties

Differential scanning calorimetry

The *telechelic PEG-diamines* show an increasing melting point with increasing PEG chain length ranging from 42 °C to 58 °C as listed in Table 4.3. In contrast, Jeffamine ED 900 exhibits a melting point at 23 °C which is lower compared to PEG$_{1k}$-diamine with a similar molecular weight due to the PPO units. The increased crystallinity of the PEG-diamines is further indicated by an increasing melt enthalpy ΔH_m with longer PEG chain length. Upon cooling a supercooled crystallization is observed with crystallization temperatures around 23 to 34 °C for the PEG-diamines and -5 °C for Jeffamine ED 900.

Table 4.3: DSC data of neat PEG$_{1k, 2k, 4k}$-diamines and Jeffamine. Data of 2nd heating and cooling cycle are given.

PEG-diamine	T_m (°C)[a]	ΔH_m (Jg^{-1})[a]	$T_{cryst.}$ (°C)[a]	ΔH_c (Jg^{-1})[a]
PEG$_{1k}$-diamine	41.5	147.5	22.7	-135.4
PEG$_{2k}$-diamine	55.6	160.3	32.3	-155.1
PEG$_{4k}$-diamine	58.1	162.8	33.8	-160.1
Jeffamine ED-900	22.7	106.4	-4.5	-85.5

[a] Determined by DSC with a heating/cooling rate of 10 K min^{-1}.

The DSC measurements of the *(ABAC)$_n$ segmented copolymers* with different ratios of PDMS to PEG and PDMS to Jeffamine are shown in Figure 4.10. It can be seen that for almost all PEG based systems the distinct melting point of the crystalline PEG block $T_{m, PEG}$ is observed. Solely for **PDMS-PEG$_{1k}$ (93/7)** no melting point was detected which can be explained by the short PEG chain length and the low content of 7 wt.% within this copolymer. However, the observed $T_{m, PEG}$ are significantly lower compared to the PEG-diamine monomers. The melting points of **PDMS-PEG$_{1k}$ (59/41)** was found to be at 11.6 °C and for **PDMS-PEG$_{1k}$ (10/90)** at 19.5 °C. Here the PEG$_{1k}$ content increases from 41 wt.% to 90 wt.%. The reference material **PDMS-PEG$_{1k}$ (0/100)** shows a melting temperature of 28 °C which is also a significantly lower $T_{m, PEG}$ compared to the telechelic PEG-diamine (T_m = 41.5 °C) which shows that the aggregated urea units in the (ABAC)$_n$ segmented copolymer hinder the PEG crystallization. The PEG crystallization at lower PEG content is additionally disturbed by the amorphous PDMS segments within the copolymer backbone, reducing also the degree of crystallization. The crystallization temperatures T_{cryst} show the reverse behavior, with lower PEG$_{1k}$ content the T_{cryst} decreases even further. The crystallization is prolonged by an increasing content of amorphous PDMS while at higher PEG$_{1k}$ content it crystallizes faster due to less interruption by the PDMS phase. Further it is observed that with increasing PEG$_{1k}$ content the melt enthalpy as well as the crystallization enthalpy increases due to a larger amount of meltable and crystallizable PEG units. With increasing PEG chain length, the same trend as for PEG$_{1k}$ can be seen. For PDMS-PEG$_{2k}$ copolymers the melting temperatures of the PEG segment increases from 34 °C for **PDMS-PEG$_{2k}$ (85/15)** to 43 °C for **PDMS-PEG$_{2k}$ (0/100)**. For PDMS-PEG$_{4k}$ copolymers an increase from 46 °C for **PDMS-PEG$_{4k}$ (77/23)** to 56 °C for **PDMS-PEG$_{4k}$ (0/100)** is

observed. The effect of a reduced melting point compared to neat PEG-diamine is less pronounced for PEG$_{4k}$ showing that with increasing PEG chain length the crystallization is facilitated regardless a second amorphous phase.

A different behavior is observed for PDMS-Jeffamine copolymers, no crystallization of the PEG unit can be detected. Due to the PPO units at both ends of the central PEG unit and the presence of aggregated urea units as well as amorphous PDMS segments within the backbone of the copolymer, the overall crystallization of the Jeffamine is suppressed. However, weak and very important broad transitions at higher temperatures around 83 °C are observed which are assigned to the hard segment disaggregation (melting) as discussed earlier in chapter 3.2.3 for the poly(urea-siloxane)s.
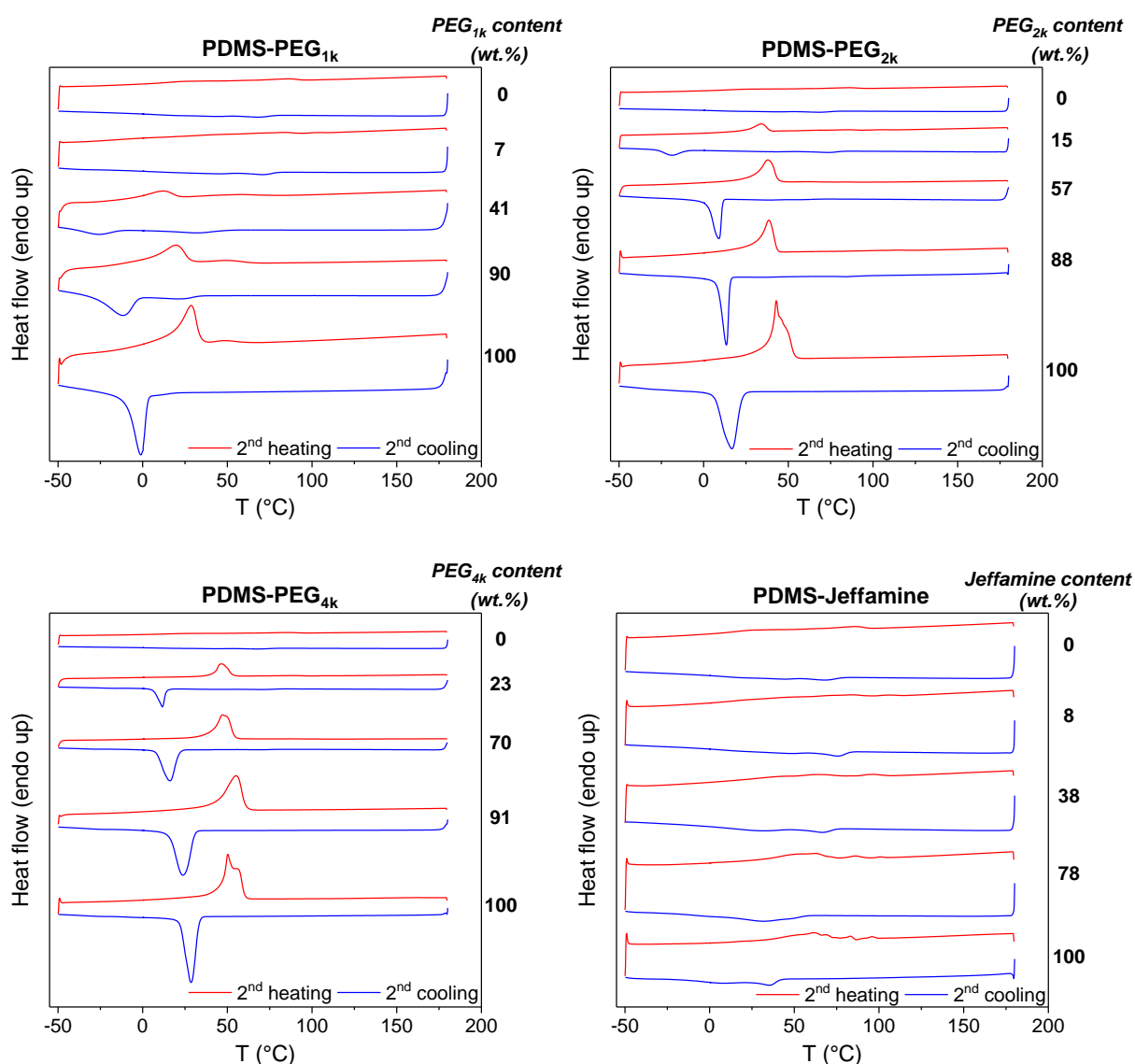
Figure 4.10: DSC curves of the (ABAC)$_n$ segmented copolymers with different compositions of hydrophobic to hydrophilic segments based on the different PEG diamines (PEG$_{1k}$, PEG$_{2k}$ and PEG$_{4k}$) and Jeffamine. With increasing PEG content all copolymers show an increasing melt enthalpy ΔH_m. The melting temperatures are not significantly influenced by the different ratio of PDMS to PEG. 2nd heating / cooling curves are shown (heating and cooling rate: 10 K min^{-1}).

A closer look at the DSC data show that next to the PEG melting point weak and broad multistep transitions can be observed. In Figure 4.11 these additional melting signals are shown in magnification. of PDMS-PEG copolymers with the lowest PEG content. As discussed previously, a broad transition at 57 °C was observed for poly(urea-siloxane) **PDMS-PEG (100/0)** attributed to the hard segment disaggregation (compare Figure 3.8 in chapter 3.2.3). Based on these results the additional transitions within the amphiphilic copolymers, which are around 85 °C, are assigned to the urea hard segment transition. It is noticeable that for **PDMS-PEG$_{4k}$ (9/91)** and the reference polymers **PDMS-PEG$_{2k}$ (0/100)** and **PDMS-PEG$_{4k}$ (0/100)** no such transition was observed.
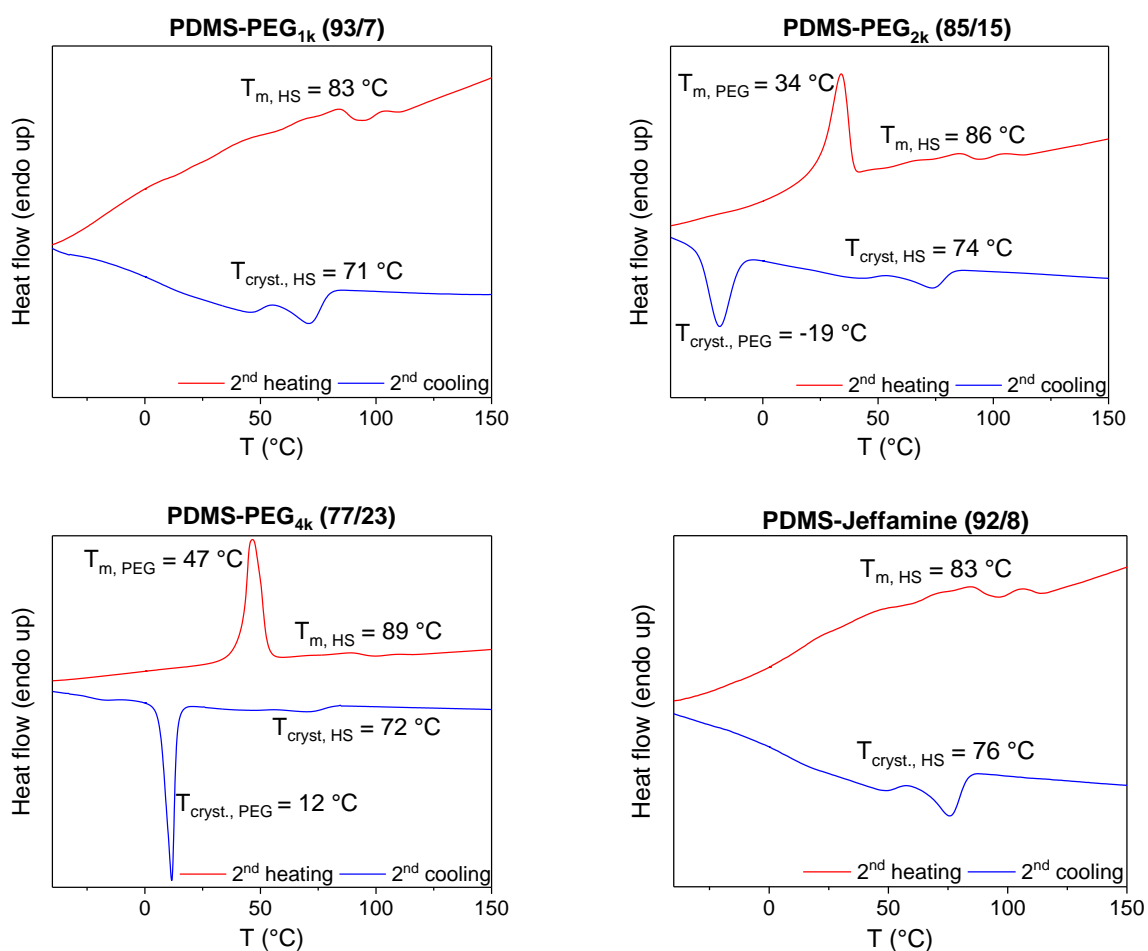
Figure 4.11: Magnification of DSC curves of the (ABAC)$_n$ segmented copolymers with 7, 15 and 23 wt.% hydrophilic PEG$_{1k, 2k, 4k}$ content and 8 wt.% Jeffamine content. The weak signals around 85 °C are attributed to the hard segment disaggregation upon heating and their aggregation upon cooling. 2nd heating/cooling curves are shown (heating and cooling rate: 10 K min^{-1}).

All DSC data including melt temperature of the PEG unit ($T_{m, PEG}$), its melting enthalpy ($\Delta H_{m, PEG}$) as well as the melting temperature of the hard segments ($T_{m, HS}$) with their respective melt enthalpies ($\Delta H_{m, HS}$) and the crystallization behavior are summarized in the appendix in Table A-6.1.

Polarized optical light microscopy

The crystallinity of the amphiphilic copolymers was investigated by polarized optical light microscopy. The copolymers were heated from 30 °C to 60 °C with a heating rate of 10 K min^{-1}. In Figure 4.12 the polarized optical light microscopy images of PDMS-PEG$_{2k}$ copolymers are shown upon heating. Poly(urea-siloxane) **PDMS-PEG$_{2k}$ (100/0)** does not show any birefringence neither at 30 °C nor at 60 °C owed to the amorphous PDMS matrix and nano-sized hard segment domains which are too small to be detectable by polarized optical light microscopy. For the copolymer **PDMS-PEG$_{2k}$ (85/15)** no birefringence was detected at 30 °C due to extremely small PEG crystal domains which cannot be visualized by polarized optical light microscopy. However, DSC measurements showed a melting point of the PEG crystals. With increasing PEG$_{2k}$ content (**PDMS-PEG$_{2k}$ (43/57)** and **PDMS-PEG$_{2k}$ (12/88)**) the material shows birefringence at 30 °C resulting from the PEG crystallization. Upon heating, the PEG crystallites melt at around 42 °C and an isotropic melt is obtained. Upon cooling the reverse behavior is observed (not shown). The melting temperatures determined by polarized optical light microscopy are about 4 °C higher than determined by DSC which can be explained by the fact that for the DSC the maximum of the melting signal is evaluated while with the polarized optical light microscopy the final melting of the crystals is detected. The reference material **PDMS-PEG$_{2k}$ (0/100)** also shows birefringence at 30 °C with a transition into an isotropic melt at 43 °C.

For the other amphiphilic copolymers **PDMS-PEG$_{1k}$ (93/7)** and **PDMS-PEG$_{1k}$ (59/41)** no PEG crystallization was observed at 30 °C (appendix Figure A-6.21). Concluding from DSC data, **PDMS-PEG$_{1k}$ (93/7)** did not show any PEG melting and the melting temperature of **PDMS-PEG$_{1k}$ (59/41)** is significantly lower at 12 °C. Only for **PDMS-PEG$_{1k}$ (10/90)** the crystallinity at 30 °C could be visualized with a transition to an isotropic phase at 43 °C. The reference material **PDMS-PEG$_{1k}$ (0/100)** also shows birefringence at 30 °C, however it does not form an isotropic melt at 60 °C or even higher temperatures.

Amphiphilic copolymers based on PDMS-PEG$_{4k}$ show a similar behavior to PDMS-PEG$_{2k}$ copolymers with higher melting temperatures at about 49 °C (appendix Figure A-6.22). For none of the amphiphilic copolymers the disaggregation of the hard segments could be visualized by optical light microscopy owed to their size being smaller than the visible light wavelength.
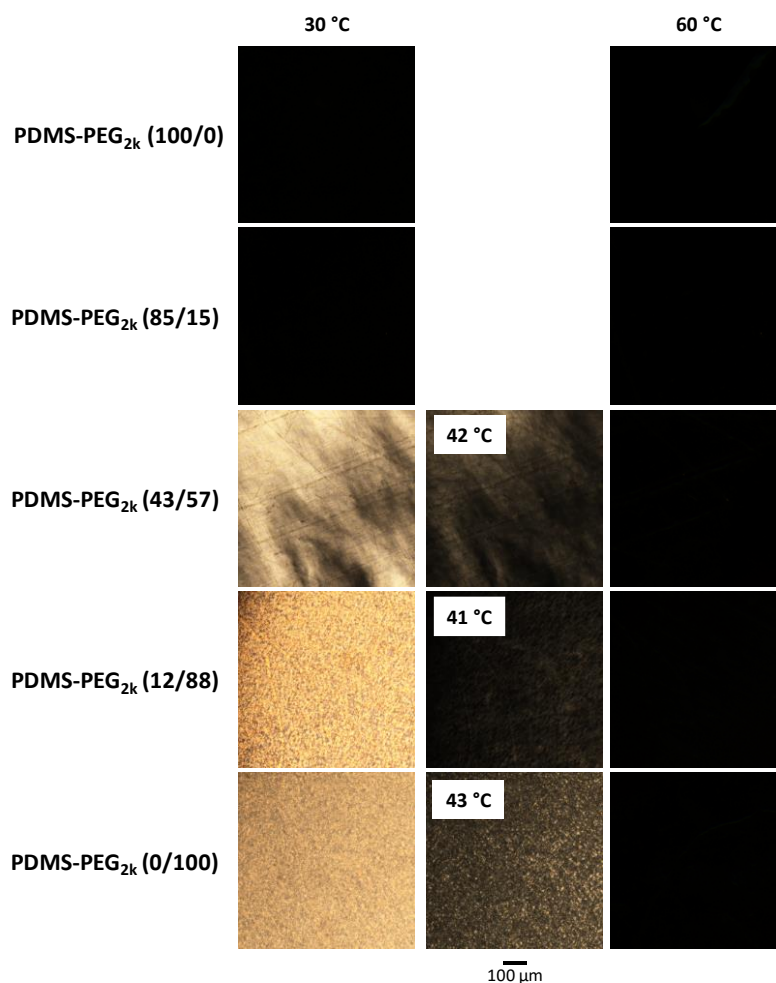
Figure 4.12: Polarized optical light microscopy images upon heating (10 K min⁻¹) of reference materials **PDMS-PEG$_{2k}$ (100/0)** and **PDMS-PEG$_{2k}$ (0/100)** as well as of PDMS-PEG$_{2k}$ copolymers with different ratios of PDMS to PEG$_{2k}$. **PDMS-PEG$_{2k}$ (100/0)** is completely amorphous, while with increasing PEG$_{2k}$ content the PEG crystallinity is observed. Melting of the PEG$_{2k}$ block occurs around 42 °C which is significantly lower than for neat PEG$_{2k}$-diamine with T_m = 56 °C.

For the PDMS-Jeffamine copolymers no PEG crystallization could be detected by DSC. Only weak and broad transitions upon heating were observed owed to the hard segment disaggregation. In the polarized light microscopy at 30 °C each composition of PDMS-Jeffamine is completely amorphous, upon heating to 60 °C no change is observed, and a completely isotropic melt was obtained.

Rheological properties

Knowledge about rheological properties are important for optional melt processing. Thus oscillating shear rheology measurements were conducted investigating the transition temperature between the elastic and viscous behavior as well as the melt viscosity as function of the temperature. As discussed in chapter 3.2.3, owed to the thermal stability of the materials mainly influenced by the urea back reaction, no temperatures higher than 140 °C are employed to preserve the material properties. Oscillating shear rheology measurements were conducted of the *(ABAC)$_n$ segmented PDMS-PEG$_{1k, 2k, 4k}$ copolymers* **PDMS-PEG$_{1k}$ (93/7)**, **PDMS-PEG$_{2k}$ (85/15)** and **PDMS-PEG$_{4k}$ (77/23)**. Samples prepared from the solution cast films were heated in the rheometer to 140 °C prior measurement (1st heating). Subsequently the storage *G'* and loss modulus *G''* of 1st cooling, followed by 2nd heating are measured. The results are shown in Figure 4.13. With an increasing PEG chain length, the storage modulus *G'* and loss modulus *G''* at 140 °C increase. The storage modulus increases from 160 Pa over 420 Pa to 1280 Pa comparing the PEG$_{1k, 2k, 4k}$ based copolymers. This can be explained by an increasing restriction of chain mobility as a consequence of the incompatibility of the PDMS and PEG phases. Upon cooling the three copolymers show a similar trend.
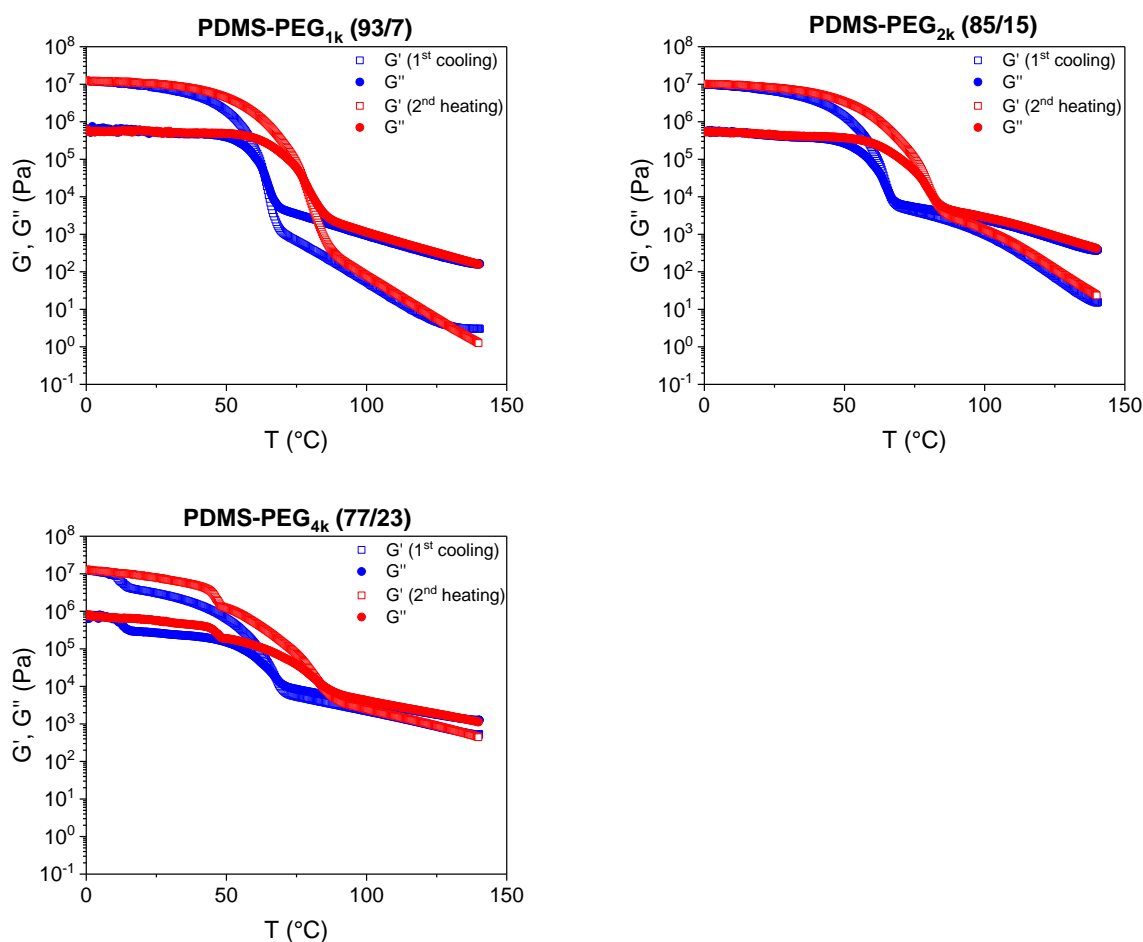
Figure 4.13: Oscillating shear rheology measurements of **PDMS-PEG$_{1k}$ (93/7)**, **PDMS-PEG$_{2k}$ (85/15)** and **PDMS-PEG$_{4k}$ (77/23)**. A cooling/heating rate of 2 K min^{-1} and a frequency of 1 Hz were applied. Shear storage G' and loss modulus G'' of 1st cooling and 2nd heating are shown as a function of temperature.

Initially the moduli increase moderately before a steep increase is observed combined with the crossover of the storage and the loss modulus. This effect is assigned to the HMDI hard segment aggregation. The crossover temperature T_{cross} for all three polymers was determined between 63 °C and 68 °C. At temperatures lower than about 50 °C the moduli reach a plateau. For **PDMS-PEG$_{4k}$ (77/23)** the PEG crystallization is observed between 15 °C and 10 °C shown by a steep and increased moduli. For the other two systems with shorter PEG chains, **PDMS-PEG$_{1k}$ (93/7)** and **PDMS-PEG$_{2k}$ (85/15)**, it is not detected. The crystallization takes place below 0 °C as shown by DSC which is not within the temperature range used for the rheological measurements. At 0 °C the moduli for both copolymers are similar at G' = 0.6 MPa and G'' = 10 MPa. Upon heating, the materials show the reverse behavior with a typical hysteresis which was also found earlier in this work typical for HMDI based polymers.

The complex viscosity was determined for the three copolymers at 120 °C ($\eta^*_{120 °C}$). With increasing PEG chain length the viscosity increases from 55 Pa·s over 155 Pa·s to 370 Pa·s for **PDMS-PEG$_{1k}$ (93/7)**, **PDMS-PEG$_{2k}$ (85/15)** and **PDMS-PEG$_{4k}$ (77/23)**, respectively. Since the molecular weight of these copolymers do not differ considerably (Table 4.1), this effect originates from a different behavior such as a restriction of chain mobility and phase separation of the two incompatible hydrophobic and hydrophilic segments in the melt. The complex viscosity as a function of the temperature is shown in the appendix in Figure A-6.23 **(A)**. The rheology data of copolymers **PDMS-PEG$_{1k, 2k, 4k}$** are summarized in Table 4.4.

Table 4.4: Crossover temperature T_{cross} upon 1st cooling and 2nd heating as well as the complex viscosity determined at 120 °C of **PDMS-PEG$_{1k, 2k, 4k}$** copolymers.

Copolymer	T_{cross} (°C)[a] 1st cooling	$T_{cryst. PEG}$ (°C)[a]	T_{cross} (°C)[a] 2nd heating	$T_{m PEG}$ (°C)[a]	$\eta^*_{120 °C}$ (Pa·s)[a]
PDMS-PEG$_{1k}$ (93/7)	63	n.o.[b]	77	n.o.[b]	55
PDMS-PEG$_{2k}$ (85/15)	66	n.o.[b]	82	n.o.[b]	155
PDMS-PEG$_{4k}$ (77/23)	68	12	83	46	370

[a] Determined by oscillating shear rheology measurements with a cooling/heating rate of 2 K min^{-1} and a frequency of 1Hz.
[b] Not observed within the temperature range of the oscillating shear rheology measurements.

It was shown that the copolymers **PDMS-PEG$_{1k}$ (59/41)**, **PDMS-PEG$_{1k}$ (10/90)**, **PDMS-PEG$_{2k}$ (43/57)**, **PDMS-PEG$_{2k}$ (12/88)**, **PDMS-PEG$_{4k}$ (30/70),** and **PDMS-PEG$_{4k}$ (9/91)** were more difficult to characterize by rheology. The loss modulus was determined to be above the storage modulus at 140 °C and 5% shear strain, meaning that the material is still in the elastic and not in the viscous regime. This on the one hand can be attributed to the increased molecular weight and restricted chain mobility due to remaining phase separation. Thus these materials are poor candidates for melt processing techniques with thin capillaries such as extrusion-based 3D printing where low viscous polymer melts (< 250 Pa·s) are required. However, it was shown that these materials still behave thermoplastic since they can be melt processed at 120 °C and 100 bar for 1 min into thin films.

In addition, to gain a closer insight into the thermal properties of the *(ABAC)$_n$ segmented PDMS-Jeffamine copolymers* **PDMS-Jeffamine (92/8)**, **PDMS-Jeffamine (62/38)**, and **PDMS-Jeffamine (22/78)**, oscillating shear rheology measurements were also conducted with these polymers. As can be seen in Figure 4.14 the PDMS-Jeffamine copolymers with different built-in ratios of PDMS to Jeffamine show a similar general behavior as the (ABAC)$_n$ segmented copolymers based on PEG discussed before. However, independent of the copolymer composition they exhibit a viscous behavior (G'' > G') at 140 °C. Upon cooling the moduli increase steadily. Near the transition temperature from a viscous to an elastic behavior (G'' = G') the moduli steeply increase before reaching a plateau. Upon heating an analogous behavior with a hysteresis is observed: Below T_{cross} the storage and loss modulus are running parallel before they abruptly decrease. After the crossover the moduli continuously decrease. For the three investigated built-in ratios the shear storage and loss modulus are in the same order of magnitude at the plateau. The difference occurs at high temperatures when the moduli decrease less with increasing Jeffamine content upon heating. While for **PDMS-Jeffamine (92/8)** G' = 55 Pa and G'' = 0.8 Pa are determined at 140 °C, the moduli increase to G' = 3900 Pa and G'' = 560 Pa for a built-in ratio of 22/78. The crossover temperatures are in the range of 55 – 63 °C upon cooling and show a hysteresis of about 15 °C upon heating, where T_{cross} was determined between 70 – 79 °C. The results are summarized in Table 4.5. The (AB)$_n$ segmented copolymers **PDMS-Jeffamine (100/0)** (Figure 3.11) and **PDMS-Jeffamine (0/100)** show a similar rheological behavior. Upon cooling the storage and loss modulus increase steadily before a steep increase is observed in combination with a crossover temperature ending in a plateau. It is noticeable that the transition temperature of the (AB)$_n$ segmented copolymers are lower than for the (ABAC)$_n$ segmented amphiphilic copolymers. T_{cross} of the (AB)$_n$ segmented poly(urea-siloxane) **PDMS-Jeffamine (100/0)** is observed at 55 °C upon cooling (Table 3.5). **PDMS-Jeffamine (0/100)** shows this transition at 46 °C upon cooling. This is assumed as a result from a single matrix *versus* a matrix with two incompatible segments being chemically crosslinked.
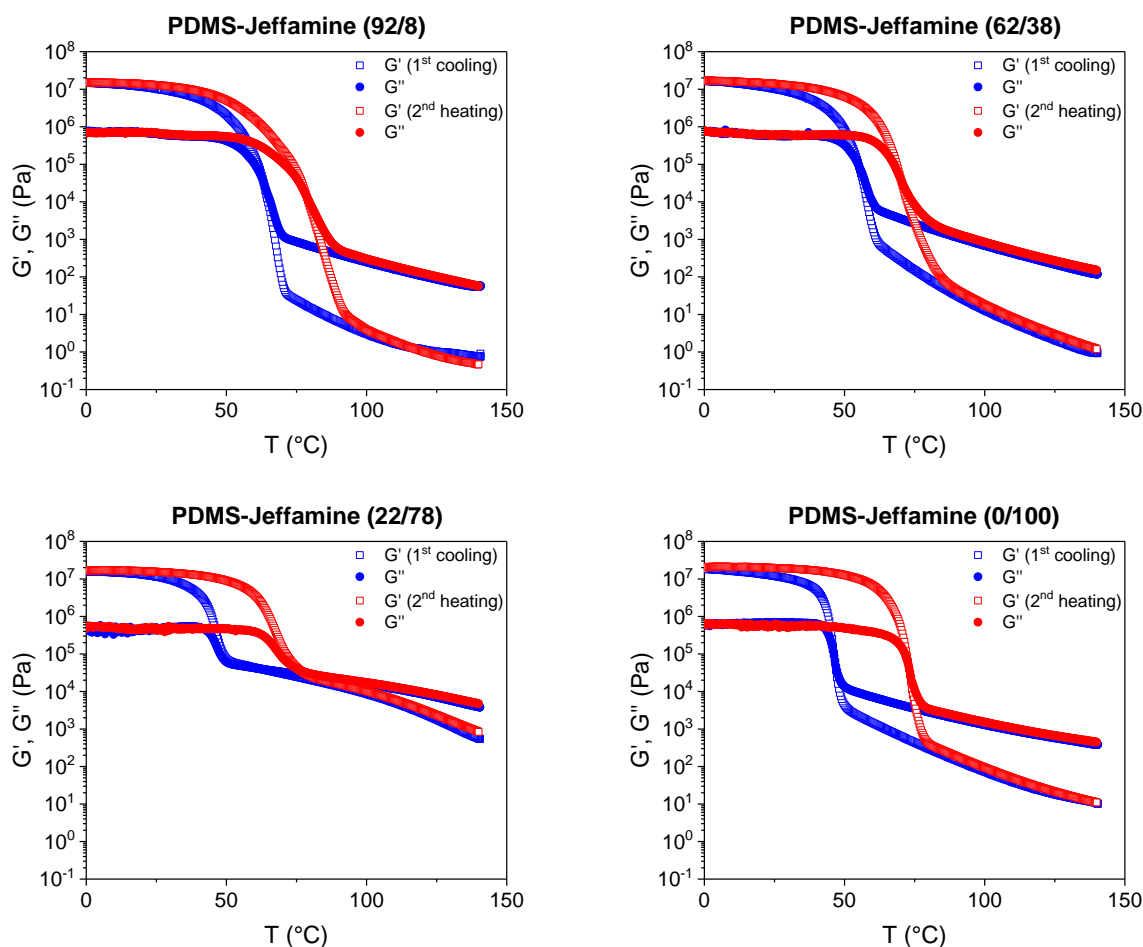
Figure 4.14: Oscillating shear rheology measurements of three PDMS-Jeffamine copolymers with different built-in ratios of PDMS and Jeffamine as well as the reference material Jeffamine-urea **PDMS-Jeffamine (0/100)**. (Reference material **PDMS-Jeffamine (100/0)** can be found in Figure 3.11 as **1a**). A cooling/heating rate of 2 K min⁻¹ and a frequency of 1 Hz were applied. Shear storage *G'* and loss modulus *G''* of 1st cooling and 2nd heating are shown as a function of temperature.

The complex viscosity $\eta*$ of the PDMS-Jeffamine copolymers was determined at 120 °C and compared for the different built-in ratios (Table 4.5). The viscosity increases significantly with increasing amount of Jeffamine. At a built-in ratio of PDMS to Jeffamine of 92/8 a complex viscosity of 17 Pa·s was determined while with a Jeffamine content of 78 wt.% $\eta*_{120 °C}$ dramatically increased to 1425 Pa·s. This dramatic increase cannot solely be explained by an increase in molecular weight from 35 kg mol⁻¹ to 47 kg mol⁻¹ (Table 4.1). These results imply that two incompatible soft segments being chemically bonded via urea units must have an enormous effect on the thermal properties of the amphiphilic copolymers. This influence of the morphology on this phenomenon will be investigated in more detail within the next chapter. The complex viscosities as a function of temperature are shown in the appendix in Figure A-6.23 **(B)**. From previous results based on PDMS-PEG$_{1k, 2k, 4k}$ copolymers, it can be concluded that the ratio of PDMS to PEG has a significant impact on the melting behavior and the viscosity of the material. This trend can also be observed as shown in Figure 4.14 for varying ratios of PDMS to Jeffamine.

Using Jeffamine instead of PEG allows a higher Jeffamine content in the $(ABAC)_n$ segmented copolymers accompanied by a lower melt viscosity. This is attributed to the chemical nature of the telechelic PEG with the short PPO segments. Comparing the results to the reference materials it can be seen that the complex viscosities of **PDMS-Jeffamine (100/0) (1a)** $\eta^*_{120\,°C}$ = 150 Pa·s and **PDMS-Jeffamine (0/100)** $\eta^*_{120\,°C}$ = 105 Pa·s behave differently than for the amphiphilic copolymers (Table 4.5). Both viscosities are at a moderately level allowing melt processing by extrusion based printing techniques. Again this can be related to a matrix based on one phase compared to an incompatible two phase matrix within the amphiphilic PDMS-Jeffamine copolymers.

Table 4.5: Crossover temperature T_{cross} upon 1st cooling and 2nd heating, the complex viscosity determined at 120 °C of PDMS-Jeffamine copolymers and their reference materials, **PDMS-Jeffamine (100/0)** and **PDMS-Jeffamine (0/100).**

Copolymer	T_{cross} (°C)[a] 1st cooling	T_{cross} (°C)[a] 2nd heating	$\eta^*_{120\,°C}$ (Pa·s)[a]
PDMS-Jeffamine(100/0)	55	70	150
PDMS-Jeffamine (92/8)	63	79	17
PDMS-Jeffamine (62/38)	55	70	43
PDMS-Jeffamine (22/78)	62	76	1425
PDMS-Jeffamine (0/100)	46	73	105

[a] Determined by oscillating shear rheology measurements with a cooling/heating rate of 2 K min^{-1} and a frequency of 1Hz.

Dynamic mechanical thermal analysis

In addition, dynamic mechanical thermal analysis was performed to gain more information about the thermo-mechanical behavior of the *$(ABAC)_n$ segmented PDMS-Jeffamine copolymers*. A single cantilever bending geometry was utilized to determine the glass transitions T_g of the soft segments and the transition temperature T_{cross} of the hard segments upon heating. The specimens were prepared from solution cast films. The elastic storage modulus *E'* and *tan δ* are shown as a function of temperature of PDMS-Jeffamine systems in Figure 4.15. It has to be noted that the measured values are not absolute values in Pa but relative arbitrary units (a.u.). The $(AB)_n$ segmented poly(urea-siloxane) **PDMS-Jeffamine (100/0)** was discussed before in Figure 3.15 (referred to as **1a**). First it can be seen that the modulus decreases in multiple steps upon heating while the *tan δ* shows corresponding maxima which is defined as the following (equation **(4.1)**):

$$\tan \delta = \frac{E''}{E'}$$

(4.1)

With *E''* being the elastic loss and *E'* the elastic storage modulus.

These are consistent with the glass transition temperature of the PDMS and the Jeffamine segments as well as the crossover temperature of the disaggregating urea units. This confirms a two phase system since for both the PDMS and Jeffamine segments a separate T_g is observed with a $T_{g,\,PDMS}$ around -118 °C and a $T_{g,\,Jeffamine}$ around -54 °C. The intensity of the signals correlates with the built-in ratio. The

146

steep decrease of moduli in the range of 57 °C to 72 °C is assigned to the change from an elastic to a viscous behavior and the corresponding T_{cross} are in good agreement with the rheology measurements. Below the T_g of the PDMS segment the material appears brittle while above the upper limit the material flows and can be shaped by melt processing.
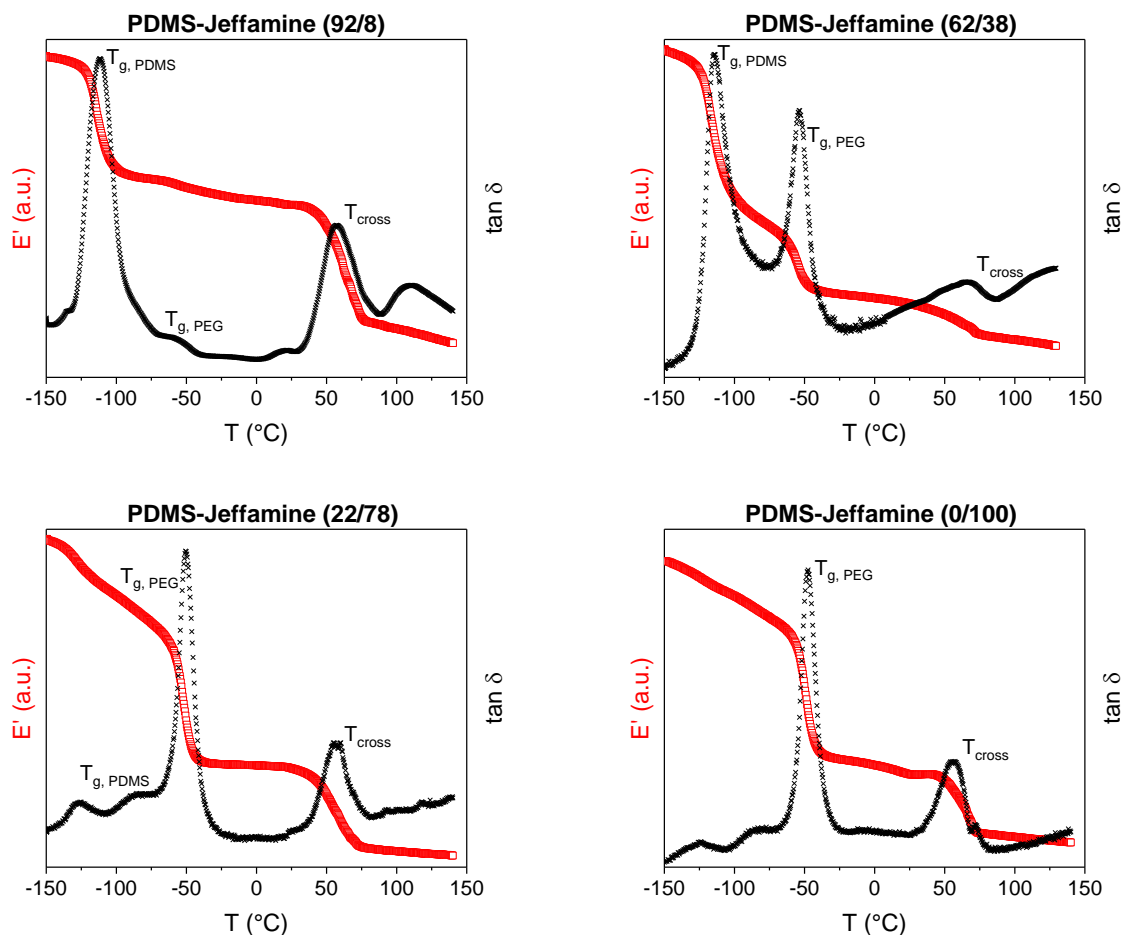
Figure 4.15: Storage moduli E' as a function of the temperature upon 1st heating of the **PDMS-Jeffamine** copolymers based on HMDI and different ratios of PDMS to Jeffamine determined via a single cantilever bending experiment utilizing a metal specimen holder applying a heating rate of 5 K min^{-1} and a frequency of 2 Hz. In addition, the reference (AB)$_n$ segmented copolymer **PDMS-Jeffamine (0/100)** is also shown.

The nine *(ABAC)$_n$ segmented PDMS-PEG$_{1k, 2k, 4k}$ copolymers* show the same behavior as the PDMS-Jeffamine copolymers (appendix Figure A-6.24 – Figure A-6.26). As listed in Table 4.6, the T_g for both, the hydrophobic PDMS and the hydrophilic PEG segment, can be seen by DMA independently of the built-in ratio, proving a phase separated morphology. The copolymers with higher PEG content which could not be analyzed by rheology, exhibit a T_{cross} between 44 °C and 86 °C.

For the reference (AB)$_n$ segmented copolymers **PDMS-PEG$_{1k, 2k, 4k}$ (0/100)** and **PDMS-Jeffamine (0/100)** (Table 4.1) solely two transitions could be determined. T_g of the PEG segments increase with increasing PEG chain length and also T_{cross}. The results of all (ABAC)$_n$ segmented amphiphilic copolymers as well as their reference (AB)$_n$ segmented copolymers are summarized in Table 4.6.

Table 4.6: Thermal transitions of the amphiphilic, physically crosslinked copolymers and their reference materials determined via DMTA utilizing a single cantilever bending experiment.

Copolymer		$T_{g\ PDMS\text{-}block}$ (°C)[a]	$T_{g\ PEG\text{-}block}$ (°C)[a]	T_{cross} (°C)[a] *1st heating*
PDMS-PEG$_{1k}$	(100/0)	-115	-	54
	(93/7)	-114	-44	54
	(59/41)	-115	-50	58
	(10/90)[b]	-110	-46	68
	(0/100)	-	-48	56
PDMS-PEG$_{2k}$	(85/15)	-112	-44	48
	(43/57)	-114	-42	45
	(12/88)	-124	-43	44
	(0/100)	-	-44	46
PDMS-PEG$_{4k}$	(77/23)	-113	-39	54
	(30/70)	-121	-45	51
	(9/91)	-125	-44	50
	(0/100)	-	-28	52
PDMS-Jeffamine	(92/8)	-113	-57	62
	(62/38)	-114	-54	72
	(22/78)	-126	-50	57
	(0/100)	-	-47	56

[a] Determined by DMTA via a single cantilever bending experiment utilizing a metal specimen holder with a heating rate of 5 K min^{-1} and a frequency of 2 Hz.
[b] Theoretical PEG content due to insufficient solubility for ^{1}H-NMR in CDCl$_3$.

As a final remark it was shown that the amphiphilic PDMS-PEG$_{1k,\ 2k,\ 4k}$ copolymers, independent of PEG chain length or composition show a phase separated morphology. Further, it was shown that the melt viscosities of these (ABAC)$_n$ segmented copolymers can be significantly reduced by using Jeffamine, the modified PEG being flanked with PPO units.

4.2.4. Mechanical properties

The mechanical properties of the *(ABAC)ₙ segmented PDMS-Jeffamine copolymers* were determined by tensile tests. Specimens were punched out of the solution cast films. A stress-strain diagram of the amphiphilic copolymers and the corresponding reference materials is depicted in Figure 4.16. Up to a Jeffamine content of 38 wt.% the two copolymers behave similar to the neat Jeffamine-urea copolymer **PDMS-Jeffamine (0/100)**. A relatively short ultimate elongation of 59% and 37% for **PDMS-Jeffamine (92/8)** and **PDMS-Jeffamine (62/38)** was observed with a stress at break of 2.3 MPa and 4.1 MPa, respectively. **PDMS-Jeffamine (0/100)** showed a strain at break of 75% and a stress at break of 3.0 MPa (Figure 4.16). A dramatic difference occurs when the Jeffamine content is increased to 78 wt.% as it was already observed for the rheological properties. The ultimate elongation increases to 940% with a stress at break of 9.6 MPa. This is assumed to be a results of the incompatibility of the separated phases. This influence of morphology will be discussed in more detail in the following chapter 4.2.5. Summarizing all results (Table 4.7) it is shown that the toughness of the amphiphilic, physically crosslinked copolymers being defined as the area below the stress-strain curve increases with increasing Jeffamine content.

The Young's modulus of the PDMS-Jeffamine copolymers increases compared to the reference materials due to the two soft segments improving the overall mechanical strength at room temperature. For the amphiphilic copolymers, however, a decreasing Young's modulus with increasing Jeffamine content from 67 MPa to 57 MPa for **PDMS-Jeffamine (92/8)** and **PDMS-Jeffamine (22/78)** is observed. This can be explained by the reduced elastic PDMS content. The results of the tensile tests are summarized in Table 4.7.
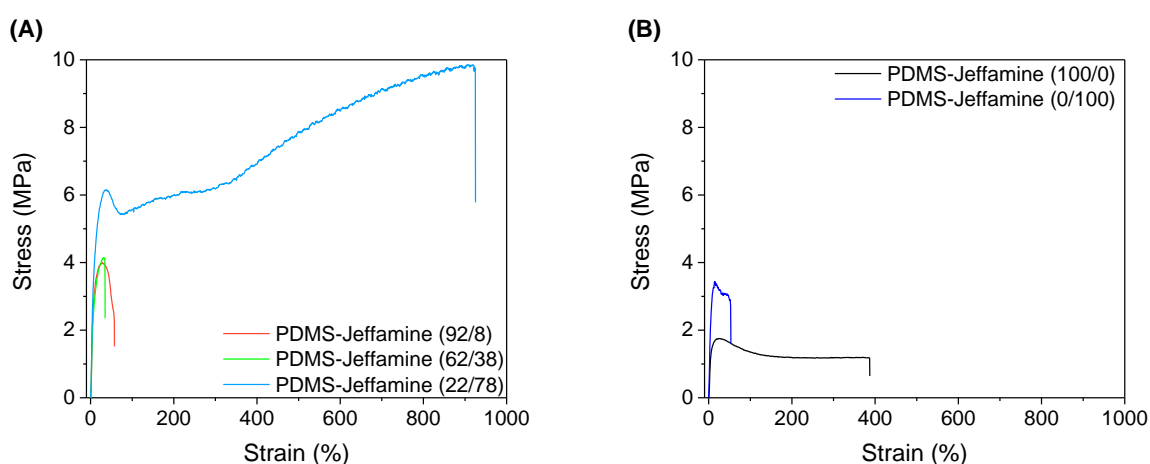
Figure 4.16: Stress-strain diagrams of **(A) PDMS-Jeffamine** copolymers with varying Jeffamine content and **(B)** of the reference materials **PDMS-Jeffamine (100/0)** and **PDMS-Jeffamine (0/100)**. Detailed experimental data can be found in chapter 5.2.

Table 4.7: Tensile properties determined via stress-strain tests of (ABAC)$_n$ segmented PDMS-Jeffamine copolymers with different Jeffamine content and their (AB)$_n$ segmented reference materials. The average values of at least five specimens is given. Detailed experimental data can be found in chapter 5.2.

Copolymer	Young's modulus (MPa)	Strain at break (%)	Stress at break (MPa)	Toughness (Jm^{-3}10^4)
PDMS-Jeffamine (100/0)	36.6 ± 1.0	367 ± 15	1.23 ± 0.01	482 ± 19
PDMS-Jeffamine (92/8)	67.3 ± 1.7	59 ± 3	2.32 ± 0.12	193 ± 8
PDMS-Jeffamine (62/38)	59.7 ± 1.3	37 ± 1	4.13 ± 0.09	112 ± 12
PDMS-Jeffamine (22/78)	57.4 ± 2.8	942 ± 26	9.62 ± 0.18	6929 ± 319
PDMS-Jeffamine (0/100)	49.5 ± 2.7	75 ± 26	2.97 ± 0.28	250 ± 92

It is remarkable that the amphiphilic copolymer **PDMS-Jeffamine (22/78)** shows tremendously divergent thermal as well as mechanical properties compared to the copolymers with less Jeffamine content. This includes a significantly increased storage and loss modulus above T_{cross}, complex viscosity as well as a pronounced increase of the ultimate strain and stress at break.

4.2.5. Morphological investigation

Small angle X-ray scattering

In the *(ABAC)n segmented PDMS-PEG$_{1k, 2k, 4k}$ copolymers* **PDMS-PEG$_{1k}$ (59/41)**, **PDMS-PEG$_{2k}$ (43/57)**, and **PDMS-PEG$_{4k}$ (30/70)** the influence of the PEG segment on the morphology was investigated at room temperature by small angle X-ray scattering (Figure 4.17). The samples were prepared from solution cast films being pressed into aluminum discs with a 1 mm hole. The measurements were jointly conducted with Paul Reichstein, Macromolecular Chemistry I. As shown in the previous chapters, the nonpolar PDMS and polar PEG segments phase separate in the copolymers. Each (ABAC)n segmented copolymer shows one broad scattering signal indicating some periodicity within the morphology. From the maxima of the scatting vector q_{max} the interdomain spacing d is calculated which ranges between 12.6 nm and 28.4 nm. This is at least 2.5 times larger than for the reference (AB)n segmented poly(urea-siloxane) **PDMS-PEG$_{1k, 2k, 4k}$ (100/0)** (d = 4.8 nm) (chapter 3.2.5). This (AB)n segmented poly(urea-siloxane) shows one single broad scattering maxima implying a phase separation of the urea hard segment domains and the PDMS matrix (chapter 3.2.5, Figure 3.19). Further with an increasing PEG chain length q_{max} decreases and the interdomain spacing increases implying that the PEG segment primarily sets the characteristic interdomain spacing length within the (ABAC)n segmented copolymers. This trend was also shown by SAXS measurements by Sijbesma *et al.*[182] However, no distinct or highly ordered morphology such as spherical, cylindrical, or lamellar is observed, since no higher order reflections are detected.
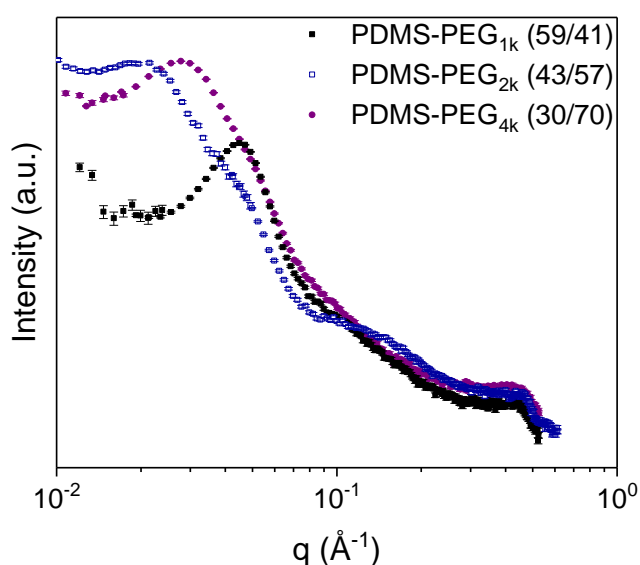
Figure 4.17: Small angle X-ray scattering spectra of (ABAC)n segmented copolymers **PDMS-PEG$_{1k}$ (59/41)**, **PDMS-PEG$_{2k}$ (43/57)**, and **PDMS-PEG$_{4k}$ (30/70)**. The q_{max} shifts towards lower q values or longer distances with increasing PEG chain length.

The maxima of the scattering vector q_{max} and the calculated interdomain spacing d (according to $d = \frac{2\pi}{q_{max}}$) are listed in Table 4.8.

Table 4.8: Small angle X-ray scattering data: Maximum scattering vector q and resulting interdomain spacing $d = \frac{2\pi}{q_{max}}$.

Copolymer	q_{max} (nm^{-1})[a]	d (nm)
PDMS-PEG$_{1k}$ (59/41)	0.50	12.6
PDMS-PEG$_{2k}$ (43/57)	0.22	28.4
PDMS-PEG$_{4k}$ (30/70)	0.28	22.6

[a] SAXS measurements of dry copolymer films embedded in aluminum discs with a 1 mm hole were conducted at room temperature.

The *(ABAC)$_n$ segmented PDMS-Jeffamine copolymers* were also investigated by SAXS. Here the varying built-in ratios and its influence on a change of morphology was of interest. In Figure 4.18 the SAXS spectra show also single broad scattering maxima without higher order reflections. Moreover, the maxima shift to smaller scattering vector values with increasing Jeffamine content, resulting as expected in larger interdomain spacing with increasing Jeffamine content. For **PDMS-Jeffamine (92/8)** an interdomain spacing of d = 4.8 nm was determined which is in the same order of magnitude as the reference (AB)$_n$ segmented poly(urea-siloxane) **PDMS-Jeffamine (100/0)** (d = 4.8 nm). Increasing the Jeffamine content to 38 wt.% in the (ABAC)$_n$ segmented **PDMS-Jeffamine (62/38)** copolymer, the interdomain spacing increasing to 12.8 nm. This is similar to **PDMS-PEG$_{1k}$ (59/41)**, owed to similar chain length of Jeffamine ED-900 and PEG$_{1k}$. For the amphiphilic copolymer **PDMS-Jeffamine (22/78)**, with the largest Jeffamine content of 78 wt.%, an interdomain spacing of 16.3 nm, was detected.
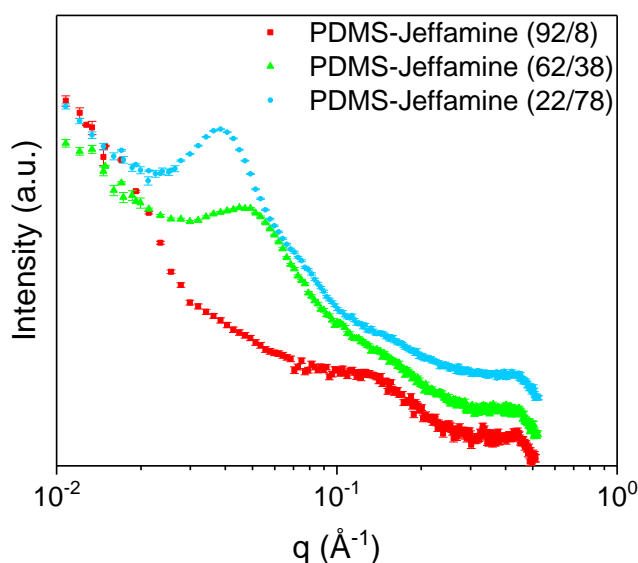
Figure 4.18: Small angle X-ray scattering spectra of (ABAC)$_n$ segmented PDMS-Jeffamine copolymers **PDMS-Jeffamine (92/8)**, **PDMS-Jeffamine (62/38)**, and **PDMS-Jeffamine (22/78)**. The broad scattering signal shifts to lower q values with increasing Jeffamine content.

The SAXS data including q_{max} and d are summarized in Table 4.9. No distinct difference of morphology can be observed by SAXS in the series of amphiphilic (ABAC)$_n$ segmented PDMS-Jeffamine copolymers. Concluding, the hydrophilic Jeffamine content and chain length has a significant influence on the interdomain spacing but no highly ordered morphology is obtained.

Table 4.9: Small angle X-ray scattering data: Maximum scattering vector q and resulting interdomain spacing $d = \frac{2\pi}{q_{max}}$.

Copolymer	q_{max} (nm^{-1})[a]	d (nm)
PDMS-Jeffamine (92/8)	1.30	4.8
PDMS-Jeffamine (62/38)	0.49	12.8
PDMS-Jeffamine (22/78)	0.38	16.3

[a] SAXS measurements of dry copolymer films embedded in aluminum discs with a 1 mm hole were conducted at room temperature.

Transmission electron microscopy

To gain more information on the morphology of the *amphiphilic (ABAC)ₙ segmented PDMS-Jeffamine copolymers*, transmission electron microscopy (TEM) of solution cast films were performed. The TEM measurements were jointly conducted with Marco Schwarzmann (Inorganic Chemistry I) and Markus Drechsler (Bavarian Polymer Institute). The thin specimens were prepared with a cryo-ultramicrotome. The samples were investigated without staining. As stated in literature for other PDMS containing copolymers, the PDMS phase appears darker compared to the Jeffamine phase upon exposure to the electron beam.[187]

Both, the hydrophobic (AB)ₙ segmented **PDMS-Jeffamine (100/0)** copolymer and the hydrophilic (AB)ₙ segmented **PDMS-Jeffamine (0/100)** copolymer, as shown in Figure 4.19, show a very fine grainy morphology without particular features.

PDMS-Jeffamine (100/0)   **PDMS-Jeffamine (0/100)**
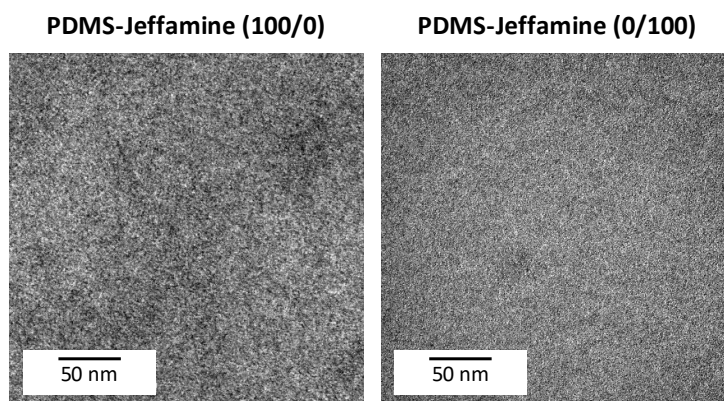
Figure 4.19: TEM images of the (AB)ₙ segmented poly(urea-siloxane) copolymer **PDMS-Jeffamine (100/0)** and the (AB)ₙ segmented poly(urea-Jeffamine) copolymer **PDMS-Jeffamine (0/100)** showing a very fine grainy morphology without particular features. The films were sectioned with a cryo-ultramicrotome and investigated without staining.

The morphology of the (ABAC)ₙ segmented PDMS-Jeffamine copolymers is shown in Figure 4.20. For the (ABAC)ₙ segmented **PDMS-Jeffamine (92/8)** copolymer with a high PDMS content of 92 wt.% also a similar fine and grainy morphology is observed. A Jeffamine content of 8 wt.% seems to have no significant influence on the morphology which is also in agreement with the SAXS data. The interdomain spacing of **PDMS-Jeffamine (92/8)** with d = 4.8 nm is similar to the (AB)ₙ segmented **PDMS-Jeffamine (100/0)** copolymer. However, this clearly changes for **PDMS-Jeffamine (62/38)**. Irregular long darker and brighter features with a thickness of about 10 – 15 nm are visible. The amphiphilic (ABAC)ₙ segmented copolymer **PDMS-Jeffamine (62/38)** reveals a distinct microphase separation of the two incompatible PDMS and Jeffamine segments. Increasing the Jeffamine content further to 78 wt.% as for the (ABAC)ₙ segmented copolymer **PDMS-Jeffamine (22/78)** a similar morphology is visible. In a phase inversion the PDMS segments are embedded here in the hydrophilic Jeffamine phase.

PDMS-Jeffamine (92/8)   PDMS-Jeffamine (62/38)   PDMS-Jeffamine (22/78)
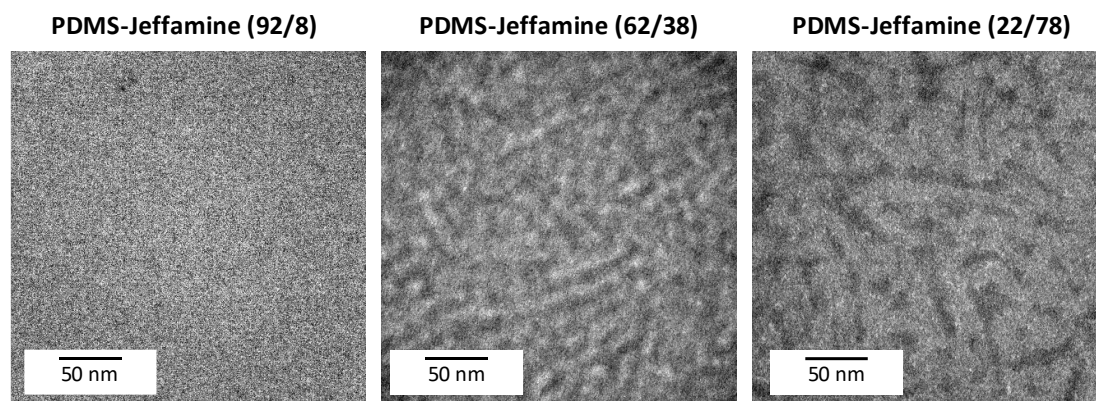
Figure 4.20: TEM images of the amphiphilic (ABAC)$_n$ segmented PDMS-Jeffamine copolymers with increasing Jeffamine content from 8 wt.% to 38 wt.% and 78 wt.%. The films were sectioned with a cryo-ultramicrotome and investigated without staining. The PDMS block appear darker by the higher electron contrast of Si and the darker domains are attributed to the PDMS segments whereas the brighter domains correspond to the Jeffamine segments.

In Figure 4.21 the evaluation of a Fast Fourier Transformation (FFT) of the amphiphilic (ABAC)$_n$ segmented copolymers **PDMS-Jeffamine (62/38)** and **PDMS-Jeffamine (22/78)** is shown. Here a larger area was used. The layer distances calculated from the FFT are around 16 nm and 21 nm, and reflects the trend of the SAXS analysis (13 nm and 16 nm).

PDMS-Jeffamine (62/38)   PDMS-Jeffamine (22/78)
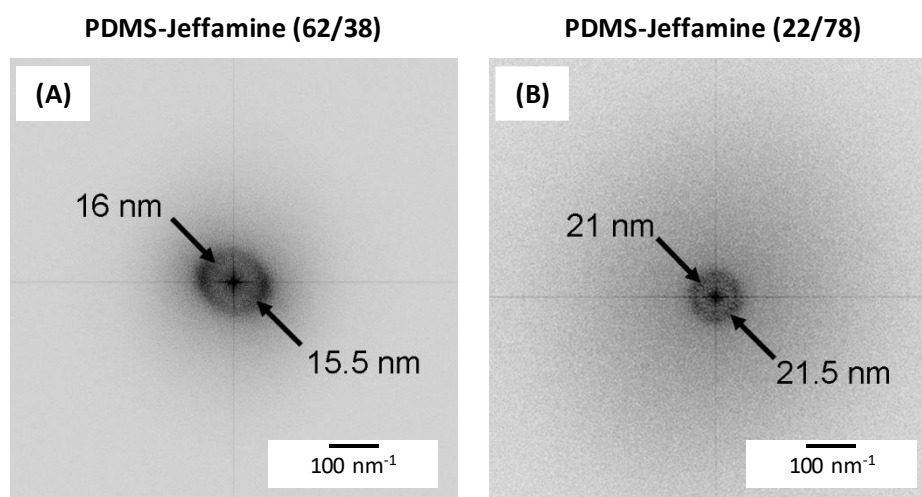
Figure 4.21: Fast Fourier Transform (FFT) analysis of TEM images taken from **(A) PDMS-Jeffamine (62/38)** and **(B) PDMS-Jeffamine (22/78)**. The layer distance of copolymer **PDMS-Jeffamine (62/38)** range from 13 nm to 23 nm with an average of 16 nm **(A)**, whereas for copolymer **PDMS-Jeffamine (22/78)** a distance of 16 nm to 30 nm with an average of 21 nm was calculated **(B)**. These data show the same trend as the SAXS analysis with an interdomain spacing of 13 nm and 16 nm, respectively.

In Figure 4.22 an additional TEM image of **PDMS-Jeffamine (22/78)** is depicted were, on an extremely thin film layer at the edge of the specimen, single layer strands of dark wormlike structures are visible. These wormlike structures have a length of about 50 nm and a width of 10 nm. A grey shade analysis of Figure 4.22 resulted in a content of close to 20% dark domains which is close to the build-in ratio of the PDMS segments in the $(ABAC)_n$ segmented copolymer (22 wt.%).
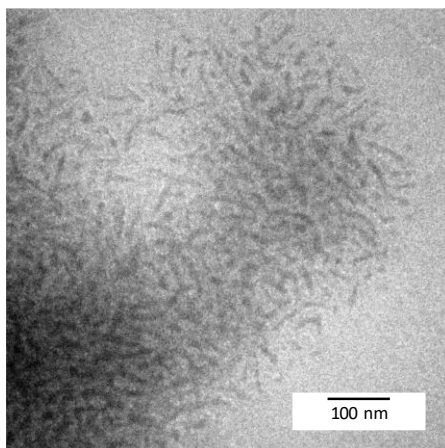
Figure 4.22: TEM image of **PDMS-Jeffamine (22/78)** depicting a sequence of a very thin film with single layer strands of dark wormlike structures representing the hydrophobic PDMS domains next to the substrate. Here a grey shade analysis resulted in a content of close to 20% dark domains, which is close to the build-in ratio in the copolymer of 22 wt.%.

4.2.6. Hydrogel properties

The amphiphilic (ABAC)$_n$ segmented copolymers were synthesized aiming at mechanical stable hydrogels with tunable water uptake and swelling capacity. This is realized by adjusting the ratios of the hydrophobic PDMS and hydrophilic PEG/Jeffamine segments and by varying the PEG chain length. The swelling capacity and the water uptake as function of the PEG content were characterized after swelling the copolymers in deionized (DI) water for four to five days to reach an equilibrium water uptake. The swelling capacity and the water uptake were analyzed by measuring the weight loss at 120 °C until a constant dry weight was reached. The equilibrium degree of swelling Q and the water content W were calculated according to equation **(4.2)** and **(4.3)**, respectively.[191] Detailed experimental data are included in chapter 5.2.

$$Q\,(\%) = \frac{m_{\text{swollen}} - m_{\text{dry}}}{m_{\text{dry}}} \cdot 100 \qquad \textbf{(4.2)}$$

$$W\,(\%) = \frac{m_{\text{swollen}} - m_{\text{dry}}}{m_{\text{swollen}}} \cdot 100 \qquad \textbf{(4.3)}$$

With $m_{swollen}$ being the mass of the completely swollen specimen and m_{dry} the mass of the completely dried sample.

Hydrogels based on PDMS-PEG$_{1k}$ copolymers

The calculated degree of swelling Q and water content W of *(ABAC)$_n$ segmented PDMS-PEG$_{1k}$ copolymers* in dependency of the copolymer composition are shown in Figure 4.23. For comparison the values of the reference (AB)$_n$ segmented copolymers **PDMS-PEG$_{1k}$ (100/0)** and **PDMS-PEG$_{1k}$ (0/100)** are also shown. A clear tendency of higher swelling and water uptake with increasing PEG$_{1k}$ content is observed. Owed to an increasing amount of hydrophilic PEG$_{1k}$ segments and a decreasing hydrophobic PDMS content, the copolymers can take up more water. For the (AB)$_n$ segmented poly(urea-siloxane) **PDMS-PEG$_{1k}$ (100/0)** a degree of swelling and water content of 1% was determined caused by the hydrophilic urea units in combination with the completely hydrophobic nature of PDMS. By increasing the hydrophilic content to 7 wt.% the degree of swelling increased to 10% with a water uptake of 9%. Further increasing the PEG$_{1k}$ content to 41 wt.% a degree of swelling of 131% and a water uptake of 57% was obtained. The degree of swelling increases drastically to 630% with a total PEG$_{1k}$ content of 90 wt.%. The water content reaches 86%. It must be noted that the reference (AB)$_n$ segmented copolymer **PDMS-PEG$_{1k}$ (0/100)** is not water soluble which is due to strong intermolecular interactions.

(A)

(B)
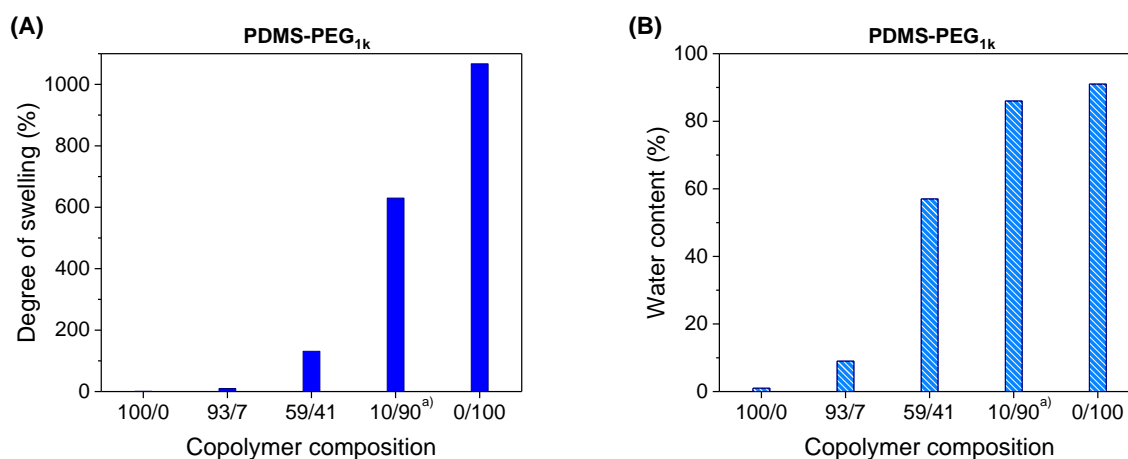
Figure 4.23: (A) Degree of swelling and **(B)** water content in dependency of the amphiphilic (ABAC)$_n$ segmented PDMS-PEG$_{1k}$ copolymer composition (**PDMS/PEG$_{1k}$**) and the reference (AB)$_n$ segmented copolymers **PDMS-PEG$_{1k}$ (100/0)** and **PDMS-PEG$_{1k}$ (0/100)** after equilibrium swelling in DI water. Detailed experimental data are included in chapter 5.2.
[a)] Theoretical PEG$_{1k}$ content due to insufficient solubility for ^{1}H-NMR in CDCl$_3$.

In addition to the swelling capacity of the hydrogels the mechanical gel stability is another important characteristic. Within this thesis, the mechanical stability was qualitatively investigated by swelling the (ABAC)$_n$ segmented PDMS-PEG$_{1k}$ copolymers in DI water for several hours and removing them after certain time intervals with a tweezer to demonstrate their stability in the swollen state. In Figure 4.24 the PDMS-PEG$_{1k}$ based amphiphilic copolymers with increasing PEG$_{1k}$ content are shown in dry state (0 h) and in the hydrogel state after 0.5, 1, 2 and 20 h after immersing in DI water. It can be seen that all hydrogels, independent of their composition, are mechanically stable over the entire time in water. In addition, the increasing water uptake and swelling with increasing hydrophilic PEG$_{1k}$ content is optically visualized by an increase in all dimensions.
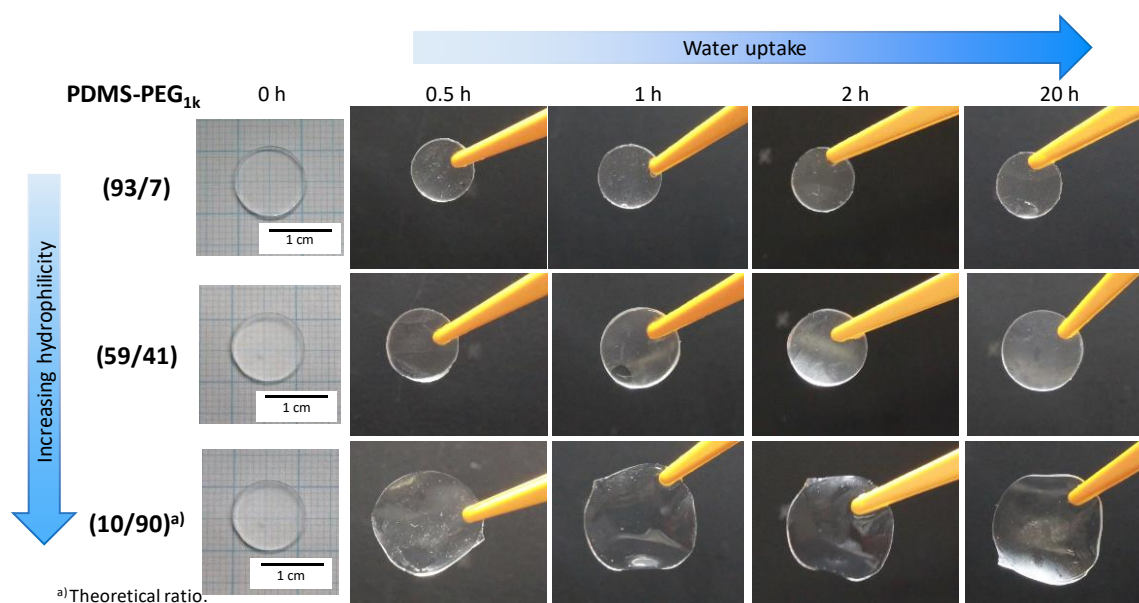
Figure 4.24: Investigation of gel stability of amphiphilic (ABAC)$_n$ segmented PDMS-PEG$_{1k}$ hydrogels. The photographs show vertically the dry copolymer films with increasing PEG$_{1k}$ content and horizontally the hydrogels after increasing time periods swollen in water. With increasing PEG$_{1k}$ content, the hydrogels show a larger swelling. All gels show good mechanical stability.

Hydrogels based on PDMS-PEG$_{2k}$ copolymers

To study the influence of an increasing PEG chain length on the hydrogel properties, *(ABAC)$_n$ segmented PDMS-PEG$_{2k}$ copolymers* were investigated in the same manner. In Figure 4.25 the degree of swelling as well as the water uptake as function of the (ABAC)$_n$ segmented copolymer composition is shown. The reference (AB)$_n$ segmented copolymers **PDMS-PEG$_{2k}$ (100/0)** and **PDMS-PEG$_{2k}$ (0/100)** are given for comparison. With a PEG$_{2k}$ content of 15 wt.% a degree of swelling of 34% and a water uptake of 25% was determined. Increasing the PEG$_{2k}$ content to 57 wt.% the degree of swelling reached 205% and the water uptake 67%. A maximum Q of 765% and W of 88% was determined with a PEG$_{2k}$ content of 88 wt.%. The reference (AB)$_n$ segmented copolymer **PDMS-PEG$_{2k}$ (0/100)** is completely soluble in water. In summary, doubling the PEG chain length, increases the degree of swelling and the water uptake owed to a doubled amount of hydrophilic segments.
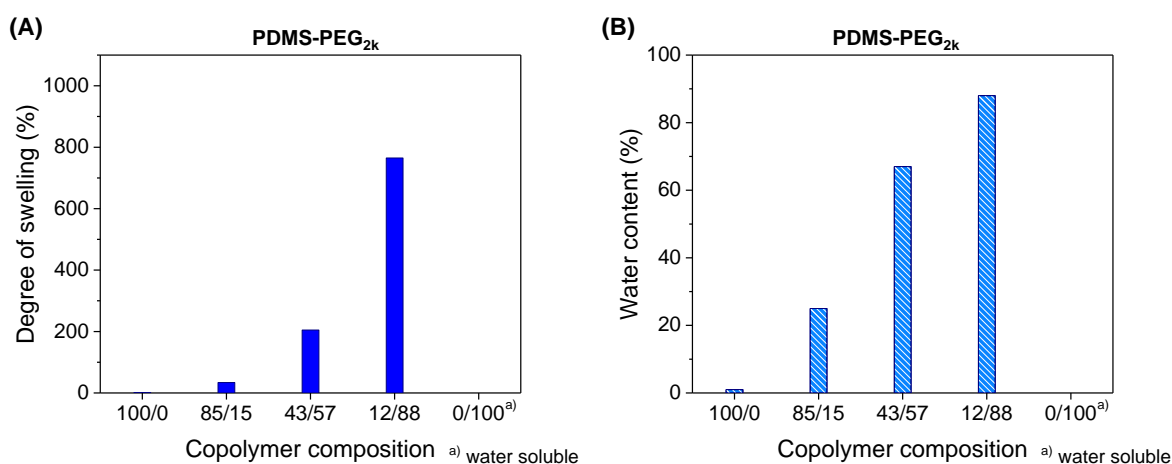
Figure 4.25: (A) Degree of swelling and **(B)** water content in dependency of the amphiphilic (ABAC)$_n$ segmented PDMS-PEG$_{2k}$ copolymer composition (**PDMS/PEG$_{2k}$**) and the reference (AB)$_n$ segmented copolymers **PDMS-PEG$_{2k}$ (100/0)** and **PDMS-PEG$_{2k}$ (0/100)** after equilibrium swelling in DI water. Detailed experimental data are included in chapter 5.2.

These hydrogels, are stable over several hours in water up to a PEG$_{2k}$ content of 57 wt.% and a water uptake of 67%. Increasing the PEG$_{2k}$ content to 88 wt.% the hydrogel is initially stable but after several hours ($\geq$ 20 h) loses its shape and cannot be handled anymore without falling apart into small non-water soluble gel fragments. Thus the hydrophobic PDMS improves the mechanical stability and simultaneously protects the hydrogen bonded urea units while the hydrophilic PEG$_{2k}$ regulates the water swelling. With higher PEG$_{2k}$ content the PDMS content is too low to maintain the gel stability. Concluding from these results, PDMS-PEG$_{2k}$ hydrogels are only mechanical stable over long time up to a water uptake of 67% and a PEG$_{2k}$ content of 57 wt.%.
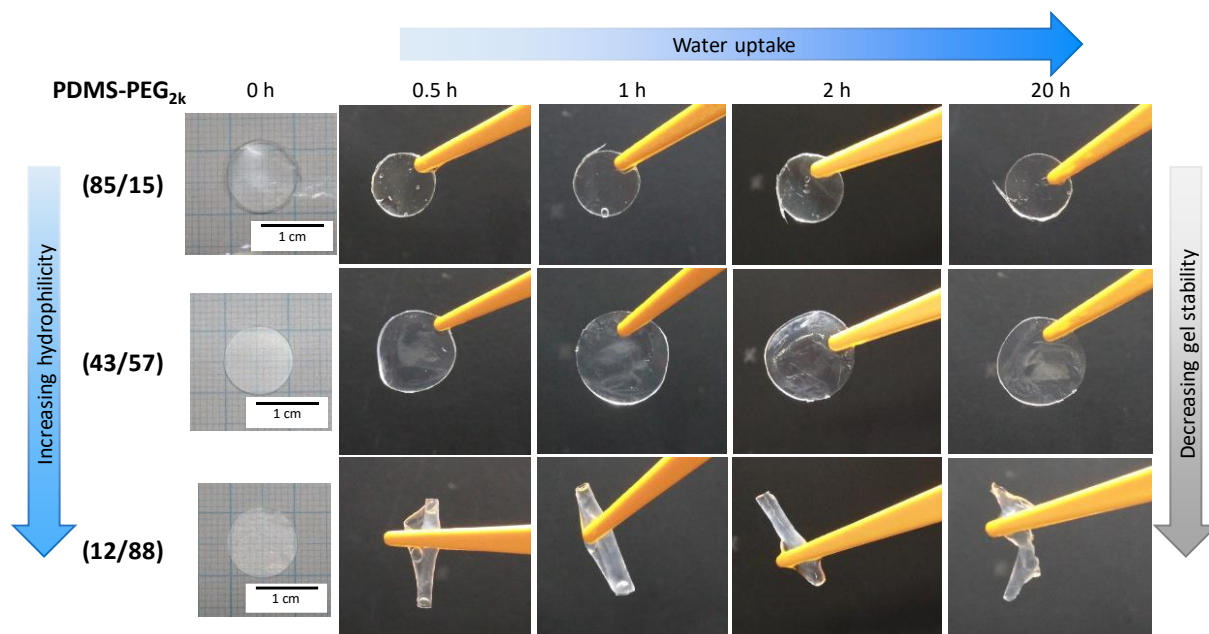
Figure 4.26: Investigation of gel stability of amphiphilic (ABAC)$_n$ segmented PDMS-PEG$_{2k}$ hydrogels. The photographs image with increasing PEG$_{2k}$ content (vertically) the dry copolymer films and the hydrogels after increasing time periods swollen in water (horizontally). With increasing PEG$_{2k}$ content, the hydrogels show an increasing swelling but with 88 wt.% PEG$_{2k}$ content also a significant decreased gel stability (vertically).

Hydrogels based on PDMS-PEG$_{4k}$ copolymers

Increasing the PEG chain length further to PEG$_{4k}$ in the *(ABAC)$_n$ segmented PDMS-PEG$_{4k}$ copolymers*, the degree of swelling and the water content is again increased as shown in Figure 4.27. The maximum degree of swelling was determined to be about 1500% corresponding to a water uptake of 94% at a total PEG$_{4k}$ content of 91 wt.%. Reference (AB)$_n$ segmented copolymer **PDMS-PEG$_{4k}$ (0/100)** is completely water soluble, as already found for **PDMS-PEG$_{2k}$ (0/100)**.
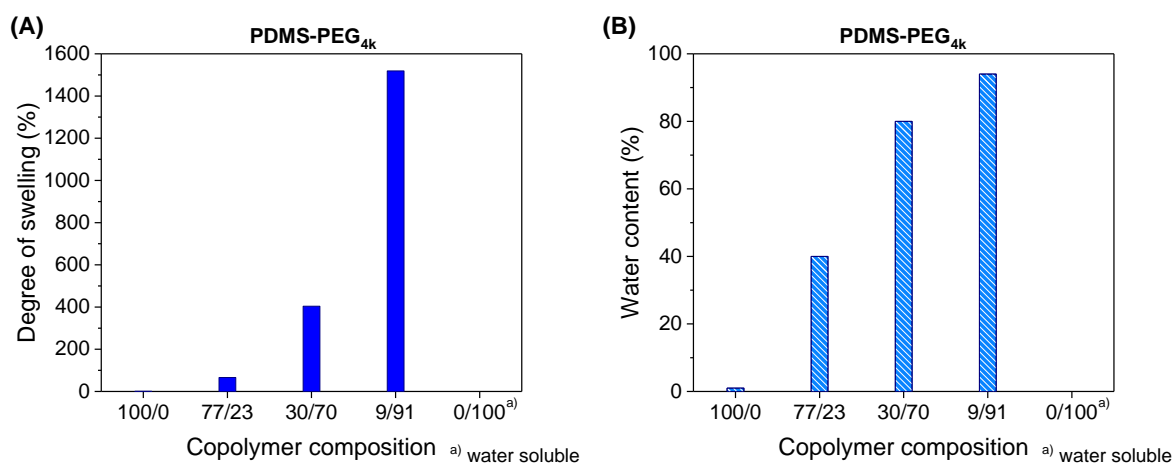
Figure 4.27: (A) Degree of swelling and **(B)** water content in dependency of the amphiphilic (ABAC)$_n$ segmented PDMS-PEG$_{4k}$ copolymer composition (**PDMS/PEG$_{4k}$**) and the reference (AB)$_n$ segmented copolymers **PDMS-PEG$_{4k}$ (100/0)** and **PDMS-PEG$_{4k}$ (0/100)** after equilibrium swelling in DI water. Detailed experimental data are included in chapter 5.2.

On the one hand, a longer PEG$_{4k}$ chain length means a higher hydrophilicity and thus higher water content but on the other hand a poorer gel stability (Figure 4.28). The PDMS supports the mechanical stability while reducing the swelling capacity owed to the hydrophobic character. Nevertheless, due to the longer PEG$_{4k}$ chain length the hydrogel loses its mechanical stability at a PEG$_{4k}$ content of 70 wt.% within short time. After 2 h storing in DI water the hydrogel is already extremely fragile while after 20 h it completely lost its stability. At the highest PEG$_{4k}$ content of 91 wt.% the hydrogel cannot be handled after 30 min storing in DI water due to its extremely fragile behavior. However, the hydrogels do not dissolve in water, merely losing their mechanical stability.
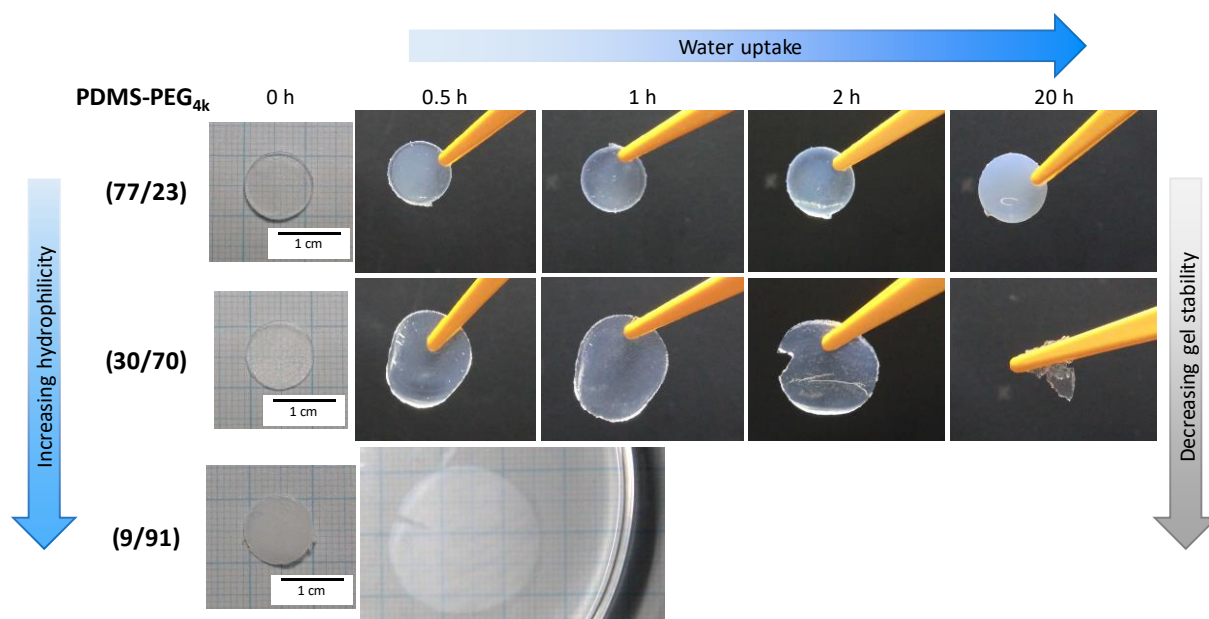
Figure 4.28: Investigation of gel stability of amphiphilic (ABAC)$_n$ segmented PDMS-PEG$_{4k}$ hydrogels. The photographs show with increasing PEG$_{4k}$ content (vertically) the dry copolymer films and the hydrogels after increasing time periods swollen in water (horizontally). With increasing PEG$_{4k}$ content, the hydrogels show an increasing swelling. The hydrogels become extremely brittle and fragile with a PEG content of 70 wt.% and a water uptake of 80%.

Concluding, hydrogels based on amphiphilic (ABAC)$_n$ segmented PDMS-PEG copolymers from mechanical stable hydrogels. However, a certain amount of hydrophobic PDMS has to be incorporated to maintain the mechanical stability and prevent the hydrogel from falling apart. The water content within the hydrogels could be tuned by varying on the one hand the PEG content and on the other hand the PEG chain length within the (ABAC)$_n$ segmented copolymers. This dependency is illustrated in Figure 4.29. In the 3-dimensional diagram the influence of the (ABAC)$_n$ segmented PDMS-PEG copolymer composition (PDMS/PEG) and PEG chain length is shown in dependency of the water content. With increasing PEG content and PEG chain length the copolymers can take up more water. Being able to adjust the hydrogel properties, these materials can be tuned for desired application.
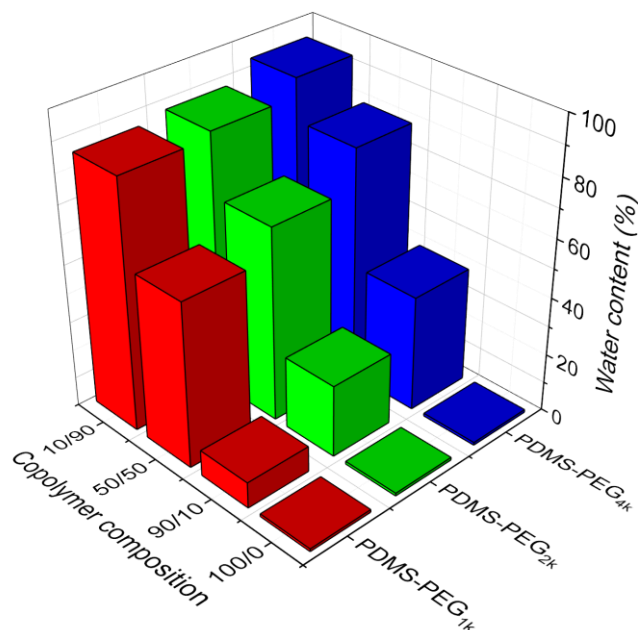
Figure 4.29: 3-dimensional diagram illustrating the influence of the (ABAC)$_n$ segmented copolymer composition (PDMS/PEG) and PEG chain length on the water uptake. With increasing PEG content and PEG chain length, the water uptake increases. By varying these two parameters the water uptake can be adjusted.

Hydrogels based on PDMS-Jeffamine copolymers

Finally, the influence of the *(ABAC)$_n$ segmented PDMS-Jeffamine copolymers* was also investigated regarding the gel stability. These PDMS-Jeffamine hydrogels were characterized concerning their ability of swelling in DI water (Figure 4.30). In DI water a similar degree of swelling Q and water content W in dependency of the Jeffamine content compared with the PDMS-PEG$_{1k}$ hydrogels were observed due to the similar PEG chain length. Yet a slightly smaller Q value is observed for the PDMS-Jeffamine hydrogels since the molecular weight of the Jeffamine including the PPO units is slightly smaller than of the PEG$_{1k}$. The reference (AB)$_n$ segmented **PDMS-Jeffamine (0/100)** copolymer is completely water soluble due to the lack of shielding of the urea units as also seen for the reference (AB)$_n$ segmented **PDMS-PEG$_{2k}$ (0/100)** and **PDMS-PEG$_{4k}$ (0/100)** copolymers. Further a buffer solution which is mainly used for cell studies acting as growth medium in the biomedical field was used. Storing the amphiphilic (ABAC)$_n$ segmented PDMS-Jeffamine copolymers in the buffer solution it can be seen that Q and W follow the same trend as in DI water. Remarkable is that a lower degree of swelling and water uptake is observed.
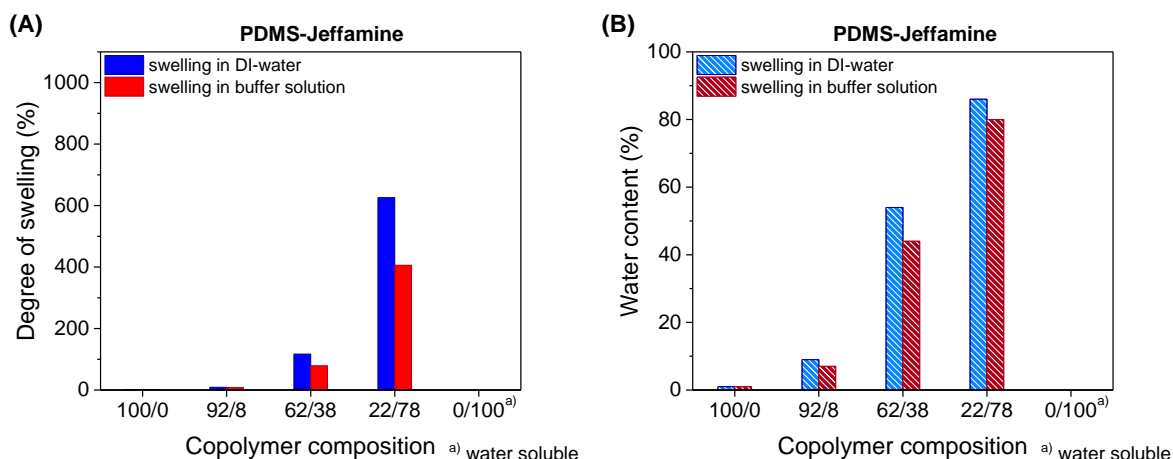
Figure 4.30: (A) Degree of swelling and **(B)** water content in dependency of the amphiphilic (ABAC)$_n$ segmented PDMS-Jeffamine copolymer composition (PDMS/Jeffamine) and the reference (AB)$_n$ segmented copolymers **PDMS-Jeffamine (100/0)** and **PDMS-Jeffamine (0/100)** after equilibrium swelling in DI water and buffer solution. Detailed experimental data are included in chapter 5.2.

The gel stability of the PDMS-Jeffamine hydrogels was also investigated in dependency of the hydrogel composition as depicted in Figure 4.31. Both hydrogels, **PDMS-Jeffamine (92/8)** and **PDMS-Jeffamine (62/38)**, are mechanical stable over several hours in DI water. The water uptake can additionally be detected by the dimensional change of the specimen. However, **PDMS-Jeffamine (22/78)** is not stable in DI water, after 30 min disintegrates into non-water soluble gel fragments. This is again explained by the high hydrophilic Jeffamine content and insufficient protection of the urea units by the hydrophobic PDMS.
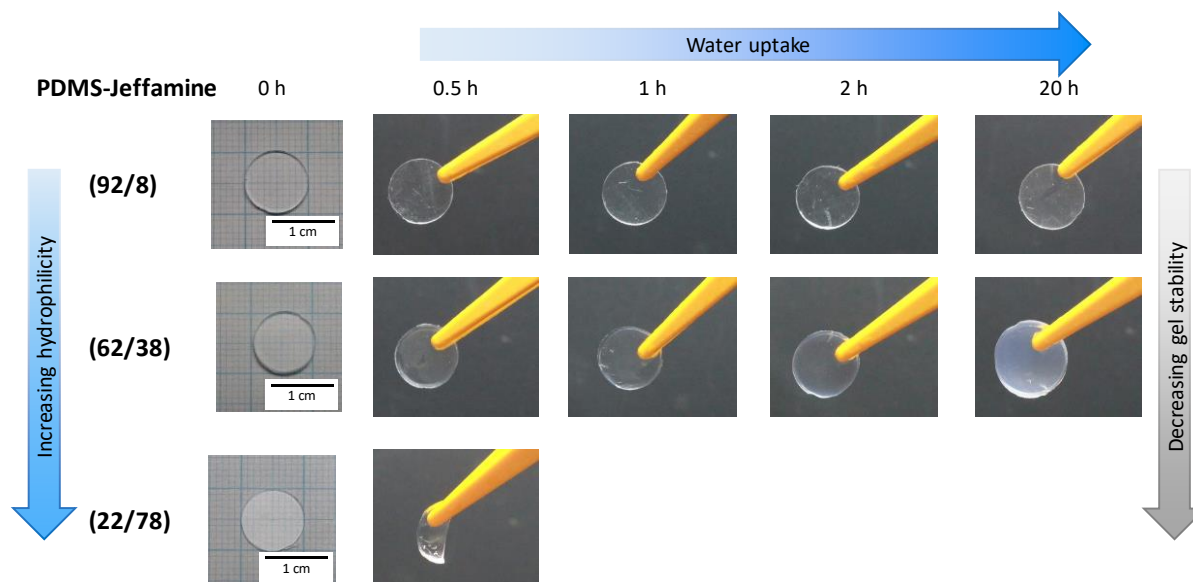
Figure 4.31: Investigation of gel stability of amphiphilic (ABAC)$_n$ segmented PDMS-Jeffamine hydrogels. The photographs depict with increasing Jeffamine content (vertically) the dry copolymer films and the hydrogels after increasing time periods swollen in water (horizontally). With increasing Jeffamine content, the hydrogels show an increasing swelling. The hydrogel becomes fragile and brittle with a Jeffamine content of 78 wt.% and water uptake of 86%.

Contact angle measurements

The amphiphilic properties of the *(ABAC)$_n$ segmented PDMS-Jeffamine copolymers* are characterized furthermore by contact angle (CA) measurements. The contact angle is given as a measure of wettability of a solid by a liquid, here Millipore water. The contact angle is defined as the angle between the liquid-vapor and solid-liquid interfaces of a solid-liquid-vapor system.[192] In case of a completely hydrophilic material a complete wetting with a contact angle of 0° is obtained. Between 0° and 90° a material is hydrophilic and with a contact angle above 90° the solid is not wettable, and hydrophobic. Ultrahydrophobic materials approach the contact angle limit of 180° (lotus effect).[193]

For the contact angle experiments the (ABAC)$_n$ segmented PDMS-Jeffamine copolymers were initially melt pressed at 120 °C and 100 bar for 1 min between PTFE foils to obtain a smooth and homogenous surface for CA determination. One droplet (5 µL) of Millipore water was placed onto the surface of the copolymer while recording a video over 300 sec. The CAs were determined right after placing the droplet onto the material surface (0 sec) and additionally after 60 sec and 300 sec to analyze the interface behavior of the amphiphilic copolymers. The sessile drop analysis is included in the appendix (Figure A-6.27). Detailed experimental data can be found in chapter 5.2 with respect to the contact angle measuring method.

As reference the (AB)$_n$ segmented **PDMS-Jeffamine (100/0)** copolymer and the **PDMS-Jeffamine (0/100)** copolymer were investigated. The expected behavior of a hydrophobic and a hydrophilic material is observed (Figure 4.32). The (AB)$_n$ segmented poly(urea-siloxane) **PDMS-Jeffamine (100/0)** with its purely hydrophobic PDMS soft segment shows a contact angle of 107° (0 sec). The CA decreases slightly within 300 sec to 101° (6%) which can only be explained by the hydrophilic urea hard segment. For the (AB)$_n$ segmented **PDMS-Jeffamine (0/100)** copolymer a contact angle of 61° was initially observed indicating a hydrophilic material resulting from the polar Jeffamine matrix present. Within only 20 sec (Figure 4.32 (c)) the water droplet flattens to a contact angle of 22° and is then completely absorbed by the copolymer. A photograph of the absorbed water droplet after 20 sec is shown (c) and highlighted by the purple arrow. Since the copolymer is water soluble, the water droplet is fully absorbed in the material within a few seconds.

For the amphiphilic (ABAC)$_n$ segmented PDMS-Jeffamine copolymers a constantly decreasing contact angle (CA) with increasing Jeffamine content due to the increasing hydrophilic character is expected. The CA in dependency of the copolymer composition and time is shown in Figure 4.32. **PDMS-Jeffamine (92/8)** shows initially a lower contact angle of 100° as the reference (AB)$_n$ segmented **PDMS-Jeffamine (100/0)**. This is indicative for a hydrophobic material. However, within 300 sec the CA decreases to 92°. The changing CA over time is an evidence for the nonpolar PDMS migrating to the surface upon melt pressing with hydrophobic PTFE surface and upon changing the contact medium into water a rearrangement within the copolymer morphology takes place and the polar Jeffamine

chains are moving to the surface owed to their water affinity.[187,194] For the (ABAC)$_n$ segmented **PDMS-Jeffamine (62/38)** copolymer an initial CA of 97° was observed, which also implies an hydrophobic nature. Yet, within 300 sec the CA decreases to 86° (a), indicating a more hydrophilic nature. A photograph of the water droplet after 300 sec is shown (a) and the water affinity is illustrated by the grey arrow. This increased water affinity is owed to a higher Jeffamine content. A completely different behavior is observed for the (ABAC)$_n$ segmented **PDMS-Jeffamine (22/78)** copolymer. An even smaller CA would be expected owed to a significantly higher hydrophilic Jeffamine content. Nevertheless, a CA of 113° decreasing to 112° within 150 sec (b) is observed which is even higher than for the hydrophobic reference (AB)$_n$ segmented **PDMS-Jeffamine (100/0)** copolymer. Hence, a rearrangement of the hydrophobic and hydrophilic soft segments at the interface is also assumed and even faster and more pronounced than for the (ABAC)$_n$ segmented **PDMS-Jeffamine (62/38)** copolymer. At 0 sec the copolymer surface is completely flat while within only 150 sec a concave meniscus is formed (b) caused by the material uptake into the water droplet sophisticating the real CA, illustrated by the green arrow.
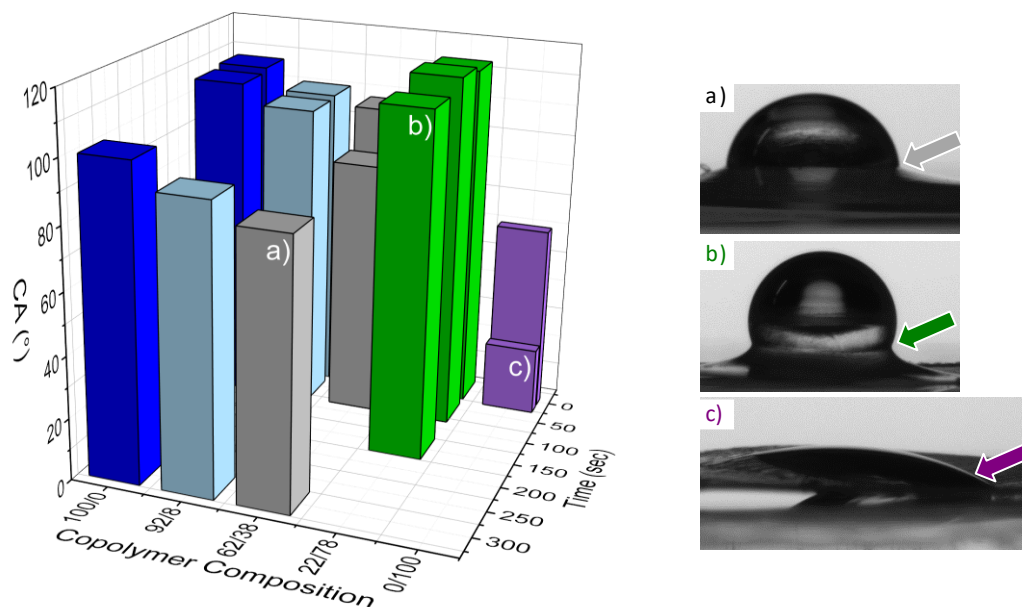
Figure 4.32: Left: 3-dimensional diagram illustrating the dependency of the copolymer composition and time on the contact angle (CA). The CA of the reference (AB)$_n$ segmented **PDMS-Jeffamine (100/0)** confirms the hydrophobic nature while the CA of the reference **PDMS-Jeffamine (0/100)** confirms the hydrophilic behavior. The (ABAC)$_n$ segmented PDMS-Jeffamine copolymers show a decreasing CA with increasing Jeffamine content showing the increasing hydrophilicity of the copolymers. **PDMS-Jeffamine (22/78)** shows initially a higher, more hydrophobic CA. This is assumed to result from a rearrangement of the PDMS and Jeffamine segments at the interface and its increased affinity of water absorption. **Right:** Photographs of a water drop (a) after 300 sec on the copolymer film **PDMS-Jeffamine (62/38)**, (b) after 150 sec on **PDMS-Jeffamine (22/78)**, and (c) after 20 sec on **PDMS-Jeffamine (0/100)**. The arrows indicating the increased water affinity. The copolymer films with a thickness of 30 - 80 µm were prepared by melt pressing (120 °C, 1 min, 100 bar).

4.2.7. Conclusion of chapter 4.2.

A variety of novel amphiphilic (ABAC)$_n$ segmented copolymers combining hydrophobic PDMS and hydrophilic PEG or Jeffamine segments were designed to tune the hydrogel properties. This was accomplished not solely by adjusting the molecular weight of the hydrophilic segment but also by incorporating a second hydrophobic segment. An additional objective was to enable melt processing of these materials to allow melt extrusion-based 3D printing to fabricate defined constructs which are of great interest in biofabrication.

Synthesis: The (ABAC)$_n$ segmented copolymers are an extension of the previously discussed (AB)$_n$ segmented, physically crosslinked poly(urea-siloxane)s. Here an additional hydrophilic poly(ethylene glycol) (PEG) containing segment is incorporated. As basis the poly(urea-siloxane) based on the *short chain PDMS* (M$_n$ = 1513 g mol^{-1}, x = 18) and *1,6-hexamethylene diisocyanate* was selected due to its excellent mechanical properties, a low melt viscosity, and its solidification behavior upon cooling as discussed before. In the (ABAC)$_n$ segmented copolymers a second segment based on PEG with different molecular weights (PEG$_{1k}$: 1.2 kg mol^{-1}, y = 26; PEG$_{2k}$: 2.2 kg mol^{-1}, y = 48; PEG$_{4k}$: 4.0 kg mol^{-1}, y = 88) and a commercially available telechelic PEG with poly(propylene oxide) (PPO) units and amine endgroups (Jeffamine ED-900, M$_n$ = 894 g mol^{-1}) was additionally introduced. The (ABAC)$_n$ segmented copolymers were synthesized via polyaddition in THF on a scale between 10 and 25 grams.

Material properties: It was shown that (ABAC)$_n$ segmented copolymers based on PEG$_{1k, 2k, 4k}$ show a different thermal and especially rheological behavior than the Jeffamine based copolymers. At temperatures around 140 °C only the (ABAC)$_n$ segmented copolymers **PDMS-PEG$_{1k}$ (93/7)**, **PDMS-PEG$_{2k}$ (85/15)**, and **PDMS-PEG$_{4k}$ (77/23)** show a viscous behavior. The other copolymers with higher PEG$_{1k, 2k, 4k}$ content did not form low viscous melts. This limiting behavior can be avoided by incorporating Jeffamine ED-900 instead of PEG. Jeffamine based (ABAC)$_n$ segmented copolymers show a viscous behavior at temperatures above 70 °C and elastic properties below the crossover temperature with low melt viscosities optimal for melt processing. However, it is interesting that the melt viscosity of **PDMS-Jeffamine (22/78)** with the highest Jeffamine content of 78 wt.% dramatically increased to $\eta^*_{120\,°C}$ = 1425 Pa·s compared to the copolymers with less Jeffamine content as for **PDMS-Jeffamine (92/8)** with $\eta^*_{120\,°C}$ = 17 Pa·s and for **PDMS-Jeffamine (62/38)** with $\eta^*_{120\,°C}$ = 43 Pa·s. The same trend is observed for the mechanical properties evaluated by tensile tests. The toughness increases from 193 J m^{-3}10^4 for **PDMS-Jeffamine (92/8)** to 6929 J m^{-3}10^4 for **PDMS-Jeffamine (22/78)**. Small angle X-ray scattering (SAXS) was conducted revealing one broad signal without higher order. With increasing Jeffamine content this signal shifts towards lower *q* values. The interdomain spacing *d* increased from 4.8 nm for **PDMS-Jeffamine (92/8)** to 12.8 nm for **PDMS-Jeffamine (62/38)** and to 16.3 nm for **PDMS-Jeffamine (22/78)**. The morphology of the (ABAC)$_n$ segmented copolymers was

further analyzed by transmission electron microscopy (TEM). For **PDMS-Jeffamine (92/8)** a fine and grainy morphology was observed while for **PDMS-Jeffamine (62/38)** long, darker, and brighter features with a thickness of about 10 – 15 nm were visible. In **PDMS-Jeffamine (22/78)** larger PDMS domains are formed which impedes a sufficient mixing of the phases. This phase separation supports and reinforces the material properties while simultaneously restricting a low viscous melt to form due to the incompatibility of the separated phases.

Hydrogel properties: Determining the hydrogel properties of the amphiphilic (ABAC)$_n$ segmented copolymers it was found that a certain hydrophobic PDMS content has to be incorporated to maintain the hydrogel stability and prevent it from falling apart. The gel stability is not solely dependent on the PDMS content but also on the PEG chain length. Stable hydrogels with a water uptake depending on the PEG chain length and more significantly, on the PEG content were realized. For example, **PDMS-Jeffamine (62/38)** with a Jeffamine content of 38 wt.% forms a stable hydrogel with an equilibrium water content of 54%. Adjusting the ratio of the hydrophobic PDMS and hydrophilic PEG segments, the hydrogel properties can be tuned for the desired application.

The increasing hydrophilicity of the (ABAC)$_n$ segmented PDMS-Jeffamine copolymers was also demonstrated by contact angle measurements. Here a rearrangement of the hydrophobic PDMS and hydrophilic Jeffamine segments at the surface was postulated. Initially the hydrophobic nature dominates at the copolymer/air interface. Upon contact with water within few seconds the hydrophilic Jeffamine segments migrate to the interface due to the dynamic nature of the materials.

In conclusion, these amphiphilic (ABAC)$_n$ segmented copolymers enable the fabrication of a hydrogel with tunable properties. This includes gel stability and swelling capacity in dependency of the hydrophilic segment chain length and the built-in ratio of the hydrophobic PMDS and hydrophilic PEG segments while maintaining melt processability. Utilizing Jeffamine, the melt viscosity of the copolymer system is sufficiently low for additive manufacturing techniques. The (ABAC)$_n$ segmented copolymers based on PEG are primarily processable by melt pressing only due to their significantly higher melt viscosities within the thermal stability range. These copolymers are predestinated for non-degradable, swellable supporting structures in biofabrication.

4.3. Melt extrusion-based 3D printing

Especially the emerging research field of extrusion-based 3D printing from the melt is gaining more and more importance owed to the ease of fabricating complex 3D structures. Therefore, in the following, the melt processing via extrusion-based 3D printing of the (ABAC)$_n$ segmented copolymers including the variation of printing parameters is discussed regarding fiber diameter and printing accuracy as well as the hydrogel behavior of the printed structures.

4.3.1. Extrusion-based 3D printing setup

The commercial available Cellink+ bioprinter shown in Figure 4.33 is based on a pneumatic micro-extrusion technique. The printer contains two separate controllable printing heads for alternating printing of two materials. Within this thesis only one printing head was used. The polymer is molten in a heated aluminum syringe at 130 °C equipped with a stainless steel cannula of an inner diameter of 410 μm and equilibrated for 10 min before printing. The cannula was shortened to about 5 mm to prevent solidification of the polymer within the cannula. The temperature of 130 °C was chosen to ensure a homogenous melt and a sufficient low melt viscosity, as determined by oscillating shear rheology in chapter 4.2.3. A compressed air pressure ranging from 1.5 to 3 bar was applied. By moving the collector plate in x-, y-, and z-direction controlled by an external software the polymer jet is precisely deposited on a silicon wafer.
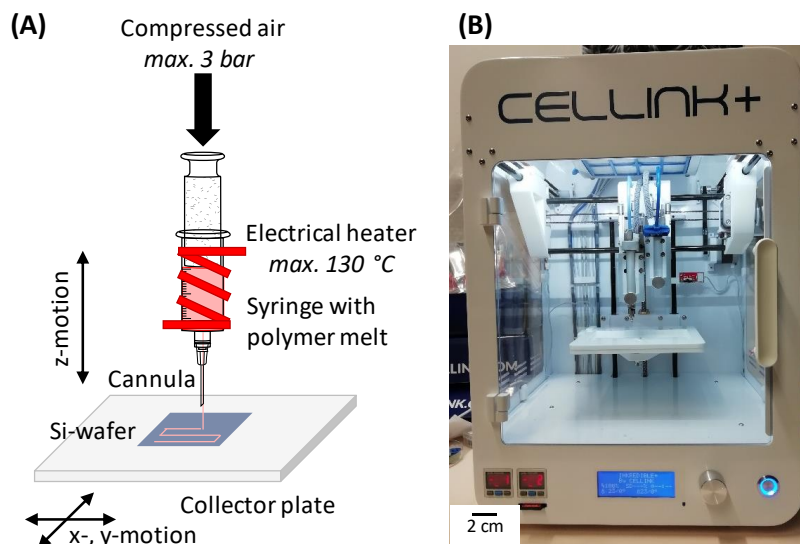
Figure 4.33: (A) Schematic setup of the extrusion-based Cellink+ 3D bioprinter. Compressed air is applied to an aluminum syringe which can be heated up to a maximum of 130 °C. A stainless steel cannula with an inner diameter of 410 μm and a length of 5 mm is utilized. The polymer jet is deposited in a controlled fashion by moving the collector plate in x-, y-, and z-direction. **(B)** shows a photograph of the commercial available printer.

4.3.2. Material selection

(ABAC)$_n$ segmented copolymers with physical crosslinks are intrinsically perfect candidates for melt processing due to their thermoreversible nature. However, it was shown within this thesis that not all synthesized amphiphilic (ABAC)$_n$ segmented copolymers are able to form low enough viscous polymer melts around 120 - 130 °C to be printed with the Cellink+ bioprinter. Is the viscosity of the material too high, the material cannot be processed since the back pressure within the cannula is too high. The supplier suggests processing of materials at viscosities less than 250 Pa·s. The (ABAC)$_n$ segmented copolymers **PDMS-PEG$_{1k}$ (93/7)**, **PDMS-PEG$_{2k}$ (85/15)**, and **PDMS-PEG$_{4k}$ (77/23)** show viscosities at 130 °C ranging from 35 to 270 Pa·s allowing in principle melt processing via extrusion-based 3D printing. However, the copolymers with a higher PEG$_{1k, 2k, 4k}$ content showed an elastic behavior at 130 °C (chapter 4.2.3), resulting in too high viscosities which is why these copolymers are not suitable candidates for extrusion-based 3D printing.

As for the (ABAC)$_n$ segmented PDMS-Jeffamine copolymers **PDMS-Jeffamine (92/8)** and **PDMS-Jeffamine (62/38)** the complex viscosities determined by rheology at 130 °C are in the promising range for extrusion-based 3D printing, ranging from 11 Pa·s to 28 Pa·s. Both copolymers form stable hydrogels with a water content of 9% and 54%. Since the fabrication of 3D structures with stable gel properties in water and hydrogels with different water contents are desirable these two copolymers will be processed utilizing extrusion-based 3D printing within the frame of this thesis. **PDMS-Jeffamine (22/78)** shows on the contrary a dramatically increased viscosity of 935 Pa·s at 130 °C which is too high for this extrusion-based 3D printing technology as well as poor gel stability in the swollen state.

4.3.3. Fabrication and characterization of 3D printed scaffolds and hydrogels

PDMS-Jeffamine (92/8) was processed by extrusion-based 3D printing applying different pressures and printing velocities to study the influence on strand width and deposition accuracy. The lowest applied pressure to generate a stable melt jet was found to be 1.5 bar at 130 °C which was determined by sequentially increasing the pressure. The printed scaffolds are composed of three layers with a total length of 10 mm and a width of 10 mm. The first (bottom layer) and third (top layer) layer consists of 6 rows in y-axis and the second layer (middle layer) of 6 rows in x-axis. A schematic illustration of the printed pattern (2 layers) is shown in Figure 4.34.
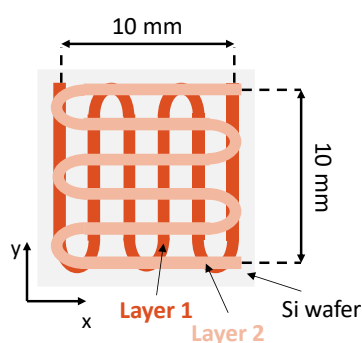
Figure 4.34: Schematic illustration of the extrusion-based 3D printing pattern (2 layers) using the Cellink+ bioprinter. The printed structure has a total length of 10 mm and a width of 10 mm. The 1st layer (bottom layer) with 6 rows is printed in y-axis, while the 2nd layer, also consisting of 6 rows, is printed in x-axis.

In Figure 4.35 SEM images of the dry scaffold printed at 130 °C, 1.5 bar, and 200 mm min^{-1} are depicted. A crossing point of three layers is shown **(A)**. Single strands without coalescence, yet with a smooth surface were obtained owed to the fast solidification of the material. The first layer is printed homogenously onto the silicon wafer while additional layers are accurately deposited as round strands as seen in the tilted image **(B)**. For this scaffold printed at 1.5 bar and with a velocity of 200 mm min^{-1} a strand width of 553 ± 85 μm was determined.
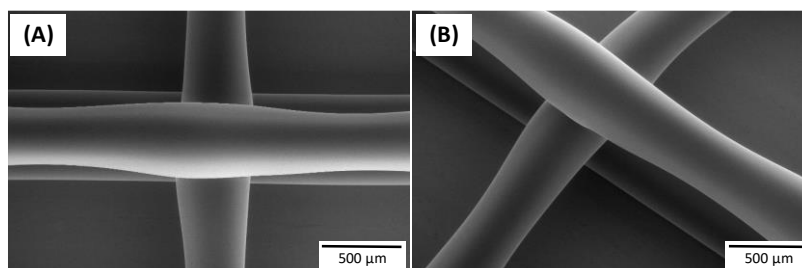
Figure 4.35: SEM image of a scaffold based on the (ABAC)$_n$ segmented **PDMS-Jeffamine (92/8)** copolymer. **(A)** showing in top view an accurate strand deposition and **(B)** in tilted view good stacking. The 1st layer shows an increased spreading on the wafer surface whereas the 2nd and 3rd layer form round strands. Homogenous and smooth strand surfaces are observed. Printing conditions: 130 °C, 1.5 bar, 200 mm min^{-1}.

With decreasing printing velocity, the strand width increases. Applying 1.5 bar and 100 mm min^{-1} a strand width of 623 ± 60 μm is obtained. Increasing the applied pressure, the strand width increases further due to an increasing flow rate. Increasing the applied pressure to 2.0 bar the strand width increases to 887 ± 146 μm at 100 mm min^{-1} and to 576 ± 115 μm at 200 mm min^{-1}. The relatively high

standard deviation results from inhomogeneities within the strand width due to dragging of the strand. The final strand widths are larger than the cannula inner diameter (410 µm) which is owed to squeezing of the melt through the cannula.

Printing the more amphiphilic $(ABAC)_n$ segmented **PDMS-Jeffamine (62/38)** copolymer, a higher pressure of 3.0 bar was necessary to obtain a homogenous and stable melt jet at 130 °C, thus reaching the processing limits of the setup. Neither higher pressures nor temperatures are possible utilizing this setup. In Figure 4.36 **(A)** a SEM image of a printed scaffold is imaged applying a printing velocity of 100 mm min^{-1}. Single strands with an average strand width of 585 ± 109 µm and a smooth surface were obtained which did not fuse together. The bottom layer appears more flat than round owed to squeezing of the melt. Increasing the printing speed to 200 mm min^{-1} **(B)** the strands become thinner with an average strand width of 346 ± 57 µm. However, the shape appears a lot more inaccurate in size especially at the junctions where they are thicker and then being stretched due to dragging of the melt jet. The strand width can be significantly decreased to 298 ± 31 µm by increasing the printing velocity to 800 mm min^{-1}, however, sacrificing a homogenous strand width and deposition **(C)**. Further, beading occurs along the single strand owed to a non-continuous melt jet. In summary, scaffolds of **PDMS-Jeffamine (62/38)** can be fabricated by extrusion-based 3D printing, but the strand dimensions are limited by the device parameters and the copolymer viscosity.
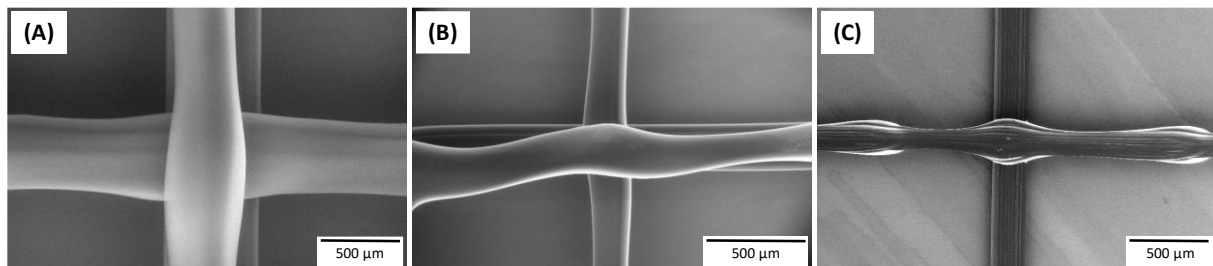
Figure 4.36: SEM images of scaffolds based on **PDMS-Jeffamine (62/38)** with increasing printing velocity. Increasing printing velocity leads to significant lower strand width sacrificing homogenous strand width. Printing conditions: 130 °C, 3 bar, **(A)** 100 mm min^{-1}, **(B)** 200 mm min^{-1} and **(C)** 800 mm min^{-1}, respectively.

The **PDMS-Jeffamine (22/78)** could not be printed with the Cellink+ bioprinter due to the high viscosity of the copolymer ($\eta^*_{130\,°C}$ = 935 Pa·s) and the setup restrictions of max. pressure of 3 bar and max. temperature of 130 °C.

The swelling behavior of the 3D printed scaffolds fixed on a silicon wafer was investigated by swelling the scaffolds for 24 h in DI water. Figure 4.37 shows photographs of the dry and swollen scaffolds based on **PDMS-Jeffamine (92/8)** and **PDMS-Jeffamine (62/38)**. The scaffolds were printed at 130 °C and 100 mm min^{-1} at a pressure of 1.5 bar and 3.0 bar, respectively. For the more hydrophobic $(ABAC)_n$ segmented **PDMS-Jeffamine (92/8)** copolymer the scaffold dimensions do only marginal change upon water uptake. As known from the hydrogel properties (chapter 4.2.6) this hydrogel only shows an equilibrium water content of 9% which is extremely low and cannot be optically quantified. However, the scaffold based on the more hydrophilic copolymer **PDMS-Jeffamine (62/38)** deforms and increases in size upon water uptake. The overall equilibrium water content of the hydrogel was determined previously to be 54%. The single strands swell in z-direction and grow in altitude but are still fixed on the substrate.
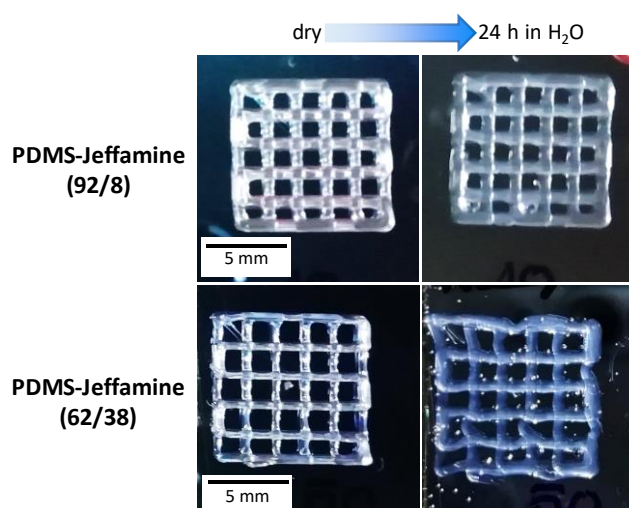
Figure 4.37: Images of printed dry and swollen scaffold of **PDMS-Jeffamine (92/8)** and **PDMS-Jeffamine (62/38)**. After storing in DI water for 24 h no change is observed for the more hydrophobic **PDMS-Jeffamine (92/8)** while the more hydrophilic **PDMS-Jeffamine (62/38)** hydrogel deforms and increases in altitude due to water uptake. Printing parameters: 130 °C, 100 mm min^{-1}, 1.5 bar and 3.0 bar, respectively.

The swelling of the hydrogel scaffolds was also qualitatively investigated by environmental scanning electron microscopy (ESEM). ESEM images allow a detailed view on the swollen and dry state of the printed 3D structures. The measurements were jointly conducted with Andreas Frank, Macromolecular Chemistry I. The dry scaffolds were swollen *ex-situ* in DI water for 7 days prior measurement. The hydrogel scaffolds were transferred in the sample chamber of the microscope. The samples were dried *in-situ* to determine the dimensional change upon water evaporation. In Figure 4.38 **(A)** the intersection of three layers of **PDMS-Jeffamine (92/8)** is shown in the swollen state. The dried scaffold is depicted in **(B)**. In both states, the surface morphology of the strand was smooth and uniform. The swollen scaffold releases water upon drying at 5 °C and 300 Pa for 1 h (humidity: 34%). **(C)** visualizes the superposition of the dried and swollen state. The yellow strand indicates the dried scaffold while the green represents the swollen state. A deswelling of 4.7% in strand width was determined from the dimensional change.

swollen state | dried state | superposition of swollen and dried state
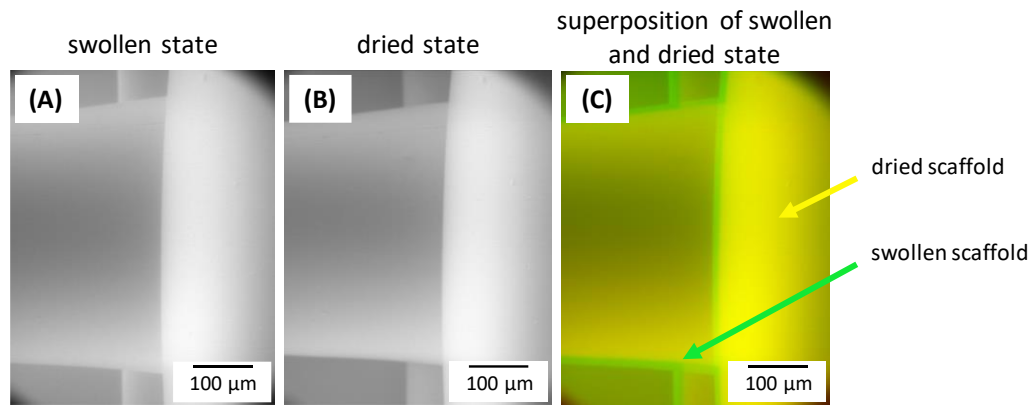
Figure 4.38: ESEM image of **(A)** the swollen and **(B)** dried scaffold based on **PDMS-Jeffamine (92/8)** at the intersection of the bottom, middle, and top layers. **(C)** Visualization of the volume change upon superposition of the swollen and dried 3D hydrogel structure. The scaffold was swollen for 7 days in DI water and dried *in-situ* at 5 °C and 300 Pa for 1 h (humidity: 34%). A deswelling of 4.7% in strand width was observed. Printing parameters: 130 °C, 1.5 bar, 200 mm min^{-1}.

By *in-situ* drying at a humidity of 34% at 5 °C and 300 Pa for 1 h the deswelling of the swollen **PDMS-Jeffamine (62/38)** based scaffold (two layers) was also investigated by ESEM as shown in Figure 4.39. **(A)** depicting the swollen state, **(B)** the dried state showing in both states a uniform surface. In **(C)** the superposition of the swollen and dried state is shown. A deswelling of 7.1% in strand width, reveal a more hydrophilic behavior of the hydrogel compared to **PDMS-Jeffamine (92/8)**, owed to the increased Jeffamine content.

swollen state | dried state

superposition of swollen and dried state
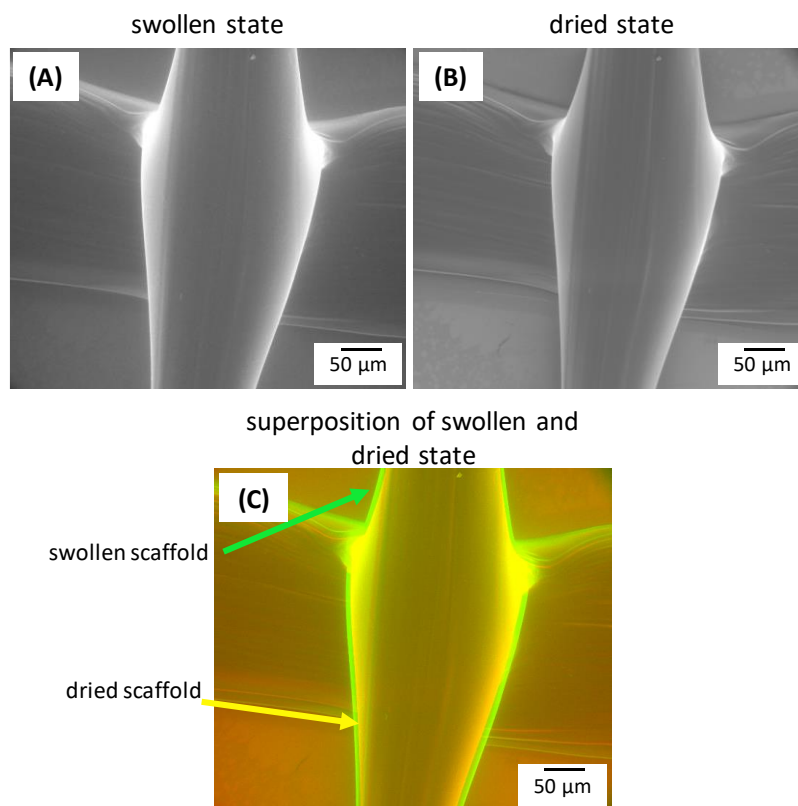
Figure 4.39: ESEM image of **(A)** the swollen and **(B)** dried scaffold based on **PDMS-Jeffamine (62/38)** at the intersection of two layers. **(C)** Visualization of the volume change upon superposition of the swollen and dried 3D hydrogel structure. The scaffold was swollen for 7 days in DI water and dried *in-situ* at 5 °C and 300 Pa for 1 h (humidity: 34%). A deswelling of 7.1% was observed. Printing parameters: 130 °C, 3.0 bar, 800 mm min^{-1}.

174

4.3.4. Conclusion of chapter 4.3.

Since additive manufacturing from the melt is an important tool in biofabrication it was demonstrated that the $(ABAC)_n$ segmented copolymers **PDMS-Jeffamine (92/8)** and **PDMS-Jeffamine (62/38)** are excellent candidates for *extrusion-based 3D printing* with the Cellink + bioprinter. This is due to their suitable melt viscosities at processing temperature of 130 °C and their thermal stability during the processing period. Both copolymers were processed into defined 3D constructs. Varying the processing parameters including pressure and printing velocity while maintaining a stable melt jet, the average strand width and deposition can be controlled. It was shown that for **PDMS-Jeffamine (62/38)** a higher pressure of 3.0 bar was necessary to obtain a stable melt jet compared to **PDMS-Jeffamine (92/8)** utilizing 1.5 bar. At low printing velocities of 100 mm min^{-1} accurate strand deposition of uniform and smooth strands was achieved. While increasing the speed, the strands become more inhomogeneous due to dragging of the melt jet, before at a velocity of 800 mm min^{-1} bead formation and a large variation of the strand width and inaccurate strand deposition is observed.

These 3D scaffold structures were swollen in DI water demonstrating the water uptake. The water uptake correlates to the Jeffamine content which increases with increasing Jeffamine content. This behavior was investigated in more detail utilizing environmental scanning electron microscopy, showing the drying process of the hydrogel scaffolds *in-situ*.

4.4. Hydrogel gradient with continuously changing hydrophilicity

Within this chapter the synthesized amphiphilic (ABAC)$_n$ segmented copolymers are used for the fabrication of a hydrogel gradient material with a continuously changing hydrophilicity. Gradient materials are of interest due to their potential in biofabrication and to study cell adhesion, proliferation, and growth.

As for many applications in biofabrication mechanical gradient materials are of interest. They can mediate between soft tissue and hard bones or allow studies of cell adhesion, proliferation, and growth due to continuously changing mechanical properties. Cells are known to migrate towards a defined substrate modulus, where they proliferate and grow.[195] However, for biofabrication besides a mechanical gradient also a continuous change in hydrophilicity is of interest. Thus, gradient materials combining continuously varying mechanical properties and hydrophilicity on a centimeter length scale are ideal candidates for cell studies. The amphiphilic (ABAC)$_n$ segmented copolymers introduced in chapter 4.2 combine hydrophobic and inert properties of the PDMS segment with hydrophilic ones owed to the PEG segment. These materials can absorb water in a tunable fashion depending on the composition of PDMS to PEG and on the chain length of the hydrophilic segment.

In the following the fabrication of a longitudinal mechanical stable hydrogel gradient with a continuously changing water swelling capacity along the specimen axis is targeted. This should be achieved by choosing two amphiphilic (ABAC)$_n$ segmented copolymers with on the one hand a low and on the other hand a high hydrophilicity combined with different mechanical properties. For this reason, binary mixtures of two components were prepared and characterized to select two suitable components with a sufficient gel stability over the entire gradient region to exclude a fragile and brittle hydrogel gradient. Further determine their properties in dependency of the composition of the binary mixtures including swelling and mechanical properties since from these results the gradient properties can be concluded. PDMS-Jeffamine copolymers are chosen over PDMS-PEG copolymers because of their solubility in common organic solvents, good thermo-mechanical properties, and improved hydrogel stability independent of the built-in ratio of PDMS and Jeffamine.

4.4.1. Binary mixtures of the PDMS-Jeffamine copolymers

First the two *(ABAC)$_n$ segmented copolymers* **PDMS-Jeffamine (92/8)** and **PDMS-Jeffamine (22/78)** with a large difference in their amphiphilic behavior (water content: W = 9% *vs.* 86%), showing the possibility to generate a gradient with a large property variation, were selected. Five binary mixtures with different ratios of 90/10, 70/30, 50/50, 30/70 and 10/90 (wt.%/wt.%) were prepared. In the following the overall Jeffamine content of these binary mixtures is discussed which is the sum of the percentage resulting from both Jeffamine contents. As for the mixing ratio 90/10 a total Jeffamine content of 15 wt.% is calculated from 90% of 8 wt.% plus 10% of 78 wt.% Jeffamine content. The mixtures were prepared from a 20 wt.% solution in THF being cast into a Teflon® mold and dried under ambient conditions to obtain dry films. These were characterized concerning their equilibrium degree of swelling *Q* and their water content *W* in dependency of the overall Jeffamine content following the same procedure of the amphiphilic (ABAC)$_n$ segmented copolymers as described in detail in chapter 5.2.

As can be seen in Figure 4.40 **(A)** the degree of swelling increases with increasing Jeffamine content. The boundary conditions are given by the two amphiphilic copolymers **PDMS-Jeffamine (92/8)** and **PDMS-Jeffamine (22/78)** with Q = 9% and Q = 626%, respectively (chapter 4.2.6), indicated by open symbols. The data of the binary mixtures are shown as closed symbols. The water content as a function of the total Jeffamine content is also raising with increasing amount of **PDMS-Jeffamine (22/78)**. However, the hydrogels of the binary mixtures are not mechanical stable over the entire Jeffamine content range. Above a total Jeffamine content of 43 wt.% the hydrogels turn into fragile and brittle materials, losing their form stability and falling apart into non-water soluble gel fragments.
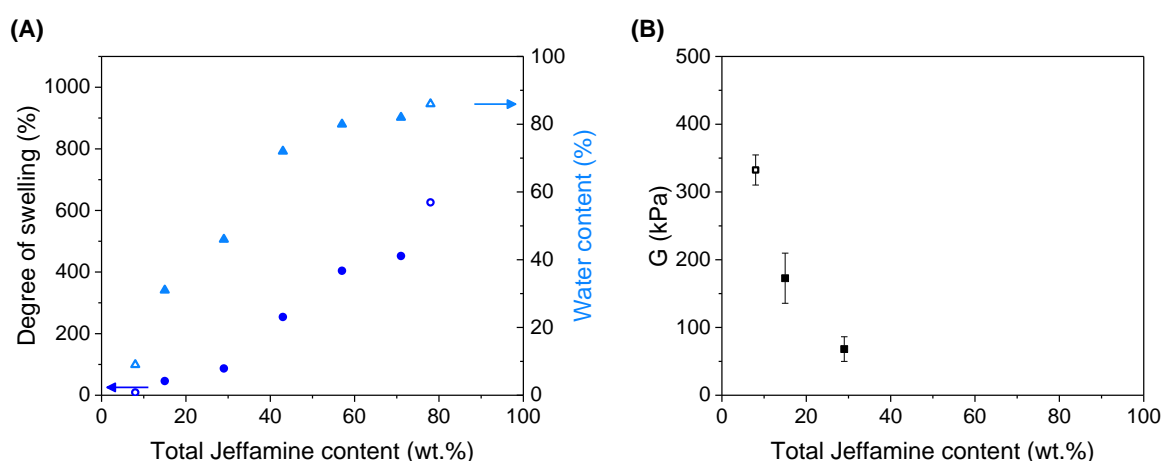
Figure 4.40: (A) Degree of swelling and water content as a function of the total Jeffamine content of binary mixtures of **PDMS-Jeffamine (92/8)** and **PDMS-Jeffamine (22/78)**. The open symbols represent the properties of the **PDMS-Jeffamine (92/8)** and **PDMS-Jeffamine (22/78)** while the closed symbols represent the data of the binary mixtures. **(B)** shows the shear modulus as a function of the total Jeffamine content. Indentation measurements could only be conducted up to 29 wt.% Jeffamine content and a water uptake of 46%. The hydrogel become mechanical instable at a Jeffamine content larger than 43 wt.% and a water uptake of 72%. Detailed experimental data are included in chapter 5.2.

Additionally, indentation measurements were conducted to determine the mechanical properties, more specifically the shear modulus, of the hydrogels. The shear moduli of the hydrogels were determined by the indentation method using a sphere with a diameter of 4 mm and fitting the force-displacement curves according to Segedin's model.[196,197] An average of at least five measurements is given. In Figure 4.40 **(B)** the shear modulus G is plotted in dependency of the overall Jeffamine content. Only three values could be determined due to the insufficient mechanical stability of the hydrogel during measurement. Nevertheless, with a Jeffamine content of 8 wt.% a shear modulus of 332 ± 22 kPa was determined which decreases to 68 ± 18 kPa for a hydrogel with a hydrophilic Jeffamine content of 29 wt.%. With an increasing amount of hydrophilic component, the hydrogel mixtures take up more water and the shear modulus simultaneously decreases. This phenomenon is limited by the hydrophobic PDMS content which is responsible for the mechanical strength while reducing the swelling capacity. It was found that a PDMS content of 57 wt.% is necessary to maintain a form stable specimen (chapter 4.2.6). These results show that by combining these two amphiphilic (ABAC)$_n$ segmented copolymers a sufficient gel stability can only be achieved up to a total Jeffamine content of 43 wt.% with a degree of swelling of 328% and a water content of 77%. A higher Jeffamine content results in fragile and brittle hydrogels.

To identify the mechanical stable hydrogel region in combination with the degree of swelling and water uptake in dependency of the Jeffamine content in more detail, binary mixtures of the *(ABAC)$_n$* *segmented copolymers* **PDMS-Jeffamine (92/8)** *and* **PDMS-Jeffamine (62/38)** were prepared. As discussed previously both copolymers form mechanical stable hydrogels thus it is expected that each mixture forms also a mechanical stable hydrogel. Again binary mixtures with ratios of 90/10, 70/30, 50/50, 30/70, and 10/90 (wt.%/wt.%) were prepared from a 20 wt.% THF solution. The overall Jeffamine content is discussed in the following. In Figure 4.41 **(A)** the degree of swelling Q and the water uptake W in dependency of the total Jeffamine content is plotted. As expected, both Q and W raise with increasing Jeffamine content and are limited by the boundary conditions of the two amphiphilic hydrogels **PDMS-Jeffamine (92/8)** and **PDMS-Jeffamine (62/38)** (open symbols). Each binary hydrogel mixture exhibits good gel stability. The PDMS content in these systems sufficiently supports the mechanical strength of the hydrogels. The mechanical properties of these hydrogels were also investigated by indentation measurements. The shear modulus G is shown in Figure 4.41 **(B)** as a function of the total Jeffamine content. An inverted behavior to the water content is observed. With increasing Jeffamine content and consequently a larger amount of absorbed water, the shear modulus decreases implying a softer hydrogel. The shear modulus declines from 332 ± 22 kPa to 87 ± 17 kPa for **PDMS-Jeffamine (92/8)** and **PDMS-Jeffamine (62/38)**.
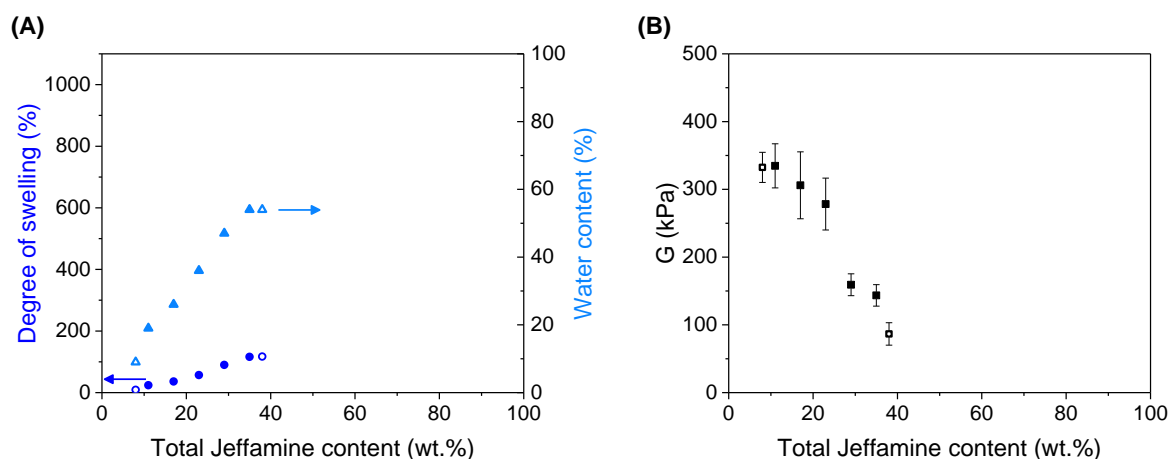
Figure 4.41: (A) Degree of swelling, water content and **(B)** shear modulus as a function of total Jeffamine content of binary mixtures of **PDMS-Jeffamine (92/8)** and **PDMS-Jeffamine (62/38)**. The open symbols represent the properties of the **PDMS-Jeffamine (92/8)** and **PDMS-Jeffamine (62/38)** while the closed symbols represent the data of the binary mixtures. The shear modulus *G* indicates a softening of the hydrogel with increasing Jeffamine content. Detailed experimental data are included in chapter 5.2.

It was shown that by combining the two copolymers **PDMS-Jeffamine (92/8)** and **PDMS-Jeffamine (62/38)** mechanical stable hydrogels with linearly increasing swelling capacity and water content in dependency of the total Jeffamine content could be prepared. Hence, these two amphiphilic (ABAC)$_n$ segmented copolymers were chosen to fabricate a hydrogel gradient on a cm-scale.

4.4.2. Fabrication and characterization of hydrogel gradients

For the fabrication of a hydrogel gradient with a continuously changing hydrophilic behavior along the specimen axis a low-pressure high precision syringe pump setup introduced by Claussen *et al.* was used.[147,156] Here in this case the gradients were prepared from solution. The setup used shows a close resemblance to the setup used in chapter 3.4, yet without any heating elements. Two glass syringes, each containing one component, a more hydrophobic and a more hydrophilic one, respectively, are connected via disposable tubes to a disposable static mixer. A flow profile is applied by an external software allowing the extrusion of the gradient mixture into a Teflon® mold being mounted on a linear moving platform. For optical visualization and characterization 0.02 wt.% Lumogen® Red F300 was added to the softer, more hydrophilic component. The detailed experimental setup is described in the experimental part in chapter 5.2.

The gradient was fabricated from a 50 wt.% isopropanol solution utilizing a high precision syringe pump setup at room temperature. 50 wt.% isopropanol solution was found to be ideal for this processing technique. Melt processing was not conducted due to a limited amount of material. The applied flow profile is shown in Figure 4.42 **(A)**. First the more hydrophobic component **PDMS-Jeffamine (92/8)** is added constantly for 6 s at a flow rate of 100 µL s^{-1} before the flow rate is continuously lowered to 0 µL s^{-1} over 50 s. The second, more hydrophilic component **PDMS-Jeffamine (62/38)** is added after 6 s while the flow rate is continuously raised from 0 µL s^{-1} to 100 µL s^{-1} over 50 s before it is constantly added for additional 14 s. Starting the fabrication process, the static mixer is filled according to the flow profile. The actual filling of the mold starts after 14 s, after the dead volume of the static mixer is filled. For optical visualization and characterization 0.02 wt.% of the dye Lumogen$^{®}$ Red F300 was added to the second more hydrophilic and softer component **PDMS-Jeffamine (62/38)**. Figure 4.42 **(B)** shows a photograph of the fabricated amphiphilic gradient. The UV-Vis characterization along the sample is shown in **(C)**. A continuously increasing absorption over the first 50 mm is observed, demonstrating the gradient region. Afterwards a plateau (linear region) of only the second, more hydrophilic component **PDMS-Jeffamine (62/38)** is present. The prepared strip was dried at room temperature for 72 h. The dry sample with a thickness of about 0.6 mm was removed from the mold.
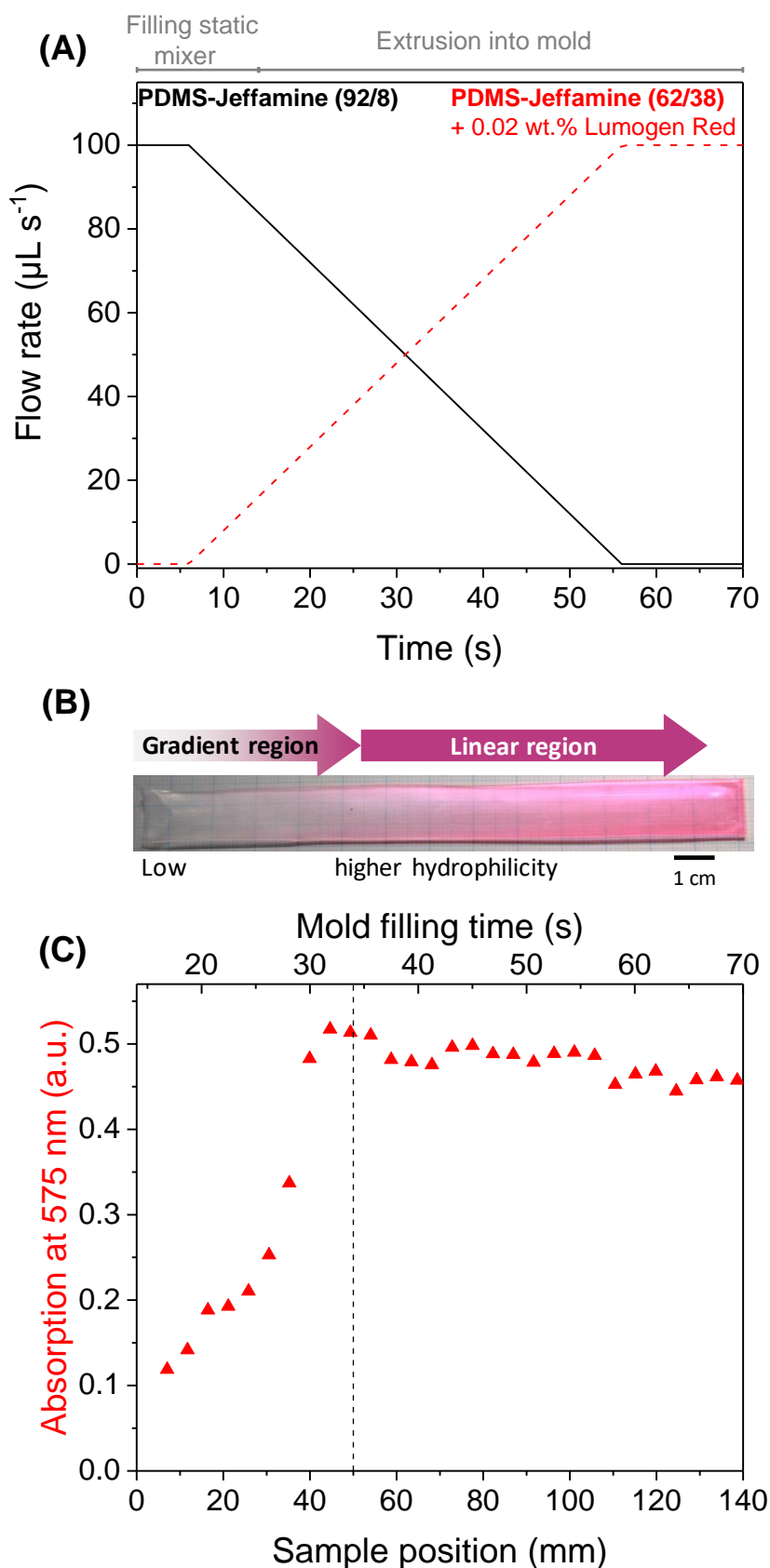
Figure 4.42: (A) Flow profile of solution processed amphiphilic gradient (isopropanol, 50 wt.%). First the more hydrophobic component **PDMS-Jeffamine (92/8)** is pumped steadily before it is reduced continuously to a flow rate of 0 μL s^{-1}. The second, more hydrophilic and softer component **PDMS-Jeffamine (62/38)** is fed the opposite way and for optical characterization 0.02 wt.% Lumogen® Red F300 was added. In **(B)** a photograph of the fabricated gradient is shown. The optical characterization of the gradient by UV-Vis measurements is shown in **(C)**. The continuous increasing absorbance of the added dye is detected confirming the generated gradient region of 50 mm.

The dried gradient strip (a) was swollen in DI water for several hours and images were taken to visualize the water uptake and swelling of the gradient as well as the gel stability. As can be seen in Figure 4.43 after 2.5 h (b) the gradient started to expand along the axis with increasing **PDMS-Jeffamine (62/38)** content, after 24 h (c) the maximum swelling was reached. The more hydrophilic component **PDMS-Jeffamine (62/38)** is able to take up a higher amount of water than the more hydrophobic component **PDMS-Jeffamine (92/8)**. This is due to the increased amount of polar segments and the absorption of water into these domains. After drying (d) the hydrogel gradient for several days at 30 °C, the original shape and geometry is obtained again demonstrating the reversible water uptake and release.
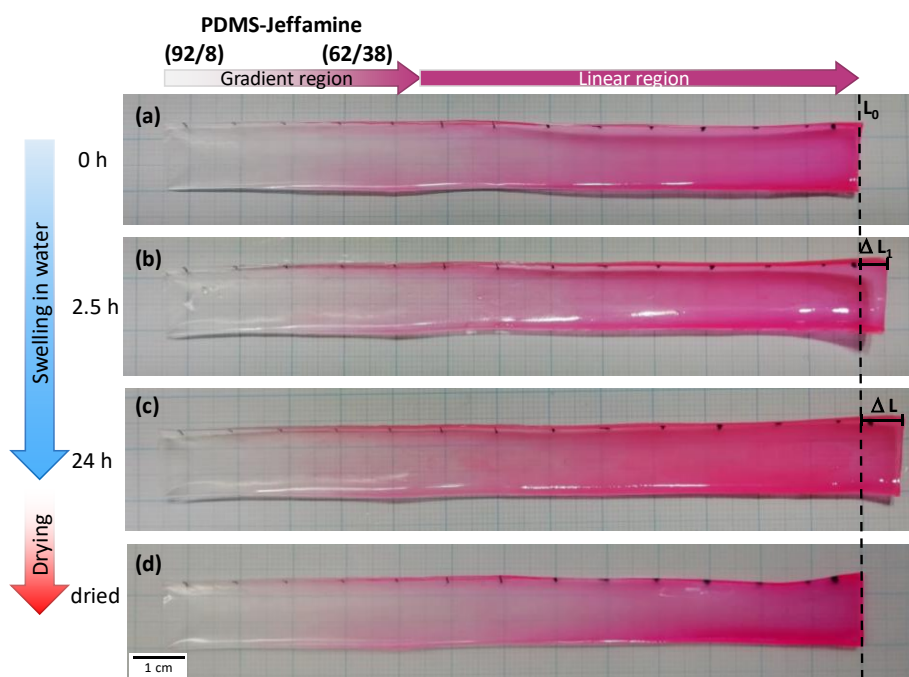
Figure 4.43: Photograph of solution processed amphiphilic gradient, continuously changing its composition from **PDMS-Jeffamine (92/8)** (transparent) to **PDMS-Jeffamine (62/38)** (pink). For optical visualization 0.02 wt.% Lumogen® Red F300 was added to the latter component. The gradient is shown **(a)** in dry state (0 h), **(b)** after 2.5 h, and **(c)** 24 h swollen in DI water. The increasing water uptake towards the colored component is clearly visible while at the starting point with only 8 wt.% Jeffamine swelling is not obvious. **(d)** After drying the gradient, the original geometry is again observed, demonstrating the dynamic uptake and release of water.

The amphiphilic behavior of the gradient material was characterized in more detail by contact angle measurements along the longitudinal axis of the gradient region. The gradient sample was initially melt pressed at 120 °C and 100 bar for 1 min between PTFE foils to obtain a homogenous flat surface. The contact angle (CA) of a water droplet was recorded and analyzed directly after placing the droplet onto the surface (0 sec), after 1 min, and 5 min. In Figure 4.44 these water sessile drops are shown as a function of time and sample position within the gradient region as determined by UV-Vis spectroscopy. With increasing Jeffamine content along the gradient axis from 1 cm to 5 cm the CA decreases at 0 sec from 98° to 90°. These CA, however, indicate a more hydrophobic origin as due to the migration of the PDMS polymer chains to the surface as discussed in chapter 4.2.6. Yet over time the CA decrease, indicating a more hydrophilic behavior owed to rearrangement of the polymer chains at the interface. The polar Jeffamine chains migrate to the surface suppressing the hydrophobic PDMS segments due to change of contact medium from air to water. As a consequence, the CA decrease from 87° to 67°.
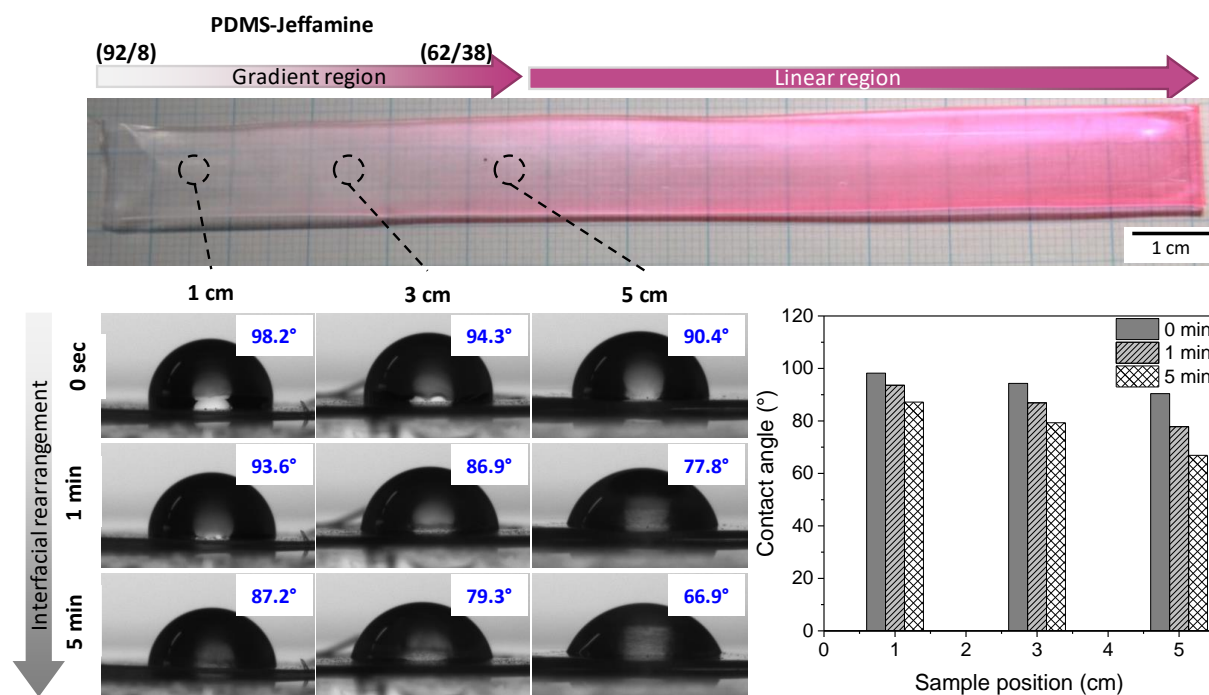
Figure 4.44: Contact angle measurements along the amphiphilic, physically crosslinked gradient in dependency of sample position and time. Along the gradient region a decreasing CA was observed proving the increasing hydrophilicity due to an increasing Jeffamine content. Within 5 min the CA further decrease due to soft segment rearrangement at the interface resulting in an overall more hydrophilic nature. Detailed experimental data are included in chapter 5.2.

These continuously decreasing CA in dependency of the sample position prove even more the gradient structure and the continuously varying polarity. For the first time it was shown that amphiphilic (ABAC)$_n$ segmented PDMS-Jeffamine copolymers can form mechanical stable hydrogels up to a Jeffamine content of 38 wt.%. A gradient in hydrophilicity from hydrophobic (0 cm) to hydrophilic (5 cm) was accomplished suitable for cell experiments on a short distance. Within this gradient moduli ranging from 332 kPa to 87 kPa and a water uptake from 9% to 54% could be realized on a 50 mm length scale.

4.4.3. Conclusion of chapter 4.4.

Within this chapter it was shown that the synthesized amphiphilic (ABAC)$_n$ segmented PDMS-Jeffamine copolymers introduced in chapter 4.2 are ideal candidates for the fabrication of a *gradient material with a continuously changing hydrophilic behavior*. First the amphiphilic copolymers with different hydrophilic Jeffamine content of 8 wt.% and 38 wt.%, **PDMS-Jeffamine (92/8)** and **PDMS-Jeffamine (62/38)**, and different swelling capacities were mixed in solution at different ratios to obtain binary mixtures. At each composition stable hydrogels in the equilibrium swollen state were formed and thus selected for the fabrication of the hydrogel gradient. At an overall Jeffamine content higher than 38 wt.%, the hydrogels become fragile and brittle followed by losing the mechanical gel stability and break up into small non-water soluble gel fragments.

The gradient was processed from an isopropanol solution using the more hydrophobic copolymer **PDMS-Jeffamine (92/8)** and the more hydrophilic copolymer **PDMS-Jeffamine (62/38)** which was colored with a dye to visualize the gradient. The obtained gradient region of 50 mm was determined by UV-Vis spectroscopy demonstrating the continuous and linear increasing content of the softer, more hydrophilic **PDMS-Jeffamine (62/38)** component along the gradient axis followed by a linear region. Also, contact angle (CA) measurements confirmed the increasing hydrophilicity within the gradient region indicated by decreasing CA along the specimen axis.

To sum up, (ABAC)$_n$ segmented PDMS-Jeffamine copolymers based on hydrophobic PDMS and hydrophilic Jeffamine segments as well as *1,6-hexamethylene diisocyanate* segments are excellent candidates for biofabrication owed to their ease and flexibility of processing from solution as well as from the melt.

5. Experimental Part

5.1. Materials

The reagents were purchased from Gelest (PDMS-diamines: DMS-A12, DMS-A15, DMS-A21), Sigma Aldrich (1,6-hexamethylene diisocyanate, isophorone diisocyanate, 4,4'-methylene bis(cyclohexyl isocyanate), toluene-2,4-diisocyanate, benzylamine, poly(ethylene glycol), Jeffamine ED-900, triethyl-amine) and VWR (aqueous ammonia solution, 25%). All chemicals were used as received. Further chemicals were purchased from Kremer Farbpigmente (Lumogen® Red F300) and Merck (0.1 N HCl in isopropanol).

Solvents were distilled before use. Tetrahydrofuran was distilled over KOH. All polymerizations were performed in oven-dried glassware under an inert argon atmosphere. Argon was purchased from Linde (Argon 4.8) and dried over molecular sieves (3 Å). Deuterated solvents were purchased from Deutero.

The molecular weights of the diamines were determined by end group titration.

5.2. Characterization methods

End group titration

The number average molecular weight M_n of the diamines (PDMS-diamines, PEG-diamines, Jeffamine ED-900) was determined by potentiometric titration of the amine end groups using an 809 Titrando titration robot with an Solvotrode easyClean electrode from Metrohm. The prepolymers were weight into a 100 mL flask and dissolved in 60 mL of equal volume mixture of isopropanol (p.a.) and tetrahydrofuran (p.a.). The PEG-diamines were initially dried at 60 °C under high vacuum for at least 16 h. To titrate the amine end groups a standard titrant of 0.1 N HCl in isopropanol (Merck) was used. The number average molecular weight of the diamines was calculated according to equation **(5.1)**. An average of three measurements is given.

$$M_n = \frac{m_{polymer} \cdot \xi}{c \cdot V} \qquad \textbf{(5.1)}$$

With $m_{polymer}$ being the mass of the diamines, ξ the number of functional end groups (here: 2), c the concentration of the titrant and V being the consumed volume.

Fourier-transform infrared spectroscopy (FT-IR)

FT-IR measurements were performed on a Perkin Elmer FTIR Spectrum 100 spectrometer using the attenuated total reflectance unit (ATR). The spectra were recorded from $4000 - 550$ cm^{-1} using 16 scans and a resolution of 4 cm^{-1}.

Temperature dependent infrared spectroscopy (FT-IR)

Temperature dependent FT-IR measurements were conducted in transmission mode on a Perkin Elmer FTIR Spectrum 100 spectrometer. Initially two silicon wafers ($1 \cdot 1$ cm^2) were cleaned with ethanol, followed by preparing a melt sandwich of the polymer at 150 °C. The FT-IR spectra were recorded from 4000 – 450 cm^{-1} utilizing 16 scans and a resolution of 4 cm^{-1}. A heating / cooling profile from 30 to 170 °C in 10 K steps was applied. The measurements were conducted without equilibration times. The setup was cooled against room temperature.

^{1}H-Nuclear magnetic resonance spectroscopy (^{1}H-NMR)

^{1}H-NMR spectroscopy was performed on a BRUKER Avance 300 spectrometer with an operating frequency of 300 MHz. Deuterated chloroform and deuterated THF-d$_8$ were used as solvents. Chemical shifts are reported in ppm relative to the known value of residual solvent signal.

The built-in ratio of the amphiphilic, physical crosslinked copolymers was determined according to equation **(5.2)**:

$$\text{PEG/Jeffamine content (\%)} = \left(\frac{\frac{A_{PEG}}{4 \cdot y}}{\frac{A_{PEG}}{4 \cdot y} + \frac{A_{PDMS}}{6 \cdot x}} \right) \cdot 100 \qquad \textbf{(5.2)}$$

With A_{PEG} being the integral of the PEG/Jeffamine protons, A_{PDMS} the integral of the PDMS protons, y the repetition unit of the PEG/Jeffamine block (y = 26, 48, 88/12.5) and x being the repetition unit of the PDMS unit (x = 18).

Size exclusion chromatography (SEC)

Size exclusion chromatography was performed utilizing a Waters 515 HPLC pump and THF with 0.25 wt.% tetrabutylammonium bromide (TBAB) as eluent at a flow rate of 0.5 mL min^{-1}. A volume of 100 µL of polymer solution (5 mg mL^{-1}) was injected with a 707 Waters auto-sampler into a column setup comprising a guard column (Agilent PLgel Guard MIXED-C, 5 × 0.75 cm, particle size: 5 µm) and two separation columns (Agilent PLgel MIXED-C, 30 × 0.75 cm, particle size: 5 µm). Polymer size distributions were monitored with a Waters 414 refractive index (RI) detector. Narrow distributed polystyrene standards were used for calibration and 1,2-dichlorobenzene as an internal reference.

Differential scanning calorimetry (DSC)

Differential scanning calorimetry was conducted on a DSC^{3+} STAR^e System from Mettler Toledo. The heating and cooling runs were performed at a scan rate of 10 K min^{-1} under a constant flow of dry nitrogen (50 mL min^{-1}). Indium was used for calibration.

Thermogravimetric analysis (TGA)

Thermogravimetric analyses were performed on a Mettler Toledo TGA/DSC^{3+} STAR^{e} System at a heating rate of 10 K min^{-1} under constant flow of nitrogen.

Rheology

Oscillatory shear experiments were performed on a Bohlin CVO-100 rheometer from Bohlin instruments and a Kinexus rheometer from Malvern at a heating rate of 2 K min^{-1} and a frequency of 1 Hz. The measurements were performed using a plate-plate geometry with a plate diameter of 25 mm maintaining a distance between the plates of 1 mm.

The isothermal rheology measurements were conducted on a Bohlin CVO-100 rheometer in a continuous shear viscosity mode, using a cone-plate geometry (5.4°) with a plate diameter of 25 mm. The distance between cone and plate was kept at 150 μm. The frequency was set to 0.5 Hz and the set isothermal temperature was kept constant by the rheometer at ±0.2 K.

Dynamic mechanical thermal analysis (DMTA)

Dynamic mechanical thermal analysis of bulk material in tension mode was conducted on a DMTA IV Rheometric Scientific at a heating rate of 2 K min^{-1} and a frequency of 1 Hz. The specimen dimensions were 4 mm in width with a length of 10 mm and a thickness of about 1 mm individually determined with a caliper.

DMTA of thin polymer films were measured within a metal pocket in a single cantilever mode using a DMA 1 Star^{e} System from Mettler Toledo at a heating rate of 5 K min^{-1} and a frequency of 2 Hz.

Tensile testing

The mechanical properties of the thermoplastic elastomers were determined with tensile tests according to DIN EN ISO 527-1. These experiments were conducted on an Instron 5565 universal tester with pneumatic clamps and a 100 N load cell. A strain rate of 200 mm min^{-1} was applied. The thickness of each dry solution cast specimen was determined with a caliper ranging from about 0.7 to 1.6 mm. Width and length are given by the DIN 53 504 S3A mold dimensions (Figure 5.1). The Young's moduli were calculated from the initial slope of the stress-strain curves within the linear elastic regime (1 – 4%) and the average of at least five specimens is given.
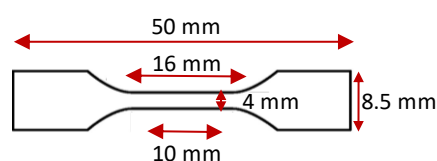
Figure 5.1: Specifications of a S3A mold according to DIN 53 504.

The poly(urea-siloxane) gradients were tested utilizing the same testing machine with a 100 N load cell and a video extensometer. The gradient with a total length of 14 cm and a width of 1 cm was clamped at both ends and the measurement was conducted between two markers with a distance of 1 cm. A strain rate of 0.3 mm min^{-1} was applied and the specimen was strained up to 0.5%. The Young's moduli were calculated from the initial slope of the linear elastic regime at 0.05 to 0.15%.

Small angle X-ray scattering (SAXS)

Small angle X-ray scattering measurements were conducted on a Double Ganehsa AIR purchased from SAXSLAB. As X-ray source a copper anode (MicoMax 007HF, Rigaku Corporation) with an emission wavelength of $\lambda = 0.154$ nm was used. The scattering intensity was recorded by a PILATUS 300K detector in a scattering range of $0.0004 - 0.4$ nm. The measurements were performed at room temperature on samples being embedded in a hole of a 1 mm thick aluminum discs (diameter: 1 mm). For temperature dependent SAXS measurements the samples were equilibrated for 10 min at each temperature before measuring. The raw data was analyzed using the software SASfit and being corrected towards the background (air).

Transmission electron microscopy (TEM)

Transmission electron microscopy was conducted on a Zeiss Leo EM922 Omega microscope operated at 80 kV. The $(AB)_n$ segmented copolymer samples were prepared from a 10 mg mL^{-1} THF solution via drop casting and were annealed at 60 °C for 15 min followed by a moderately cooling to room temperature. No additional staining was applied.

TEM samples of the amphiphilic, physically crosslinked $(ABAC)_n$ segmented copolymers were prepared by cryo-ultramicrotomy of solution cast films, the darker domains of the images are attributed to the PDMS phase. TEM measurements were performed on the Zeiss CEM 902 (Carl Zeiss Microscopy GmbH, Jena) energy filtering transmission electronmicroscope (EFTEM) operated at an acceleration voltage of 80 kV. Zero-loss filtered micrographs ($\Delta E \sim 0$ eV) were recorded with a side mounted CCD camera system (Orius SC200W, Gatan) and processed with DigitalMicrograph 2.3 image processing software (Gatan). Additional measurements were performed with a JEOL JEM-2200FS (JEOL GmbH, Freising) field emission energy filtering transmission electronmicroscope (FE-EFTEM) operated at an acceleration voltage of 200 kV. Zero-loss filtered micrographs ($\Delta E \sim 0$ eV) were recorded with a bottom mounted CMOS camera system (OneView, Gatan) and processed with DigitalMicrograph 3.3 image processing software (Gatan). FFT calculations were performed with DM 3.3.

Scanning electron microscopy (SEM)

All samples were sputtered with approximately 1.3 nm of platinum in a Cressing 208HR sputter and analyzed by SEM Zeiss Leo 1530 (Zeiss, Jena, Germany) at 3.0 kV.

The scaffold fabricated by MEW was characterized using a Crossbeam 340 scanning electron microscope from Carl Zeiss Microscopy GmbH, Germany at 3.0 kV.

The poly(urea-siloxane) foam samples were prepared initially by cryo fracture of the specimen.

Environmental scanning electron microscopy (ESEM)

The printed scaffolds were characterized by scanning electron microscopy (SEM) using a FEI Quanta FEG 250 from Thermo Fisher Scientific. The measurements were conducted in low vacuum mode without sputtering the samples. The pressure within the sample chamber was set to 40 Pa.

The dry scaffolds were stored for seven days in DI water and then placed into the sample chamber operating in the environmental scanning electron microscopy (ESEM) mode. Before the measurement the chamber was flushed twice with water vapor and the sample holder was kept at 2 °C during the whole time. Afterwards the chamber was stabilized at a pressure of 730 Pa corresponding to a relative humidity of about 100%. To analyze the drying process, the pressure and consequently the moisture within the chamber was gradually reduced to 300 Pa at 5 °C and kept there for 1 h before investigating the dried scaffold.

The degree of swelling was determined from the dimensional change in the dry and swollen state. An average of four measurements is given.

Electrospinning Device

The electrospinning system contained three main components, the high-voltage supply, a feeding unit and a collector plate. A custom-designed apparatus was utilized with a high power (HV) supply from Schulz Electronic (HV units AK0175 and AK1026). As collector a glass slide coated with aluminum foil was used and the distance between tip and collector was kept at 3.7 cm. The electrospinning experiments were conducted at room temperature and ambient conditions. 1 mL glass syringes from Fortuna Optima with a luer lock glass tip and stainless steel needles (20G, inner diameter: 0.6 mm, shorten to 1 mm) from Unimed, Switzerland were filled with the polymer and heated by an external electrical heater. The fiber diameter is given as an average of at least 20 measurements.

Melt electrowriting Device[85,129,198]

The MEW device used is a custom-build machine with a high precision x-, y-, z-linear axes (Aerotech Inc., Pittsburgh, USA) with a resolution of 1 µm. The nozzle was moved in z-direction via a ATS03005 stage, while the aluminum collector plate was moved in x-, y-directions via PRO115-05MM-150-UF positioning stage. The axes were navigated by using a G-code (MACH 3 CNC software, ARTSOFT, Livermore Falls, USA). By applying nitrogen gas via a precision pressure control valve (FESTO, Berkheim, Germany) on the polymer melt it can flow through the nozzle. The poly(urea-siloxane) was molten in a 3 mL glass syringe from Fortuna Optima with a luer lock connection (Poulten & Graf GmbH, Wertheim, Germany). Therefor an electrical heating controller (cTRON, JMMO, Metz Cedex, France) was used. The applied high voltage source (HCP 14–20000 Power supply, FuG Electronic GmbH, Schechen, Germany) was connected to the flat-tipped nozzle (24G, inner diameter: 0.3 mm) from Unimed, Schwitzerland. The scaffold was direct-written onto glass microscope slides with dimensions of $26 \cdot 76$ mm^2 (ECN 631–1552, VWR international GmbH, Germany). All experiments were conducted at room temperature and a relative humidity of 20 - 35%.

Adjustment of MEW parameters

The critical translation speed (CTS) was determined by increasing the fiber collection with 20 mm min^{-1} speed steps above 100 mm min^{-1}, 50 mm min^{-1} speed steps above 300 mm min^{-1} and 100 mm min^{-1} speed steps above 1000 mm min^{-1}. At least four fiber arrays were direct-written for each parameter combination with ten measured fiber diameters. The average fiber diameters $f_\emptyset$ and standard deviations are calculated from a total of 40 fibers.

The deposition flow rate *dV/dt* of the fibers on the collector plate was calculated according to equation **(5.3)**. The standard deviation was calculated with respect to the error propagation taking the standard deviation of the fiber diameter and the CTS into account.

$$\frac{dV}{dt} = \left[\frac{f_\emptyset}{2}\right]^2 \cdot \pi \cdot CTS \tag{5.3}$$

Fused deposition modeling (FDM)

FDM was conducted with a desktop twin-nozzle (nozzle diameter: 450 µm) FFF 3D printer (3NTR A4, Italy). The filament supply tube was modified with shorted length of about 5 cm which is installed directly between the feeding system and the liquefier. The 3D digital model was designed (Fusion 360, Autodesk) and additionally sliced by the Slic3r software. The extrusion temperature was set to 125 °C while the bed temperature was kept at 30 °C and a printing speed of 5 mm sec^{-1} was used. The printed specimen is a single-line stacked square tube.

Extrusion-based 3D printing

The Cellink+ bioprinter from Cellink, Sweden is based on a pneumatic microextrusion technique. The device was controlled and programmed utilizing the software Heartware, AB Cellink. The printer was equipped with an alumina cartridge and a flat tipped cannula with an inner diameter of 410 µm. The cartridge can be heated up to 130 °C, whereas the cannula has been shortened to avoid thermal loss and a clogged tip. The amphiphilic copolymers were filled into the cartridge and were heated to 130 °C. The printing pressure, being adjusted between 1.5 and 3 bar, was generated by an external compressor (Wiltec AF18 2). The vertical position (z-axis) was calibrated to the height of the used silicon wafer. The motion speed was varied between 100 and 800 mm min^{-1}. Material viscosities of 0.001 – 250 Pa·s are suitable for the setup as given by the manufacturer. The printing resolution is 10 µm in x- and y-direction and 2.5 µm in z-direction. All experiments were conducted under ambient conditions at room temperature.

Optical light microscopy

Fiber diameters were evaluated using optical microscope images, which were taken with a standard microscope Olypmus BX60 equipped with a Moticam Pro camera. The diameters were evaluated using the software Image J.

Polarized light microscopy was performed using a Nikon DIAPHOT 300 optical microscope, Nikon, Japan with a HS1 Hot Stage Controller from Mettler Toledo at a heating rate of 10 K min^{-1} without λ/4 plate. The optical micrographs were recorded by a Nikon ACT-1 software using a Nikon DMX1200 digital camera.

Gradient fabrication

For gradients from the melt a mid-pressure syringe pump utilized which was purchased from Cetoni neMESYS. Metal syringes with a capacity of 20 mL and metal capillaries with an inner diameter of 2.2 mm were used. The stainless steel static mixer purchased from PMS Mischersysteme & Technik has a total length of 6 cm being embraced by a stainless steel shell. Each component is heated by an individual electrical heating coil. The moveable platform is controlled by an external software. By applying a defined flow profile the molten component are extruded into a Teflon® mold ($14 \cdot 1 \cdot 0.1$ cm^3). Poly(urea-siloxane) **3a-(10)** was initially colorized with 0.01 wt.% Lumogen® Red F300 in THF solution (solid content: 15 wt.%). The solution was cast into a Teflon® mold and the solvent was evaporated at room temperature obtaining a pink and elastic film.

For solution gradients a low-pressure syringe pump was employed. Two glass syringes with a volume of 20 mL each containing one component at 50 wt.% in isopropanol were connected to a custom-designed mixing head via PVC tubes (inner diameter: 3 mm). A commercial available disposable static mixer was used to ensure homogenous mixing of both components. The gradient solution was cast into a Teflon® mold ($14 \cdot 1.5 \cdot 0.5 \, cm^3$) mounted on a linear moving platform. **PDMS-Jeffamine (62/38)**, as the softer, more hydrophilic component, was marked with 0.02 wt.% Lumogen® Red F300, an perylene-based UV-active dye, for optical characterization.

Ultraviolet-visible spectroscopy (UV/Vis)

UV/Vis absorbance (375 – 650 nm) was measured using a Jena Analytics reader FLASH scan 530 (Jena, Germany). The UV/Vis active dye, Lumogen® Red F300, was added to the softer copolymer. The gradient samples were placed on a 384-well microplate. The distance between each well is 4.7 nm, each well is measured at four different spots, averaged, and repeated for 16 times. For comparison, the spectra were set to zero at 650 nm. The reported absorbance values are standardized to a thickness of 1 mm.

Pressure-induced batch foaming device

A custom-built high pressure autoclave for pressures up to 300 bar and temperatures up to 200 °C was used. The autoclave has a total capacity of five times 5 mL specimen holders. The samples were saturated with CO_2 within the autoclave under defined conditions (temperature, pressure, and time) followed by the foaming process which is induced by an abrupt pressure release.

Characterization of foam morphology

The SEM images of the foamed poly(urea-siloxane)s were analyzed concerning cell size and cell density using the software Image J. At least 150 cells were taken into account to calculate the average cell size and cell density.

The cell size was calculated according to equation **(5.4)**, assuming spherical cells.

$$\text{cell size} = 2 \cdot \sqrt{\frac{A_{cell}}{\pi}} \qquad \textbf{(5.4)}$$

With A_{cell} being the total area of a cell.

The cell density, which corresponds to cells per unit volume was calculated according to equation **(5.5)**.

$$\text{cell density} = \left(\frac{n}{A}\right)^{\frac{3}{2}} \cdot R_v \qquad \textbf{(5.5)}$$

with n being the number of cells in the SEM image, A the area of the SEM image and R_v the volume expansion ratio, which is a defined as the ratio of the density of the neat bulk material ρ_{neat} to the density of the foamed sample ρ_{foam} (equation **(5.6)**).

$$R_v = \frac{\rho_{neat}}{\rho_{foam}}$$
(5.6)

Determination of foam density

The foam density was determined by the water-displacement method based on the Archimedes principle which states that the buoyant force on an object submerged in a fluid is equal to the weight of the fluid that is displaced by that certain object.

The density measurements were carried out using a Mettler Toledo Excellence plus analytical balance equipped with a density measuring accessory. The foam density ρ_{foam} was calculated according to equation **(5.7)**.

$$\rho_{foam} = \frac{m_{air}}{m_{air} - m_{water}} \cdot \rho_{water}$$
(5.7)

With m_{air} being the mass of the foamed specimen in air, m_{water} being the mass of the totally immersed specimen and ρ_{water} being the density of water.

An average of six measurements is given. Utilizing the Archimedes principle to determine the foam density requires a closed-cell foam structure, since otherwise the liquid can penetrate the foam and affect the results.

Compression testing

Specimen with a diameter of 4 mm were punched out of the foamed specimens and compression tested with a TMA 2940 Thermomechanical Analyser from TA instruments. The compression was measured using a force ramp of 0.05 to 0.5 N and a stamp diameter of 6 mm. From the applied force F and the specimen area A_0 the compression stress σ can be calculated according to equation **(5.8)**. The compression strain ε can be calculated from the initial sample height L_0 and the dimension change ΔL during compression according to equation **(5.9)**.

$$\sigma = \frac{F}{A_0}$$
(5.8)

$$\varepsilon = \frac{\Delta L}{L_0} \cdot 100$$
(5.9)

The compression modulus was determined from the initial slope of the resulting stress-strain curve. The average of at least four measurements is given.

Determination of swelling properties

The swelling properties of the amphiphilic, physical crosslinked copolymers were determined by gravimetric analysis with a Sartorius MA 145 balance, AS Wägetechnik, Germany. Initially the free-standing, dry solution cast samples were stored in deionized water for 4 – 5 days to reach equilibrium swelling. The **PDMS-Jeffamine** copolymers were moreover stored in the buffer solution Gibco by life technologies being a phosphate buffered saline with pH 7.4 which was diluted with DI water in a ratio of 1:9. The samples were taken out of the water and excess surface water was removed with a filter paper. The weight loss of the complete swollen samples was determined at 120 °C until constant, dry weight was reached.

The degree of swelling Q and the water content W were calculated according to equation **(4.2)** and **(4.3)**, respectively (chapter 4.2.6).[191]

Contact angle measurement

The samples were initially melt pressed between two PTFE foils with a smooth surface at 120 °C and 100 bar for 1 min to obtain thin and homogenous polymer films with a flat surface. Contact angle measurements were performed on a Drop Shape Analyzer from Krüss. One drop (5 µL) of Millipore water was placed on the polymer surface (orientation: sessile drop). The contact angles were calculated by an ellipsoidal fit.

Indentation

Indentation is a method to determine the Young's modulus of hydrogels. By pressing a sphere into a specimen the required force in dependency of the penetration depth is traced. In Figure 5.2 a schematic illustration of the indentation setup is shown. A spherical indenter with a radius R is pressed into the specimen to a maximal depth of h_{max}. The contact radius between sphere and specimen is given by a and the contact depth between sphere and specimen is given by h. The measurements provide force curves in dependency of the penetration depth. By fitting these curves, the shear modulus G can be calculated.

For the indentation measurement a load cell K34 from ME Messsysteme GmbH with a measuring range of ±0.25 N was used. The indenter consisted of a ruby sphere with a diameter of 4 mm. The average of at least five measurements is given.
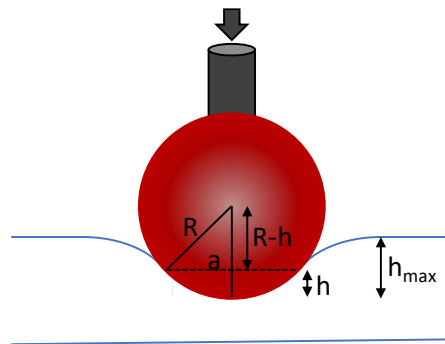
Figure 5.2: Schematic illustration of an indentation experiment. A sphere with a radius R is pressed into a specimen to a maximal depth of h_{max}. The contact radius between sphere and specimen is given by a and the contact depth between sphere and specimen is given by h.

Within this thesis the model from Segedin[196] was utilized for the calculation of the shear modulus G (equation **(5.10)**). With α being a fitting parameter and v the Poisson's ratio, which is 0.5 for polymers and liquids.

$$F = \frac{2GR^2}{1-v}[(\alpha^2+1)\tan h^{-1}\alpha - \alpha] \qquad \textbf{(5.10)}$$

The fitting parameter α is given as the ratio of the contact radius between sphere and specimen and the radius of the sphere (equation **(5.11)**).

$$\alpha = \frac{a}{R} \qquad \textbf{(5.11)}$$

The contact angle between sphere and specimen is given as the following (equation **(5.12)**).

$$a = \sqrt{2Rh^2 - h^2} \qquad \textbf{(5.12)}$$

5.3. Synthesis of (AB)$_n$ segmented poly(urea-siloxane) copolymers

The molecular weight of each PDMS-diamine monomer was initially determined by end group titration (chapter 5.2).

5.3.1. General procedure

In a dried round Schlenk flask PDMS-diamine DMS-12 (1513 g mol^{-1}, x = 18), DMS-A15 (2871 g mol^{-1}, x = 36), and DMS-21 (4926 g mol^{-1}, x = 64) (1 eq.) was solved in THF, respectively. In a dropping funnel the equivalent amount of the respective diisocyanate (*1,6-hexamethylene diisocyanate*, 168.2 g mol^{-1}; *isophorone diisocyanate*, 222.29 g mol^{-1}; *4,4'-methylene bis(cyclohexyl isocyanate)*, 262.35 g mol^{-1}; *toluene-2,4-diisocyanate,* 174.16 g mol^{-1}) (1 eq.) was solved in THF and added dropwise to the reaction solution at room temperature. The reaction with a solid content of 10 – 20 wt.% was stirred for 2.5 h at room temperature under argon atmosphere. The reaction process was controlled by FT-IR spectroscopy. The absence of a signal at υ = 2270 cm^{-1} indicated a complete isocyanate conversion. The viscous solution was poured into a Teflon® mold, followed by evaporating the solvent under ambient conditions.
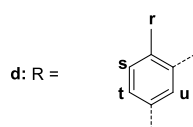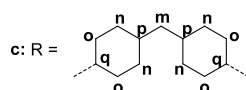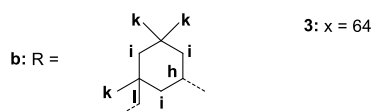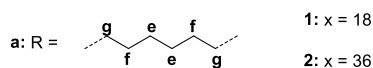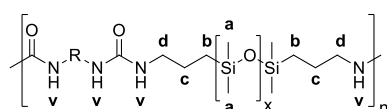
Poly(urea-siloxane)s

^{1}H-NMR (300 MHz, CDCl$_3$)**:** δ (ppm) = 7.61 (1H, Ar-H^u), 7.29 (1H, Ar-H^t), 6.85 (1H, Ar-H^s), 5 – 6 (4H, NH$_2$^{v}), 3.86 (2H, HN-CH^h), 3.75 (2H, HN-CH^q), 3.12 (4H, HN-CH$_2$^{g}), 3.12 (4H, Si(CH$_3$)$_2$-CH$_2$-CH$_2$-CH$_2$^{d}), 3.12 (2H, HN-CH$_2$^{i}), 2.53 (3H, C-CH$_3$^{r}), 1.49 – 1.69 (6H, CH$_2$^{i}), 1.12 – 1.98 (20H, CH$_2$^{m,n,o,p}), 1.47 (4H, HN-CH$_2$-CH$_2$^{f}), 1.47 (4H, Si(CH$_3$)$_2$-CH$_2$-CH$_2$^{c}), 1.30 (4H, HN-CH$_2$-CH$_2$-CH$_2$^{e}), 0.91 – 1.05 (9H, C-(CH$_3$)$_2$^{k}), 0.53 (4H, O-Si(CH$_3$)$_2$-CH$_2$^{b}), 0.08 (x·6H, O-Si-(CH$_3$)$_2$^{a})

5.3.2. Synthesis of molecular weight regulated (AB)$_n$ segmented poly(urea-siloxane)s

The synthesis was carried out according to the general procedure (chapter 5.3.1) with the exception of adding a certain amount of benzylamine (z mol%) to the PDMS-diamine solution at the beginning of the reaction to reduce the molecular weight.

For poly(urea-siloxane) **1a** 1.7 mol% benzylamine, for **3a** 5 and 10 mol% benzylamine were added to the reaction solution.

1: x = 18; 3: x = 64

Molecular weight regulated poly(urea-siloxane)s

^{1}H-NMR (300 MHz, CDCl$_3$)**:** δ (ppm) = 5 – 6 (4H, NH$_2$^{v}), 3.12 (4H, HN-CH$_2$^{g}), 3.12 (4H, Si(CH$_3$)$_2$-CH$_2$-CH$_2$-CH$_2$^{d}), 1.47 (4H, HN-CH$_2$-CH$_2$^{f}), 1.47 (4H, Si(CH$_3$)$_2$-CH$_2$-CH$_2$^{c}), 1.30 (4H, HN-CH$_2$-CH$_2$-CH$_2$^{e}), 0.53 (4H, O-Si(CH$_3$)$_2$-CH$_2$^{b}), 0.08 (x·6H, O-Si-(CH$_3$)$_2$^{a})

5.4. Synthesis of amphiphilic, physically crosslinked copolymers

5.4.1. Synthesis of PEG-diamines

The PEG-diamines were synthesized by J. Failner and S. Ganzleben.

*Synthesis of poly(ethylene glycol)-ditosylate (**PEG$_{1k, 2k, 4k}$-ditosylate**)*
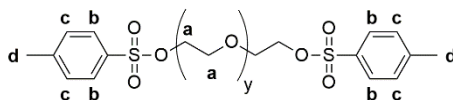
PEG$_{1k}$: y = 26

PEG$_{2k}$: y = 44

PEG$_{4k}$: y = 88

PEG (1 eq.) was dried initially overnight at 60 °C under high vacuum. Dry dichloromethane (500 mL) and *p*-toluenesulfonyl chloride (3 eq.) were added and cooled with an ice bath for 30 min. Triethylamine (3 eq., 0.728 g cm^{-3}) was added and the reaction was stirred at room temperature for 48 h (PEG$_{1k}$) and 22 h (PEG$_{2k, 4k}$), respectively.

The reaction was stopped by adding 300 mL DI water and washed five times with DI water. In case of insufficient phase separation ammonium chloride was added. The DCM phase was dried over sodium sulfate, concentrated to about 300 mL, precipitated in cold ether and filtered. The white precipitation was dried over night at 50 °C under high vacuum.

Yield:

PEG$_{1k}$-ditosylate: 89%

PEG$_{2k}$-ditosylate: 92%

PEG$_{4k}$-ditosylate: 65%

PEG-ditosylate

^{1}H-NMR (300 MHz, CDCl$_3$)**:** δ (ppm) = 7.76 (d, 4H, Ar-H^c), 7.31 (d, 4H, Ar-H^b), 3.62 (m, y·4H, O-CH$_2$^{a}-CH$_2$^{a}), 2.43 (s, 6H, Ar-CH$_3$^{d})

*Synthesis of poly(ethylene glycol)-diamine (**PEG$_{1k, 2k, 4k}$-diamine**)*
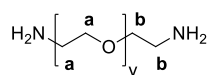
PEG$_{1k}$: y = 26

PEG$_{2k}$: y = 44

PEG$_{4k}$: y = 88

To PEG$_{1k, 2k, 4k}$-ditosylate an aqueous ammonia solution (25%) (1.8 L) was added and stirred at room temperature under argon atmosphere for 48 h (PEG$_{1k}$), 23 h (PEG$_{2k}$) and 45 h (PEG$_{4k}$), respectively. The reaction solution was extracted three times with DCM. The DCM phase was additionally extracted with water and then dried over sodium sulfate. In case of PEG$_{2k, 4k}$ the extraction with water was repeated six times. The solution was concentrated to about 250 mL and precipitated in cold ether, filtered and dried at 50 °C under high vacuum. The product was redissolved in THF (250 mL), precipitated in cold ether and dried at 30°C under high vacuum to remove last traces of impurities (Figure A-6.15).

Yield:

PEG$_{1k}$-diamine: 63%

PEG$_{2k}$-diamine: 66%

PEG$_{4k}$-diamine: 93%

PEG-diamine

^{1}H-NMR (300 MHz, CDCl$_3$)**:** δ (ppm) = 3.63 (d, y·4H, O-CH$_2^a$-CH$_2^a$), 2.87 (t, 4H, H$_2$N-CH$_2^b$)

DSC (2nd heating, 10 K min^{-1})**:**

        PEG$_{1k}$-diamine: T$_m$ = 41.5 °C ΔH$_m$ = 147.5 J g^{-1}

        PEG$_{2k}$-diamine: T$_m$ = 55.6 °C ΔH$_m$ = 160.3 J g^{-1}

        PEG$_{4k}$-diamine: T$_m$ = 58.1 °C ΔH$_m$ = 162.8 J g^{-1}

        Jeffamine ED 900[a)]: T$_m$ = 22.7 °C ΔH$_m$ = 106.4 J g^{-1}

Potentiometric end group titration (0.1 N HCl in isopropanol):

        PEG$_{1k}$-diamine: M$_n$ = 1223 g mol^{-1}

        PEG$_{2k}$-diamine: M$_n$ = 2191 g mol^{-1}

        PEG$_{4k}$-diamine: M$_n$ = 3961 g mol^{-1}

        Jeffamine ED 900[a)]: M$_n$ = 894 g mol^{-1}

[a)] Commercially purchased.

5.4.2. Synthesis of PEG-urea copolymers
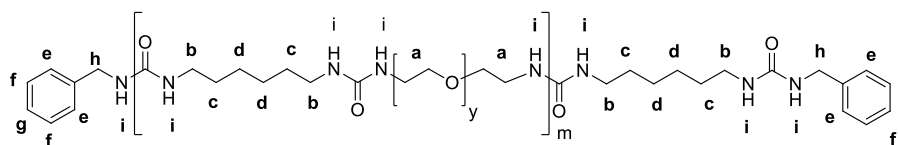
PEG$_{1k}$: y = 26

PEG$_{2k}$: y = 44

PEG$_{4k}$: y = 88
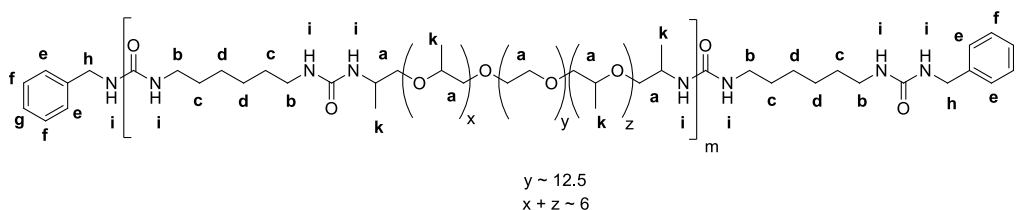
y ~ 12.5
x + z ~ 6

PEG-diamine (1 eq.) was dried[a)] under high vacuum overnight to remove traces of water. The dried PEG-diamine was solved in THF and the solution was cooled to 30 °C. 10 mol% of benzylamine (107.15 g mol^{-1}) were added to regulate the molecular weight. In a dropping funnel *1,6-hexamethylene diisocyanate* was solved in THF and added dropwise to the reaction solution which was stirred for 4 h at 30 °C. The whole reaction was carried out under argon atmosphere and a solid content of 10 – 20 wt.%. The reaction process was controlled by FT-IR spectroscopy. The absence of the isocyanate signal (υ = 2270 cm^{-1}) indicated a complete conversion. The reaction solution was cast into a Teflon® mold and the solvent was evaporated under ambient conditions.

The copolymers were purified by dialysis in DI water for 7 days. To obtain homogeneous films the dried copolymers were again dissolved in THF, cast into a Teflon® mold and the solvent was evaporated under ambient conditions.

[a)] PEG$_{1k}$: 50 °C

[a)] PEG$_{2k}$: 60 °C

[a)] PEG$_{4k}$: 70 °C

[a)] Jeffamine-ED 900: 50 °C

Yield after purification:

PDMS-PEG$_{1k}$ (0/100):   45%

PDMS-PEG$_{2k}$ (0/100):   29%

PDMS-PEG$_{4k}$ (0/100):   39%

PDMS-Jeffamine (0/100):   54%

PEG-urea copolymers

^{1}H-NMR (300 MHz, CDCl$_3$) (Figure A-6.16)**:** δ (ppm) = 5 – 6 (4H, NH$_2$^{i}), 3.65 (y·4H, O-CH$_2$^{a}-CH$_2$^{a}), 3.12 (4H, HN-CH$_2$^{b}), 1.5 (4H, HN-CH$_2$-CH$_2$^{c}), 1.3 (4H, HN-CH$_2$-CH$_2$-CH$_2$^{d}), 1.13 (18H, O-CH$_2$-CH$_2$-CH$_3$^{k})

5.4.3. General synthesis of amphiphilic copolymers

Based on PEG$_{1k}$
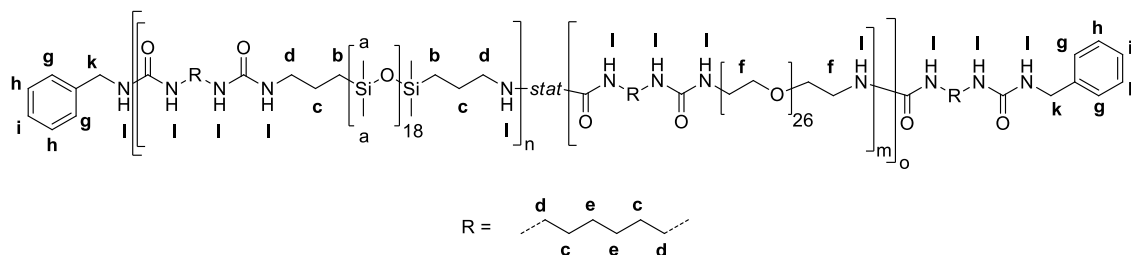
PEG$_{1k}$-diamine (1223 g mol^{-1}; m eq.[a)]) was dried under high vacuum at 50 °C overnight to remove traces of water. The dried PEG$_{1k}$-diamine was solved in THF and cooled to 30 °C. Only **PDMS-PEG$_{1k}$ (10/90)** was synthesized in isopropanol to ensure a complete solubility of the product. PDMS-diamine (1513 g mol^{-1}, x = 18; n eq.[a)]) and benzylamine (107.15 g mol^{-1}; 10 mol%) were added to the flask. *1,6-hexamethylene diisocyanate* (168.2 gmol^{-1}; 1 eq.) was solved in THF or isopropanol before being added dropwise to the reaction flask via a dropping funnel. The reaction solution was stirred for 2.5 h at 30 °C. The whole reaction was carried out under argon atmosphere and at a solid content of 10 – 20 wt.%. The reaction process was controlled by FT-IR spectroscopy. The absence of the isocyanate signal (υ = 2270 cm^{-1}) indicated a complete conversion of the diisocyanate. The reaction solution was cast into a Teflon® mold and the solvent was evaporated under ambient conditions.

The copolymers were purified by soaking the materials in a 100-fold excess of DI water for 4 – 5 days, followed by filtration and drying at 50 °C under high vacuum. To obtain homogeneous films the dried copolymers were again dissolved in THF, cast into a Teflon® mold and the solvent was evaporated under ambient conditions.

[a)] n + m = 1

n = 0.1, 0.5, 0.9

**Yield after purification:**

PDMS-PEG$_{1k}$ (93/7):   99.9%

PDMS-PEG$_{1k}$ (59/41):   95%

PDMS-PEG$_{1k}$ (10/90):   71%

PDMS-PEG$_{1k}$ copolymers

^{1}H-NMR (300 MHz, CDCl$_3$): δ (ppm) = 5 – 6 (8H, NH$_2$[l]), 3.65 (104H, O-CH$_2$[f]-CH$_2$[f]), 3.12 (12H, HN-CH$_2$[d]), 1.5 (12H, HN-CH$_2$-CH$_2$[c]), 1.3 (8H, HN-CH$_2$-CH$_2$-CH$_2$[e]), 0.53 (4H, Si-(CH$_3$)$_2$-CH$_2$[b]), 0.08 (108H, O-Si-(CH$_3$)$_2$[a])

Based on PEG$_{2k}$
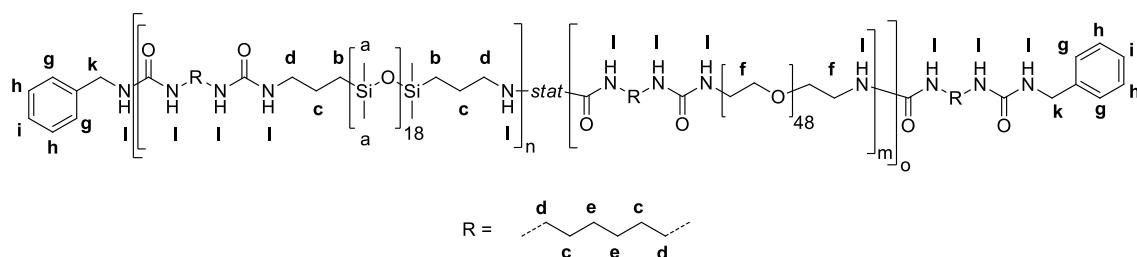
PEG$_{2k}$-diamine (2191 g mol^{-1}; m eq.$^{a)}$) was dried under high vacuum at 60 °C overnight to remove traces of water. The dried PEG$_{2k}$-diamine was solved in THF and cooled to 30 °C. PDMS-diamine (1513 g mol^{-1}, x = 18; n eq.$^{a)}$) and benzylamine (107.15 g mol^{-1}; 10 mol%) were added to the flask. *1,6-hexamethylene diisocyanate* (168.2 gmol^{-1}; 1 eq.) was solved in THF and added dropwise to the reaction flask via dropping funnel. The reaction solution was stirred for 2.5 h at 30 °C. The whole reaction was carried out under argon atmosphere and at a solid content of 10 – 20 wt.%. The reaction process was controlled by FT-IR spectroscopy. The absence of a signal at υ = 2270 cm^{-1} indicated a complete conversion of the diisocyanate. The reaction solution was cast into a Teflon® mold and the solvent was evaporated under ambient conditions.

The copolymers were purified by soaking the materials in a 100-fold excess of DI water for 4 – 5 days, followed by filtration and drying at 50 °C under high vacuum. To obtain homogeneous films the dried copolymers were again dissolved in THF, cast into a Teflon® mold and the solvent was evaporated under ambient conditions.

$^{a)}$ n + m = 1
n = 0.1, 0.5, 0.9

Yield after purification:
PDMS-PEG$_{2k}$ (85/15):   97%
PDMS-PEG$_{2k}$ (43/57):   85%
PDMS-PEG$_{2k}$ (12/88):   68%

PDMS-PEG$_{2k}$ copolymers
^{1}H-NMR (300 MHz, CDCl$_3$)**:** δ (ppm) = 5 – 6 (8H, NH$_2$^{l}), 3.65 (192H, O-CH$_2$^{f}-CH$_2$^{f}), 3.12 (12H, HN-CH$_2$^{d}), 1.5 (12H, HN-CH$_2$-CH$_2$^{c}), 1.3 (8H, HN-CH$_2$-CH$_2$-CH$_2$^{e}), 0.53 (4H, Si-(CH$_3$)$_2$-CH$_2$^{b}), 0.08 (108H, O-Si-(CH$_3$)$_2$^{a})

Based on PEG$_{4k}$
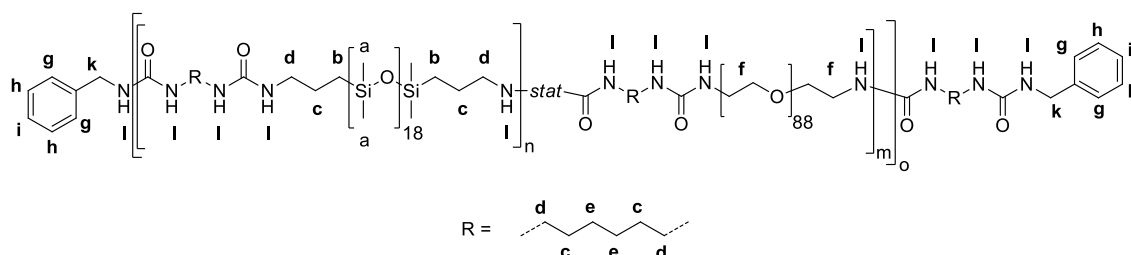
PEG$_{4k}$-diamine (3961 g mol^{-1}; m eq.[a)]) was dried under high vacuum at 70 °C overnight to remove traces of water. The dried PEG$_{4k}$-diamine was solved in THF and cooled to 30 °C, before PDMS-diamine (1513 g mol^{-1}, x = 18; n eq.[a)]) and benzylamine (107.15 g mol^{-1}; 10 mol%) were added. *1,6-hexa-methylene diisocyanate* (168.2 gmol^{-1}; 1 eq.) was solved in THF and added dropwise to the reaction flask via dropping funnel. The reaction solution was stirred for 2.5 h at 30 °C. The whole reaction was carried out under argon atmosphere and at a solid content of 10 – 20 wt.%. The reaction process was controlled by FT-IR spectroscopy. The absence of a signal at υ = 2270 cm^{-1} indicated a complete conversion of the diisocyanate. The reaction solution was cast into a Teflon® mold and the solvent was evaporated under ambient conditions.

The copolymers were purified by soaking the materials in a 100-fold excess of DI water for 4 - 5 days, followed by filtration and drying at 50 °C under high vacuum. To obtain homogeneous films the dried copolymers were again dissolved in THF, cast into a Teflon® mold and the solvent was evaporated under ambient conditions.

[a)] n + m = 1

n = 0.1, 0.5, 0.9

Yield after purification:

PDMS-PEG$_{4k}$ (77/23):   97%

PDMS-PEG$_{4k}$ (30/70):   81%

PDMS-PEG$_{4k}$ (9/91):   54%

PDMS-PEG$_{4k}$ copolymers

^{1}H-NMR (300 MHz, CDCl$_3$)**:** δ (ppm) = 5 – 6 (8H, NH$_2$[i]), 3.65 (352H, O-CH$_2$[f]-CH$_2$[f]), 3.12 (12H, HN-CH$_2$[d]), 1.5 (12H, HN-CH$_2$-CH$_2$[c]), 1.3 (8H, HN-CH$_2$-CH$_2$-CH$_2$[e]), 0.53 (4H, Si-(CH$_3$)$_2$-CH$_2$[b]), 0.08 (108H, O-Si-(CH$_3$)$_2$[a])

Based on Jeffamine ED-900

R =

y ~ 12.5
x + z ~ 6
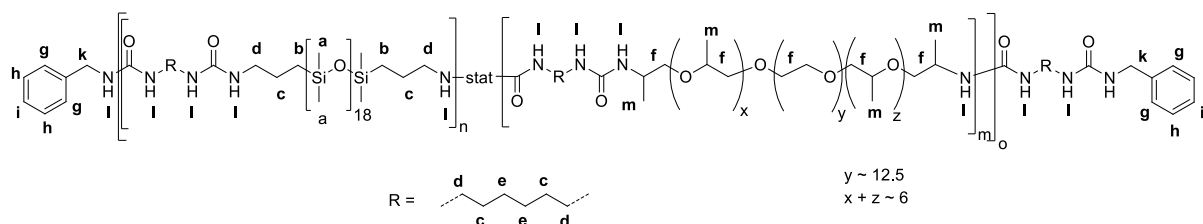
Jeffamine ED 900 (894 g mol^{-1}; m eq.[a)]) was dried under high vacuum at 50 °C overnight to remove traces of water. The Jeffamine ED-900 was solved in THF before cooling the solution to 30 °C. PDMS-diamine (1513 g mol^{-1}, x = 18; n eq.[a)]) and benzylamine (107.15 g mol^{-1}; 10 mol%) were added to the flask. *1,6-hexamethylene diisocyanate* (HMDI) (168.2 g mol^{-1}; 1 eq.) was solved in THF before being added dropwise to the solution via dropping funnel. The reaction solution was stirred for 4 h at 30 °C. The whole polymerization was carried out under argon atmosphere and at a solid content of 10 – 20 wt.%. The reaction process was controlled by FT-IR spectroscopy. The absence of the isocyanate signal (υ = 2270 cm^{-1}) indicated a complete conversion. The reaction solution was cast into a Teflon® mold and the solvent was evaporated under ambient conditions.

The copolymers were purified by soaking the materials in a 100-fold excess of DI water for 4 - 5 days, followed by filtration and drying at 50 °C under high vacuum. To obtain homogeneous films the dried copolymers were again dissolved in THF, cast into a Teflon® mold and the solvent was evaporated under ambient conditions.

[a)] n + m = 1

n = 0.1, 0.5, 0.9

Yield after purification:

PDMS-Jeffamine (92/8):   99%

PDMS-Jeffamine (62/38):   86%

PDMS-Jeffamine (22/78):   60%

PDMS-Jeffamine copolymers

^{1}H-NMR (300 MHz, CDCl$_3$): δ (ppm) = 5 – 6 (8H, NH$_2$^{l}), 3.65 (50H, O-CH$_2$^{f}-CH$_2$^{f}), 3.12 (12H, HN-CH$_2$^{d}), 1.5 (12H, HN-CH$_2$-CH$_2$^{c}), 1.3 (8H, HN-CH$_2$-CH$_2$-CH$_2$^{e}), 1.13 (18H, O-CH$_2$-CH$_2$-CH$_3$^{m}), 0.53 (4H, Si-(CH$_3$)$_2$-CH$_2$^{b}), 0.08 (108H, O-Si-(CH$_3$)$_2$^{a})

6.   Appendix

(A)

(B)
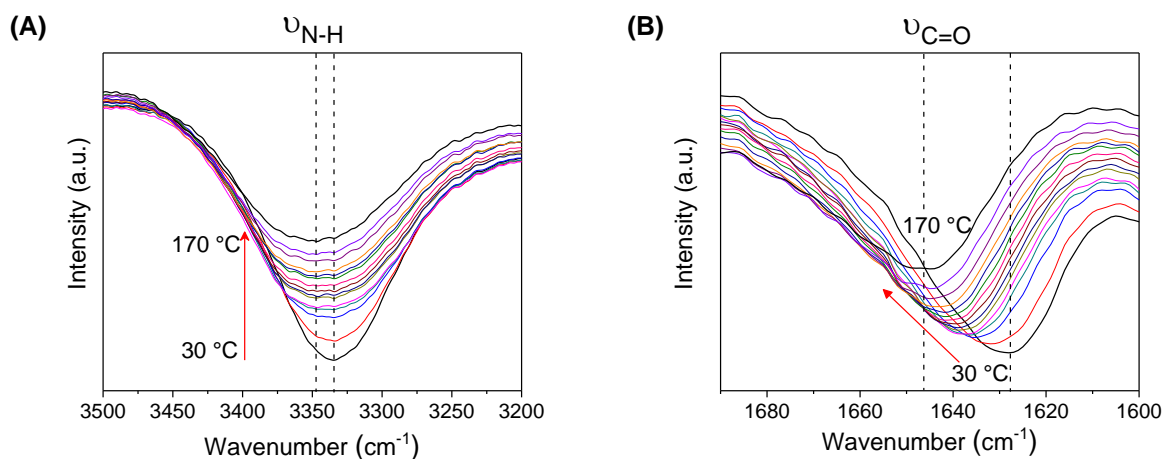
Figure A-6.1: Temperature dependent FT-IR spectra of poly(urea-siloxane) **1a** upon 1st heating recorded from 30 – 170 °C in 10 K steps. **(A)** showing the N-H vibration and **(B)** the carbonyl vibration. The disaggregation of the hydrogen bonded urea units upon heating leads to a shift of wavenumbers towards higher values (dashed lines) and a decreasing intensity. Detailed experimental data are included in chapter 5.2. [Adapted and printed with permission from [85]; © 2018 WILEY-VCH]

(A)

(B)
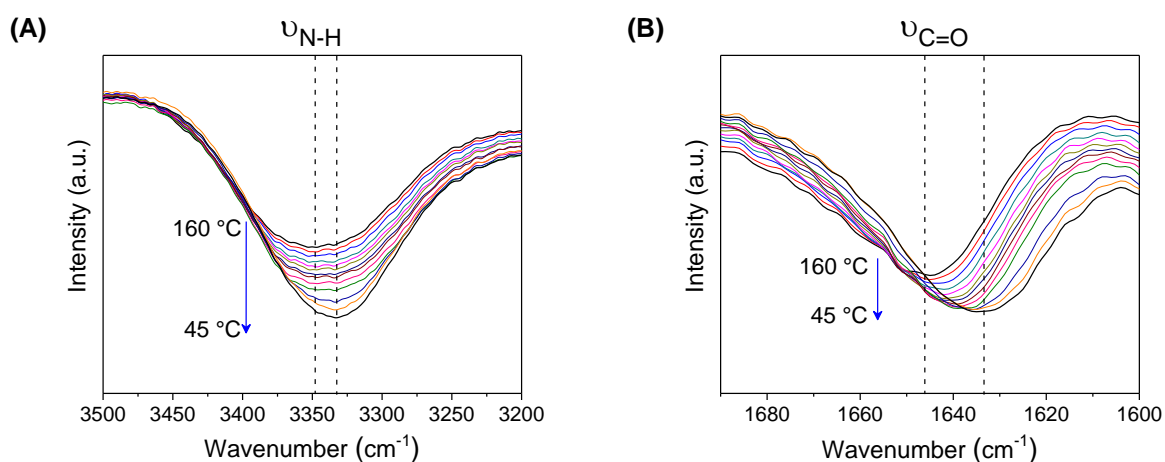
Figure A-6.2: Temperature dependent FT-IR spectra of poly(urea-siloxane) **1a** upon 1st cooling recorded from 160 – 45 °C in 10 K steps. **(A)** showing the N-H vibration and **(B)** the carbonyl vibration. The aggregation and formation of an ordered, hydrogen bonded form is traced by the shift towards lower wavenumbers (dashed lines) and an increasing intensity. Detailed experimental data are included in chapter 5.2. [Adapted and printed with permission from [85]; © 2018 WILEY-VCH]
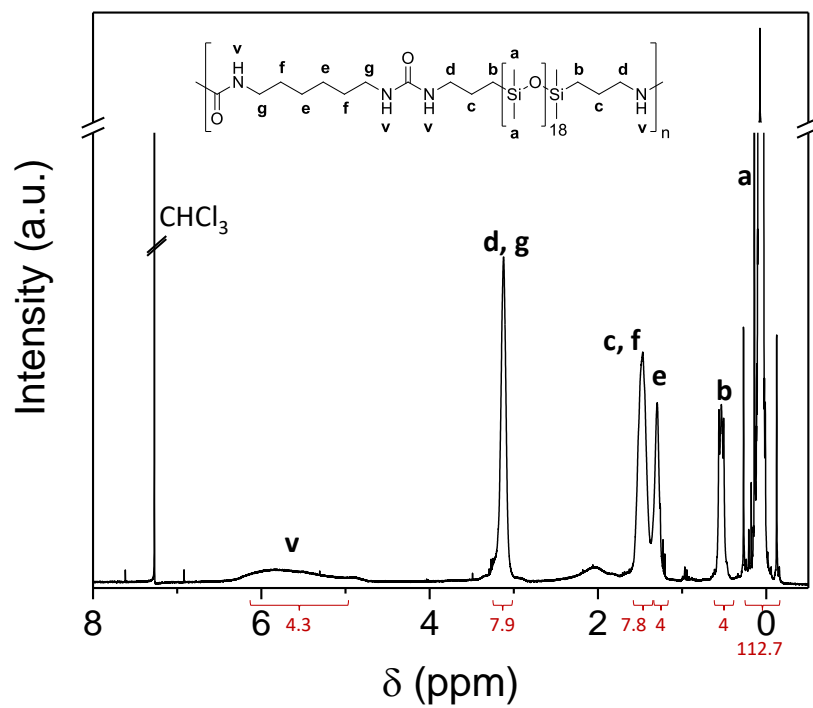
Figure A-6.3: ¹H-NMR spectrum of **1a** (300 MHz, CDCl₃).
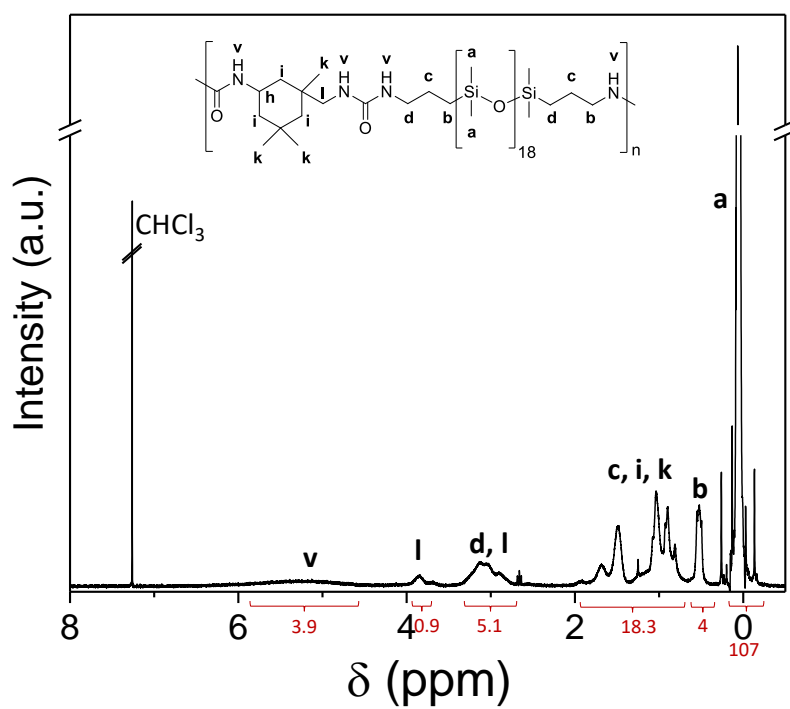
Figure A-6.4: ¹H-NMR spectrum of **1b** (300 MHz, CDCl₃).
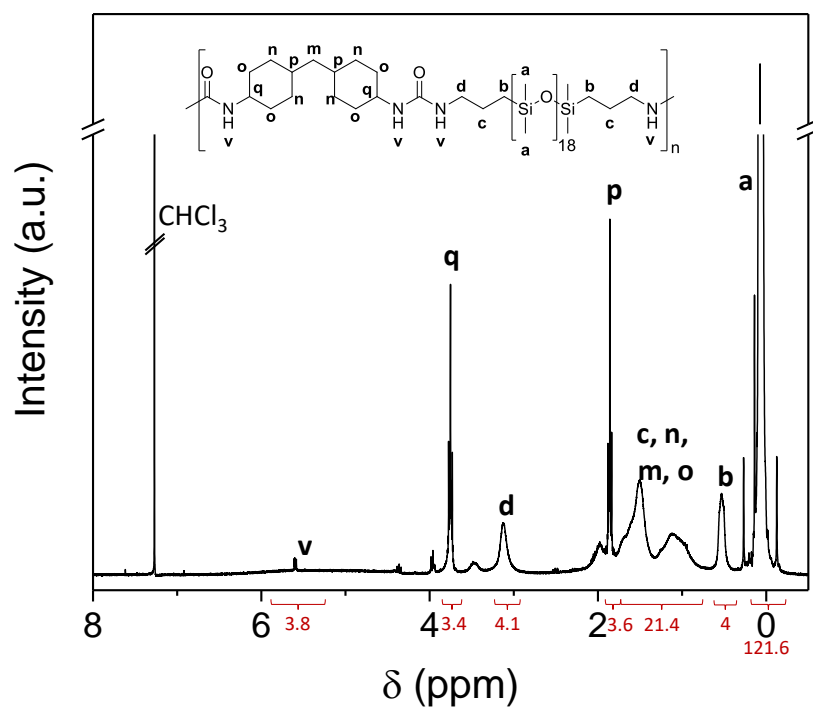
Figure A-6.5: ^{1}H-NMR spectrum of **1c** (300 MHz, CDCl₃).
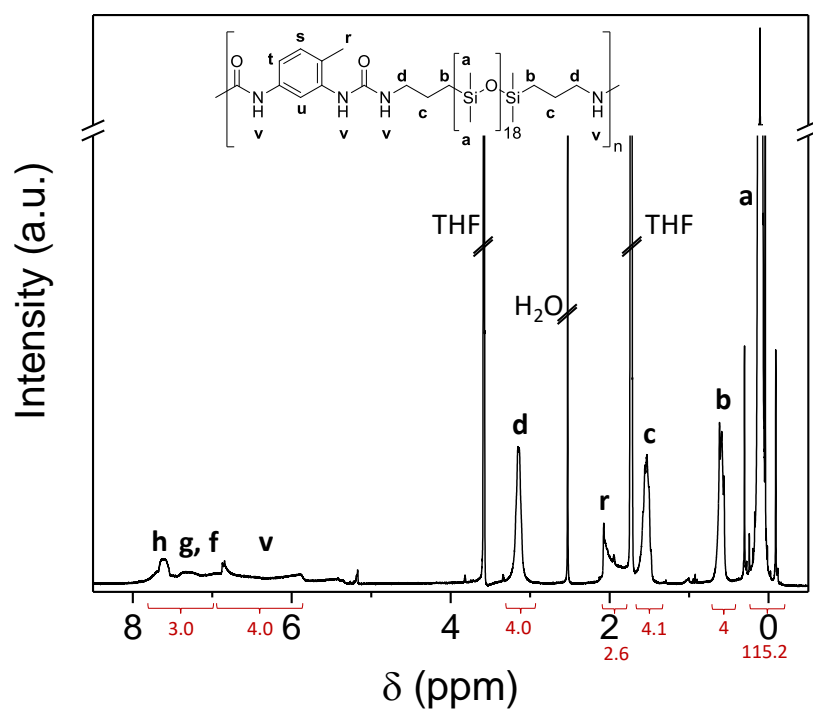
Figure A-6.6: ^{1}H-NMR spectrum of **1d** (300 MHz, CDCl₃).

1b (x = 18); **2b** (x = 36); **3b** (x = 64)

1c (x = 18); **2c** (x = 36); **3c** (x = 64)

1d (x = 18); **2d** (x = 36); **3d** (x = 64)
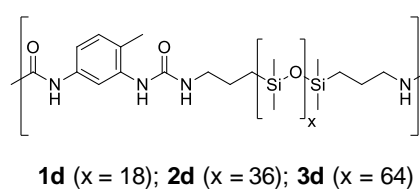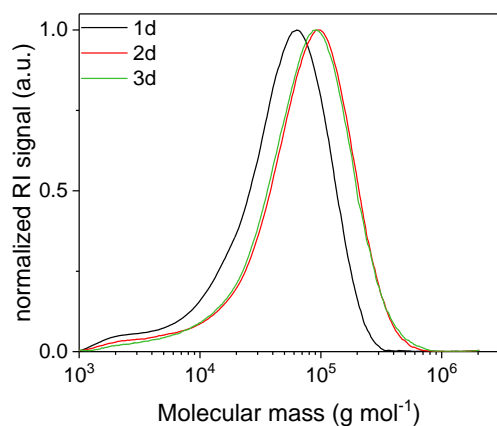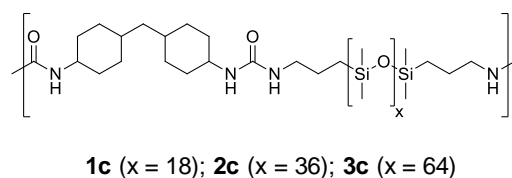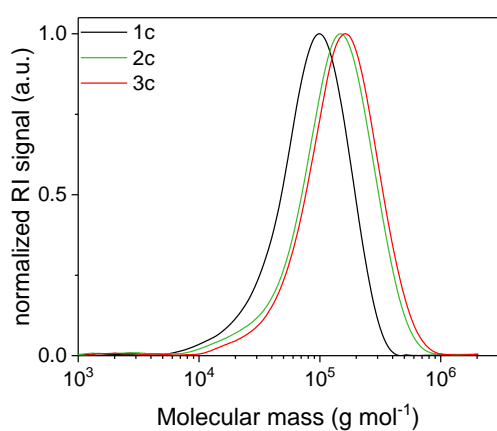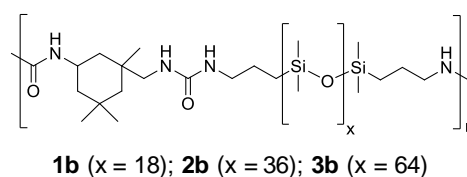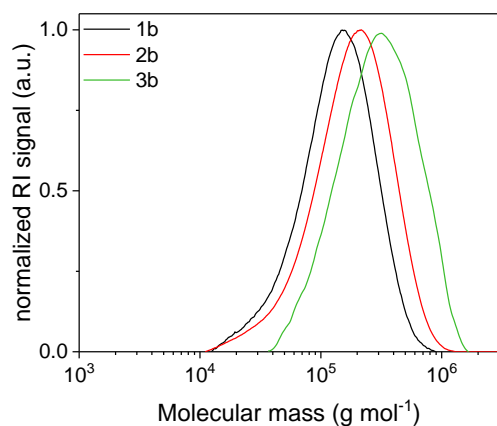
Figure A-6.7: SEC chromatograms of poly(urea-siloxane)s based on IPDI **(1-3b)**, mbCHDI **(1-3c)** and 2,4-TDI **(1-3d)**. The SEC experiments were carried out with THF containing 0.25 wt.% tetrabutylammonium bromide as eluent. $\overline{M_n}$ and $\overline{M_w}$ were calculated based on a polystyrene calibration.
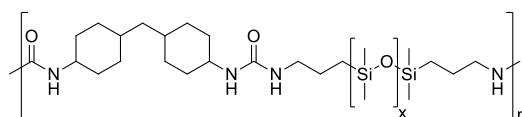
2c (x = 36); **3c** (x = 64)
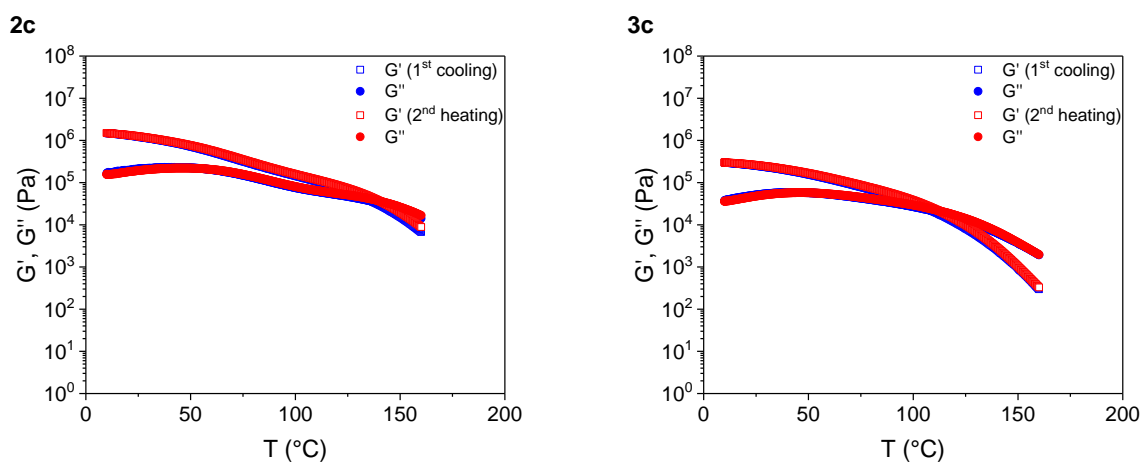
Figure A-6.8: Oscillating shear rheology measurements of poly(urea-siloxane)s **2c** and **3c** applying a heating/cooling rate of 2 K min⁻¹ and a frequency of 1 Hz. Shear storage *G'* and loss modulus *G''* of 1st cooling and 2nd heating are shown in dependency of the temperature.
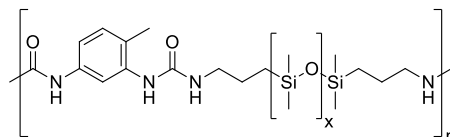
2d (x = 36); **3d** (x = 64)
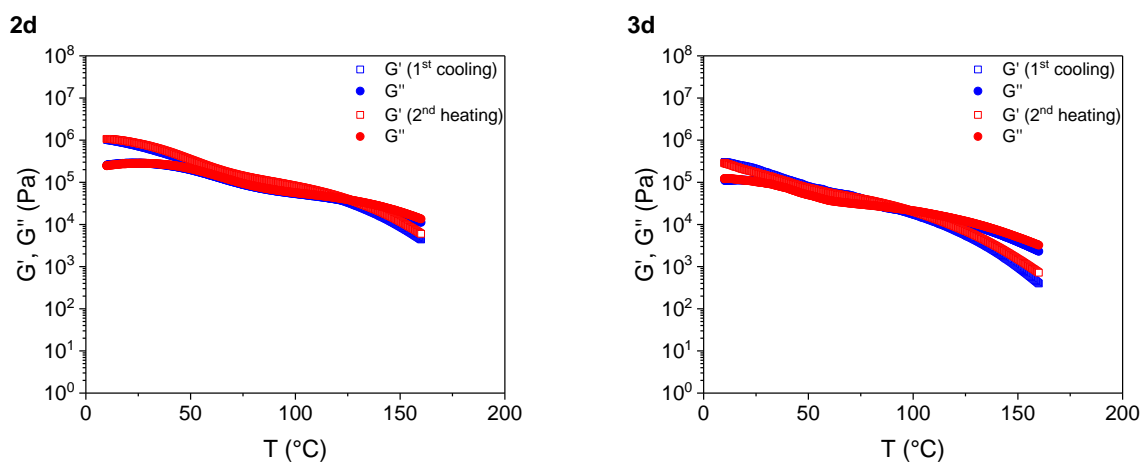
Figure A-6.9: Oscillating shear rheology measurements of poly(urea-siloxane)s **2d** and **3d** applying a heating/cooling rate of 2 K min⁻¹ and a frequency of 1 Hz. Shear storage *G'* and loss modulus *G''* of 1st cooling and 2nd heating are shown in dependency of the temperature.
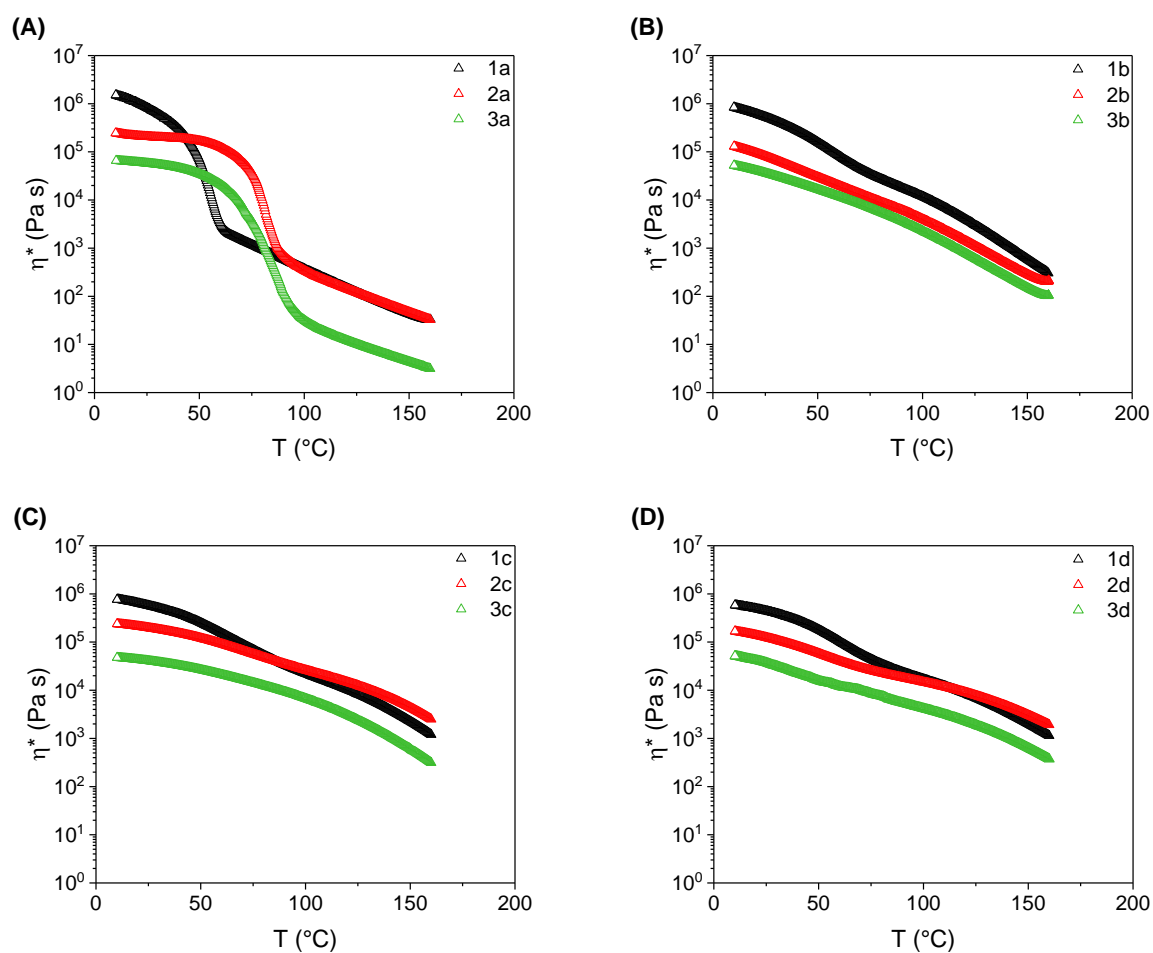
Figure A-6.10: Complex viscosity $\eta*$ of poly(urea-siloxane)s based on **(A)** HMDI, **(B)** IPDI, **(C)** mbCHDI, and **(D)** 2,4-TDI with different PDMS chain length in dependency of the temperature (1st cooling). A cooling rate of 2 K min^{-1} and a frequency of 1 Hz was applied.
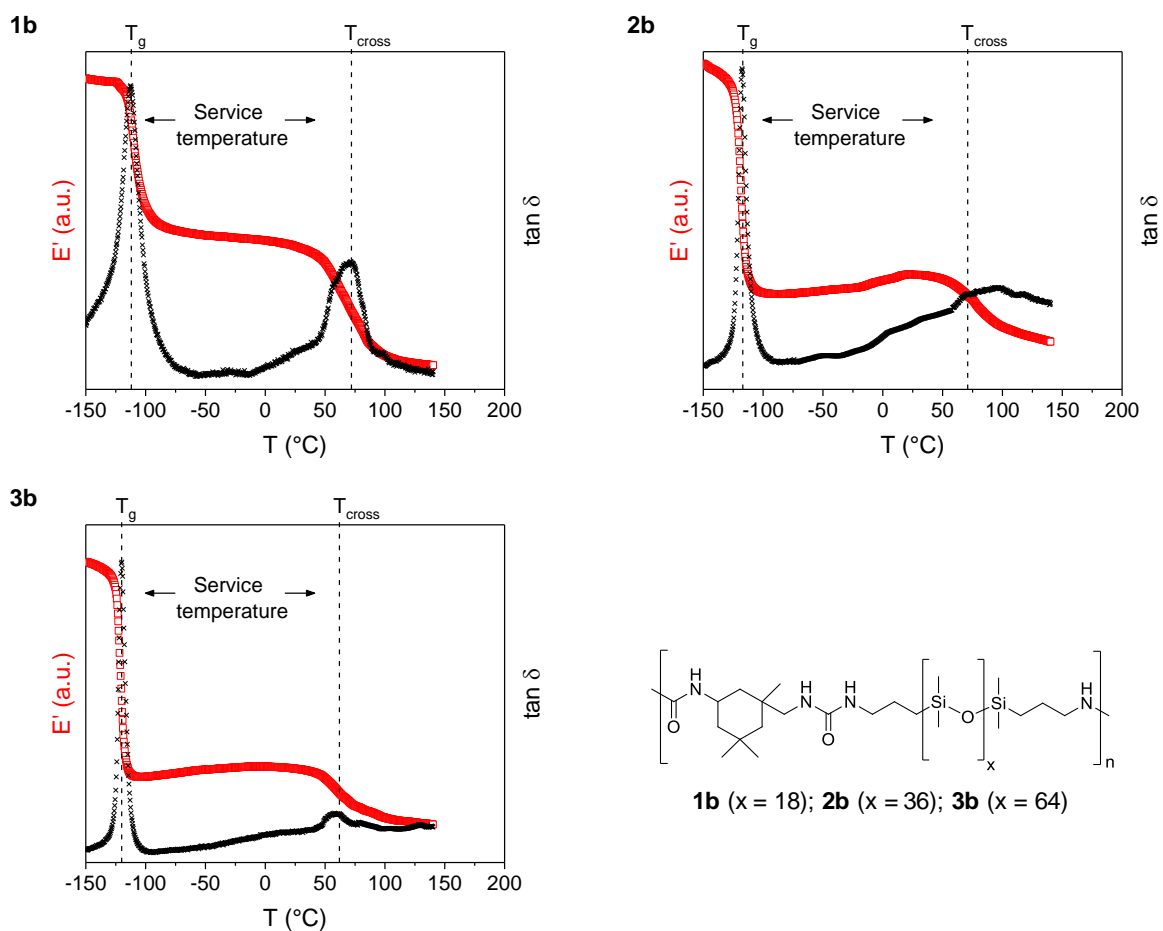
Figure A-6.11: Elastic storage modulus *E'* and *tan δ* as a function of temperature upon 1st heating of poly(urea-siloxane)s based on IPDI and different PDMS soft segment length determined via a single cantilever bending experiment utilizing a metal specimen holder with an applied frequency of 2 Hz and a heating rate of 5 K min-1.
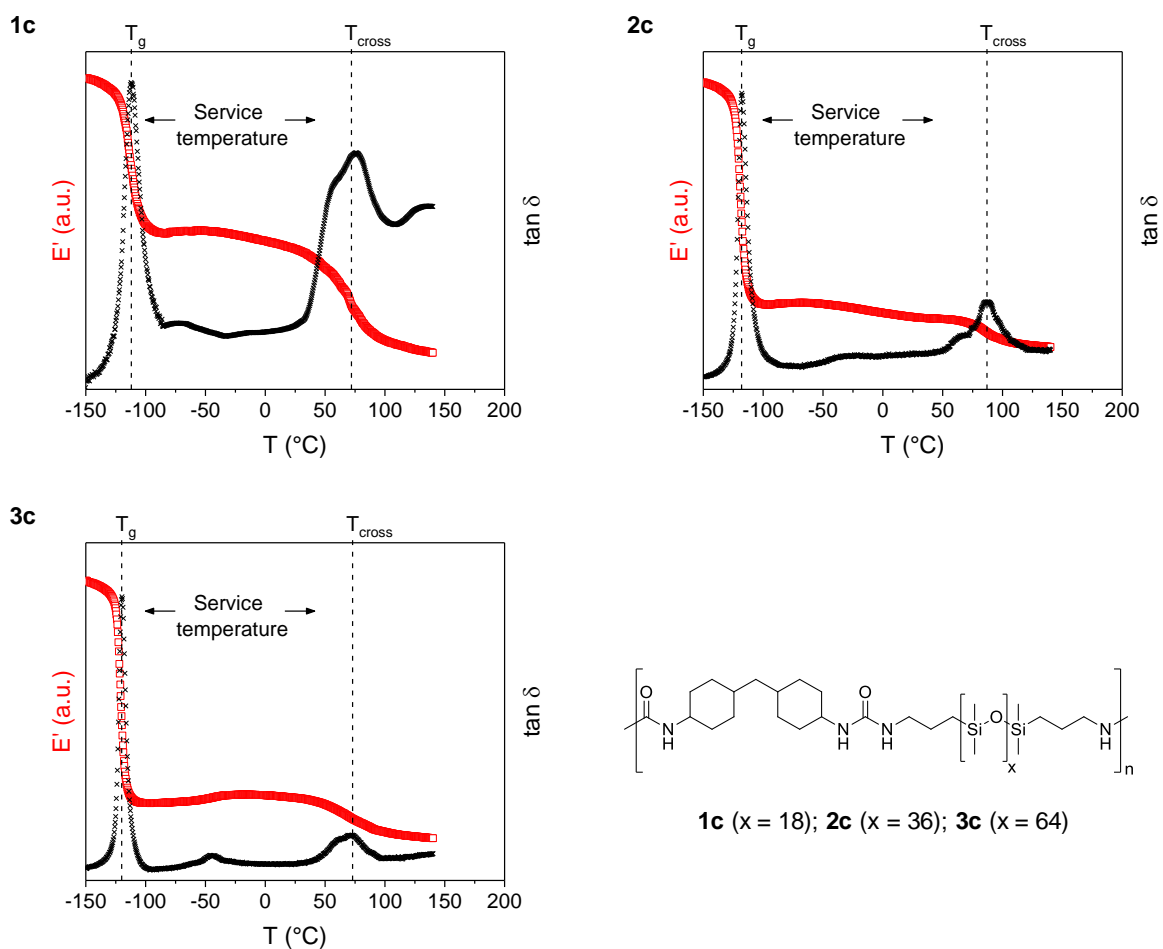
Figure A-6.12: Elastic storage modulus E' and $tan\ \delta$ as a function of the temperature upon 1st heating of poly(urea-siloxane)s based on mbCHDI and different PDMS soft segment length determined via a single cantilever bending experiment utilizing a metal specimen holder with an applied frequency of 2 Hz and a heating rate of 5 K min^{-1}.
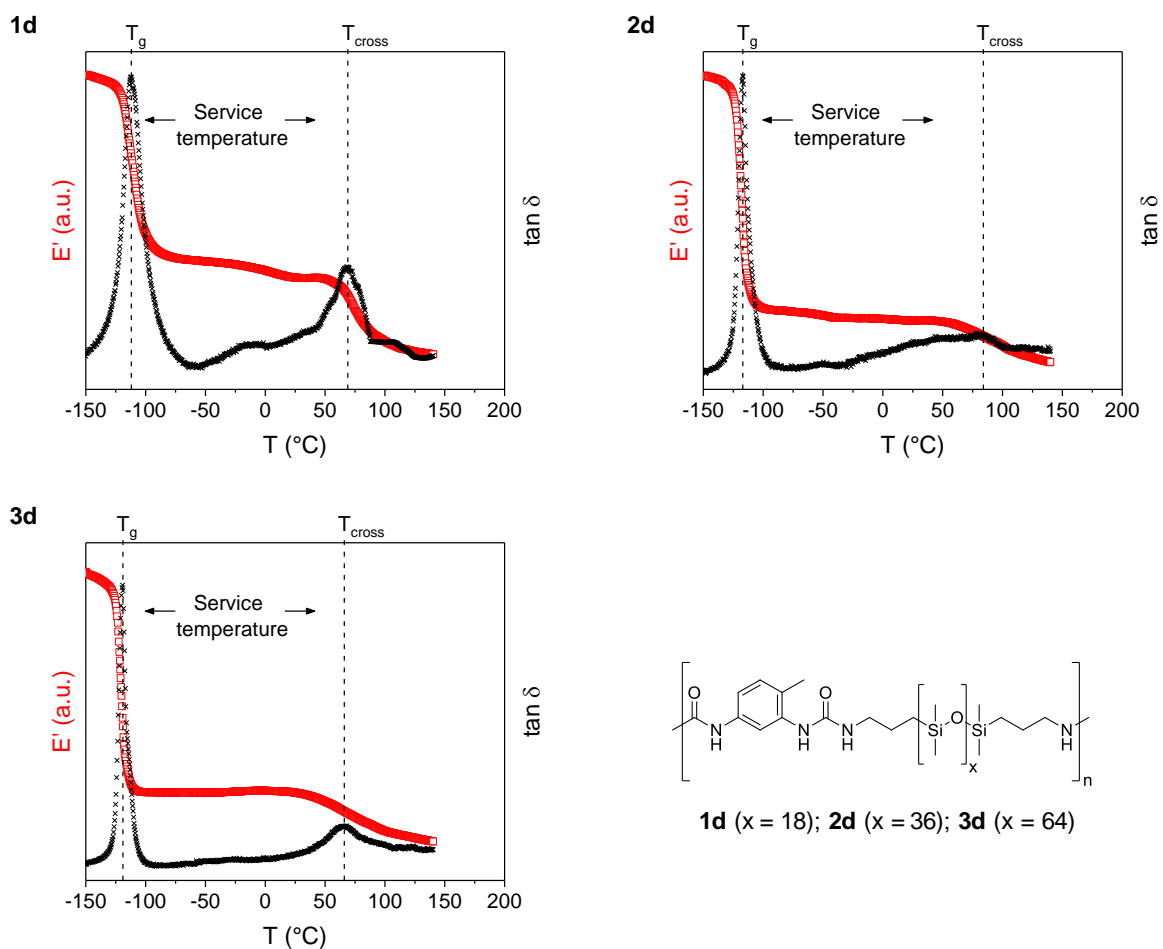
Figure A-6.13: Elastic storage modulus *E'* and *tan δ* as a function of the temperature upon 1st heating of poly(urea-siloxane)s based on 2,4-TDI and different PDMS soft segment length determined via a single cantilever bending experiment utilizing a metal specimen holder with an applied frequency of 2 Hz and a heating rate of 5 K min^{-1}.
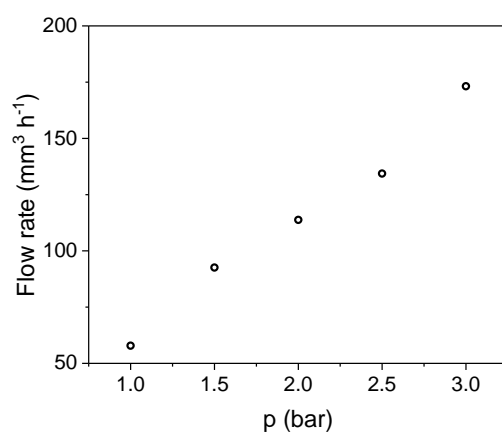
Figure A-6.14: Flow rate as a function of the applied pressure. The processing temperature and voltage were kept constant at 90 °C and 10 kV, respectively with a tip to collector distance of 8.5 mm. A linear dependency of the flow rate on the applied pressure can be observed.
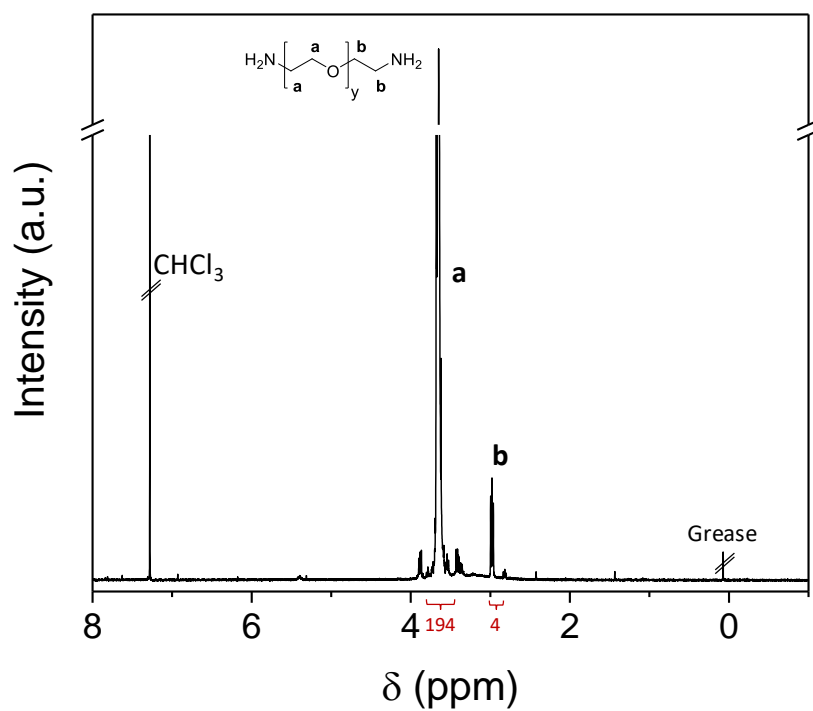
Figure A-6.15: ¹H-NMR spectrum of **PEG₂ₖ-diamine** (y = 48) (300 MHz, CDCl₃).
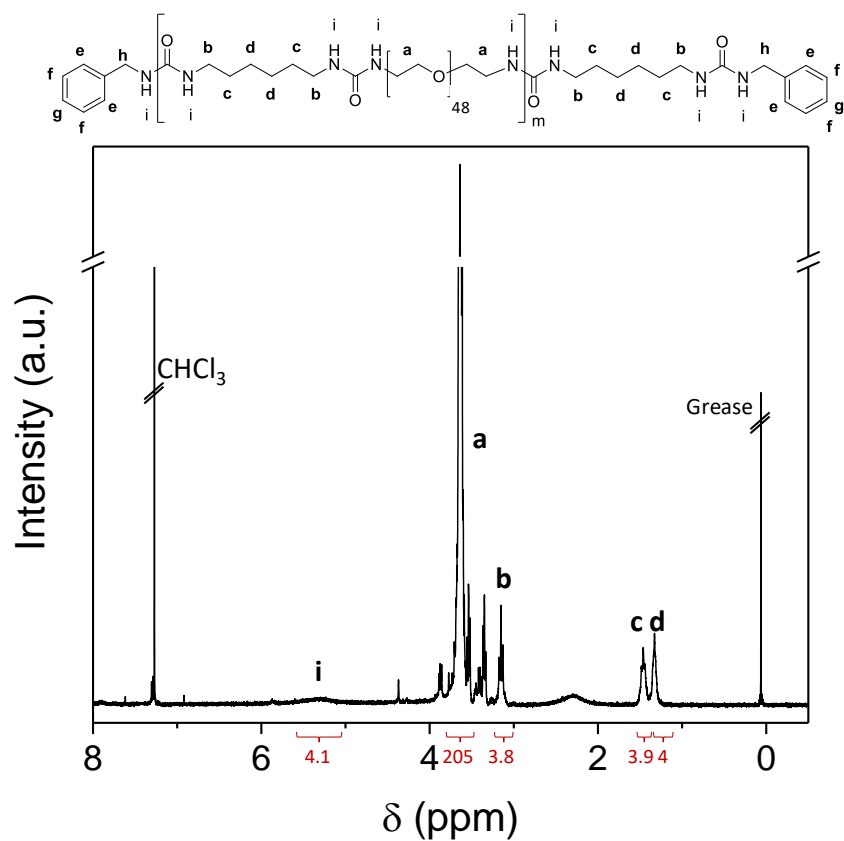
Figure A-6.16: ¹H-NMR spectrum of **PDMS-PEG₂ₖ (0/100)** (reference material based on short chain PDMS-diamine, PEG₂ₖ-diamine and *1,6-hexamethylene diisocyanate*) (300 MHz, CDCl₃).
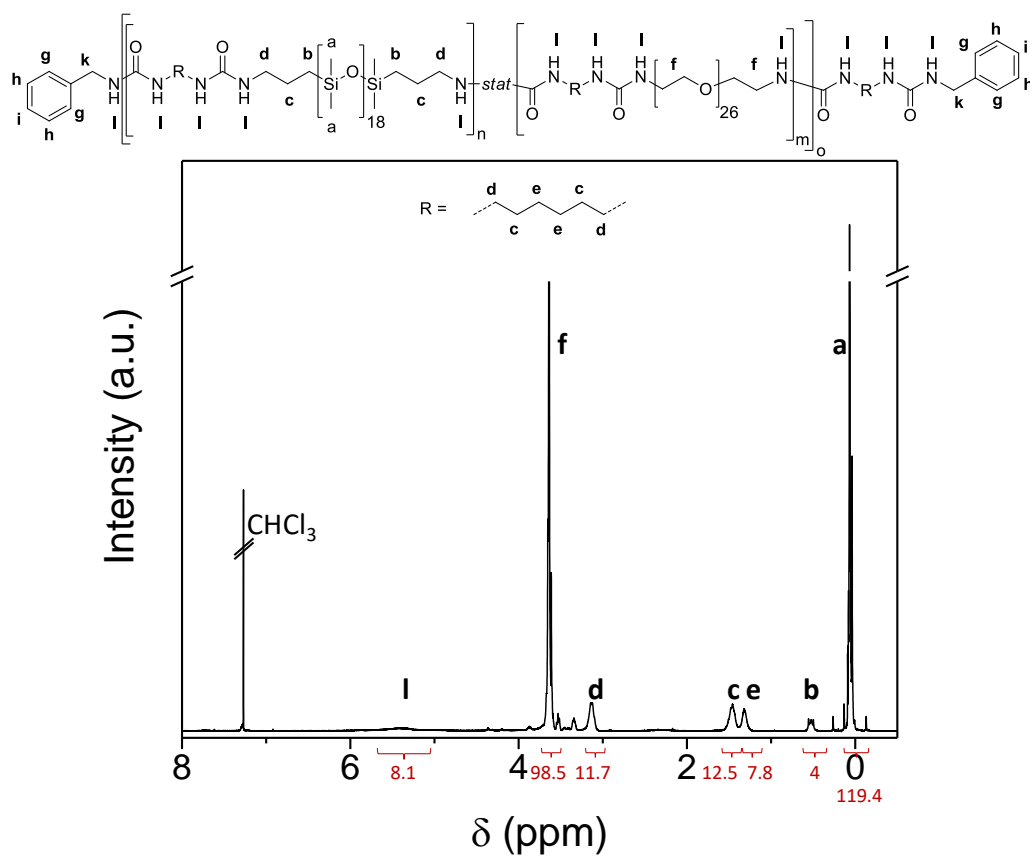
Figure A-6.17: ^{1}H-NMR spectrum of **PDMS-PEG$_{1k}$ (59/41)** (300 MHz, CDCl$_3$).
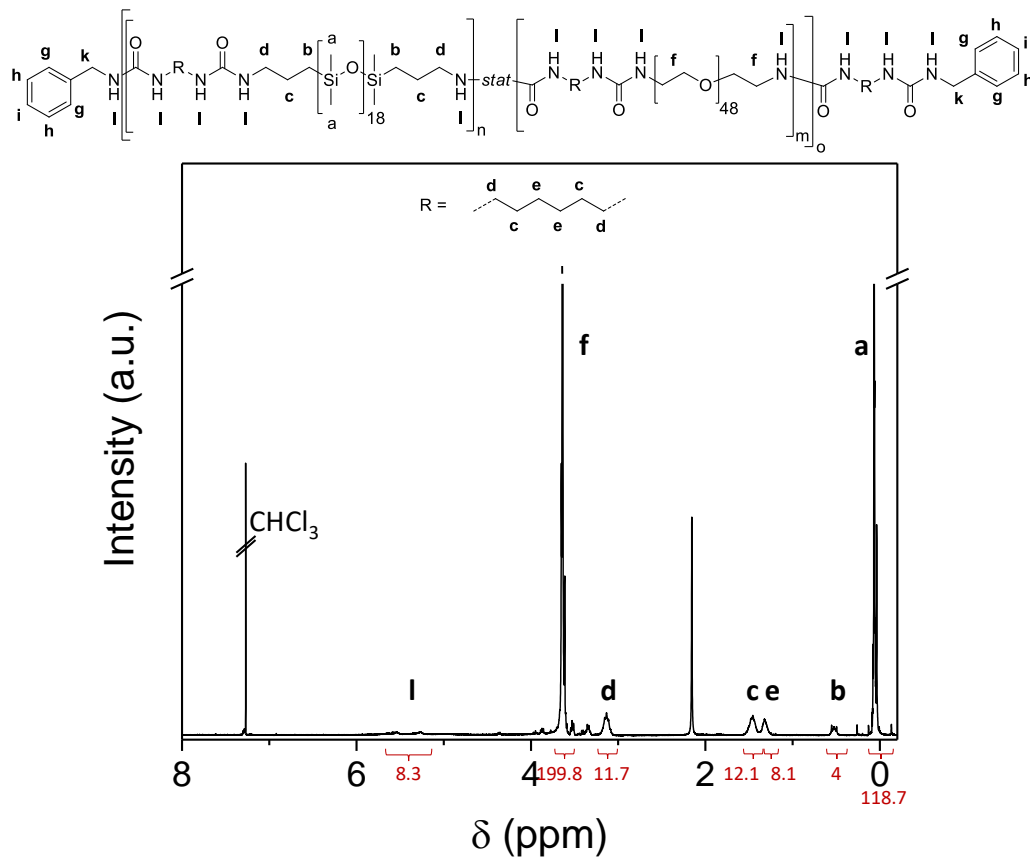
Figure A-6.18: ^{1}H-NMR spectrum of **PDMS-PEG$_{2k}$ (43/57)** (300 MHz, CDCl$_3$).
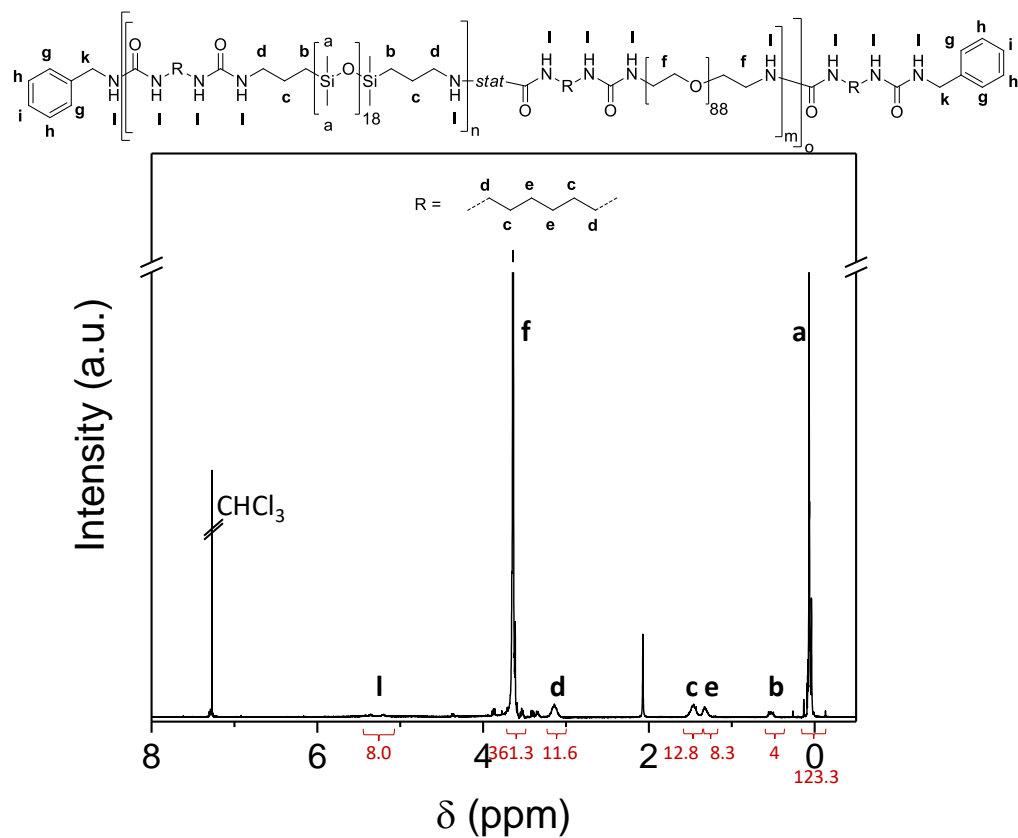
Figure A-6.19: ^{1}H-NMR spectrum of **PDMS-PEG$_{4k}$ (30/70)** (300 MHz, CDCl$_3$).
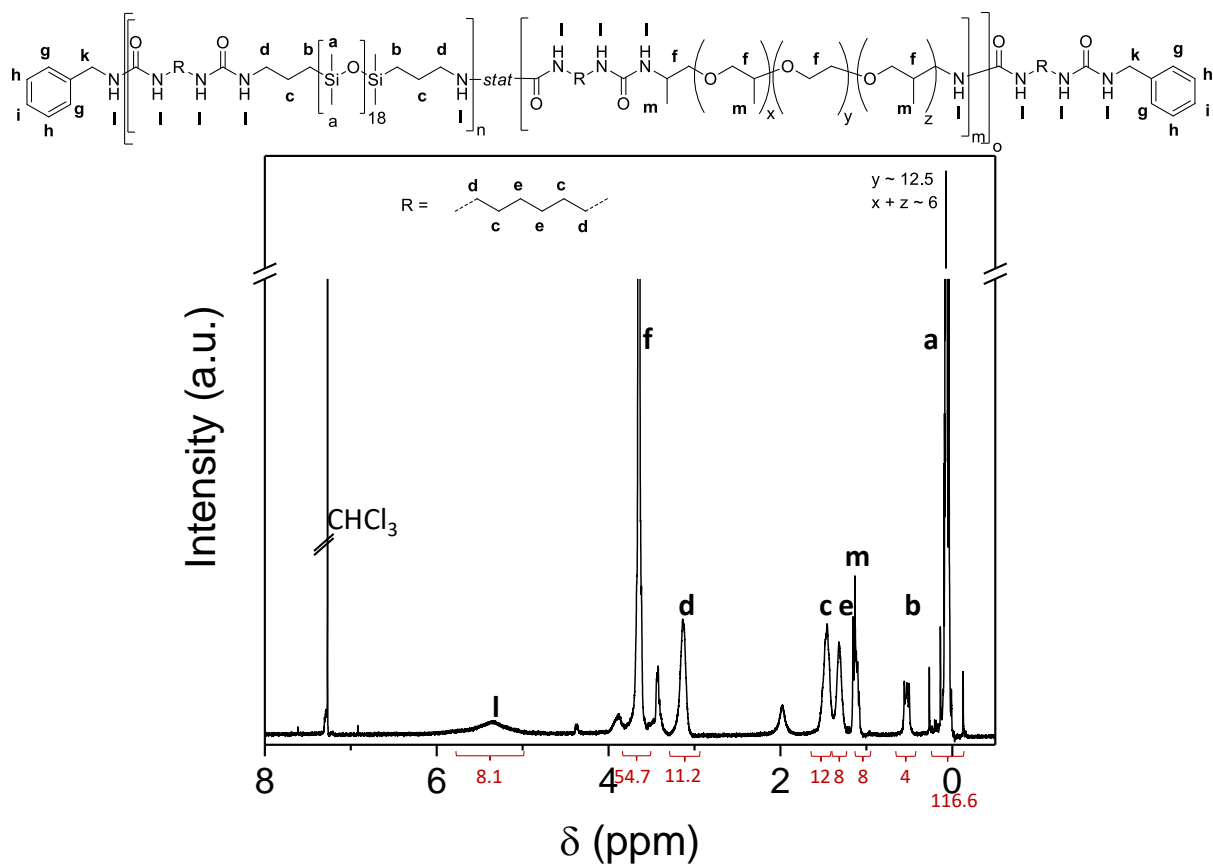
Figure A-6.20: ^{1}H-NMR spectrum of **PDMS-Jeffamine (62/38)** (300 MHz, CDCl$_3$).

Calculation of built-in ratios:

$$\text{PEG content (mol\%)} = \frac{\frac{A_{PEG}}{4 \cdot y}}{\frac{A_{PEG}}{4 \cdot y} + \frac{A_{PDMS}}{6 \cdot x}} \cdot 100 \qquad \textbf{(6.1)}$$

With A_{PEG} being the integral of the PEG protons, A_{PDMS} the integral of the PDMS protons, x the repetition units of the PDMS block ($x = 18$) and y the repetition unit of the PEG block (PEG$_{1k}$: $y = 26$, PEG$_{2k}$: $y = 48$, PEG$_{4k}$: $y = 88$, Jeffamine ED 900: $y = 12.5$).

$$\text{PEG content (wt. \%)} = \frac{n_{PEG} \cdot M_{n,PEG}}{n_{PEG} \cdot M_{n,PEG} + n_{PDMS} \cdot M_{n,PDMS}} \cdot 100 \qquad \textbf{(6.2)}$$

With n_{PEG} being the PEG content in mol of PEG being incorporated in the (ABAC)$_n$ segmented copolymer determined by ^{1}H-NMR and $M_{n, PEG}$ the molecular weight of the PEG segment (PEG$_{1k}$: $M_n = 1223$ g mol^{-1}, PEG$_{2k}$: $M_n = 2191$ g mol^{-1}, PEG$_{4k}$: $M_n = 3961$ g mol^{-1}, Jeffamine ED 900: $M_n = 894$ g mol^{-1}). n_{PDMS} and $M_{n, PDMS}$ are the corresponding PDMS content in mol and molecular weight of the PDMS segment ($M_{n, PDMS} = 1513$ g mol^{-1}).

Table A-6.1: DSC date of amphiphilic, physically crosslinked **PDMS-PEG$_{1k, 2k, 4k}$** and **PDMS-Jeffamine** copolymers. Data of 2nd heating and cooling are given.

| Amphiphilic copolymer	PEG segment		Hard segment		PEG segment		Hard segment	
	T_m[a] (°C)	ΔH_m[a] (Jg^{-1})	T_{cross}[a] (°C)	ΔH_m[a] (Jg^{-1})	T_{cryst}[a] (°C)	ΔH_{cryst}[a] (Jg^{-1})	T_{cryst}[a] (°C)	ΔH_{cryst}[a] (Jg^{-1})
PDMS-PEG (100/0)[b]	-	-	85.6	6.0	-	-	67.7	-5.1
PDMS-PEG$_{1k}$ (93/7)	-	-	83.4	1.4	-	-	70.6	-7.9
PDMS-PEG$_{1k}$ (59/41)	11.6	8.0	56.9	2.24	-26.2	-6.9	32.3	-5.3
PDMS-PEG$_{1k}$ (10/90)[c]	19.5	22.1	50.7	2.18	-11.9	-24.6	23.1	-2.8
PDMS-PEG$_{1k}$ (100/0)	28.6	36.2	49.0	1.0	-1.05	-44.7	-	-
PDMS-PEG$_{2k}$ (85/15)	34.0	8.6	85.6	1.5	-18.9	-7.02	73.7	-1.8
PDMS-PEG$_{2k}$ (43/57)	38.0	29.0	62.7	0.3	8.9	-29.0	37.6	-1.0
PDMS-PEG$_{2k}$ (12/88)	38.4	38.7	114.7	0.7	13.4	-38.8	84.1	-1.1
PDMS-PEG$_{2k}$ (0/100)	42.9	72.1	-	-	16.6	-69.8	-	-
PDMS-PEG$_{4k}$ (77/23)	46.5	18.8	89.0	1.0	11.7	-15.3	71.7	-0.9
PDMS-PEG$_{4k}$ (30/70)	47.2	45.1	89.0	0.3	16.1	-47.7	71.0	-0.5
PDMS-PEG$_{4k}$ (9/91)	55.1	84.0	-	-	23.7	-80.1	-	-
PDMS-PEG$_{4k}$ (0/100)	50.2	86.6	-	-	28.7	-84.4	-	-
PDMS-Jeffamine (92/8)	-	-	82.9	3.1	-	-	75.9	-2.2
PDMS-Jeffamine (62/38)	-	-	62.9	1.3	-	-	66.8	-2.1
PDMS-Jeffamine (22/78)	-	-	62.2	8.5	-	-	31.9	-6.1
PDMS-Jeffamine (0/100)	-	-	61.6	9.9	-	-	35.4	-9.10

[a] Determined by DSC with a heating/cooling rate of 10 K min^{-1}.

[b] **PDMS-PEG (100/0)** equals **1a**.

[c] Theoretical PEG content due to insufficient solubility for ^{1}H-NMR.

¹ Theoretical ratio due to insufficient
Solubility in CDCl₃ for ¹H-NMR
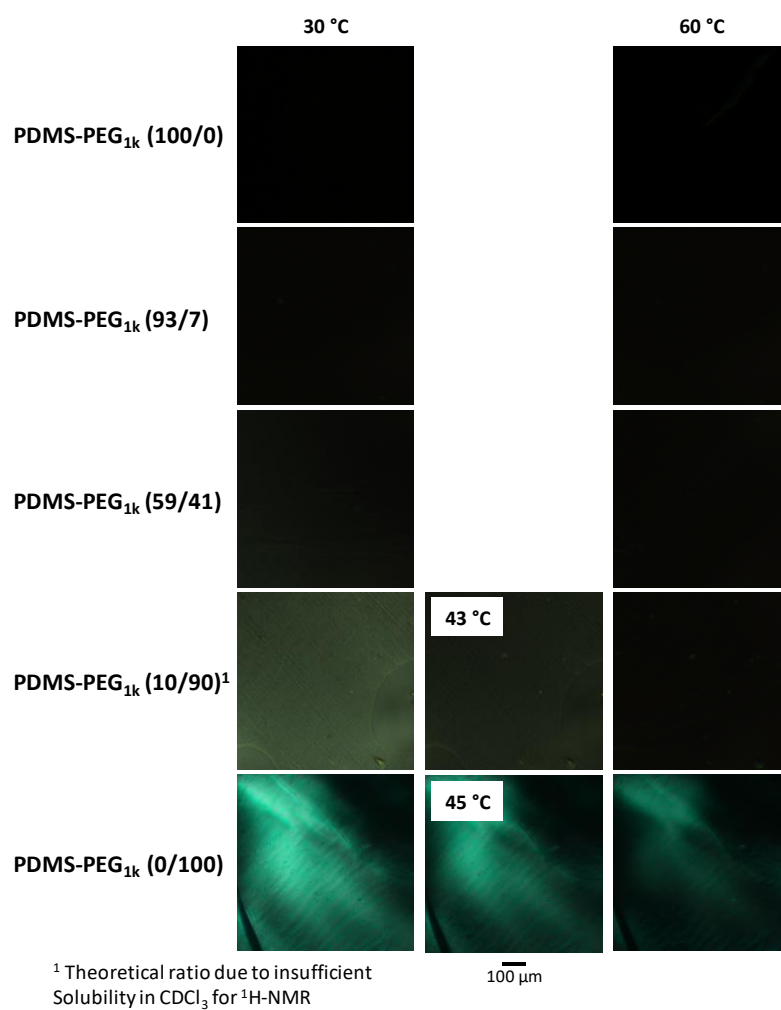
Figure A-6.21: Polarized optical light microscopy images upon heating (10 K min⁻¹) of reference materials **PDMS-PEG₁k (100/0)** and **PDMS-PEG₁k (0/100)** as well as of **PDMS-PEG₁k** copolymers with different ratios of PDMS to PEG₁k. **PDMS-PEG₁k (100/0)** is completely amorphous, while with increasing PEG₁k content crystallinity is observed at 30 °C. Melting of these crystallites is observed around 43 °C. The melting temperature is in the same range as for neat PEG₁k-diamine (T_m = 41 °C). For neat PEG₁k-urea copolymer **PDMS-PEG₁k (0/100)** there are still some crystalline structures observed at 60 °C assuming chemical crosslinking.
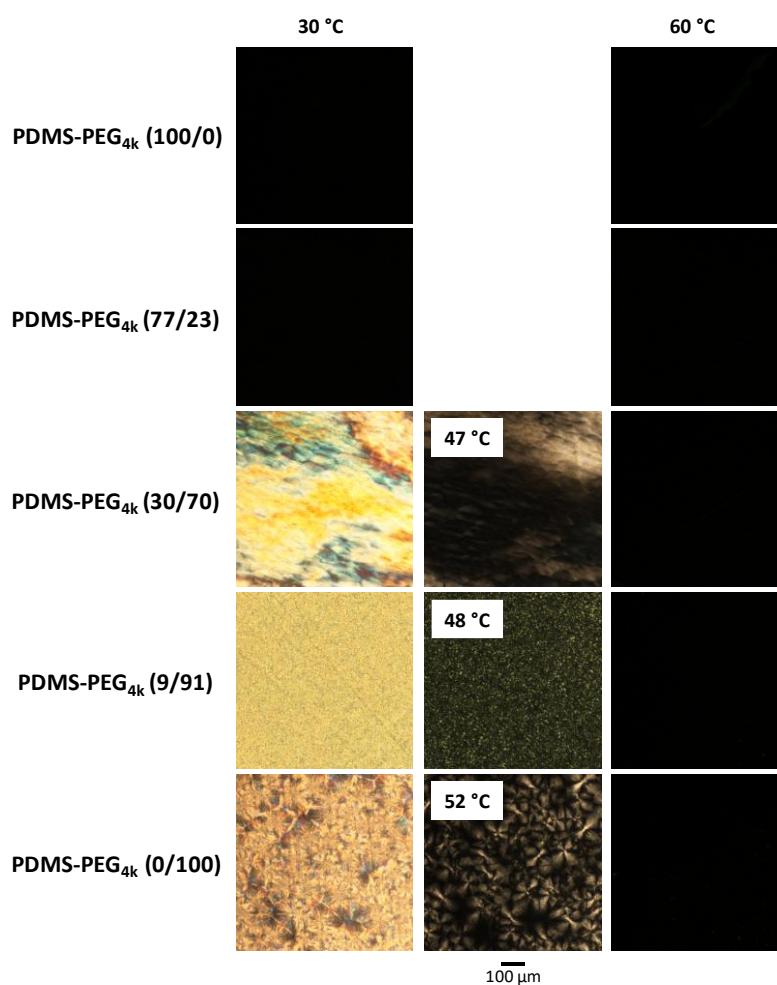
Figure A-6.22: Polarized optical light microscopy images upon heating (10 K min⁻¹) of reference materials **PDMS-PEG₄ₖ (100/0)** and **PDMS-PEG₄ₖ (0/100)** as well as of **PDMS-PEG₄ₖ** copolymers with different ratios of PDMS to PEG₄ₖ. **PDMS-PEG₄ₖ (100/0)** is completely amorphous, while with increasing PEG₄ₖ content crystallinity is observed. Melting of these crystallites is observed around 49 °C which is significantly lower than for neat PEG₄ₖ-diamine with T_m = 58 °C.
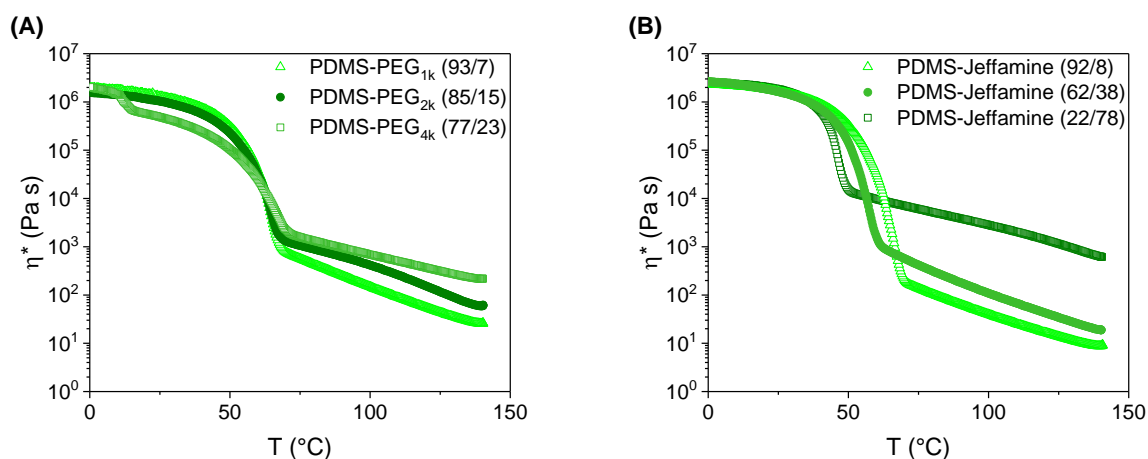
Figure A-6.23: (A) Complex viscosities η^* of **PDMS-PEG$_{1k}$ (93/7)**, **PDMS-PEG$_{2k}$ (85/15)**, and **PDMS-PEG$_{4k}$ (77/23)** as a function of temperature upon 1st cooling. With increasing PEG chain length, the viscosity increases at elevated temperatures. The crystallization of the PEG$_{4k}$ block results in an additional steep increase of the viscosity around 10 °C. **(B)** Complex viscosities of **PDMS-Jeffamine** copolymers with different built-in ratios of PDMS to Jeffamine as a function of temperature upon 1st cooling. The viscosity increases significantly with increasing Jeffamine content at elevated temperatures. Further for all amphiphilic copolymers the steep increasing viscosity is attributed to the aggregation of the urea hard segment. The complex viscosities were determined via oscillating shear rheology measurements (2 K min^{-1}, 1 Hz).
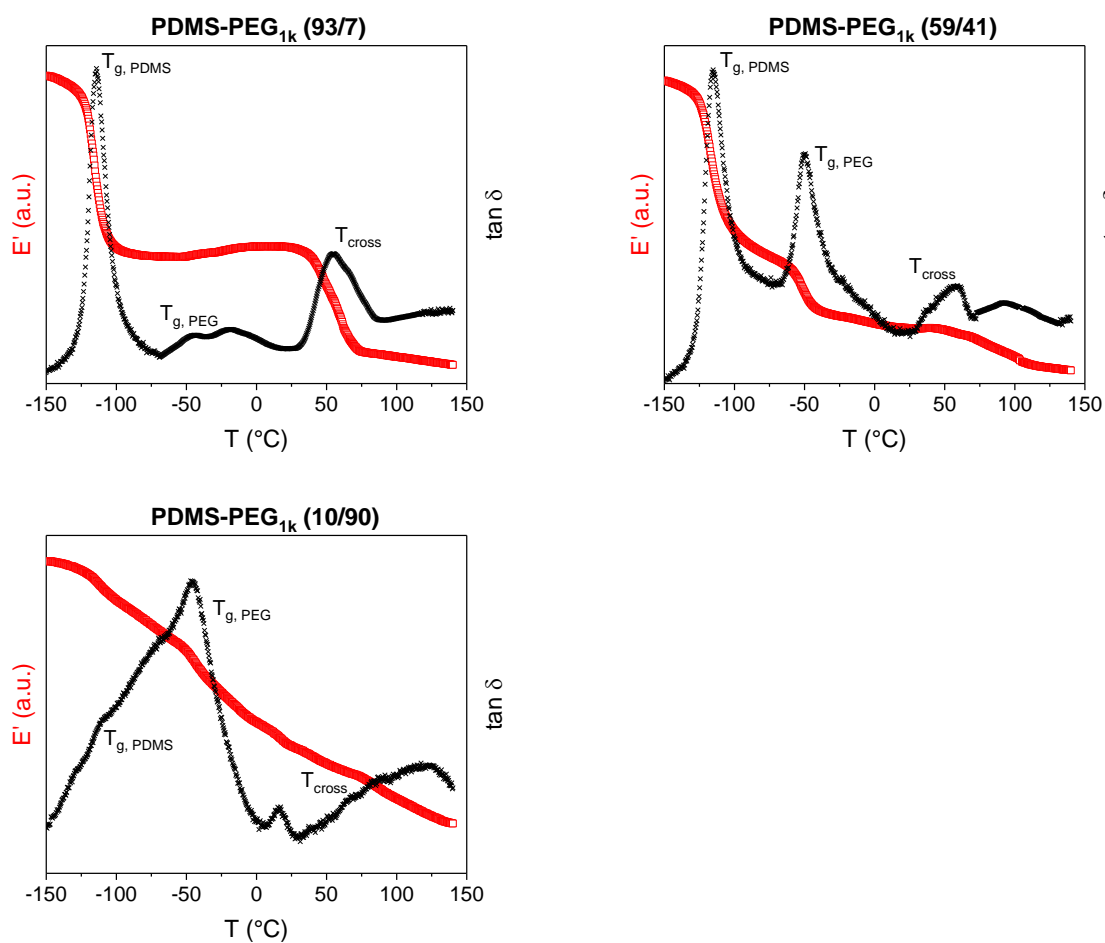
Figure A-6.24: Elastic storage modulus E' as a function of temperature upon 1st heating of **PDMS-PEG$_{1k}$** copolymers based on HMDI and different ratios of PDMS to PEG$_{1k}$ determined via a single cantilever bending experiment utilizing a metal specimen holder applying a heating rate of 5 K min^{-1} and a frequency of 2 Hz.
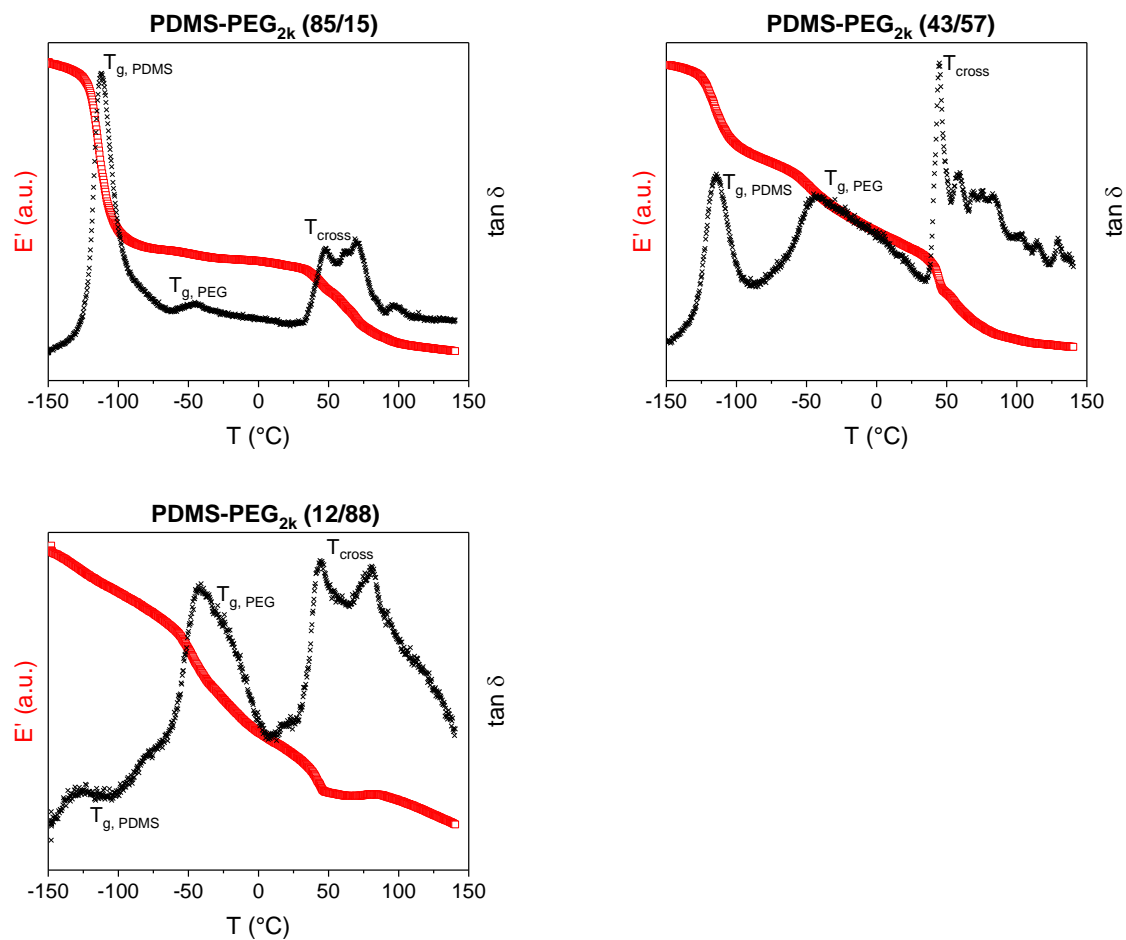
Figure A-6.25: Elastic storage modulus *E′* as a function of temperature upon 1st heating of **PDMS-PEG₂ₖ** copolymers based on HMDI and different ratios of PDMS to PEG₂ₖ determined via a single cantilever bending experiment utilizing a metal specimen holder applying a heating rate of 5 K min⁻¹ and a frequency of 2 Hz.
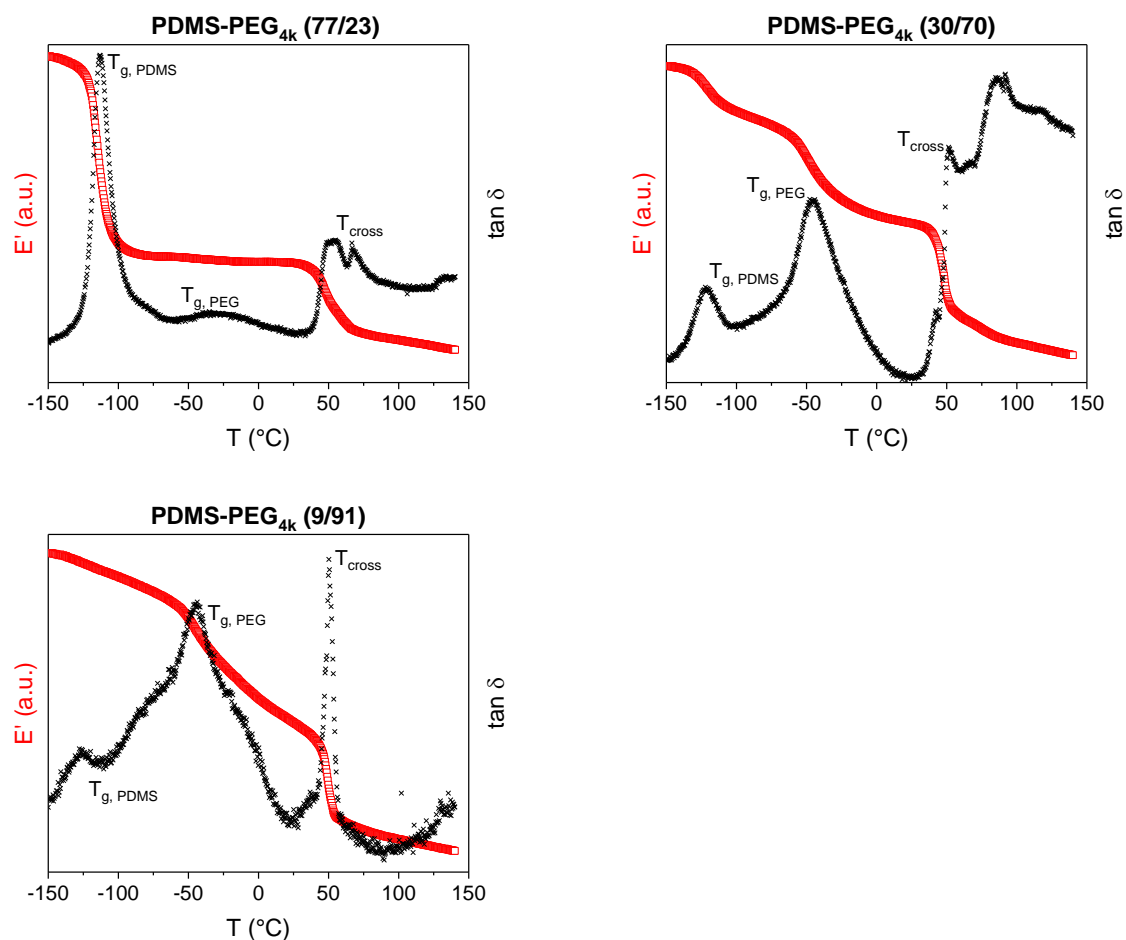
Figure A-6.26: Elastic storage modulus *E'* as a function of temperature upon 1st heating of **PDMS-PEG₄ₖ** copolymers based on HMDI and different ratios of PDMS to PEG₄ₖ determined via a single cantilever bending experiment utilizing a metal specimen holder applying a heating rate of 5 K min⁻¹ and a frequency of 2 Hz.
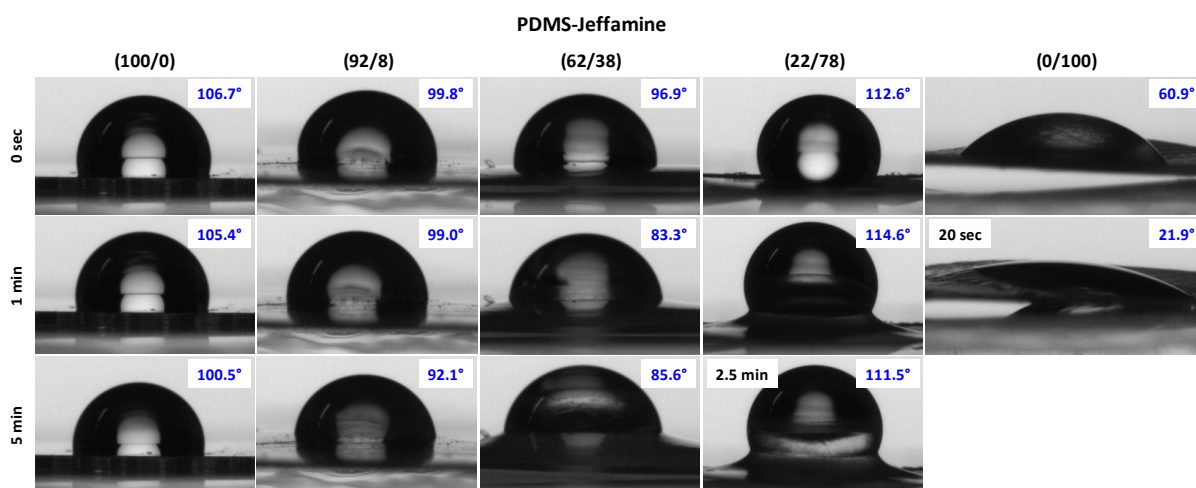
Figure A-6.27: Contact angle measurements of reference materials **PDMS-Jeffamine (100/0)** and **PDMS-Jeffamine (0/100)** and **PDMS-Jeffamine** copolymers with increasing Jeffamine content. The sessile drops are shown at different times indicating a rearrangement of the soft segments at the interface over time. The polymer films with a thickness of 30 - 80 µm were prepared by melt pressing (120 °C, 1 min, 100 bar). Detailed experimental data are included in chapter 5.2.

7. References

[1] Q. Guo (Ed.), *Thermosets: Structure, properties and applications*, Elsevier, Amsterdam, Netherlands **2018**.

[2] M. Szycher, *Szycher's Handbook of Polyurethanes*, CRC Press Taylor & Francis Group, Boca Raton, FL **1999**.

[3] S. Koltzenburg, M. Maskos, O. Nuyken, *Polymere: Synthese, Eigenschaften und Anwendungen*, Springer, Berlin, Heidelberg **2014**.

[4] B. Erman, J. E. Mark, C. M. Roland (Eds.), *The science and technology of rubber*, Academic Press, Waltham, Mass. **2013**.

[5] M. Matzner, A. Noshay, J. E. McGrath, *Trans. Soc. Rheol.* **1977**, *21*, 273.

[6] L. W. McKeen, *Fatigue and tribological properties of plastics and elastomers*, William Andrew, Amsterdam, Oxford **2010**.

[7] S. Fakirov, *Handbook of condensation thermoplastic elastomers*, Wiley-VCH, Weinheim, Great Britain **2005**.

[8] J. G. Drobny, *Handbook of thermoplastic elastomers*, William Andrew Publishing, Oxford, UK **2014**.

[9] D. Tyagi, G. L. Wilkes, I. Yilgr, J. E. McGrath, *Polym. Bull.* **1982**, *8*, 535.

[10] W.-F. Su, *Principles of Polymer Design and Synthesis*, Springer, Berlin, Heidelberg **2013**.

[11] Odian Georg, *Principles of Polymerization*, John Wiley & Sons, New York **2004**.

[12] G. Collins, J. Federici, Y. Imura, L. H. Catalani, *J. Appl. Phys.* **2012**, *111*, 44701.

[13] L.-H. Zhang, X.-P. Duan, X. Yan, M. Yu, X. Ning, Y. Zhao, Y.-Z. Long, *RSC Adv.* **2016**, *6*, 53400.

[14] N. Bhardwaj, S. C. Kundu, *Biotechnol. Adv.* **2010**, *28*, 325.

[15] S. Agarwal, M. Burgard, A. Greiner, J. Wendorff, *Electrospinning: A practical guide to nanofibers*, De Gruyter, Berlin, Boston **2016**.

[16] C. Mota, D. Puppi, F. Chiellini, E. Chiellini, *J. Tissue Eng. Regen. M.* **2015**, *9*, 174.

[17] S. C. Ligon, R. Liska, J. Stampfl, M. Gurr, R. Mülhaupt, *Chem. Rev.* **2017**, *117*, 10212.

[18] S. H. Huang, P. Liu, A. Mokasdar, L. Hou, *Int. J. Adv. Manuf. Technol.* **2013**, *67*, 1191.

[19] A. Boschetto, L. Bottini, *Int. J. Adv. Manuf. Technol. (The International Journal of Advanced Manufacturing Technology)* **2014**, *73*, 913.

[20] M. Jin, R. Giesa, C. Neuber, H.-W. Schmidt, *Macromol. Mater. Eng.* **2018**, *303*, 1800507.

[21] K. S. Prakash, T. Nancharaih, V. S. Rao, *Materials Today: Proceedings* **2018**, *5*, 3873.

[22] H. Kodama, *Revi. Sci. Instrum.* **1981**, *52*, 1770.

[23] C. R. Deckard, *Method and apparatus for producing parts by selective sintering US5017753A* **1990**.

[24] T. D. Brown, P. D. Dalton, D. W. Hutmacher, *Adv. Mater.* **2011**, *23*, 5651.

[25] S. Santoro, L. Russo, V. Argenzio, A. Borzacchiello, *J. Appl. Biomater. Biom.* **2011**, *9*, 127.

[26] A. Muntz, L. N. Subbaraman, L. Sorbara, L. Jones, *J. Optom.* **2015**, *8*, 2.

[27] J. Lee, G. Tae, Y. H. Kim, I. S. Park, S.-H. Kim, S. H. Kim, *Biomaterials* **2008**, *29*, 1872.

[28] C.-T. Chiu, J.-S. Lee, C.-S. Chu, Y.-P. Chang, Y.-J. Wang, *J. Mater. Sci: Mater. Med.* **2008**, *19*, 2503.

[29] S. Affattato, *Wear of orthopaedic implants and artificial joints*, Woodhead Publishing Limited, Cambridge **2012**.

[30] H. Brandon, K. Jerina, C. Wolf, V. L. Young, *Aesthet. Surg. J.* **2000**, *20*, 122.

[31] L. E. Fisher, A. L. Hook, W. Ashraf, A. Yousef, D. A. Barrett, D. J. Scurr, X. Chen, E. F. Smith, M. Fay, C. D. J. Parmenter, R. Parkinson, R. Bayston, *J. Control Release* **2015**, *202*, 57.

[32] H. Dong, G. M. Walker, *Smart Mater. Struct.* **2012**, *21*, 42001.

[33] Y. Wang, A. Guan, I. Isayeva, K. Vorvolakos, S. Das, Z. Li, K. S. Phillips, *Biomaterials* **2016**, *95*, 74.

[34] S. Strandman, X. X. Zhu, *Gels* **2016**, *2*, 1.

[35] R. Dong, Y. Pang, Y. Su, X. Zhu, *Biomater. Sci.* **2015**, *3*, 937.

[36] X. Du, J. Zhou, J. Shi, B. Xu, *Chem. Rev.* **2015**, *115*, 13165.

[37] M. Guo, L. M. Pitet, H. M. Wyss, M. Vos, P. Y. W. Dankers, E. W. Meijer, *JACS* **2014**, *136*, 6969.

[38] T. L. Sun, T. Kurokawa, S. Kuroda, A. B. Ihsan, T. Akasaki, K. Sato, M. A. Haque, T. Nakajima, J. P. Gong, *Nat. Mater.* **2013**, *12*, 932.

[39] J. Cui, M. A. Lackey, A. E. Madkour, E. M. Saffer, D. M. Griffin, S. R. Bhatia, A. J. Crosby, G. N. Tew, *Biomacromolecules* **2012**, *13*, 584.

[40] J. P. Gong, Y. Katsuyama, T. Kurokawa, Y. Osada, *Adv. Mater.* **2003**, *15*, 1155.

[41] R. E. Webber, C. Creton, H. R. Brown, J. P. Gong, *Macromolecules* **2007**, *40*, 2919.

[42] Y. Okumura, K. Ito, *Adv. Mater.* **2001**, *13*, 485.

[43] T. Sakai, T. Matsunaga, Y. Yamamoto, C. Ito, R. Yoshida, S. Suzuki, N. Sasaki, M. Shibayama, U.-I. Chung, *Macromolecules* **2008**, *41*, 5379.

[44] M. Song, Y. H. Shin, Y. Kwon, *J. Nanosci. Nanotechnol.* **2010**, *10*, 6934.

[45] Paul Böhm, *Functional Silicones and Silicone-Containing Block Copolymers*, Mainz **2019**.

[46] E. Yilgor, I. Yilgor, G. L. Wilkes, J. P. Sheth, *Segmented urea and siloxane copolymers and their preparation methods US 2008/0027201 A1* **2004**.

[47] R. Ward, J. Anderson, R. McVenes, K. Stokes, *J. Biomed. Mater. Res. Part A* **2006**, *77*, 580.

[48] P. Ducheyne, *Comprehensive biomaterials*, Elsevier, Amsterdam **2011**.

[49] K. E. Polmanteer, *Rubber Chem. Technol.* **1981**, *54*, 1051.

[50] K. E. Polmanteer, M. J. Hunter, *J. Appl. Polym. Sci.* **1959**, *1*, 3.

[51] E. Yilgör, I. Yilgör, *Prog. Polym. Sci.* **2014**, *39*, 1165.

[52] Ì. Yílgör, A. K. Sha'aban, W. P. Steckle, D. Tyagi, G. L. Wilkes, J. E. McGrath, *Polymer* **1984**, *25*, 1800.

[53] D. Tyagi, I. Yílgör, J. E. McGrath, G. Wilkes, *Polymer* **1984**, *25*, 1807.

[54] J. C. Saam, F. W. G. Fearon, *Ind. Eng. Chem. Prod. Res. Dev.* **1971**, *10*, 10.

[55] H. A. Vaughn, *J. Polym. Sci. B Polym. Lett.* **1969**, *7*, 569.

[56] A. Noshay, M. Matzner, C. N. Merriam, *J. Polym. Sci. A-1 Polym. Chem.* **1971**, *9*, 3147.

[57] D. Tyagi, G. L. Wilkes, I. Yilgör, J. E. McGrath, *Polym. Bull.* **1982**, *8*, 543.

[58] E. Yılgör, İ. Yılgör, E. Yurtsever, *Polymer* **2002**, *43*, 6551.

[59] E. Yilgör, E. Burgaz, E. Yurtsever, İ. Yilgör, *Polymer* **2000**, *41*, 849.

[60] I. Yilgör, E. Yilgör, G. L. Wilkes, *Polymer* **2015**, *58*, A1-A36.

[61] E. Yılgör, I. Yilgör, *Polymer* **2001**, *42*, 7953.

[62] I. Yilgor, T. Eynur, S. Bilgin, E. Yilgor, G. L. Wilkes, *Polymer* **2011**, *52*, 266.

[63] I. Yilgor, T. Eynur, E. Yilgor, G. L. Wilkes, *Polymer* **2009**, *50*, 4432.

[64] E. Yilgor, G. Ekin Atilla, A. Ekin, P. Kurt, I. Yilgor, *Polymer* **2003**, *44*, 7787.

[65] E. Delebecq, J.-P. Pascault, B. Boutevin, F. Ganachaud, *Chem. Rev.* **2013**, *113*, 80.

[66] G. Riess, M. S. Mendolia, H.-W. Schmidt, *Macromol. Symp.* **2002**, *181*, 123.

[67] G. Riess, H.-W. Schmidt, *Monatsh. Chem.* **2006**, *137*, 935.

[68] M. S. Mendolia, J. P. Vincenti, R. A. Esposito, H.-W. Schmidt, H. P. Chen, G. Riess, H.-J. Wu, *Zusammensetzung mit Wasserstoffbindenden Gruppen WO 97/036572* **1997**.

[69] J. M. Sirrine, S. A. Schexnayder, J. M. Dennis, T. E. Long, *Polymer* **2018**, *154*, 225.

[70] D. J. Buckwalter, M. Zhang, D. L. Inglefield, R. B. Moore, T. E. Long, *Polymer* **2013**, *54*, 4849.

[71] D. J. Buckwalter, D. L. Inglefield, J. S. Enokida, A. G. Hudson, R. B. Moore, T. E. Long, *Macromol. Chem. Phys.* **2013**, *214*, 2073.

[72] O. Colombani, L. Bouteiller, *New J. Chem.* **2004**, *28*, 1373.

[73] O. Colombani, C. Barioz, L. Bouteiller, C. Chanéac, L. Fompérie, F. Lortie, H. Montès, *Macromolecules* **2005**, *38*, 1752.

[74] N. E. Botterhuis, D. J. M. van Beek, G. M. L. van Gemert, A. W. Bosman, R. P. Sijbesma, *J. Polym. Sci. A Polym. Chem.* **2008**, *46*, 3877.

[75] S. Li, X. Kong, S. Feng, *RSC Adv.* **2015**, *5*, 90313.

[76] M. M. Coleman, M. Sobkowiak, G. J. Pehlert, P. C. Painter, T. Iqbal, *Macromol. Chem. Phys.* **1997**, *198*, 117.

[77] Y. Ni, F. Becquart, J. Chen, M. Taha, *Macromolecules* **2013**, *46*, 1066.

[78] W. P. Cox, E. H. Merz, *J. Polym. Sci.* **1958**, *28*, 619.

[79] T. G. Mezger, *The rheology handbook: For users of rotational and oscillatory rheometers*, Vincentz, Hannover **2006**.

[80] F.-S. Chuang, H.-Y. Tsi, J.-D. Chow, W.-C. Tsen, Y.-C. Shu, S.-C. Jang, *Polym. Degrad. Stab.* **2008**, *93*, 1753.

[81] A. Tasic, M. Pergal, M. Antic, V. Antic, *J. Serb. Chem. Soc.* **2017**, *82*, 1395.

[82] R. M. Versteegen, R. Kleppinger, R. P. Sijbesma, E. W. Meijer, *Macromolecules* **2006**, *39*, 772.

[83] L. Yang, Y. Lin, L. Wang, A. Zhang, *Polym. Chem.* **2014**, *5*, 153.

[84] A. Ballistreri, S. Foti, P. Maravigna, G. Montaudo, E. Scamporrino, *J. Polym. Sci. Polym. Chem. Ed.* **1980**, *18*, 1923.

[85] G. Hochleitner, E. Fürsattel, R. Giesa, J. Groll, H.-W. Schmidt, P. D. Dalton, *Macromol. Rapid Commun.* **2018**, *39*, e1800055.

[86] D. H. Merino, A. T. Slark, H. M. Colquhoun, W. Hayes, I. W. Hamley, *Polym. Chem.* **2010**, *1*, 1263.

[87] J. P. Sheth, A. Aneja, G. L. Wilkes, E. Yilgor, G. E. Atilla, I. Yilgor, F. L. Beyer, *Polymer* **2004**, *45*, 6919.

[88] A. Formhals, *Process and Apparatus for preparing artificial threads 1975504* **1934**.

[89] L. Larrondo, R. St. John Manley, *J. Polym. Sci. Polym. Phys. Ed.* **1981**, *19*, 909.

[90] L. Larrondo, R. St. John Manley, *J. Polym. Sci. Polym. Phys. Ed.* **1981**, *19*, 921.

[91] L. Larrondo, R. St. John Manley, *J. Polym. Sci. Polym. Phys. Ed.* **1981**, *19*, 933.

[92] H. Zhou, T. B. Green, Y. L. Joo, *Polymer* **2006**, *47*, 7497.

[93] E. Zhmayev, H. Zhou, Y. L. Joo, *J. Non-Newtonian Fluid Mech.* **2008**, *153*, 95.

[94] M. Dasdemir, M. Topalbekiroglu, A. Demir, *J. Appl. Polym. Sci.* **2013**, *127*, 1901.

[95] P. D. Dalton, M. L. Muerza-Cascante, D. W. Hutmacher, *Electrospinning: Principles, practice and possibilities*, Royal Society of Chemistry, Croydon **2015**.

[96] D. W. Hutmacher, P. D. Dalton, *Chem. Asian J.* **2011**, *6*, 44.

[97] P. D. Dalton, D. Grafahrend, K. Klinkhammer, D. Klee, M. Möller, *Polymer* **2007**, *48*, 6823.

[98] R. Nayak, I. L. Kyratzis, Y. B. Truong, R. Padhye, L. Arnold, *J. Mater. Sci.* **2012**, *47*, 6387.

[99] S. N. Malakhov, A. Y. Khomenko, S. I. Belousov, A. M. Prazdnichnyi, S. N. Chvalun, A. D. Shepelev, A. K. Budyka, *Fibre Chem.* **2009**, *41*, 355.

[100] A. Baji, Y.-W. Mai, S.-C. Wong, M. Abtahi, P. Chen, *Compos. Sci. Technol.* **2010**, *70*, 703.

[101] D. H. Reneker, A. L. Yarin, *Polymer* **2008**, *49*, 2387.

[102] S. Agarwal, A. Greiner, J. H. Wendorff, *Prog. Polym. Sci.* **2013**, *38*, 963.

[103] C. Subramanian, S. C. Ugbolue, S. B. Warner, P. K. Patra, *Mater. Res. Soc. Symp. Proc.* **2008**, *1134*, 33.

[104] G. Taylor, *Proc. Roy. Soc. A-Math. Phy.* **1969**, *313*, 453.

[105] Y. K. Kang, C. H. Park, H. Chang, K. Minn, C. Y. Park, *J. Appl. Polym. Sci.* **2008**, *110*, 3267.

[106] M. Demir, I. Yilgor, E. Yilgor, B. Erman, *Polymer* **2002**, *43*, 3303.

[107] E. Yilgor, O. Kaymakci, M. Isik, S. Bilgin, I. Yilgor, *Appl. Surf. Sci.* **2012**, *258*, 4246.

[108]   P. D. Dalton, J. Lleixà Calvet, A. Mourran, D. Klee, M. Möller, *Biotechnol. J.* **2006**, *1*, 998.

[109]   A. Karchin, F. I. Simonovsky, B. D. Ratner, J. E. Sanders, *Acta Biomater.* **2011**, *7*, 3277.

[110]   Q. P. Pham, U. Sharma, A. G. Mikos, *Tissue Eng.* **2006**, *12*, 1197.

[111]   C. Wei, J. Dong, *J. Micromech. Microeng.* **2013**, *23*, 25017.

[112]   C. Mota, D. Puppi, M. Gazzarri, P. Bártolo, F. Chiellini, *Polym. Int.* **2013**, *62*, 893.

[113]   G. Hochleitner, A. Youssef, A. Hrynevich, J. N. Haigh, T. Jungst, J. Groll, P. D. Dalton, *BioNanoMaterials* **2016**, *17*, 2387.

[114]   T. D. Brown, A. Slotosch, L. Thibaudeau, A. Taubenberger, D. Loessner, C. Vaquette, P. D. Dalton, D. W. Hutmacher, *Biointerphases* **2012**, *7*, 13.

[115]   B. L. Farrugia, T. D. Brown, Z. Upton, D. W. Hutmacher, P. D. Dalton, T. R. Dargaville, *Biofabrication* **2013**, *5*, 25001.

[116]   T. Jungst, M. L. Muerza-Cascante, T. D. Brown, M. Standfest, D. W. Hutmacher, J. Groll, P. D. Dalton, *Polym. Int.* **2015**, *64*, 1086.

[117]   J. Visser, F. P. W. Melchels, J. E. Jeon, E. M. van Bussel, L. S. Kimpton, H. M. Byrne, W. J. A. Dhert, P. D. Dalton, D. W. Hutmacher, J. Malda, *Nat. Commun.* **2015**, *6*, 6933.

[118]   G. Hochleitner, T. Jüngst, T. D. Brown, K. Hahn, C. Moseke, F. Jakob, P. D. Dalton, J. Groll, *Biofabrication* **2015**, *7*, 35002.

[119]   T. D. Brown, F. Edin, N. Detta, A. D. Skelton, D. W. Hutmacher, P. D. Dalton, *Mater. Sci. Eng. C, Materials for biological applications* **2014**, *45*, 698.

[120]   S. J. Kim, D. H. Jang, W. H. Park, B.-M. Min, *Polymer* **2010**, *51*, 1320.

[121]   H. Zhou, T. B. Green, Y. L. Joo, *Polymer* **2006**, *47*, 7497.

[122]   P. D. Dalton, K. Klinkhammer, J. Salber, D. Klee, M. Möller, *Biomacromolecules* **2006**, *7*, 686.

[123]   P. D. Dalton, J. Lleixà Calvet, A. Mourran, D. Klee, M. Möller, *Biotechnol. J.* **2006**, *1*, 998.

[124]   P. D. Dalton, N. T. Joergensen, J. Groll, M. Moeller, *Biomed. Mater. (Bristol, England)* **2008**, *3*, 34109.

[125]   N. Detta, T. D. Brown, F. K. Edin, K. Albrecht, F. Chiellini, E. Chiellini, P. D. Dalton, D. W. Hutmacher, *Polym. Int.* **2010**, *59*, 1558.

[126]   F. Chen, G. Hochleitner, T. Woodfield, J. Groll, P. D. Dalton, B. G. Amsden, *Biomacromolecules* **2016**, *17*, 208.

[127]   J. Lyons, C. Li, F. Ko, *Polymer* **2004**, *45*, 7597.

[128]   X. Wang, Z. Huang, *Chin. J. Polym. Sci.* **2010**, *28*, 45.

[129]   G. Hochleitner, J. F. Hümmer, R. Luxenhofer, J. Groll, *Polymer* **2014**, *55*, 5017.

[130]   Q. Sun, G. M. Rizvi, C. T. Bellehumeur, P. Gu, *Rapid Prototyping J.* **2008**, *14*, 72.

[131]   B. N. Turner, R. Strong, S. A. Gold, *Rapid Prototyping J.* **2014**, *20*, 192.

[132]   R. Melnikova, A. Ehrmann, K. Finsterbusch, *IOP Conf. Ser.: Mater. Sci. Eng.* **2014**, *62*, 12018.

[133]   S. H. Masood, K. Mau, W. Q. Song, *Mater. Sci. Forum* **2010**, *654-656*, 2556.

[134]   R. Singh, S. Singh, *J. Inst. Eng. India Ser. C* **2014**, *95*, 103.

[135]   Ostalb3D, https://www.ostalb3d.de/, 14.07.2020.

[136]   SainSmart, https://www.sainsmart.com/products/all-colors-tpu-flexible-filament-1-75mm-1kg-2-2lb-1, 21.08.2019.

[137]   FilamentWorld, https://www.filamentworld.de/shop/special-filament/flexibles-filament/tpu-filament-medium-extrudr-1-75-mm-rot/, 21.08.2019.

[138]   E. Fürsattel, *Polymer gradient materials on basis of urea-siloxane thermoplastic elastomers (Master thesis)*, University of Bayreuth **2016**.

[139]   T. D. Brown, P. D. Dalton, D. W. Hutmacher, *Prog. Polym. Sci.* **2016**, *56*, 116.

[140]   C. S. Kalra, M. Kossitsyn, K. Iskenderova, A. Chirokov, Y. I. Cho, A. Gutsol, A. Fridman, *Electrical discharges in the Reverse Vortex Flow – Tornado Discharges*, Taormina, Italy **2003**.

[141]   F. M. Wunner, M.-L. Wille, T. G. Noonan, O. Bas, P. D. Dalton, E. M. De-Juan-Pardo, D. W. Hutmacher, *Adv. Mater.* **2018**, *30*, e1706570.

[142]   T.-M. Wang, J.-T. Xi, Y. Jin, *Int. J. Adv. Manuf. Technol.* **2007**, *33*, 1087.

[143]   J. M. Chacón, M. A. Caminero, E. García-Plaza, P. J. Núñez, *Materials & Design* **2017**, *124*, 143.

[144]   C. S. Lee, S. G. Kim, H. J. Kim, S. H. Ahn, *J. Mater. Proc. Tech.* **2007**, *187-188*, 627.

[145]   V. Kishore, C. Ajinjeru, A. Nycz, B. Post, J. Lindahl, V. Kunc, C. Duty, *Addit. Manuf.* **2017**, *14*, 7.

[146]   N. Roy, E. Buhler, J.-M. Lehn, *Chemistry (Weinheim an der Bergstrasse, Germany)* **2013**, *19*, 8814.

[147]   K. U. Claussen, T. Scheibel, H.-W. Schmidt, R. Giesa, *Macromol. Mater. Eng.* **2012**, *297*, 938.

[148]   K. U. Claussen, R. Giesa, H.-W. Schmidt, *Polymer* **2014**, *55*, 29.

[149]   K. Min, J. Kwon Oh, K. Matyjaszewski, *J. Polym. Sci. A Polym. Chem.* **2007**, *45*, 1413.

[150]   X. Li, J. Xie, J. Lipner, X. Yuan, S. Thomopoulos, Y. Xia, *Nano letters* **2009**, *9*, 2763.

[151]   L. G. Bracaglia, B. T. Smith, E. Watson, N. Arumugasaamy, A. G. Mikos, J. P. Fisher, *Acta Biomater.* **2017**, *56*, 3.

[152]   S. Suresh, *Science* **2001**, *292*, 2447.

[153]   J. H. Waite, H. C. Lichtenegger, G. D. Stucky, P. Hansma, *Biochemistry* **2004**, *43*, 7653.

[154]   J. Genzer, *Soft matter gradient surfaces: Methods and applications*, Wiley, Hoboken, N.J **2012**.

[155]   P. Fratzl, H. S. Gupta, F. D. Fischer, O. Kolednik, *Adv. Mater.* **2007**, *19*, 2657.

[156]   K. U. Claussen, R. Giesa, T. Scheibel, H.-W. Schmidt, *Macromol. Rapid Commun.* **2012**, *33*, 206.

[157]   K. U. Claussen, E. S. Lintz, R. Giesa, H.-W. Schmidt, T. Scheibel, *Macromol. Biosci.* **2013**, *13*, 1396.

[158]   K. U. Claussen, M. Tebbe, R. Giesa, A. Schweikart, A. Fery, H.-W. Schmidt, *RSC Adv.* **2012**, *2*, 10185.

[159]   B. A. Glatz, M. Tebbe, B. Kaoui, R. Aichele, C. Kuttner, A. E. Schedl, H.-W. Schmidt, W. Zimmermann, A. Fery, *Soft matter* **2015**, *11*, 3332.

[160]   A. E. Schedl, C. Neuber, A. Fery, H.-W. Schmidt, *Langmuir* **2018**, *34*, 14249.

[161]   A. E. Schedl, P. T. Probst, C. Meichner, C. Neuber, L. Kador, A. Fery, H.-W. Schmidt, *Soft matter* **2019**, *15*, 3872.

[162]   S. Yu, Y. Sun, Y. Ni, X. Zhang, H. Zhou, *ACS applied materials & interfaces* **2016**, *8*, 5706.

[163]   E. Fuersattel, R. Giesa, H.-W. Schmidt, *Abstracts of Papers, 255th ACS National Meeting & Exposition, New Orleans, LA, United States, March 18-22, 2018, POLY-785* **2018**.

[164]   X. Hu, E. M. Wouterson, M. Liu, *Handbook of Manufacturing Engineering and Technology: Polymer Foam Technology*, Springer, London **2013**.

[165]   C. Okolieocha, D. Raps, K. Subramaniam, V. Altstädt, *Eur. Polym. J.* **2015**, *73*, 500.

[166]   S.-T. Lee, Chul B. Park, *Foam Extrusion*, Taylor & Francis Inc, Bosa Roca **2014**.

[167]   A. Mohebbi, F. Mighri, A. Ajji, D. Rodrigue, *Cellular Polymers* **2015**, *34*, 299.

[168]   F.-L. Jin, M. Zhao, M. Park, S.-J. Park, *Polymers* **2019**, *11*, 953.

[169]   D. Raps, N. Hossieny, C. B. Park, V. Altstädt, *Polymer* **2015**, *56*, 5.

[170]   M. Altan, *Recent Research in Polymerization: Thermoplastic Foams: Processing, Manufacturing, and Characterization*, InTech **2008**.

[171]   G. Wypych, *Handbook of foaming and blowing agents*, ChemTec Publishing, Toronto **2017**.

[172]   M. Mokhtari Motameni Shirvan, M. H. N. Famili, A. Golbang, *PAPT* **2016**, *4*, 11.

[173]   S. G. Bhoir, *Popular Plastics & Packaging* **2017**, *62*, 33.

[174]   P. A. Netti (Ed.), *Biomedical foams for tissue engineering applications*, Elsevier Woodhead Publishing, Amsterdam, Boston, Cambridge **2014**.

[175]   S. A. Guelcher, V. Patel, K. M. Gallagher, S. Connolly, J. E. Didier, J. S. Doctor, J. O. Hollinger, *Tissue Eng.* **2006**, *12*, 1247.

[176]   S. A. Guelcher, *Tissue Eng. Part B, Reviews* **2008**, *14*, 3.

[177]   J. Cremer, *Polyurethane foam containing silicone WO 2010/069821 A1* **2009**.

[178]   V. Stanjek, *Foams containing silicon WO 2003/080696* **2003**.

[179]   V. Stanjek, P. Ball, R. Weidner, J. Cremer, *Siliconhaltige Schaumstoffe DE 10 2006 013 416 A1* **2006**.

[180]   H. Ying, Y. Zhang, J. Cheng, *Nat. Commun.* **2014**, *5*, 3218.

[181]   G. Wang, G. Zhao, G. Dong, Y. Mu, C. B. Park, G. Wang, *Eur. Polym. J.* **2018**, *103*, 68.

[182]   G. M. Pawar, M. Koenigs, Z. Fahimi, M. Cox, I. K. Voets, H. M. Wyss, R. P. Sijbesma, *Biomacromolecules* **2012**, *13*, 3966.

[183]   Y. Cui, M. Tan, A. Zhu, M. Guo, *J. Mater. Chem. B* **2014**, *2*, 2978.

[184]   Y. Cui, M. Tan, A. Zhu, M. Guo, *J. Mater. Chem. B* **2015**, *3*, 2834.

[185]   N. Yang, H. Yang, Z. Shao, M. Guo, *Macromol. Rapid Commun.* **2017**, *38*, 1700275.

[186]   J. Mechau, *Dissertation*, Makromolekulare Chemie I, Universität Bayreuth **in preparation**.

[187]   D. J. Kinning, *J. Adhesion* **2001**, *75*, 1.

[188]   J. P. Sheth, E. Yilgor, B. Erenturk, H. Ozhalici, I. Yilgor, G. L. Wilkes, *Polymer* **2005**, *46*, 8185.

[189]   Y. Lin, D. He, H. Hu, P. Yi, X. Liu, J. Huang, S. Wu, G. Li, *ACS Appl. Bio Mater.* **2019**, *2*, 4377.

[190]   J. Cui, M. A. Lackey, G. N. Tew, A. J. Crosby, *Macromolecules* **2012**, *45*, 6104.

[191]   S.-J. Choi, J.-H. Lee, Y.-H. Lee, D.-Y. Hwang, H.-D. Kim, *J. Appl. Polym. Sci.* **2011**, *121*, 3516.

[192]   E. L. Decker, B. Frank, Y. Suo, S. Garoff, *Colloids and Surfaces A* **1999**, *156*, 177.

[193]   K.-Y. Law, *J. Phys. Chem. Lett.* **2014**, *5*, 686.

[194]   J. H. Park, Y. H. Bae, *Biomaterials* **2002**, *23*, 1797.

[195]   A. Schneider, G. Francius, R. Obeid, P. Schwinté, J. Hemmerlé, B. Frisch, P. Schaaf, J.-C. Voegel, B. Senger, C. Picart, *Langmuir* **2006**, *22*, 1193.

[196]   C. M. Segedin, *Mathematika* **1957**, *4*, 156.

[197]   I. Argatov, G. Mishuris, *Indentation testing of biological materials*, Springer, Cham, Switzerland **2018**.

[198]   M. de Ruijter, A. Hrynevich, J. N. Haigh, G. Hochleitner, M. Castilho, J. Groll, J. Malda, P. D. Dalton, *Small* **2018**, *14*, 1702773.

8. Acknowledgment

9. (Eidesstattliche) Versicherungen und Erklärungen

(§ 9 Satz 2 Nr. 3 PromO BayNAT)

Hiermit versichere ich eidesstattlich, dass ich die Arbeit selbstständig verfasst und keine anderen als die von mir angegebenen Quellen und Hilfsmittel benutzt habe (vgl. Art. 64 Abs. 1 Satz 6 BayHSchG).

(§ 9 Satz 2 Nr. 3 PromO BayNAT)

Hiermit erkläre ich, dass ich die Dissertation nicht bereits zur Erlangung eines akademischen Grades eingereicht habe und dass ich nicht bereits diese oder eine gleichartige Doktorprüfung endgültig nicht bestanden habe.

(§ 9 Satz 2 Nr. 4 PromO BayNAT)

Hiermit erkläre ich, dass ich Hilfe von gewerblichen Promotionsberatern bzw. -vermittlern oder ähnlichen Dienstleistern weder bisher in Anspruch genommen habe noch künftig in Anspruch nehmen werde.

(§ 9 Satz 2 Nr. 7 PromO BayNAT)

Hiermit erkläre ich mein Einverständnis, dass die elektronische Fassung meiner Dissertation unter Wahrung meiner Urheberrechte und des Datenschutzes einer gesonderten Überprüfung unterzogen werden kann.

(§ 9 Satz 2 Nr. 8 PromO BayNAT)

Hiermit erkläre ich mein Einverständnis, dass bei Verdacht wissenschaftlichen Fehlverhaltens Ermittlungen durch universitätsinterne Organe der wissenschaftlichen Selbstkontrolle stattfinden können.

……………………………………………………………………………….
Ort, Datum   *Unterschrift*